University College London

Mechanical Characteristics of Monopile Foundation in Sand for Offshore Wind Turbine

Nuo Duan

Department of Civil, Environmental and Geomatic Engineering

University College London (UCL)

A thesis submitted for the degree of

Doctor of Philosophy

September 2016

Abstract

The behaviour of monopile foundations for offshore wind turbines deviates from classical assumptions and accumulated experience mainly due to their large diameters and reduced slenderness. The offshore environment, which is characterised by a large number of load cycles from wind and waves, poses an additional challenge because cyclic loads may change the soil properties which in turn influence the pile's responses to the loads. Both of these issues are still not well understood and not being properly incorporated in current design guidelines.

In drained sands, the accumulating displacements can lead to foundation failure. In addition, the effects of long-term cyclic loading on the foundation's deformation and especially on its serviceability must also be studied.

The purpose of this work was to provide an insight into both aspects, by developing a reasonable numerical tool for the soil-pile interaction. In order to achieve these goals, the investigations were designed to firstly carry out a comprehensive literature review on related issues such as the *p-y* analysis, cyclic induced soil deformation and stiffness effects, and the simulation of soil foundation interaction by means of numerical model tests in a reduced scale using the Discrete Element Method (DEM).

Several DEM models were developed in this research, including (1) a modified method of generating specimens for 2D DEM centrifuge model, (2) DEM analysis of rigid pile installation effects (3) a micromechanics study of rigid monopile under monotonic loading using DEM, (4) a discrete element method centrifuge model of rigid monopile under cyclic lateral loads, (5) a 2D DEM rigid monopile model under combined loading condition (appendix).

Declaration

The work presented in this thesis was carried out at the Civil, Environmental and Geomatic Engineering Department, University College London from September 2012. This dissertation is the result of my own work and includes nothing which is the outcome of work done in collaboration except where specifically indicated in the text.

This thesis is not substantially the same as any that I have submitted for any degree, diploma or other qualification at any other University. No part of this thesis has been or is being concurrently submitted for any such degree, diploma or other qualification.

It is less than 50000 words long and contains less than 80 figures.

Nuo Duan

06/09/2016

Acknowledgements

Foremost, I would like to thank my principal supervisor, Dr Helen Cheng, for her excellent guidance, unflagging encouragement, and continuous advice throughout this research. Her wisdom and insight have guided to me to conduct research of interest. Without her support, this thesis would not have been possible.

I wish to extend my greatest gratitude to: Dr Susana Lopez-Querol, Dr Beatrice Baudet, Professor Itai Einav, Professor Junwei Liu, Professor Bin Zhu and Dr Xiaomin Xu for mentoring me throughout the course of my PhD study, and for their help and support. My sincere thanks also go to Professor Matthew Richard Coop, Dr Liang Cui for their kind advices, encouragement and valuable comments.

I would like to thanks all my friends and family, both in the UK and China, who have supported and encouraged me throughout the study. Finally, I am eternally grateful to thank my parents for their steadfast love and support, their financial and consistent love allowed me to stay abroad and successfully finish my research.

Nuo Duan

Table of Contents

List of Figures

List of Tables

Notation

a: the gradient of the regression line for a logarithmic scale

b_1, b_1: material parameters (determined in triaxial tests)

d_{pile} : diameter of pile

d_{10} : 10% particle diameter

d_{50} : 50% particle diameter

d_{60} : 60% particle diameter

d_l : distance of measurement circle overlap

d_{pd} : distance between the centre of pile and model boundary

d_{pp} : distance between the centres of two adjacent pile clump particles

d_{pile} : pile diameter

E: elasticity modulus

E_p: pile Young's modulus

E_s: elasticity modulus of the soil

E_{s1}: secant moduli of 1 cycle

E_{sN}: secant moduli of *N* cycles

F_L: the factor base upon cyclic load ratio

F_I: the factor base upon installation method

F_D: the factor base upon soil density

g : gravity

h_{model} : the height of model

H_{laterl} : the vertical applied load

k_1 : soil-pile stiffness at 1th cycle

k_n : particle normal contact stiffness

k_N : soil-pile stiffness at N^{th} cycle

k_s : particle shear contact stiffness

$K_{modulus}$: initial modulus of subgrade reaction

L_{pile} : pile length

$L_{embedded}$: pile embedded depth

I_p: moment of inertia of the pile

m : degradation parameter

m_r : the radius of measurement circle

M_R: the static moment capacity of the pile

N : number of cycles

N_s : the scaling number

n_p : the ratio of pile diameter to d_{50}

n_m : the ratio of model diameter to pile diameter

n_h : coefficient of soil reaction

$n_{h,1}$: the coefficient of subgrade reaction for the first cycle of load

$\tilde{P}_{mom}$: ultimate static lateral capacity of the pile from a monotonic test

p: soil reaction

P_{max} : maximum applied forces in cyclic loading

P_{min} : minimum applied forces in cyclic loading

P_R : maximum bearing capacity from the static test

P_u : ultimate resistance

P_{ud} : modified block flow failure of the soil at deeper levels

P_{us} : modified shear wedge failure

w_{model} : the width of model

$R_{rigidity}$: pile rigidity factor

R_d : average relative densities

T: the pile/soil relative stiffness ratio

T_b, T_c : dimensionless functions depending on the load characteristics and relative density

u : the displacement of pile bottom

y : displacement

y : penetration depth

$Y_{max,N}$: the displacement at the maximum horizontal load for the N^{th} cycle

$Y_{max,1}$: the displacement at the maximum horizontal load for the 1st cycle

x : the coordination of x plane

X : the cyclic stress ratio (dependent on the initial stress state (confining stress) and on the cyclic load level)

X_c : the cyclic stress ratio (in situ); 1 and 0 define states of loading and unloading; This parameter X characterizes the increase of the stress level in each element under cyclic load and can thus be used for the determination of the stiffness decrease. For the initial stress state (Index (0)) as well as for the state under action of the cyclic load (Index (1))

z_{depth} : distance to soil surface

α: controlled the relative contribution of soil resistance and deflection and was applied so change in p-y relation with depth could be incorporated. Changing the α factor provided no improvement in results, so a constant value of α = 0.6 was applied, making the method independent of depth

β : soil density

μ : friction coefficient of the particles

η : changes with the model parameters such as soil density, load characteristic and method of installation

ξ : installation method

ξ_{1b} : load amplitude

ξ_{1c} : characteristic of the cyclic loading

ξ_{2b}: a measure of the size of the cyclic loading

ξ_{2c}: quantifies the characteristics of the cyclic load

$\sigma_{1,f}$: main principal stress at failure in a monotonic test

$\sigma_{1,cyclic}$: the major principal stress for the cyclic stress state under consideration

σ_h: lateral soil stresses

ϕ : cyclic load ratio

γ': effective density

θ_1: rotation after the first load cycle

θ_N: rotation at *N* cycles

θ_s: rotation in a static test at a load equivalent to the one provided by the maximum cyclic Load

Ω : frequency band

ζ_b, ζ_c : load characteristic parameters

Chapter 1

Introduction

1.1 Background

The offshore wind industry is experiencing rapid expansion in many countries. This trend is driven by rising demand for renewable, sustainable and green energy sources and strong public support. Increasing political and social pressures to reduce carbon dioxide emissions and society's overdependence on fossil fuels have increased the need for sustainable energy sources such as wind energy (Doherty and Gavin, 2012).

Wind power currently offers a very competitive source of renewable energy, and therefore the market for offshore wind farms is projected to expand rapidly within the next decade. Building offshore wind turbines is an essential part of the European government strategy to achieve the target of 20% of energy from renewable sources by 2020 (Lombardi *et al*., 2011). Both the UK and Irish governments aim to provide 30-35% of their electricity generation from renewables by 2020 (Gavin *et al*., 2011).

The offshore wind industry currently relies on subsidy schemes by the government to be competitive with fossil-fuel-based energy sources. For the wind industry to survive, it is vital that costs are significantly reduced for future projects. This can be partly achieved by introducing new technologies and partly through optimization of existing technologies and design methods (Kallehave *et al*., 2015). One of the areas where costs can be reduced is in the support structure, where better designs, cheaper fabrication and quicker installation might all be possible.

The prevailing support structure design is the monopile structure, where the simple design is well suited to mass-fabrication and the installation approach, based on conventional impact driving, is relatively low-risk and robust for most soil conditions. The range of

application of the monopile for future wind farms can be extended by using more accurate engineering design methods, specifically tailored to offshore wind industry design.

Support foundations for offshore wind farms are generally more complex than for onshore, involving greater technical challenges such as design requirements to withstand the harsh marine environment and the long-term impact under large wave loading. In fact, various support foundation concepts employed in the wind industry (see Figure 1.1.1) have been adopted from the offshore oil and gas industry. The choice of foundation solution depends on local seabed conditions, water depth and financial constraints (Igoe *et al.*, 2013).

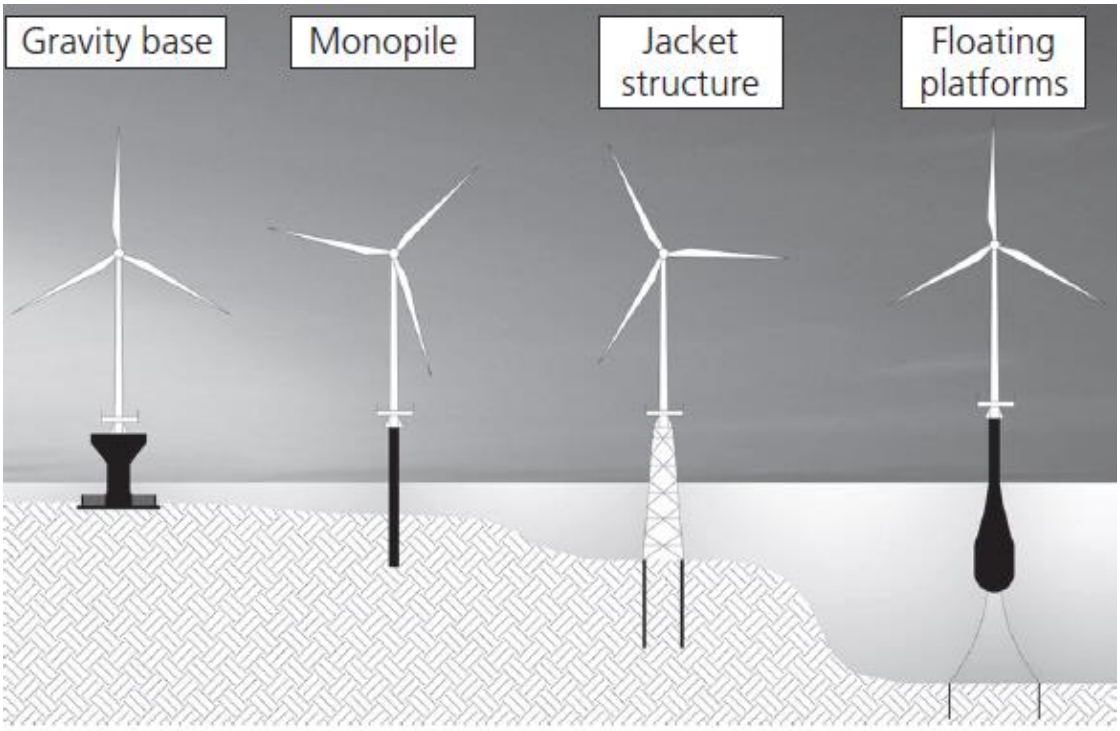

Figure 1.1.1 Foundation concepts for offshore wind turbines (Doherty and Gavin, 2012).

The most common type of support structure used so far is the monopile (see Figure 1.1.2). This type of structure is therefore the main focus point of this study. The current research will focus on investigating the complex behaviour of the offshore rigid monopile under the effects of various loadings and determining the governing soil mechanisms that control the

long-term accumulated rotation and deformation. Its focus lies exclusively on pile foundations embedded in sands.

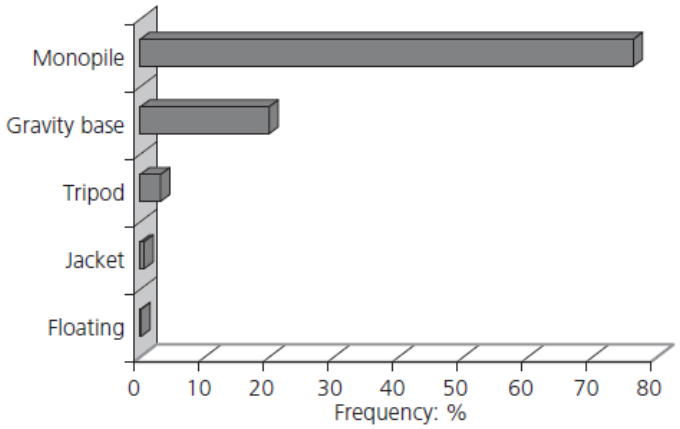

Figure 1.1.2. Foundation distribution for offshore wind turbines.(Doherty and Gavin, 2012)

Gravity base is the basic foundation for the oil and gas platform. Jacket structure is more suitable for deeper water and heavier turbines (Esteban *et al*., 2011, Fischer, 2011). In the future, it is expected that floating structures, which are currently under the research and development stage, will be widely used, especially for water depths greater than 50 m (Saleem, 2011). Such floating platforms for wind turbines will impose many new design challenges.

From the various foundation systems described above, only monopiles will be researched in this thesis since these are by far the most popular solution used worldwide, with 75% in share, compared to only 5% for jacket/tripod options (Achmus and Abdel-Rahman, 2005, Climate and Renewables, 2011). However, it is estimated that by 2020, between 50% and 60% of new offshore wind turbines (OWT) will be supported by monopiles and a further 35-40% by jacket/tripod systems. The main reason for this shift is the attraction of jacket/tripod systems for deeper sea locations, which provide consistently higher wind speeds and hence greater wind energy (Tempel and Molenaar, 2002).

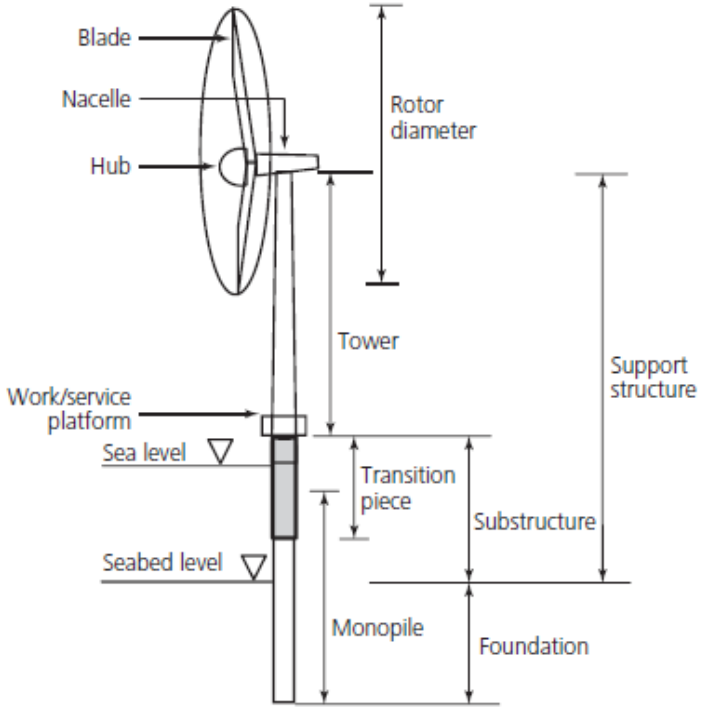

Figure 1.1.3. Foundation concepts for monopile (Arshad and O'Kelly, 2013).

Figure 1.1.3 shows the main components of an OWT system, including a typical monopile foundation, the substructure, transition piece, tower, rotor blades and nacelle (hub). The nacelle contains key electromechanical components of the wind turbine, including the gearbox and generator. The gearbox may cause efficiency losses for the wind turbine and is a particular source of noise. The substructure connects the transition piece or tower to the foundation at seabed level. The transition piece provides a means of correcting for any vertical misalignment of the foundation that may have occurred during its installation. In some cases, the foundation can extend to above the water surface, thereby also serving as a substructure by connecting directly to the transition piece or tower. The tower is made of a steel plate rolled into conical subsections that are cut and rolled into the required shape, and then welded together. The towers are usually manufactured in 20 m to 30 m sections, with transportation to the site being the limiting factor (Malhotra, 2010). OWTs are currently installed with either pitch-regulated blades or variable rotational speed systems in order to allow optimization of power production over a wide range of prevailing wind

speeds. The rotational speed of the main rotor shaft is typically between 10 and 20 rpm (Alderlieste, 2011, Malhotra, 2010). Most of the existing wind farms lie in relative shallow water, which is less than 10 m depth in most cases (total length of monopile from 30 m to 40m), and monopiles with diameters ranging from 2 to 4 m are used to support those 1.5-3.5 MW turbines (Peralta, 2010). Doherty *et al*. (2011) predicted that 70% of the wind farms, either in construction or in planning, will be located in deeper water in the future. In addition, larger diameter wind turbines are coming into service as they have a higher capacity of 5 to 7 MW. Since its introduction in the offshore, the monopile has become larger, heavier and has been installed in deeper depths. The diameter limit these days is around 6 m and there are already concepts of 7 m; the maximum weight can be as massive as 1000 tonnes. It was believed that monopiles could only be installed in water depths up to 25 metres but they were installed up to depths of 34 metres at the Greater Gabbard wind farm in 2011. This development can be attributed to the increasing diameters of the monopiles. According to experts, an increase in the diameter of the monopile by 1 metre generally means that the pile can be installed in water with depths 10 metres deeper. This implies that a 7 m diameter monopile might be installable in water depths around 40m (Saleem, 2011).

At present, monopiles are by far the most widely adopted substructure-foundation system for modern offshore wind farms located in shallow water depths ($\leqslant$40 m). Cyclic lateral and moment loading on the monopile are resisted by horizontal earth pressures mobilised in the surrounding soil along the monopile embedded length. The monopile embedment length is dependent on seabed characteristics and total applied load. An embedment length of 30 m is usually considered sufficient to meet design criteria, including vertical stability and horizontal deflection requirements which are set for the 10% pile diameter in most research (Tricklebank, 2008, Musial *et al*., 2006). Both deeper water depth and larger turbines will generate higher magnitude of wind and wave loading. All of these will increase the probability of extreme environmental conditions.

Criteria for rigid monopile behaviour have been proposed by various researchers (Poulos and Hull, 1989, Doherty and Gavin, 2012, Leblanc *et al*., 2010b, Klinkvort and Hededal, 2013). Table 1.1.1 summarised the rigid monopile characteristics.

Table 1.1.1 Rigid monopile characteristic

Parameters	Dimension of rigid monopile
Depth in seabed ($L_{embedded}$)	18-30 m (5-6 times the diameter)
Pile diameter (d_{pile})	5-6 m
Slenderness ratio ($L_{embedded}$ /d_{pile})	4-6
Elastic modulus of the soil (E_s)	1. <14 MPa (the transition from rigid to flexible pile behaviour occurs in the range from $E_s \approx 14$ MPa to $E_s \approx 1121$ MPa, this definition was followed the equation $4.8 < \left(\frac{E_s L^4}{E_p I_p}\right) < 388.6$ (Poulos and Hull, 1989, Leblanc *et al*., 2010b)) 2. <100 MPa (in very stiff sand) (Doherty and Gavin, 2012)
Pile wall thickness	0.05-0.07 m (Leblanc *et al*., 2010b)
Material	Steel (Klinkvort and Hededal, 2013)
Rigidity parameter ($R_{rigidity}$)	$R_{rigidity} = (\frac{E_p I_p}{E_s})^{0.25}$ (Poulos and Hull, 1989)

For the uniform soil which is having constant stiffness parameters with depth, Poulos and Hull (1989) suggested that a pile behaves rigidly if the length is less than $1.48R_{rigidity}$ and behaves flexibly if the length exceeds $4.44R_{rigidity}$. When the soil is a non-homogeneous soil where stiffness increases linearly with depth, form zero at the surface, this will be referred to as a "Gibson" soil. A pile behaves rigidly if the length is less than $1.1R_{rigidity}$ and behaves flexibly if the length exceeds $3.3R_{rigidity}$ (Poulos and Hull, 1989). In Figure 1.1.4,

the length normalised by the rigidity parameter ($L_{pile}/R_{rigidity}$) is plotted as a function of slenderness ratio (L_{pile}/d_{pile}) for piles with a wall thickness of 0.05m where L is L_{pile} , R is $R_{rigidity}$ and D is d_{pile}. Figure 1.1.4 (a) indicates that the monopiles with slenderness ratios in the range 4-6, and installed in loose sand (E_s = 10 MPa) are very likely to exhibit rigid failure according to the relationships proposed by Poulos and Hull (1989). However, for very stiff sand with an E_s value of 100 MPa, the failure mechanism is less certain (see Figure 1.1.4 (b)), with typical monopile geometries falling in the transition range between rigid and flexible behaviour.

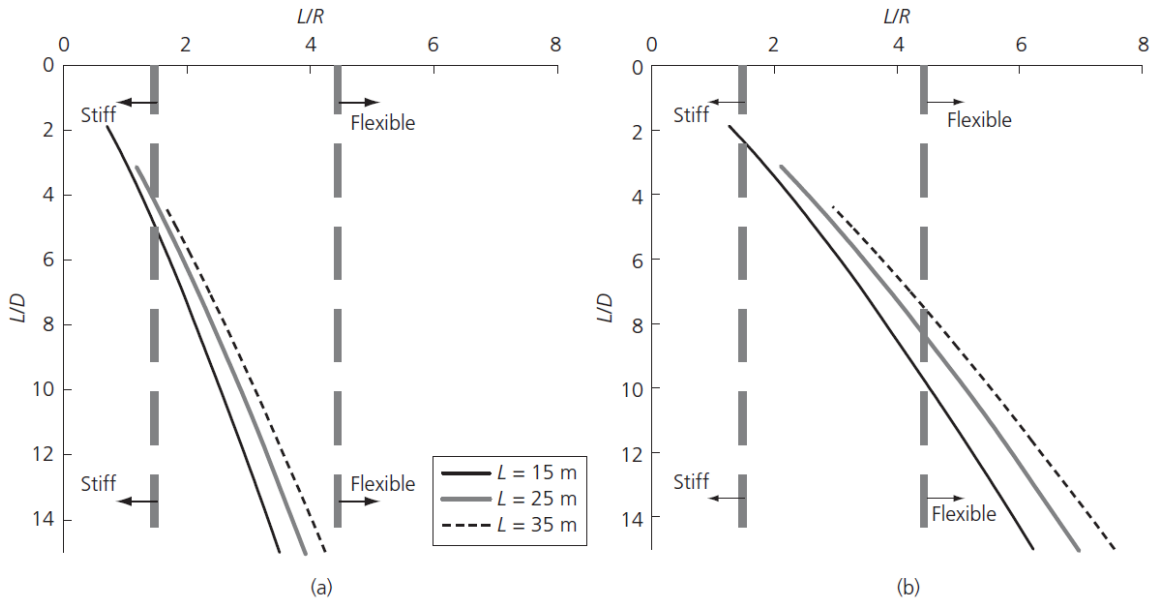

Figure 1.1.4 Pile failure mechanism for soils with (a) Es=10 MPa and (b) Es=100 MPa (Doherty and Gavin, 2012)

Poulos and Hull (1989) indicated that the rigid case would happen when the E_s < 10 MPa, however, Doherty and Gavin (2012) mentioned that the monopile behaviour tends toward the rigid case when the soil stiffness is significantly less than 100 MPa. On balance, the value of E_s (10 MPa) mentioned by Poulos and Hull (1989) is also falling in the range E_s < 100 MPa proposed by Doherty and Gavin (2012). By observations from model tests of monopiles installed in dense sand subjected to lateral loads, Leblanc *et al*. (2010b) also

pointed out that for most sands encountered the monopile behaviour tended toward the rigid case when the soil stiffness was significantly less than 100 MPa.

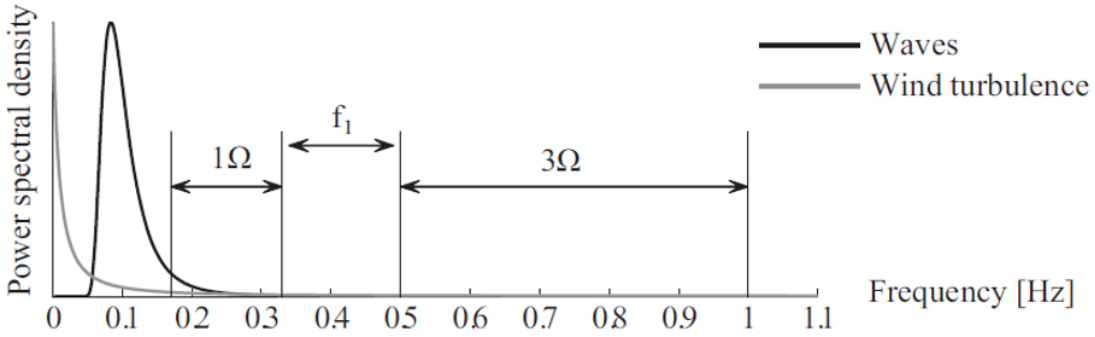

Figure 1.1.5. Typical excitation ranges of a modern offshore wind turbine (Leblanc, 2009).

Dynamic amplification and large excitation forces affect monopiles in a cumulatively unfavourable manner. Site-specific spectral densities for wind and waves can be derived from available measured data, met-ocean databases or numerical models. The excitation ranges, 1Ω and 3Ω, and the realistic normalised power spectra representing aerodynamic and hydrodynamic excitation are illustrated in Figure 1.1.5 (1Ω and 3Ω denote the frequency bands of the rotor rotation and the blade passing, typically in the range of 0.3 Hz and 1 Hz respectively.). So far, offshore wind turbines are designed with the first natural frequency, f_1, in the range between 1Ω and 3Ω. In the wind industry sector this is referred to as a "soft-stiff" structure. However, it is possible to design a "soft-soft" structure with the first natural frequency below 1Ω, or a "stiff-stiff" structure with the first natural frequency above 3Ω. The choice of frequency range for f_1 sets criteria for the stiffness of the foundation; in general, less steel is required for a soft structure. Also, a softer structure requires a smaller diameter of the tower and monopile body which reduce the hydrodynamic loads (Leblanc, 2009, Cui and Bhattacharya, 2015, Cuéllar, 2011, Arshad and O'Kelly, 2013). However, issues of fatigue or ultimate capacity may become the dominant design drivers (Leblanc, 2009). In addition, it is anticipated that each of these foundations will experience many millions of cycles of loading during their intended design

life of 25 to 30 years (Lombardi *et al*., 2013). Therefore, one of the biggest concerns with the design of monopiles is their behaviour under very large numbers of cycles of lateral and moment loads.

1.2 Monopile design guidelines API

The design of a monopile relies on standards and empirical data originating from the offshore oil and gas sector. However, the loading of an OWT is very different, in both magnitude and character, from that of the oil and gas installations. The completed structure is subjected to a large number of cyclic, lateral and moment loads (due to both wind and wave loading) in addition to axial loads. Compared with the platform of the oil and gas sector, the type of cyclic loading is different from other forms of cyclic loading such as earthquake loading in terms of frequency, amplitude, and number of cycles. The cyclic loading occurs not only during extreme conditions but also during normal service conditions. This can lead to an accumulated rotation of the wind turbine tower, adversely affecting its ultimate strength or fatigue life. Therefore it is of great importance to investigate the effects of cyclic loading to monopile (Leblanc *et al*., 2010). The inadequacy of the current methodology for predicting the cyclic loading response of pile means that improved models, incorporating factors affecting the cyclic behaviour, must be developed. A series of recommended practices for OWT has been published through the American Petroleum Institute (API) under their Subcommittee on Offshore Structures (API, 1969, API, 2000, API, 2007). Several design and certification guidelines for offshore wind turbines have been developed. Most of them are based on the experience from offshore wind turbines installed in European coastal areas. Of these guidelines, Det Norske Veritas (DNV) also is the general design code for offshore wind turbine structures, but in practice much focused on bottom-fixed structures. In DNV, an installation tolerance is specified together with a tolerance for the total rotation owing to installation and permanent accumulated deformations. This is usually expressed as a requirement to the rotation or tilt of the pile at the pile head, where the pile head is defined as the position along the pile in

level with the seabed. If, for example, the tolerance for the total rotation at seabed is 0.5° and the installation tolerance at seabed is 0.25°, then the limit for the permanent accumulated rotation becomes 0.25° at seabed.

The API is a leader in the development of petroleum and petrochemical equipment and operating standards. These standards represent more than 60 years of industry design experience. Many API standards have been incorporated into state and federal regulations and adopted by the International Organization for Standards (ISO) for worldwide acceptance. Originally, API developed by O'Neill and Murchison (1983) was based on the model of an elastically supported beam with non-linear springs for the lateral load-deflection. The relationship between the lateral stress *p* and the lateral displacement *y* was then called the "*p-y* curve". However, the development of *p-y* relationship relies to a high degree on empiricism, using data obtained primarily from two full-scale load tests reported by Cox *et al*. (1974). These tests were conducted using two slender piles, with diameter 0.61 m and length 21 m. The piles were subjected to static and cyclic lateral load. To assess the validity of the method, systematic studies were conducted by Murchison and O'Neill (1984), which proved the method to be superior to other methods. However, the validity of the method relies on very few tests on relatively flexible driven steel piles subjected to cyclic loading.

$$p(y) = A\,P_u(z)\,tanh\left(\frac{K_{modulus}z}{A\,P_u}y\right)$$

1.2.1

For the API *p-y* formulation shown in equation 1.2.1, there are four important governing parameters:

- Ultimate resistance P_u

Ultimate resistance at a given depth is determined by the minimum of P_{us} (modified shear wedge failure) and P_{ud} (modified block flow failure of the soil at deeper levels). The *C* coefficient can be chosen from Figure 1.2.1.

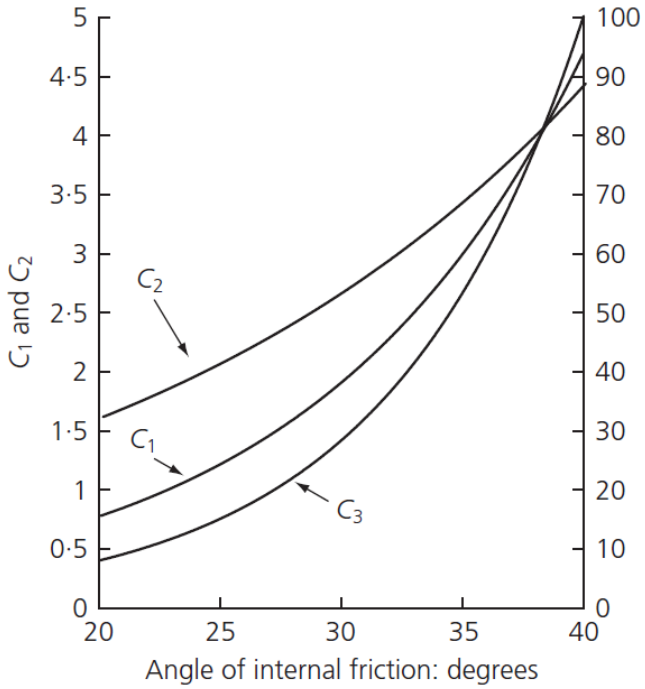

Figure 1.2.1. C coefficients and for API RP2A (API, 2007).

$$P_u = min\ (P_{us}, P_{ud})$$

1.2.2

$$P_{us} = (C_1 z_{depth} + C_2 d_{pile})\gamma z_{depth}$$

1.2.3

$$P_{ud} = C_3 d_{pile} \gamma z_{depth}$$

1.2.4

- Initial modulus of subgrade reaction $K_{modulus}$

The applied initial subgrade reaction modulus is obtained from Meyer and Reese (1979) and directly evaluated from Reese *et al*. (1974). The initial subgrade reaction modulus is defined from the theory of linear elasticity (Terzaghi, 1955).

- The initial stiffness distribution with depth z_{depth}

z_{depth} is the distance to soil surface. The current *p-y* formulation assumes the initial stiffness to increase linearly with depth, however, as is well recognised for sand, and the response is governed by the isotropic stress level.

- The representation of the strain level

The effect of long-term cyclic loading of monopiles placed in sand is possible to be a critical design factor and the effect of change in load characteristics, sand parameters, and the number of load cycles have not been properly examined. Lateral and moment cycling increase pile head stiffness, independently of the relative density. This contrasts with the current degradation of API *p-y* curves to account for load cycling. The cyclic *p-y* envelope curves do not account for any cyclic load characteristics or number of cycles. Initial stiffness of the *p-y* curve is independent of the pile diameter d_{pile} and increases linearly with depth z_{depth}. More consistent results are apparently obtained by making the initial stiffness less sensitive to depth in sands and more dependent on the pile diameter (Sørensen *et al*., 2010). Doherty and Gavin (2012) found that for loads above 50 kN the API method would be expected to under predict the moment resistance of the pile as the lateral load resistance was significantly under estimated.

API *p-y* formulation does not properly account for changes in strain levels in the soil as a result of diameter variations. Moreover, the formulation seems to provide a poor representation of the small strain stiffness variation with depth and the rate of stiffness degradation with increasing shear strain. API also assumes the pile to exhibit a Rankine-type failure in determining P_U. This assumes that a frictionless interface exists between the pile and the soil (or that the pile is perfectly smooth), whereas in reality the pile will exhibit friction as the sand flows around the pile shaft (Doherty and Gavin, 2012). Achmus and Abdel-Rahman (2005), Achums (2008) and Augustesen *et al*. (2010) had compared static lateral load-deflection predictions made for large monopiles in sands under monotonic loading by both finite element and *p-y* calculations, reporting that the standard API method might not be appropriate for assessing pile head deflections.

The rigid mode of failure gives rise to considerable doubts on the validity of applying the existing *p-y* curves (which were developed to match the response of flexible piles) used to predict the behaviour of offshore monopiles. API needs to be calibrated for rigid pile behaviour to determine the initial stiffness and ultimate capacity (Doherty and Gavin, 2012), and this research will only focus on rigid pile.

1.3 Highlights on monopile research

While large-diameter monopile foundations are able to withstand larger self-weight, higher cyclic horizontal loading and more harsh loading conditions, the applicability of the present methods is questioned by various researchers (Achmus *et al*., 2010, Leblanc *et al*., 2010a, Leblanc *et al.*, 2010b, Lesny, 2010, Rasmussen *et al*., 2013). Moreover, there is generally a poor level of consideration given to the key aspects of the long-term behaviour of piles subjected to cyclic loading in current practice (for example, API and DNV). An improved design method is required that can be specifically used for the design of large-diameter monopiles.

Bond and Jardine (1991) reviewed the problems of measuring local (radial and shear) stresses accurately on displacement pile shafts, demonstrating that very stiff cells that conform very closely with the pile surface are required to obtain meaningful information, particularly in stiff soils, while they also showed that reliable local stress measurements are critically important in testing alternative hypotheses regarding the effects of pile installation, equalization and (static or cyclic) load testing. It is very difficult to get the constitutive model of particles from site experiments. Zhu *et al*. (2009), Jardine *et al*. (2009) reinforced the same points.

Klinkvort (2013) has summarised that the main limitation of the current design methodology for monopiles is that it uses a semi-empirical approach, based on testing on slender piles. Using a semi-empirical approach that is not calibrated to the given pile

behaviour should be avoided. The monopile foundation for offshore wind turbines tends to behave in a more rigid way. This is illustrated in Figure 1.3.1, showing a comparison between a rigid pile and a slender pile. It can be seen that a rigid pile tends to rotate around a rotation point and thereby generates soil pressure over the total length of the pile. A slender pile will not have a single rotation point, rather the pile deflects around multiple rotation points. The load is mainly taken by the upper layers and no deflection will develop at the pile toe. The effect of moving from a slender pile behaviour to a more rigid pile behaviour can change the response of the pile (Poulos and Hull, 1989). The main differences between the original test piles and the piles used today for wind turbines are; a) the diameter of the piles is 5-10 times larger, b) they behave in a rigid way and c) the ratio between moment and shear force is much larger. The main effects have to be investigated in order to verify that the current practice is valid also for rigid large diameter monopiles for offshore wind turbines.

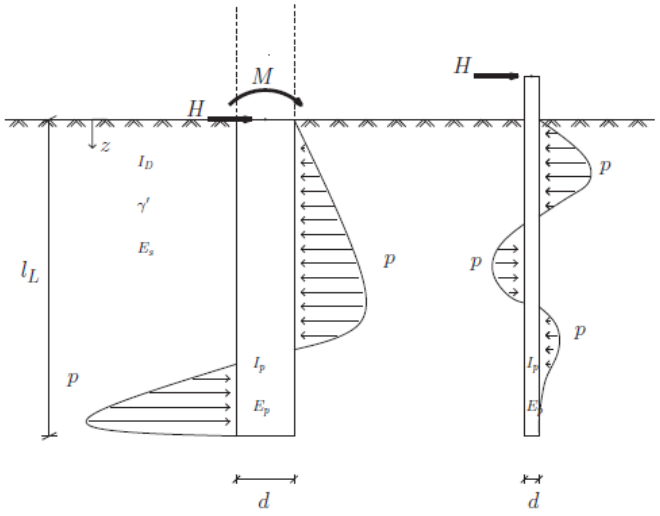

Figure 1.3.1. Rigid pile vs slender pile (Klinkvort, 2013).

From the literature, the capacity of monopile, deformation and phenomenon of loading were analysed. The lateral design of the large-diameter monopile required for OWT is normally governed by the deformational behaviour rather than by the ultimate resistance. This is because the strict serviceability conditions for pile-head rotation and for the

structure's inclination normally imply soil reactions well below the ultimate lateral resistance (Lesny, 2008).

API currently assumed that the soil stiffness will not degrade with time. However, accumulation of displacement and change in stiffness of the soil-pile system are possible over time due to cyclic loading. The relation between the cyclic loading and its parameters, such as the number of load cycles and the load amplitude is not considered in the design standards (Rasmussen *et al*., 2013). Although the cyclic parameter A=0.9 is introduced, the applicability to the large diameters of the monopile is not confirmed yet. The consideration of a cyclic loading by the factor 0.9, independent of amplitude, number of cycles and soil conditions, seems to be oversimplified. An attempt was made to derive corrections to the initial stiffness of the API *p-y* curve by adding both a stress-level and a diameter correction (Kallehave *et al*., 2012). The predicted displacement patterns are sensitive to most parameters, including very small strain stiffness, rate of stiffness degradation, and anisotropy. A need for modification of particularly the small strain stiffness variation with depth and the rate of stiffness degradation with increasing shear strain is required to obtain a more accurate determination of the soil stiffness for large-diameter piles.

Although some researches on large-diameter monopile foundation behaviour have been carried out using the FEM, this approach was not able to explain the micro mechanism. Therefore, it is important to understand the soil mechanism around monopiles.

The impact of cyclic loading depends on the loads applied and the interactions between the soil, foundation and structure. During the cycle loading tests, there also are many influential factors, such as: the pile aspect ratio (L_{pile}/d_{pile}), the pile-end soil conditions, the cyclic loading period, the soil stiffness, the responding accumulating displacements and the sequences in which different batches of cycles are applied. These factors will be the core parameters for the investigation in this research. Furthermore, there is an uncertain interdependence of the soil stiffness and the cycle number. For example, the long-term cyclic loading acting on the foundation may change the soil stiffness. However, this hypothesis will need to be verified by further research that targets longer data records. In

summary, the current design methodology is not capable of predicting either the effects of soil densification or the long-term movements of the monopile.

In this project, software PFC-2D will be used to model a framework applied to explore how cyclic loading could impact on a typical large offshore wind turbine pile, considering realistic foundation conditions and pile shape in soil-structure analyses.

1.4 Motivation and aim of this project

In the literature, there is an abundant number of experimental studies and macroscopic analytical models for soil-pile interactions, but seldom analyses of soil behaviour around the pile under cyclic lateral loading in the microscopic view. The core objective of this project is trying to use micromechanical research method to study the large scale problems, establish a connection between micromechanics and micro phenomenon. This research focuses on the investigating of the sand properties around the monopile when it is subjected to lateral cyclic loading. At the same time, it will gather detailed micromechanical information for a better understanding of the complex phenomena related to the pile-soil interaction. This will not only improve the current understanding of the behaviour of monopile under cyclic loading, it also assists the experimentalists to design better experiments in order to capture the appropriate information around the soil.

The following are the detailed objectives of the project:

1. To build a reliable numerical DEM soil model and sample which can be used for the cyclic loading test, and this model and sample can be compared to existing experiment results.
2. To understand and explain the physical phenomena during the pile installation.
3. To understand and explain the physical phenomena surrounding a pile when it is subjected to the lateral, vertical and combined loads.

4. To understand and explain the long term performance of wind farm foundations when subjected to a large number of loading cycles.
    4.1. What is the general trend of pile displacement due to cyclic lateral loading in the long term?
    4.2. What are the main factors that influence the generation of accumulated rotation and what is their relevance for the overall behaviour of the pile?
    4.3. What are the mechanical explanations of the main physical phenomena occurring in the surrounding sand in the long term?

1.5 Thesis outline

The whole thesis is divided into seven chapters. Chapter 1 is the introduction that explains the background information from literature and the motivation of this project. This introduces the analysis of the limitations of the current design approach, the gap between the current major researches, and the open questions in the offshore wind farm field.

In Chapter 2 the research methodology is mainly described and computational algorithms used in the DEM simulations are briefly introduced. This is followed by four chapters (Chapters 3-6) which report the results of the DEM simulations that have been performed during the PhD research programme. Each of these chapters includes a literature review of corresponding experimental work and/or DEM simulation work.

Chapter 3 provides results of model and sample preparation. In both cases all the simulations were performed with the mean stress held constant. The effects of pile installation are reported in Chapter 4. Chapters 5 and 6 present the monotonic loading and cyclic loading respectively. Finally, in Chapter 7, some conclusions on the work presented in this thesis are provided and further developments are suggested.

Chapter 2

Research methodology

2.1 Experimental methods

For the experimental research methods, there are several main methods such as: in situ tests, 1-g tests and centrifuge tests. Experimental approaches for in-situ test interpretations include the construction of reconstituted deposits of sands or clays with varied setups, stress regimes, and histories. These include small experimental setups with optical measurements or radiography (e.g. Allersma (1988), large 1-g model calibration chambers (e.g., Schnaid and Houlsby (1992), or centrifuge deposits subjected to miniature in-situ testing in flight (e.g., Esquivel and Silva (2000). Field prototypes can also be built, instrumented, installed, and load tested for two levels of interpretation: (1) collection of in-situ test data and information and (2) direct measurement of the full-scale response, e.g., retrieval Imperial College test pile (Jardine *et al*., 1998). The experimental methods will be detailed and discussed in the following chapters, such as: Chapter 4, sections 4.2.1.1, 4.2.2.2 and 4.2.3.1. Below is given a brief description of the centrifuge tests which were carried out by Klinkvort (2013). Due to the detailed test procedures provided by him and the suitable dimensions of the model and pile, this centrifuge test was chosen to be modelled by using DEM in this research.

In the centrifuge tests of Klinkvort (2013), the soil sample was placed in a centrifuge to ensure stress similarity. The centrifuge tests were all performed in drained dense homogeneous Fontainebleau sand with a relative density of approximately 90%, in order to model the North Sea offshore conditions. The rotation of the centrifuge introduces an increased gravitational force. The beam centrifuge facility was constructed at Danish Technological University (DTU) in 1976 (see Figure 2.1.1). The capacity of the beam centrifuge is approximately 100 g ton and is capable of providing an artificial gravitation of around 90g. The maximum arm or radius of the centrifuge is 2.63 m. The increase in

gravity (η) can be calculated from Newton's second law of motion as $\eta = R\omega^2/g$. Where R is the radius to the point of interest, ω is the rotational frequency and g is the natural gravitational acceleration. The model closed-end monopile was placed in the soil container and a loading actuator was mounted on top of the soil barrel. The load setup allowed for in-flight installation and lateral loading with a high load eccentricity to simulate full-scale conditions better and because the initial observation reported by (Klinkvort *et al*., 2010, Klinkvort and Hededal, 2010) indicated that it was important to the modelling.

Figure 2.1.1. Photograph of the geotechnical centrifuge at DTU under testing (Klinkvort, 2013).

The monopile was installed in-flight by a jack with a deformation controlled rate of 2 mm/s. The electrically powered jack has a capacity of 20 kN. The pile ready for installation is shown in Figure 2.1.2 (a). After monopile installation, the jack was removed and a beam had to be mounted for lateral loading. The fully equipped monopile, which was ready for lateral load testing is shown in Figure 2.1.2 (b).

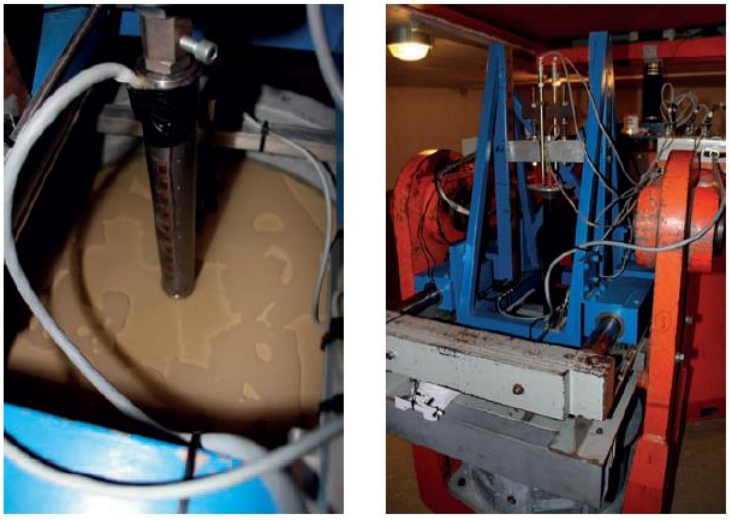

(a) (b)

Figure 2.1.2. (a), Photographs of the setup before installation; (b), Photo of the setup before laterally loading (Klinkvort, 2013).

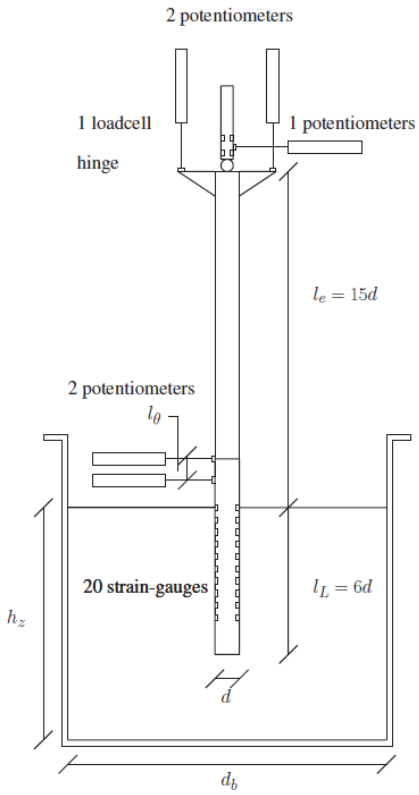

Figure 2.1.3. Sketch of centrifuge test setup (Klinkvort, 2013).

A sketch of the setup is shown in Figure 2.1.3. The strong box had a diameter of d_b = 500 mm and the height of the sand sample was h_z = 388 mm. The radius to the sand surface with this setup was 2.221 m and the diameter of the pile is 40 mm. The average grain size of the Fontainebleau sand is 0.18 mm, hence, $d_{pile}/d_{50} > 200$. The main results from the centrifuge tests were all derived from this setup.

2.2 Numerical methods

The most powerful way of modelling granular media is by numerical techniques. Numerical modelling has many advantages over the analytical models and the physical models. In numerical modelling, boundary conditions may be controlled precisely or even there can be no boundary by using a periodic cell, stresses and strains which may be measured over any volume within the sample. Any parameter may be varied while keeping the other parameters unchanged, any data are accessible at any stage of the test, and the same starting state can be used many times (Gong, 2008).

The numerical simulation offers an insight into the fundamental behaviour of the system that is normally not available by means of experimental investigations. For instance, the stress-path followed by the soil elements surrounding the pile and the stiffness evolution along the pile's embedded depth, are some of the key aspects that can be studied with a numerical model but are hardly traceable in model tests or in-situ conditions. From the preceding review of existing work, it seems clear that numerical models are a viable tool to model laterally loaded piles which allows features, such as pile/soil interface. So far, most researchers like to use Finite Element Method (FEM) and DEM (Cuéllar, 2011).

The FEM is a useful tool in the analysis of boundary value problems for any continuous medium. It also is a convenient and reliable approach to account for the continuity of the soil mass and the nonlinearity of the soil-pile interactions. There are numerous problems

in solid mechanics where the FEM is the easy tool for the analysis. For example, in the area of plasticity, performing nonlinear analysis by means of analytical or semi analytical formulations are tedious, especially for complicated geometries such as a pile in layered soil. Such nonlinear analyses can be solved with the FEM to a much easier extent. Seismic loading problems can also be solved using the FEM. In continuum analysis, the soil surrounding the pile is treated as a three-dimensional continuum with assumptions made on its stress-strain behaviour or its constitutive relationships. It is also observed that the FEM model is capable of predicting the plastic shakedown response of the pile (Giannakos, Gerolymos, & Gazetas, 2012). Yang and Jeremić (2002) have showed results from a FEM study on the behaviour of a single pile in elastic-plastic soils. The analysis included single pile behaviour in sand, clay and layered soils. Based on the results presented, it is concluded that three-dimensional finite element analysis using very simple elastic-plastic soil models can predict the pile head deflection with very good accuracy. Mardfekri *et al*. (2013) studied using FEM to account for soil-pile interactions. The results indicate that for the special case considered here the *p-y* method provides a reasonable accuracy, in spite of its simplicity, in predicting the lateral defection of single piles. A simplified linear FEM analysis of piles is also investigated and the influence of accounting for the pile diameter in the simplified linear FEM model is evaluated. It is shown that modelling the pile as a line with beam-column elements results in a reduced contribution of the surrounding soil to the lateral stiffness of the pile and an increase of up to 200% in the predicted maximum lateral displacement of the pile head. Niemunis *et al*. (2004) proposed the High-Cycle Accumulation model and accumulation law for the prediction of long-term deformations of offshore wind power plant foundations calculated through FEM.

Generally, FEM can handle a wide variety of engineering problems: Solid mechanics, Dynamics, Heat problems, Fluids and Electrostatic problems. However, the disadvantages also are obvious, because the most common numerical model FEM is inadequate to simulate grain migration and sand convection. The effect of long term loading on monopile cannot be found from the results of triaxial experiments nor numerical analysis with regular constitutive models. When using FEM to predict the trend of cyclic loading, strains are

determined for every load cycle in the load history. This can accumulate computational error when calculating strains for thousands of cycles and the process is time consuming. Hansen (2012) indicated that all strains in the soil were reversible when the numerical model was a poro-elastic model. This means that the soil is unable to attain any permanent deformation, hence features such as densification due to the cyclic shearing of the soil grains are omitted. With regard to the particles near the pile, their motion, densification and breakage will decide the influence of the long term loading. What is more, most FEM models did not contain any failure criteria, such as the commonly used Mohr-Coulomb failure criterion. The consequence is, that the FEM numerical model is unable to estimate the ultimate lateral resistance of the soil.

2.3 DEM

The discrete element method was first developed by Cundall (1971) to study rock mechanics problems and was later extended to investigate granular materials by Cundall and Strack (1979a). Cundall and Hart (1992) defined the scope of the application of the DEM and summarized fundamental principles governing the modelling of discrete element systems. In their definition, the DEM permits the computation of the finite displacement and rotation of discrete bodies, including complete detachment, and automatically recognises the establishment of new contacts as the calculation progresses. The DEM is based on the use of an explicit numerical scheme in which the interaction of the particles is modelled contact by contact and the relative motion of the particles is modelled particle by particle. Therefore, the DEM makes it possible to analyse the mechanics of granular materials at both the micro and macro scale (Itasca, 2004).

In the DEM, the interaction of the particles is treated as a dynamic process, whereby a state of equilibrium exists whenever the internal forces balance. The contact forces and displacements of a stressed assembly of particles are found by tracing the movements of the individual particles. Movements result from the propagation through the particle system

of disturbances caused by specified wall and/or particle motion, and body forces (Itasca, 2004). The dynamic behaviour is represented numerically by a time-stepping algorithm in which it is assumed that the velocities and accelerations are constant within each time-step. The solution scheme is identical to that used by the explicit finite difference method for continuum analysis. DEM is based upon the idea that the time-step is so small that, during a single time-step, disturbances cannot propagate from any particle further than its immediate neighbours. Then, at all times, the forces acting on any particle are determined exclusively by their interaction with the particles with which they are in contact.

The calculations in DEM are based on two laws: the application of Newton's second law to the particles, and a force-displacement law at the contacts between the particles (see Figure 2.3.1). Newton's second law is used to calculate the motion of each particle arising from the contact and body forces acting upon it. The force-displacement law is used to evaluate the contact force from the computed displacement, and then to update the contact forces arising from the relative motion determined at each contact point.

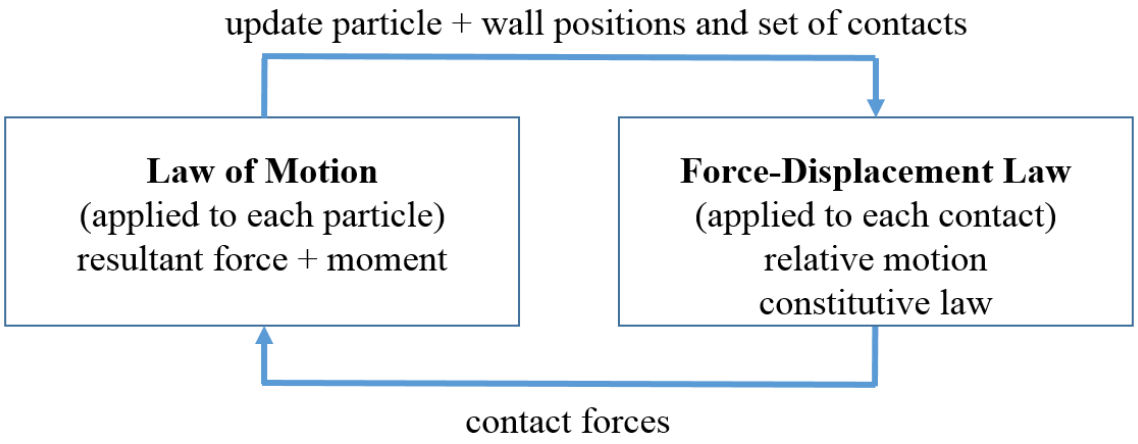

Figure 2.3.1. Calculation cycle in PFC-2D

Due to improving computer technology, DEM is becoming an important method in many scientific fields and is playing a greater role in industry. For instance, it is applied in the mining industry to simulate industrial particle flows (Cleary, 2000), in chemical engineering to simulate segregation phenomena in systems consisting of particles of

different sizes (Hoomans *et al*., 2000) and to study the fabric and structure of granular materials under loading, and for developing constitutive relations for soil using disks and spheres (Oner, 1984, Zhang and Cundall, 1986, Bathurst and Rothenburg, 1988). Recently DEM simulations are more and more used to solve selected real problems involving granular materials, especially in the geotechnical engineering field. This method involves a series of difficulties, which are related to the definition of the model itself and to the calibration of its micromechanical parameters (Calvetti, 2008).

DEM is useful when looking into macro and micro scale problems. It becomes an extremely useful tool, if applied with wisdom, to identify the correct micromechanical behaviour, as it is clear that the future of soil mechanics lies in producing accurate constitutive models that have sound micromechanical bases. In contrast to continuum modelling, the DEM assumes that the soil mass is composed of discrete particles which can displace independently from one another and interact only at contact points (Cundall and Strack, 1979a). Considering the discrete nature of soils, DEM can conceptually provide better simulations of particulate behaviour at the microscopic scale than continuum models. Consequently, DEM has been used by many researchers to model both laboratory and field behaviour (e.g. Cundall (1989); Iwashita and Oda (1998);Cheng et al. (2003), O'Sullivan and Cui (2009), Cheng (2004)).

The effect of long term loading on monopile cannot be found from the triaxial test and regular constitutive model. With regard to the particles near the pile, their motion, densification and breakage will decide the influence of the long term loading. That is why it is necessary to focus on the microscale discrete particles which cannot be modelled with FEM. With the development of modern computers, the numerical particle model can be used to simulate the whole process. Some characteristics of the constitutive model will appear from the numerical model automatically. Consequently, DEM is proved to be an efficient tool in simulating the complicated problems of granular flow and solid mechanics.

DEM analysis has been shown to accurately simulate observed soil behaviour (e.g. Thornton (2000), Cui and O'Sullivan (2006), Zhao and Evans (2009), O'Sullivan (2011b),

Cheng *et al*. (2004)). O'Sullivan (2011a) found that the application of DEM was increasing within the geomechanics research community in the past and these literature studies could be broadly classified as

- Documentations of DEM algorithm modifications;
- Validation of DEM models;
- Calibration of DEM models;
- Analyses of the relationship between microscale mechanics and the macroscale material response;
- Development of interpretation techniques;
- Simulations of element tests;
- Simulations of field-scale boundary value problems.

2.4 PFC-2D

The most common DEM simulation software used in the previous listed literature is the PFC-2D which is developed by ITASCA consulting group. As a particle-flow model, PFC-2D is used to simulate the mechanical behaviour of a system consisting of finite distinct particles. In this system, all individual particles displace independently from each other and only interact at the contacting point between two particles. Two basic terms describing the mechanical behaviour of this system are the particle movement and inter-particle force acting at the contacting point and the relationship between these two terms is based on Newton's law of motion. Initially, the default shape of the single particle is circular. However, as for other complex behaviour, particles can be bonded together to arbitrary shapes. It should be noted that the particle-flow model provided in PFC-2D is based on some basic assumptions, which are (Itasca, 2004):

1. All particles are treated as rigid bodies.

2. The contacts occur over a quite small area, such as at a contacting point.

3. A soft-contact approach is used to the behaviour at the contacts, and this allows rigid particles to overlap one another at contact points.

4. The magnitude of the overlap is related more to the contact force rather than the particle size.

5. Bonds can exist at contacts between particles.

6. All initial particles are circular, but any super-particles with arbitrary shape can be created by the clump logic.

A contact-stiffness model is usually used to reflect the elastic relationship between the contact force and relative displacement for any two touching entities (may be particle-particle or particle-wall) in normal (k_n) and shear (k_s) direction. PFC-2D provides two stiffness models: a linear model and a simplified Hertz-Mindlin model. In the linear model, the forces and relative displacements are linearly related by the constant contact stiffness, which is a function of the intrinsic stiffnesses of the two contacting entities. In the simplified Hertz-Mindlin model, the forces and relative displacements are nonlinearly related by the non-constant contact stiffness, which is a function of the geometric and material properties of the two contacting entities as well as the current value of the normal force. It is noted only the linear model is used in this study.

The linear model is the default one and it is generally adequate for most cases. This model shows the linear relationship between the contact force and the relative displacement, and it resulted from the intrinsic contact stiffness between any two touching entities. It is noted that the contact stiffness between contacting entities is not defined by users, but is computed by the particle stiffness k_n and k_s. By assuming that the stiffness of any two touching entities act in series, the contact normal secant (k_n) and shear tangent (k_s) stiffness is expressed by:

$$k^n = \frac{{k_n}^{(A)} {k_n}^{(B)}}{{k_n}^{(A)} + {k_n}^{(B)}}$$

2.4.1

$$k^s = \frac{k_s{}^{(A)} k_s{}^{(B)}}{k_s{}^{(A)} + k_s{}^{(B)}}$$

2.4.2

where the superscripts (A) and (B) denote the two entities in contact.

$$E = \frac{k_n}{2(1)}$$

2.4.3

where the *E* is the Young's modulus of assembly.

2.5 Micromechanical study using DEM

2.5.1 Measurement circle

Various parameters within a PFC-2D model can be measured over a given circular area. The location and size of the measurement circle are specified by the user.

Measurement circles can be defined to measure stress, porosity and coordination number.

2.5.2 Stress

The stress tensor is calculated in a PFC-2D model within a measurement circle. This stress is the average stress, taking into account the area of all balls with centroids within the circle.

It is not a point measure as in continuum analyses. The procedure used to calculate stress accounts for the effect of porosity.

Stress is a continuum quantity and therefore does not exist at each point in a particle assembly, because the medium is discrete. In the discrete PFC-2D model, contact forces and particle displacements are computed. These quantities are useful when studying the material behaviour on a micro-scale, but they cannot be transferred directly to a continuum model. Averaging procedures are necessary to make the step from the micro-scale to a continuum. The stress computation procedure relates the two in-plane force components of all contact and parallel-bond forces acting on each particle whose centroid lies within the measurement circle to a force per-unit-length of particle boundary, which must then be divided by a thickness value in order to obtain a stress quantity.

The average stress tensor $\bar{\sigma}_{ij}$ in a volume V of material, is defined by

$$\bar{\sigma}_{ij} = \frac{1}{V} \int_{V} \sigma_{ij} \, dV$$

2.5.1

where σ_{ij} is the stress tensor acting throughout the volume. For a particulate material, stresses exist only in the particles; thus, the integral can be replaced by a sum over the N_p particles contained within V as

$$\bar{\sigma}_{ij} = \frac{1}{V} \sum_{N_p} \bar{\sigma}_{ij}{}^{(p)} \; V^{(p)}$$

2.5.2

where $\bar{\sigma}_{ij}{}^{(p)}$ is the average stress tensor in particle (p). In the same way, the average stress tensor in a particle (p) can be written using Eq. 2.5.2 as

$$\bar{\sigma}_{ij}{}^{(p)} = \frac{1}{V^{(p)}} \int_{V^{(p)}} \sigma_{ij}{}^{(p)} \, dV^{(p)}$$

2.5.3

The identity

$$S_{ij} = \delta_{ik} S_{kj} = x_{i,k} \sigma_{ij} S_{kj} = (x_i S_{kj})_{,k} - x_i S_{kj}$$

2.5.4

holds for any tensor S_{ij} , where the notation [,i] denotes differentiation with respect to the coordinate x_i . Applying this identity to the stress in a particle, one can write

$$\bar{\sigma}_{ij}{}^{(p)} = \frac{1}{V^{(p)}} \int_{V^{(p)}} \left[(x_i \sigma_{kj}{}^{(p)})_{,k} - x_i \sigma_{kj,k}{}^{(p)} \right] dV^{(p)}$$

2.5.5

The stresses in each particle are assumed to be continuous and in equilibrium. In the absence of body forces, the equilibrium condition is $\sigma_{ij,i} = 0$. The volume integral in Eq. 2.5.5 is rewritten as a surface integral by applying the Gauss divergence theorem to the first term and noting that the second term vanishes in the absence of body forces such that

$$\bar{\sigma}_{ij}{}^{(p)} = \frac{1}{V^{(p)}} \int_{S^{(p)}} (x_i \sigma_{kj}{}^{(p)}) n_k dS^{(p)} = \frac{1}{V^{(p)}} \int_{S^{(p)}} x_i t_j{}^{(p)} \, dS^{(p)}$$

2.5.6

where $S^{(p)}$ is the particle surface; n_k is the unit outward normal to the surface; and $t_j{}^{(p)}$ is the traction vector. Since each particle is loaded by point forces acting at discrete contact locations, the above integral can be replaced by a sum over the N_c contacts as

$$\bar{\sigma}_{ij}{}^{(p)} = -\frac{1}{V^{(p)}} \sum_{N_c} x_i{}^{(c)} F_j{}^{(c)}$$

2.5.7

where $x_i^{(c)}$ and $F_j^{(c)}$ are the location and force, respectively, acting at contact (c). These forces include both forces resulting from contact at a point and parallel-bond forces.

The contact location can be rewritten as

$$x_i^{(c)} = x_i^{(p)} + \left|x_i^{(c)} - x_i^{(p)}\right| n_i^{(c,p)}$$

2.5.8

where $x_i^{(p)}$is the location of the particle centroid; and $n_i^{(c,p)}$ is the unit-normal vector directed from the particle centroid to the contact location and is a function of both the contact and the particle.

By substituting Eq. 2.5.8 into Eq. 2.5.7 and noting that

$$\sum_{N_p} F_j^{(c)} \equiv 0$$

2.5.9

for a particle in equilibrium, one obtains:

$$\bar{\sigma}_{ij}^{(p)} = -\frac{1}{V^{(p)}} \sum_{N_p} \left|x_i^{(c)} - x_i^{(p)}\right| n_i^{(c,p)} F_i^{(c)}$$

2.5.10

Note that this tensor is available for each particle.

The average stress tensor within a volume *V* of material could now be computed by applying Eqs. 2.5.2 and 2.5.10 to all of the particles within *V*. A difficulty in interpretation arises, however, when applying this procedure to the particles within the area defined by a measurement circle, since many of the particles will intersect the measurement circle. In PFC-2D, only the particles with centroids that are contained within the measurement circle

are considered in the computation of the average stress tensor. In order to account for the additional area of particles that is being neglected, a correction factor based on the porosity, is applied to the computed value of stress. The correction factor and the final expression used to compute the average stress tensor are derived in the following analysis.

The correction factor is determined by assuming that a uniform stress field σ_0 exists within the measurement circle, and writing two separate expressions for the average stress. The correct expression for the average stress $\bar{\sigma}$, within a measurement circle of volume V_m, is given by

$$\bar{\sigma} = \frac{1}{V_m}\sum_{N_p} \bar{\sigma}^{(p)} V^{(p)} = \frac{1}{V_m}\bar{\sigma}^{(p)} \sum_{N_p} V^{(p)} = \sigma_0 \left(\frac{\sum V^{(p)}}{V_m}\right) = \sigma_0(1-n)$$

2.5.11

where the summation applies to all particles and portions of particles contained within V_m, and *n* is the porosity within V_m (assuming that the particles are disks of unit-thickness). An alternate incorrect expression for the average stress $\tilde{\sigma}$ is given by

$$\tilde{\sigma} = \frac{1}{V_m}\sum_{N_p} \bar{\sigma}^{(p)} V^{(p)} = \sigma_0 \left(\frac{\sum_{N_p} V^{(p)}}{V_m}\right)$$

2.5.12

where the volume summation is only takes over the N_p balls with centroids contained within the measurement circle. The relation between the two alternate stress expressions is given by

$$\frac{\bar{\sigma}}{\tilde{\sigma}} = \left(\frac{1-n}{\sum_{N_p} V^{(p)}}\right) V_m$$

2.5.13

The final corrected expression for the average stress within the measurement circle is found by eliminating $\tilde{\sigma}$, using Eq. 2.5.12, to obtain

$$\bar{\sigma} = \left(\frac{1-n}{\sum_{N_p} V^{(p)}}\right) \sum_{N_p} \bar{\sigma}^{(p)} V^{(p)}$$

2.5.14

The final expression used in PFC-2D to compute the average stress tensor within a measurement circle is found by substituting Eq. 2.5.10 into Eq. 2.5.14 to obtain

$$\bar{\sigma}_{ij} = -\left(\frac{1-n}{\sum_{N_p} V^{(p)}}\right) \sum_{N_p} \sum_{N_c} \left| x_i{}^{(c)} - x_i{}^{(p)} \right| n_i{}^{(c,p)} F_j{}^{(c)}$$

2.5.15

where the summations take over the N_p balls with centroids contained within the measurement circle and the N_c contacts of these balls;

n is the porosity within the measurement circle;

$V^{(p)}$ is the volume of particle (*p*), taken equal to the area of particle (*p*) times a unit-thickness;

$x_i{}^{(p)}$ and $x_i{}^{(c)}$ are the locations of a particle centroid and its contact, respectively;

$n_i{}^{(c,p)}$ is the unit normal vector directed from a particle centroid to its contact location; and

$F_j{}^{(c)}$ is the force acting at contact (c) arising from both particle contact and parallel bonds.

2.5.3 Porosity

The porosity is the ratio of the area of the voids between balls within a given region of a model to the total area of that region. The porosity is related to the compacted state of the model (e.g., a low porosity implies dense packing). The porosity can be measured in a model with a measurement circle. The overlap between balls is accounted for in the porosity calculation.

The porosity *n* is defined as the ratio of total void area within the measurement circle to measurement circle area:

$$n = \frac{A^{void}}{A^{circle}} = \frac{A^{circle} - A^{ball}}{A^{circle}} = 1 - \frac{A^{ball}}{A^{circle}}$$

2.5.16

where A^{circle} and A^{void} are the area of the measurement circle and the voids, and A^{ball} is the area of the measurement circle occupied by the balls. A^{ball} is computed by

$$A^{ball} = \sum_{N_p} \left(A^{(p)}\right) - A^{overlap}$$

2.5.17

where N_p is the number of particles that intersect the measurement circle; $A^{(p)}$ is the area of particle (p) contained within the measurement circle, and $A^{overlap}$ is the area of particle overlap contained within the measurement circle. Note that both partial areas of particles that intersect the measurement circle and particle overlaps arising from compressive contact forces are accounted for in this computation.

2.5.4 Coordination number

The coordination number is the average number of contacts per ball for balls with centroids that fall within a measurement circle.

The coordination number C_n is defined as the average number of contacts per particle. Only particles with centroids that are contained within the measurement circle are considered in the computation

$$C_n = \frac{\sum_{N_b} {n_c}^{(b)}}{N_b}$$

2.5.18

where N_b is the number of balls with centroids that are contained within the measurement circle, and ${n_c}^{(b)}$ is the number of contacts of ball (b). Note that some contacts are counted twice and others once (if one ball of the pair lies outside of the measurement circle).

2.5.5 Contact force

Each contact-force vector can be resolved into normal and shear components with respect to the contact plane. Normal contact forces act normal to the contact plane, while shear contact forces act in the contact plane. Positive normal contact forces indicate compression; negative normal contact forces indicate tension.

2.6 Summary

From a large amount of literature on the DEM simulations, it is recognised that DEM has been successfully applied to various geotechnical problems. The basic concepts and general mathematical backgrounds of PFC-2D have been presented in this chapter. DEM is a

powerful tool for fundamental research on the behaviour of granular materials. The main disadvantage of DEM simulation is the enormous computational expense, since a very small timestep of simulation must be used to ensure the numerical stability and accuracy. Many particles are required to guarantee the sufficient number of contacts. It enables the investigation of the particle properties which cannot be obtained using continuum mechanics, such as interparticle friction, contact forces distribution, as well as coordination numbers. The circular shape particles tend to roll excessively and then lead to a lower strength of the assembly, so clump of complex particle shape and restraining the rotation of circular particles have been developed to solve this problem.

3D simulation is more realistic, and spherical shaped particles are not close to the realistic situation. There is also no rolling resistance applied to the particle contacts. PFC-2D was chosen in this research, the main reason was the computational time. Compared with 3D, 2D can allow a bigger model size if the tests use the same particle size. This design will reduce the computer calculation time, particles size effects and boundary effects.

DEM simulation was built as a replica of a centrifuge experiment. The determination of particle parameters (particle shape, particle rotation and friction coefficient) in the DEM were important for modelling the behaviour of granular materials. Hence, a series of indices were used to validate that the sample was homogenous and realistic. In reality, the friction angle of a soil is related more to particle shape than inter-particle friction. So, the friction values of DEM chosen were very high. Since there is no rolling resistance applied to the particle contacts. Hence, the high friction will help to model the rolling resistance. The DEM centrifuge model results, were verified by comparing the *p-y* curves in the DEM model and those on the centrifuge tests.

Chapter 3

DEM model preparation

3.1 Introduction

Normally the behaviour of natural soils is complex and hard to characterise adequately by conventional non-linear elastic models or elasto-plastic models. However, micro-mechanics can gain some insights into the behaviour of soils. This chapter presents a modified particle generation method, named as the Grid Method (GM), capable of generating homogeneous specimens for model scale centrifuge studies using the DEM. The DEM specimens were temporarily divided into grids so that soil particles could be created in batches into a smaller area. Using the specimen, a 2D DEM-centrifuge model was prepared by applying an increased gravity condition, which was then used to study the monotonic loading behaviour of a rigid monopile. This formed the DEM-centrifuge model, and it was found that the GM was efficient in preparing the dense samples because it reduced the overall sample preparation time and managed to generate more homogeneous specimens.

3.2 Literature review

Previously, two main approaches were used to study particle micromechanics. The first one uses laboratory experiments on natural sands or rods to observe the evolutions in the contact distribution within the specimen (Drescher and de Josselin de Jong, 1972, Oda, 1972). There has been a wide range of non-destructive methods that allow the microstructures of soils to be observed and a detailed review was found in Oda and Iwashita (1999). These methods include the use of nuclear magnetic resonance imaging (MRI), laser-aided tomography, X-ray tomography, photoelastic assemblies and even acoustic emission. For example, the use of X-ray scanning of computed tomography (CT) (Alfaro

and Wong, 2001, Desrues *et al*., 1996) allows internal fabric and localised patterns of deformation of a soil specimen to be observed. Optical microscope (OM) (Oda and Kazama, 1998), scanning electron microscope (SEM)(Bowman *et al*., 2001), and even environmental scanning electron microscope (ESEM) (Mao and Fahey, 1999, Bolton and Cheng, 2001), can be used to identify and study micro-structure or its change. In particular, directional voids ratio or pore size distribution function and particle shape orientation. can be obtained from SEM analysis. However, the use of a microscope with non-destructive loading tests is not easily achieved and is incapable of prepairing exact replicates of the physical system (Jiang *et al*., 2003, Cheng, 2004).

The second approach is using the numerical method, such as FEM and DEM. Soil mechanics have been described based mainly on the continuum approach (FEM) in the past. It is only recently that the idea of investigating the micro-structure of soil element was seen as important (Oda and Iwashita, 1999, Thornton and Antony, 2000, Thornton, 2000). One of the reasons for computing the micro-structure of soil behaviour is to complement the conventional method in describing soil behaviour. The main problem of modelling based on continuum approaches is parameters that have to be defined and evaluated. These parameters are obtained from a curve-fitting process, and sometimes have no clear physical meaning. Modelling using DEM, on the other hand, gives a more realistic way of reproducing the behaviour of granular soils based on a few micro-mechanical parameters (Cheng, 2004). Four different techniques are available for specimen generation: (1) Fixed Point Method; (2) Expansion Method; (3) Isotropic compression Method; (4) Multi-layer with under compaction method (UCM). Method (1) is a simple method generally used to validate DEM codes. Methods (2) and (3) generate essentially dense and loose specimens. The last method (4)'s objective was to generate homogeneous DEM specimens for a variety of density conditions ranging from very loose to dense states.

3.2.1 Fixed point method

Particle and contact data are obtained from two approaches: (a) Visual observations and laboratory testing (photos, density, normal stiffness), and (b) Theoretically derived data for regularly-packed ideal cases, such as simple cubic systems. Method (a) was used by some researchers (Katsuki *et al*., 1989), especially in the primary stage of DEM development to compare simulated DEM results with experimental observations. Method (b) is often used to verify theories and/or DEM codes (2D or 3D).

3.2.2 Expansion method

When a particle is randomly positioned, a new particle will not be placed if it would overlap another particle or a wall. If a particle overlap occurs, the position of the particle will be changed slightly to meet the requirement (Itasca, 2004). Furthermore, if after several position changes, the requirement is still not satisfied, the particle will be removed. This method needs, therefore, a rather large area to form the specimen with the desired number of particles. If the initial area is too small, a specimen of a pre-established size cannot be formed. If the initial area is too large, i.e. initial computation area is too large, computation efficiency will become low with the current techniques used in DEM. To overcome this limitation, the expansion method was proposed by a few researchers (Rothenburg and Bathurst, 1992). All particles with reduced radii are randomly positioned in a specific area, which is very close to actual desired specimen size, and no overlap/contact force is developed between any two particles. After all particles are positioned, the radii of all particles are restored gradually while the consolidation pressure is kept constant on boundaries. The overlap/contact force developed between any two particles during the growth process allows particles to move in order to turn the liquid-like specimen into a dense specimen. The rigid (or flexible) boundaries are allowed to move accordingly so that a stress state is achieved at equilibrium. Once the desired radii are restored, interparticle friction coefficients are reset to their normal values. Because the interparticle friction

coefficient is low during particle placement, the expansion method also produces dense specimen. The expansion method was shown in reference Rothenburg and Bathurst (1992) for planar elliptical particles.

3.2.3 Isotropic-compression method

First introduced by Cundall and Strack (1979b), Cundall and Strack (1979a), it has been used to generate dense specimens in DEM studies. In this method,

(1) All particles are randomly positioned in a large area (volume) in such a manner that no overlap/ contact force is developed between any two particles.

(2) The interparticle friction coefficient is set to very small values so that interparticle sliding is permitted resulting in a dense packing of the particles. Boundary walls are then moved inward, or a consolidation pressure is applied on the boundaries. This, in turn, allows particles to move so that the liquid-like particle assembly can be compacted into an even denser state. The process continues until a target void ratio or stress state is achieved at equilibrium.

(3) The interparticle friction coefficient is then reset to representative values in order to carry out the numerical simulation under any given loading conditions.

While this method is very effective in generating dense specimens, uniformity due to boundary effects may not be achieved. This may even be worse for loose to medium- dense specimens. Furthermore, equilibrium can only be attained with pressure boundaries when the specimen reaches a dense state. Thornton (2000) and Masson and Martinez (2001) modified slightly the isotropic compression method in order to generate a loose specimen by setting the interparticle/wall-particle friction coefficient to their normal values. However, the effect of their modification on specimen uniformity was not discussed in their papers, but some arching effect could explain the presence of large pores in the central

part of the specimen. This arching effect was maintained even as walls continued to move inward to compress the specimen.

3.2.4 Multi-layer with under compaction method (UCM)

Jiang *et al*. (2003) described the multi-layer with under compaction Method (UCM). Its objective was to generate homogeneous DEM specimens for a variety of density conditions ranging from very loose to dense states. Particles are divided evenly to form several layers and compacted layer by layer. When compacting the *n*th layer, all *n* layers are compacted to a state looser than the final target value in order to reduce the effect of compaction energy transferred from compaction of successive layers. Under compaction, criteria based on average planar void ratio were proposed to achieve uniformity of specimens.

3.2.5 Summary

For larger scale soil-structure interaction problems, current DEM techniques used for generating specimens hardly result in homogeneous and realistic specimens. UCM is useful for the element test, because the element sample is small, but there still are some uncertain factors for the large scale test. Hence, a modified particle generation method, referred to as the GM, is proposed here to generate a homogeneous and realistic specimen for DEM study. The detailed introduction will be in the following parts.

3.3 The proposed GM method

3.3.1 Modelling of soil properties

Centrifuge physical modelling is a widespread technique in the geotechnical field. It makes it possible to reproduce in situ stresses in a small-scale model. The main objective of the centrifuge tests is to study the stability of piles in sands and clays subject to a large variety of cyclic loading histories. Centrifuge testing has proved its efficiency in conducting extensive series of tests, as it allows a large range of parameters to be varied while keeping associated costs relatively low, when compared to in situ testing.

For the centrifuge DEM model, sample preparation is important. Current DEM techniques used for generating specimens hardly result in homogeneous and realistic specimens. Hence, a modified particle generation method, referred to as the GM, is proposed here to generate a homogeneous and realistic specimen for DEM study. In contrast to the UCM method of Jiang *et al*. (2003), this proposed technique does not need compaction, as compaction potentially induces energy transfer from the upper layers to the underlying layers affecting the sample's homogeneity. In addition, the UCM could not guarantee homogeneity within an individual layer. In order to make a specimen more homogeneous and to reduce the effort of energy transfer through successive layers, the GM based on the explosive method is used in this paper. During the process of GM specimen generation without gravity, the PFC model kept cycling until the whole system reached the equilibrium state. Then, the specific gravity was given to the existing particles. The PFC model was cycled until the equilibrium was achieved again. The final static equilibrium state was only induced by the designated 100*g* self-weight of the particles.

The scaling laws for centrifuge modelling were presented by Schofield (1980) (see Table 3.3.1). In this paper all centrifuge tests were conducted at 100 g. All DEM analyses in this investigation were performed using the GM DEM-centrifuge method under 100 g.

Table 3.3.1 Centrifuge Scaling Laws (Schofield, 1980, Thorel, 2013).

Parameter	**Scaling factor** (Model/Prototype)
Acceleration (m/s^2)	N_s
Force (N)	$1/N_s^2$
Stress (N/m^2)	1
Strain	1
Rotation	1
Frequency	N_s
Displacement (m)	$1/N_s$
Length (m)	$1/N_s$
Density	1
Mass	$1/N_s^3$
Energy	$1/N_s^3$
Time (dynamic)	$1/N_s$
Pressure	1
Bending stiffness	$1/N_s^4$

Table 3.3.2 shows the model parameters used in the numerical model. According to the PFC-2D manual, the quantitative value of sand normal stiffness is twice its Young' modulus E_p. The determination of the parameters is a trial and error process. The criteria used to assess the choice of parameters are the constant, reasonable K_0, and realistic vertical stress distribution. The material modelled is composed of disks with a maximum diameter of 9.0 mm, a minimum diameter of 6.0 mm, an average grain diameter d_{50}=5.85 mm and uniformity coefficient $C_u = d_{60}/d_{10}$ = 1.26 (see Figure 3.3.3).

Table 3.3.2 Input parameters for DEM simulations.

Density of sand particles (kg/m^3)	2650
Density of pile particles (kg/m^3)	500
Particle diameters, d (mm)	Figure 3.3.3
Sand grain size, d_{50} (mm)	5.85
Friction coefficient of the particles μ(-)	0.5
Sand Young's Modulus, E_p(Pa)	4e7
Normal stiffness of particles, k_n (N/m)	8e7
Particle, wall stiffness ratio (k_s/k_n)	0.25
Normal stiffness of walls, k_n (N/m)	6e12
Initial average porosity	0.25
Final average porosity (after add gravity)	0.185
Bulk unit weight γ bulk (kN/m^3)	2115.3

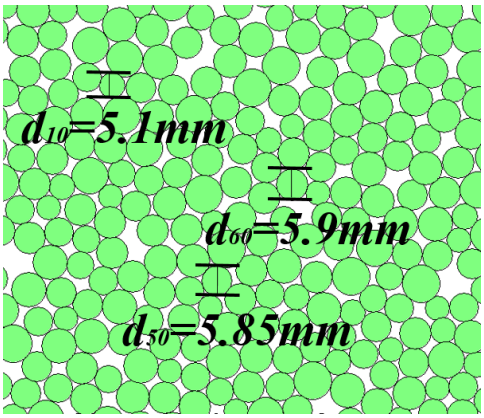

Figure 3.3.1. A typical particle assembly at equilibrium before pile installation.

3.3.2 The procedure of "GM" and initial stress state

At the beginning of GM, the planned area of sample was divided into 36 grids (see Figure 3.3.2 (a)), and there were 6 layers and 6 columns in this region. Each grid was square, and each side was of 100 mm in length. The first grid, which was named GM11, was at the bottom-left of the model. "GM" is the abbreviation of grids method, then first number of "11" means the number of layers, the second number stands for the number of columns. Figure 3.3.2 (b) shows the locations of the measurement circles (radius m_d = 50 mm) defined by the PFC intrinsic functions. These measurement circles were used to interpret the localized information within each grid. In the following simulations, 5 locations (location 1-5 of the Figure 3.3.2 (b)) were picked to compare the final results.

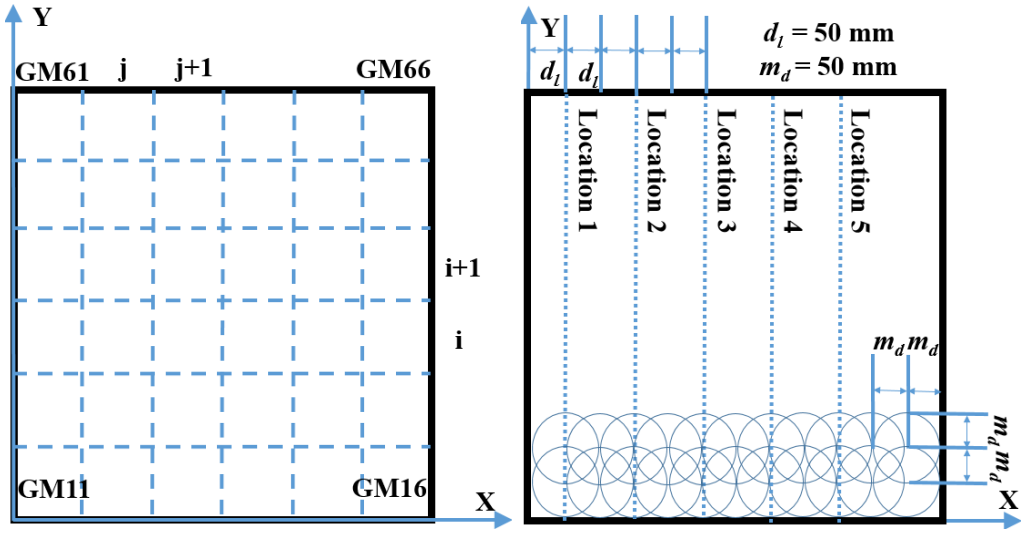

Figure 3.3.2.Schematic view of grid method and the overall dimension (length and height) of PFC model.

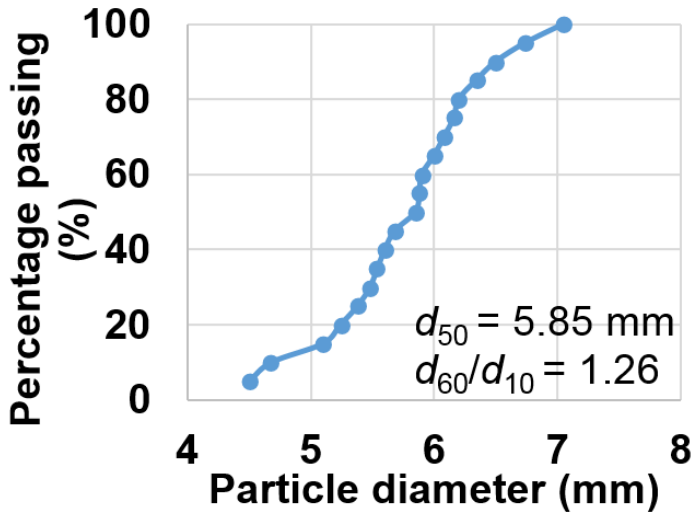

Figure 3.3.3.Distribution of grain sizes in DEM analyses.

Since the proposed GM uses the explosive method for particle generation, particles are created at their final radii in specific numbers $N_{particle}$ to achieve the desired porosity and the number of every type size (20 types followed size distribution Figure 3.3.3) are calculated in advance. The following equations 3.3.1-3.3.4 will be used for the calculation of initial porosity and particle number in every grid. A_m is the area of model, ${A_P}^i$ and $N_{(i)}$ is the total particles area of the same specific diameter $r_{(i)}$ and the quantity of corresponding diameter particles. Regarding the size distribution, there are 20 types of particles and every type is $P_{(i)}$ = 5% proportion of total particles, therefore, $N_{(i)}$ is the same quantitative value for all the types of particles. This calculation procedure can be done by the EXCEL.

$$N_{(i)} = N_{particle} P_{(i)} \tag{3.3.1}$$

$$ {A_P}^i = N_{(i)} {r_{(i)}}^2 \pi \tag{3.3.2}$$

$$A_P = A_P{}^1 + A_P{}^1 + \cdots + A_P{}^i$$

3.3.3

$$e_{initial} = \frac{A_P}{A_m}$$

3.3.4

The particles inside each grid were created by PFC code "ball" not "generate". The codes "*x*" and "*y*" were used to control the range which should exist in the corresponding grid area. Then the particles were given properties as shown in Table 3.3.2 and the number of particles in every grid is 280. In every grid, the sample followed the size distribution (see Figure 3.3.3) and initial porosity of 0.25. All particles within each grid were added the designated gravity 100g when the initial average porosity was reached. Then the model was cycled to equilibrium. The material modelled is composed of disks with a maximum diameter of 9.0 mm, a minimum diameter of 6.0 mm, an average grain diameter d_{50}=5.85 mm and uniformity coefficient $C_u = d_{60}/d_{10} = 1.26$.

Figure 3.3.4 shows the sequence when the particles were created. Rigid walls were used to simulate the model's permanent boundary and the grid's temporary boundary (see Figure 3.3.4 (a)). After the generation of GM11 (see Figure 3.3.4 (b)), it moved to GM12 (see Figure 3.3.4 (c)). When finished with this layer generation, the vertical walls located in the middle of every two grids was going to be deleted. Then the existing sample needed to cycle until equilibrium again (see Figure 3.3.4(d)). The particles of the entire layer would be generated by this technique.

When finished the entire layer generation, a certain thin depth (9 mm) of particles on the top of this layer were fixed (the green colour in Figure 3.3.4 (e)). Then the generation procedure moved to the next upper layer (see Figure 3.3.4 (e)). As the previous layer, from Figure 3.3.4 (f) to (h), the generation procedure was repeated. After the generation of the second layer, the fixed particles were be released (see Figure 3.3.4 (i)). Then the model

was cycled to equilibrium again. The same procedure was repeated until the final grid (GM66) was generated.

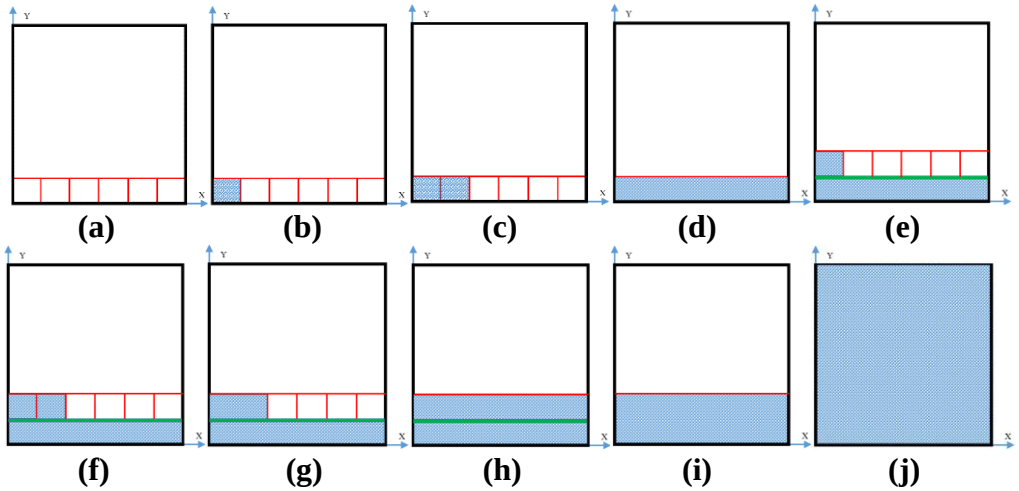

Figure 3.3.4.The procedure of "GM" for generating specimen.

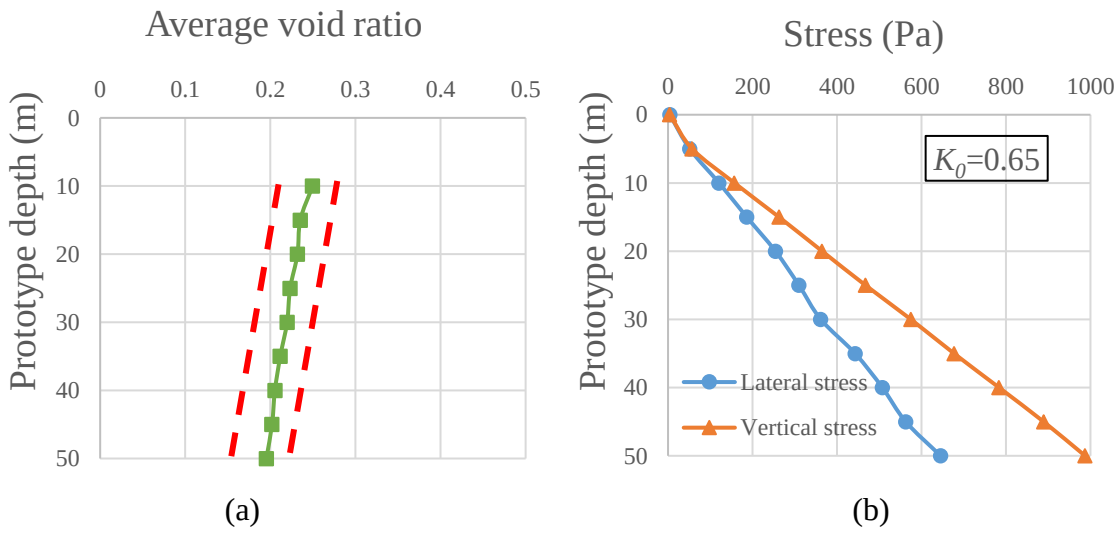

Figure 3.3.5. (a) Initial distribution of void ratio in DEM analyses; (b) Average lateral and vertical stress.

Figure 3.3.5 (a) presents the distribution of initial void ratio in the DEM model. The green line is average void ration and the red lines are the range for the different locations. With

the GM method, the distribution of void ratio is uniform and reasonable. Figure 3.3.5 (b) describes the comparison of average lateral and vertical stress distribution for different depths and shows K_0 is reasonable.

3.4 Results and discussion

From the microscopic view, soil cannot be considered as homogeneous with respect to the overall structure. Normally, density or void ratio is usually used as an index to evaluate specimen homogeneity. These properties are measured over a specific volume. The determination of the representative elementary area in a DEM sample is of the utmost importance for the evaluation of specimen homogeneity. The heterogeneity may be varied locally if the ratio of the specified length of representative elementary volume (area) to the largest particle (void) diameter is changed.

To macroscopically characterise the homogeneity of the DEM specimen generated, horizontal and vertical band porosity described by using e_i, e_j were used to evaluate the homogeneity of the specimen in both x and y directions. Regarding the measurement circle, the radius of measurement circle m_d is 50 mm and the m_d / d_{50} = 8.547 (see Figure 3.3.2 (b)). Therefore, the area of measurement circle is enough to express the exact soil characteristics belonging to the corresponding location.

Figure 3.4.1 (a) also shows that the porosity increased slightly from the bottom to the surface. Figure 3.4.1 (c), (d) and (e) present the comparison of different locations according to the three “set random” seed numbers. The red line is the boundary of minimum and maximum. Each grid was confined by rigid boundaries during particle setting. When these rigid boundaries were removed, there were gaps along each boundary, which was reflected in the porosity distribution, but the porosity variation is acceptable.

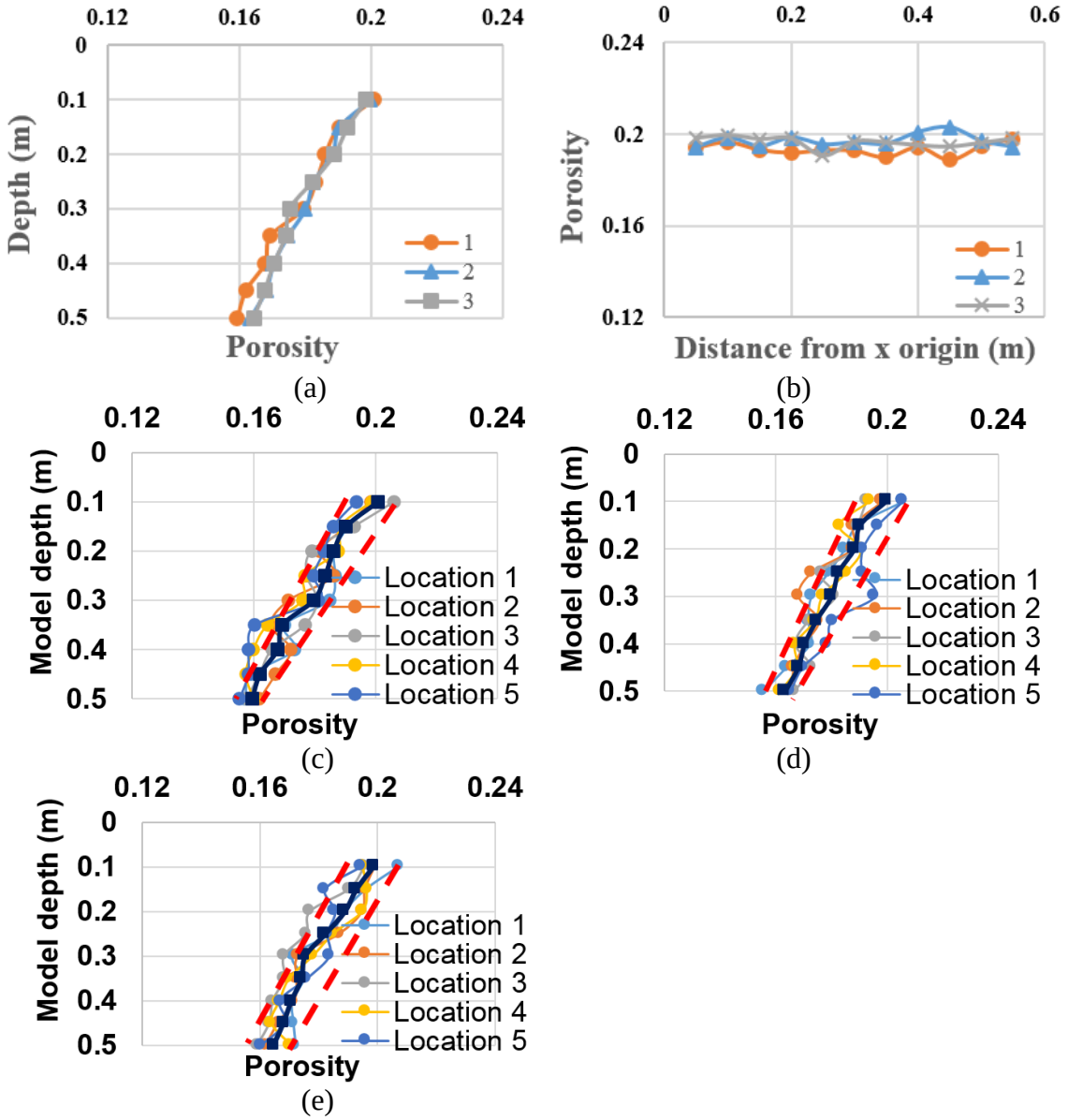

Figure 3.4.1.Comparison of specimen's porosity or Ko after sample preparation: (a) row average with 3-random seeds; (b) column average with 3-random seeds; (c) locations 1-5 with random seed=9522; (d) locations 1-5 with random seed=10000; (e) locations 1-5 with random seed=66093. (Note: in (c)-(e), the line with deep blue square marks is the row average. Locations 1-5 are shown in Figure 3.3.2(b)).

Figure 3.4.1 shows the comparison of porosity distribution. When the particles were generated, there were the variances for the code "set random" in PFC. In Figure 3.4.1 (a)

and (b), the tests 1, 2 and 3 used different random seeds, and the results of the three different simulations are similar. Then the following model test soil sample is based on the simulation using the second random seed.

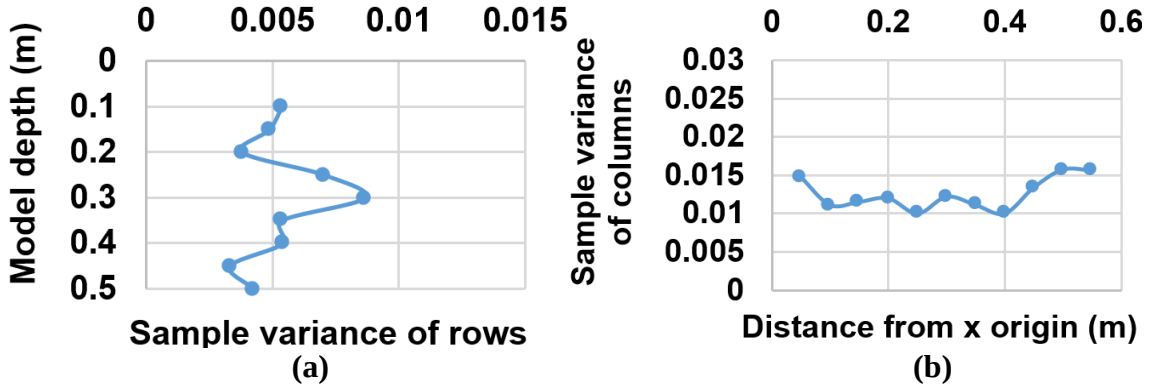

Figure 3.4.2.Sample variance: (a) S_i, (b) S_j.

For the following equations, e_{GMij} is the grid void ratio, *i* and *j* mean the number of row and column respectively. e_i, e_j is the average porosity in *i* row and *j* column obtained from Eqs 3.4.1 and 3.4.2. Sample variance S_i and S_j follow the Eqs. 3.4.3 and 3.4.4. n_{layer}, n_{column} are the number of total grids used in layer and column respectively. e_{iave}, e_{jave} are the average porosity of row and column. The value of sample variance is sufficiently small, and the fluctuation in both row and column is acceptable (see Figure 3.4.2).

$$e_i = \frac{e_{GMi1} + e_{GMi2} + \cdots + e_{GMij}}{N_i} \quad 3.4.1$$

$$e_j = \frac{e_{GM1j} + e_{GM2j} + \cdots + e_{GMij}}{N_j} \quad 3.4.2$$

$$S_i^{\,2} = \frac{1}{n_{layer} - 1} \sum_{i=1}^{m} (e_i - e_{iave})^2$$

3.4.3

$$S_j{}^2 = \frac{1}{n_{column} - 1} \sum_{j=1}^{m} (e_j - e_{jave})^2$$

3.4.4

The Figure 3.4.3 (a) and (b) show the average lateral, vertical stress distribution for vertical bands. Figure 3.4.3 (c) and (b) express the lateral stress distribution for different depths at different vertical bands (see Figure 3.3.2 (b)). For the different vertical bands, there is no significant difference. With regard to the different depths, the trend of average lateral stress is linear, and this phenomenon followed the theory. This means the uniformity of crossrange is good.

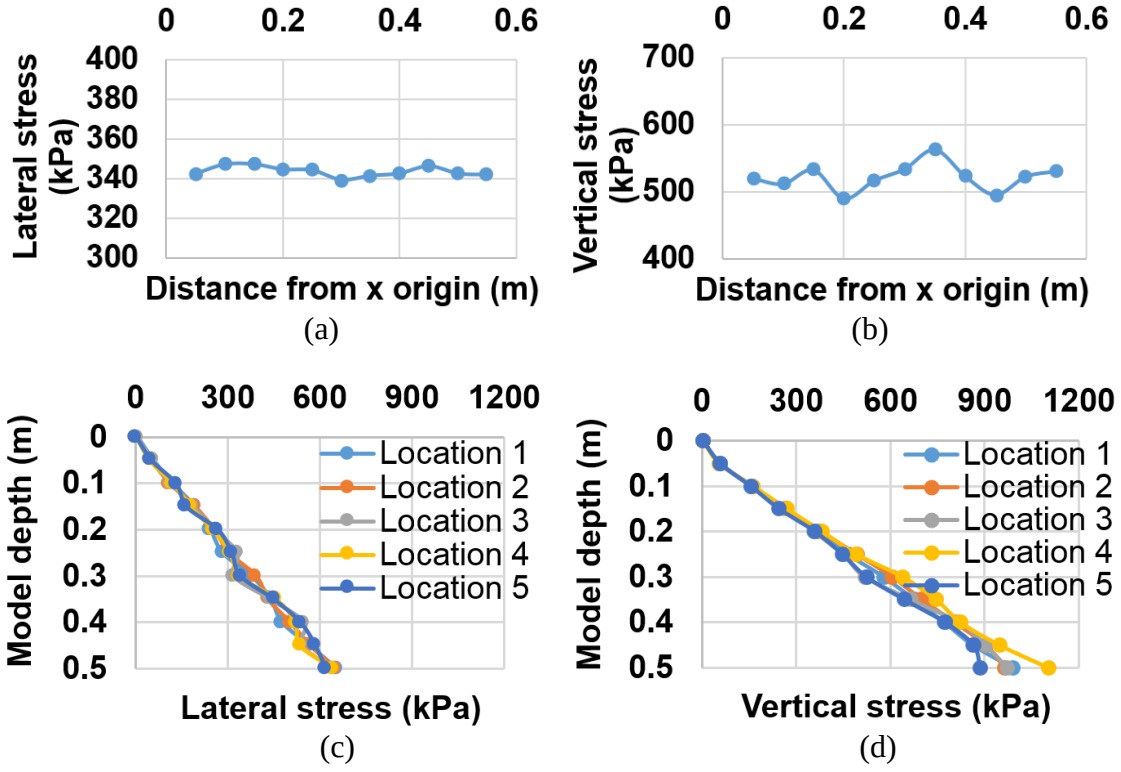

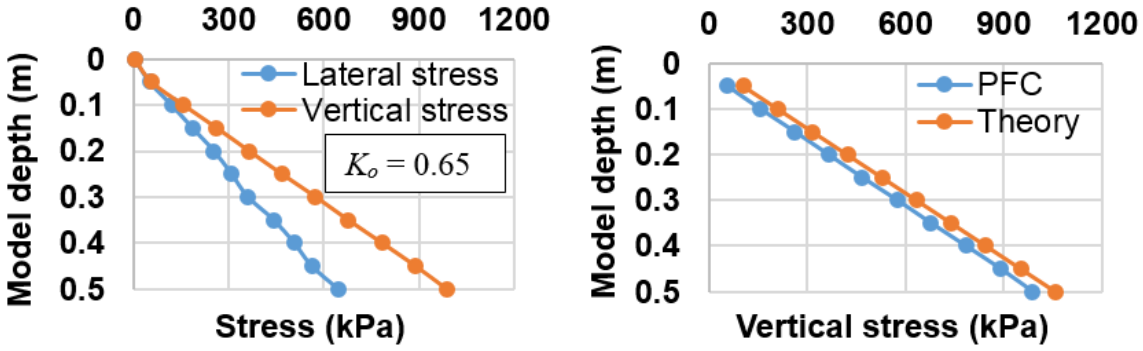

(e) (f)

Figure 3.4.3. Comparison of soil stress distribution after sample preparation: (a) average lateral stress of column at x axis; (b) average vertical stress of column at x axis; (c) lateral stress at locations 1-5; (d) vertical stress at locations 1-5; (e) average lateral and vertical stress; (f) average PFC and theory vertical stress.

Figure 3.4.3 (e) describes the comparison of average lateral and vertical stress distribution for different depths and shows K_0 is reasonable. Figure 3.4.3 (f) expresses the comparison of PFC average vertical stress and theory vertical stress distribution for different depths. For the theoretical vertical stress, the sample density was calculated after the equilibrium state. Then function $p=\rho g z_{depth}$ (p is the vertical stress, ρ is sample density, g is gravity (100g), and z_{depth} is depth) was used to calculate the theoretical vertical stress. From the Figure 3.4.3 (f), there is only a slight difference. Figure 3.4.4 shows the K_0 of GM is much closer to realistic value than RM (Duan and Cheng, 2015). These data can sufficiently prove the sample is homogeneous and close to the real sand sample.

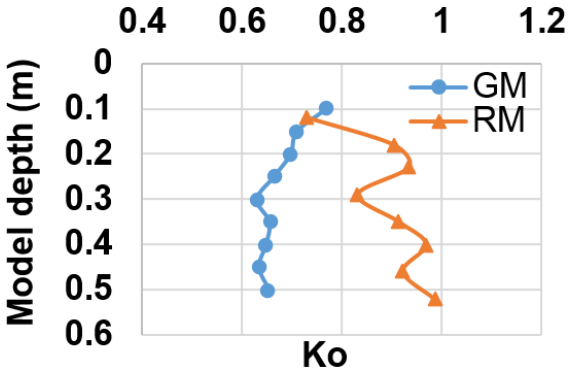

Figure 3.4.4.Compare GM K_0 value with RM (random method used in Duan and Cheng (2016a)).

3.5 Description of the pile in model

For the generation of a pile, the pile was made of 4940 particles whose radius was 1.125mm (see Figure 3.5.1). These particles overlapped each other, the distance between the centres of two adjacent particles is d_{pp}. This type was used for the four sides: right, left, bottom and top. Due to the small size particle, and the short distance between two balls, the surface of the pile is sufficiently smooth. Therefore, the roughness can be treated as the value which was set at the beginning.

Regarding the shaft resistance at a specific pile location, the Figure 3.5.2 gives the detailed explanation. In this figure, there were five particles which were touched to the two different types pile. Red arrows mean the shaft resistance between the pile and particles, and the direction shows the shaft resistance which applied on the pile. Negative means the resistance pushes the pile downward, and the positive shaft resistance shows that the pile was pushed upward. The left pile in the figure is the other proposed pile, the right one is the pile which was used in the model.

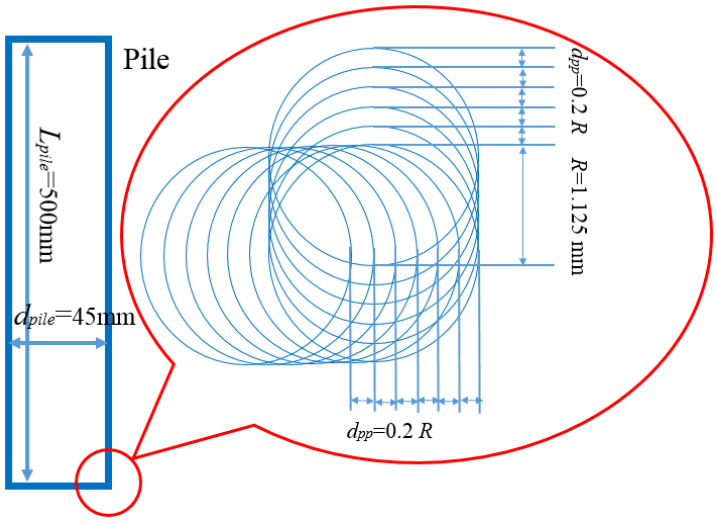

Figure 3.5.1 Composition of pile in PFC.

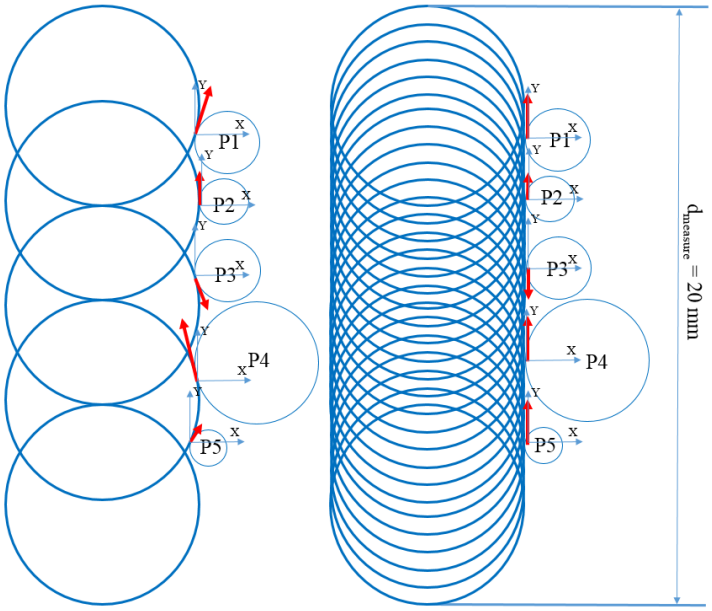

Figure 3.5.2 Method of calculation for pile shaft resistance in PFC.

At the left type of pile in Figure 3.5.2, the distance of overlap is not sufficiently large, so the surface of the pile is not smooth. When the shaft resistance of the pile was calculated, this will cause the complex process. Because of the pile surface heave, the *y* direction of the shaft resistance between pile and particle should use a math method to calculate the *y* direction component. Also the normal contact force should be considered. During this procedure, there will be caused some mistakes, then this error will be accumulatively calculated. Therefore, in this project the pile sharp chosen to be is the right type in Figure 3.5.2. This type had bigger overlap, which caused the surface of pile is smooth. The calculation of shaft resistance became easy, because the direction of the shaft resistance is the same as the y direction (vertical direction). In this model, the embedded pile length was divided in to 10 parts each with 20mm in length. In the range of this certain distance, the whole shaft resistance was summarised, then the final value was used to show the total shaft resistance of this length. In the following all analysis, the according coordination is the centre of this part in the *y* axis.

3.6 Summary

In this chapter, a modified method called GM DEM-centrifuge model was described. It was aimed to generate homogeneous DEM specimens. Particles are divided evenly to form grids. The lateral and vertical stress was calculated to verify the rationality of DEM model. The generation of rigid pile also was described, and the pile was made of "clump". The particles of clump were overlapped each other to simulate the smooth surface of pile. Finally, the K_0 of GM is much closer to realistic value than RM. In addition, the sample variance of GM is acceptable. Therefore, this research proof the GM DEM-centrifuge model is sufficient to generate an ideal sand sample for comparing with centrifuge experiment tests data.

The main content of this chapter was submitted to Geo-Chicago 2016 and published as a conference paper with title "A Modified Method of Generating Specimens for 2D DEM Centrifuge Model" (Duan and Cheng, 2016a).

Chapter 4

DEM analysis of pile installation effects

4.1 Introduction

This chapter presents a 2D-DEM model that is used to study the effects of pile installation in deep foundation. It is accepted widely that the installation method affects pile behaviour, but there are still limited studies that compare and analyse the impacts systematically. Most constructions use pile foundations and this type of foundation can be executed either by extracting soil (non-displacement pile) or by displacing soil (displacement pile). The first category includes bored piles, Strauss piles and continuous flight auger (CFA) piles; the second category includes other types of piles: driven piles (precast concrete or steel piles), Franki piles and Omega piles.

In principle, the ultimate capacity of a pile is the load at which the load-displacement curve shows a sharp plunge, and beyond which the pile undergoes dramatic settlement. The bearing capacity of a pile depends on the soil properties and the stress state with which it is surrounded. This is because the behaviour of granular material is governed by the packing of the grains and the contact stresses in between. The mean stress and the density can be described as the soil state, and the soil behaviour is determined on the basis of this state and the loading conditions. However, in the case of displacement piles, the installation process causes a considerable amount of soil displacement and high levels of (reaction) stresses. These effects of pile installation are transmitted to the soil through the interaction between sand grains and the pile, resulting in an altered soil state and properties. The purpose of this chapter is to analyse the effects of soil characteristics and pile (driven and bored) installation methods. The DEM is used to explain the pile behaviour installed in granular soils. A rigid bored pile and a rigid driven pile of the same geometry were installed into an assembly of soil prepared under a high gravitation force, mimicking the centrifuge testing conditions. The impacts of having different soil frictional angles, and when gravity

was applied at different stages were discussed. Comparisons of the corresponding pile loading behaviour were made, together with showing the different contributions of shaft and end bearing resistance. When considering the same pile friction, the driven pile performed better in the pile load test. Micro scale information of the particles near the two piles was used to explain the observed phenomena.

4.2 Literature review

4.2.1 Driven pile

Driven pile foundations can be made from concrete, steel or timber. These piles are prefabricated before being placed at the construction site. When these piles are driven into the granular soils, they displace the equal volume of soil. This helps in the compaction of soil around the sides of the piles and results in the densification of soil. The piles which compact the soil adjacent to it are also called a compaction pile. This compaction of soil increases its bearing capacity.

Field research with instrumented piles has led to greatly improved driven pile design approaches in sand (Lehane, 1992, Lehane *et al*., 1993, Lehane and Jardine, 1994, Jardine and Chow, 1996, Chow *et al*., 1997, Gavin and Lehane, 2003a, Gavin and Lehane, 2003b, Clausen *et al*., 2005, Kolk *et al*., 2005, Lehane *et al*., 2005, Schneider *et al*., 2005, Gavin and O'Kelly, 2007, Jardine and Chow, 2007, Coop *et al*., 2005). White and Bolton (2004) report detailed particle image velocimetry (PIV) measurements of the displacements and strain paths developed around the base of relatively smooth aluminium alloy 'plane strain' penetrometers during monotonic jacking into silica and carbonate sands that had been pressurised and partially unloaded.

Several numerical simulations have been performed with the Lagrangian approach of the FEM in order to investigate the installation processes of jacked, driven or vibratory driven piles (Mabsout and Tassoulas, 1994, Henke and Grabe, 2009). Broere and Tol (2006)

simulated the bearing capacity of the displacement pile in sand based on the FEM. Apart from this, De Gennaro *et al*. (2008) simulated the pile under the axial load in sand by FEM. Although there are many numerical simulations based on FEM to the behaviour of the pile and the interaction to the surrounding soil, some insuperable limitations of FEM are still pointed out. It is accepted that FEM performs not well in the simulations to discontinue such as fractured and granular. Ting *et al*. (1989) pointed out that there were potential problems with the assumption of continua, and it was due to the soil's inherent granular nature and the consequent deformation & failure modes. Li and Li (2014) also stated that the FEM was based on the small deformation theory and it was not applicable to some soil simulations, such as pile penetration, which was with the large deformation. In addition, Campos *et al*. (2005) stated that most FEM models based on the assumption of the mechanics of continua cannot provide an adequate description to one or more effects such as anisotropy, stress path dependency, dilatancy and confining stresses dependency.

4.2.2 Cone penetrometer tests

The cone penetrometer test (CPT) is a method used to determine the geotechnical engineering properties of soils and delineating soil stratigraphy. It was initially developed in the 1950s at the Dutch laboratory for soil mechanics in Delft to investigate soft soils. Based on this history it has also been called the "Dutch cone test". Today, the CPT is one of the most used and accepted in soil methods for soil investigation worldwide. The CPT is a reliable, fast and relatively economical in-situ test to obtain information about soil stratification and mechanical properties. When the cone shaped penetrometer is pushed into the ground, the soil experiences compression, shear deformation and plastic flow, thus making the mechanism of CPT complicated. Many investigations have been performed on the CPT mechanism in the past and they can be attributed to three methods in general: (1) analytical methods; (2) experimental methods; (3) numerical analysis methods.

Theoretical analyses include the bearing capacity theory (Terzaghi, 1943, Meyerhof, 1951, Hu, 1965) and the cavity expansion theory (Farrell and Greacen, 1966, Rohani and Baladixxa, 1981, Vesić, 1972, Yu, 2013, Yu and Houlsby, 1991, Salgado *et al*., 1998).

The experimental methods cover: laboratory chamber calibration tests (Ahmadi and Robertson, 2004, EI-Keiesh and Matsui, 2008), wedge penetration tests (Durgunoglu and Mitchell, 1975) and centrifuge methods (Sharp *et al*., 2010);

The aim of CPT is predicting the axial pile capacity and describing the formulations of skin friction. There are four main cone penetration tests: Simplified ICP-05, Offshore UWA-05, Fugro-05 and NGI-05. Four CPTs based methods for calculating the axial capacity of piles in sand are included in the API RP 2GEO commentary. All four CPT methods also include the effects of friction fatigue (Brucy *et al*., 1991, White and Lehane, 2004). Whereafter, this effect is taken into account by evaluating local skin friction at incremental depths along the pile relative to the depth of the pile tip.

The simplified Imperial College Pile (ICP)-05 method is a conservative approximation of the approach described in Jardine *et al*. (2005), where dilatancy is ignored and some parameter values are conservatively rounded off.

The Fugro-05 method is developed mainly from a calibration with the large Euripides pile load tests, and has a somewhat similar form to that of the ICP-05 method for the friction fatigue effects. The skin friction is a function of cone resistance, effective stress and pile diameter (Kolk *et al*., 2005).

The NGI-05 method is an empirical approach developed over many years, using the Norwegian Geotechnical Institute (NGI) database of 85 pile load tests from 35 locations and experience with the results of instrumented pile load tests. The development work is aimed at a simple formulation of skin friction. In the NGI-05 method, the skin friction depends on cone resistance (or relative density), effective stress, open- or closed-end tip, tension or compression loading and pile material (steel or concrete) (Aas *et al*., 2005).

The UWA-05 method was developed by the University of Western Australia (UWA) as part of a study to compare the three other CPT methods. It is essentially a modification and simplification of the ICP-05 method. It has a similar formulation, but reduces the number of parameters and introduces an area ratio. This is a simplified method suggested for large offshore piles (Schneider *et al*., 2008).

For the numerical analysis methods, there are the small strain finite-element method (De and Vermeer, 1984), the large strain finite-element method (Wei, 2004, Wei *et al*., 2005) and the strain path method (Baligh, 1985) and DEM.

Special finite element procedures for steady-state analysis, which neglect the transient component of the deformation, have been developed by Herrmann and Mello (1994) and Yu *et al*. (2000). In all these finite element analyses, the penetrometer was assumed to be pre-placed in the soil with a borehole, and only a limited number of penetration steps could be modelled. Even when the finite element analysis allows for finite strain (Gupta, 1991, Kiousis *et al*., 1988), modelling the whole penetration process is not possible unless large-scale sliding is permitted at the penetrometer-soil interface. Sheng *et al*. (1997) presented a finite element analysis of cone penetration in cohesive soils. Contact elements, capable of finite sliding along the penetrometer surface, were used to model the whole penetration process from the ground surface to any depth. The emphasis of their study was on pore-pressure development around the cone under different penetration speeds.

An alternative numerical method is the DEM and it is developed and used in geotechnical engineering recently. Most studies concentrate on the CPT based on the DEM numerical modelling because CPT is well-established in-situ test to classify soil and to estimate the soil properties in geotechnical engineering (Robertson, 1986, Been *et al*., 1987, Schertmann, 1977, Sladen, 1989, Yu, 2006). The first DEM numerical simulation to deep penetration in sand is applied by Huang and Ma (1994) and they found that the penetration mechanism and soil dilatancy in the granular soil are both affected by the loading history. Based on their study, Jiang *et al*. (2006) developed and improved the two dimensional DEM simulation to the deep penetration, and described the penetration mechanism from

the viewpoints of deformation patterns, displacement paths, velocity field, stress fields and stress paths. Arroyo *et al*. (2011) then developed the numerical modelling of the CPT in granular material to three dimensional and provide a potential new way to overcome the limitation of the quantitative analysis based on disc-based modelling. Apart from the CPT, a few researchers also pay attention to the penetration of the displacement pile (driven pile) in granular soils.

To date, for industrial or field scale problems, DEM is generally applied to pile installation and CPT in soil, where large deformation takes place near the cone. Campos *et al*. (2005) used DEM to model the CPT, the numerical implementation used in this research using dynamic relaxation, which consists of obtaining the solution of a static problem through its dynamic equations. This is achieved when the dynamic problem is correctly damped, avoiding oscillations. Jiang *et al*. (2006) used PFC-2D and conducted two DEM penetration tests applying different tip-soil frictions. The penetration mechanism during cone penetration was assessed via the monitoring of tip resistance, deformation pattern, displacement paths, velocity vector distributions and stress field for each penetration test. The results showed that tip resistance increases with increasing penetration depth and increasing tip-soil friction. It was also shown that penetration leads to high gradients of displacement and velocity fields near the penetrometer. Lastly it was observed that during penetration, the soil stresses near the penetrometer increased from their initial values to higher peak stresses, which subsequently became constant at values which were slightly higher than the stresses upon initiating penetration.

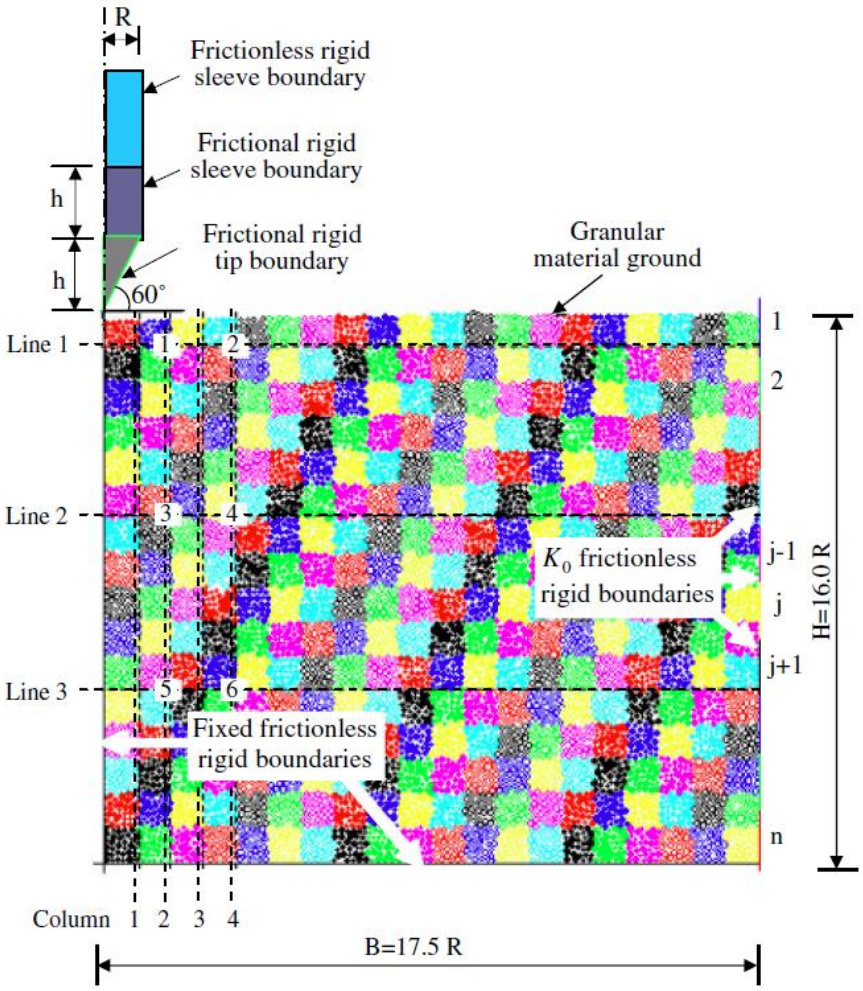

Figure 4.2.1. Boundary conditions and observance positions in the DEM analyses (Jiang et al., 2006)

While Jin and Zhou (2010) used a coupled method to model the CPT, Zhou *et al*. (2012) also used the coupled 3D version numerical simulation to reproduce the CPT test. Mcdowell *et al*. (2012) research CPT with a new method of sample preparation. Generally, the DEM approach provides an alternative to current unrealistic large-displacement FEM model for CPT in granular materials, what is more, DEM provides micro-mechanical insight into this important boundary value problem (Mcdowell *et al*., 2012, Arroyo *et al*., 2011).

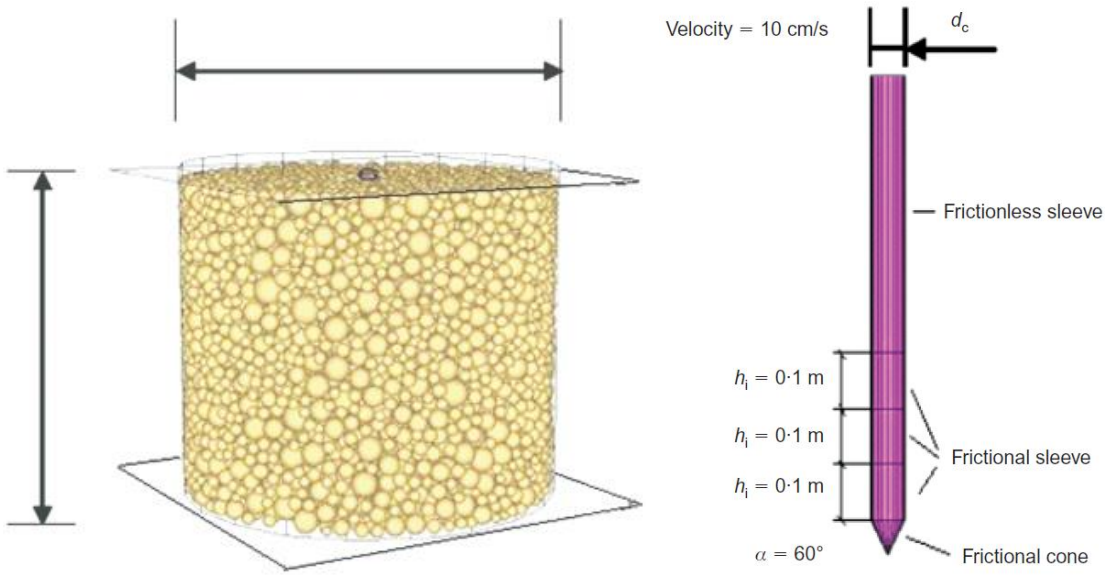

Figure 4.2.2. View of the DEM model components with indication of the main relevant dimensions: (a) calibration chamber; (b) cone (Arroyo et al., 2011)

Arroyo et al. (2011) built a virtual calibration chamber to simulate cone penetration tests in sand using a 3D DEM model. The particles were represented by single spheres which were prohibited from rotating to enable the rotational resistance of non-spherical particles to be modelled. The simulation results were compared to experimental tests conducted in Ticino sand (Jamiolkowski *et al.*, 2003). The particles used in the DEM models were scaled to 50 times larger than the Ticino sand, such that a median particle size d_{50} of 26.5mm with a cone diameter B of 71.2mm was necessary to achieve an appropriate number of particles in contact with the cone tip (see Figure 4.2.2). The results showed that under isotropic boundary stresses, their numerical results demonstrated good quantitative agreement with the predictions of experimentally derived empirical equations for Ticino sand.

4.2.3 Bored pile

The bored piles are executed by gradually removing the soil and advancing the auger in depth with up and down movements. For most bored piles, shaft friction is the important component of bearing capacity. The conventional empirical design approach has been to evaluate the available side shear by applying a reduction factor to an average undrained shear strength profile obtained from laboratory tests (Skempton, 1959, Whitaker and Cooke, 1966, Burland and Cooke, 1974).

Calibration chamber plate load tests have been used to investigate the load-settlement response of nondisplacement piles (Ghionna *et al*., 1994, Lee, 1999, Lee and Salgado, 1999). A number of numerical techniques have been identified for the same purpose (Desai and Christian, 1977, Lee *et al*., 1989, Poulos and Hull, 1989, Poulos, 1982). Wehnert and Vermeer (2004) introduced the FEM to simulate and analyse the load test on bored piles. Unfortunately, opposed to the numerical simulation of bored piles (Wehnert and Vermeer, 2004) the installation phase leads to significant stress changes compared to the undistorted state. These stress changes should be included in the modelling of displacement piles, but most codes do not permit the full simulation of the pile installation phase. The large strains and deformations that occur are unsuitable for the small strain formulations of generic geotechnical FEM codes which incorporate a Lagrangian or an updated Lagrangian scheme. Also, the modelling of the complex soil behaviour adjacent to the pile is not straightforward, as the soil behaviour is not yet fully understood.

4.2.4 Summary

The installation process of the piles influences the soil and some of its properties. Several investigations have been performed to comprehend the influence of installation effects on pile bearing capacity (De Beer, 1988, Peiffer and Van Impe, 1993). Peiffer and Van Impe (1993) investigated the development of the stress state around the pile during the pile installation processes. It is obvious that the installation process changes the stress state and

the void ratio in the surrounding soil. Albuquerque *et al*. (2011) compared the behaviour of 3 types of deep pile (bored, continuous flight auger (CFA) and precast driven piles) by the static pile load tests (SPLT) from experimental field to laboratory tests and state that the shaft and tip resistance of the bored and CFA piles are similar, although CFA pile contributes less disturbance to the surrounding soil at the tip. In addition, they state that the precast driven pile with the less cross-section shows the stiffer response and both higher shaft and tip resistance. However, the opposite observation is obtained by Adejumo and Boiko (2013) in their field tests to the driven and bored piles under the axial load. It shows that driven installation technique results in more surrounding soil displacement compared to the bored installation technique, and it also results in the decreasing of the bearing capacity of the pile (by approximately 12 - 18%) in a fully mobilised soil resistance and loading case.

In parallel with field investigation and laboratorial experimental study, numerical simulations were also undertaken to elucidate the mechanic behaviour as well as the complex mechanisms involved in the pile installation. The numerical approach to modelling installation effects is very promising, and will give valuable additional information about the simulated stress-strain behaviour of soil due to installation effects.

4.3 General model description

All DEM analyses in this investigation were performed using an increased gravity field of 100 g; details which can be found in Duan and Cheng (2016a). A schematic view of the model is shown in Figure 4.3.1, which includes a rigid pile with diameter d_{pile} = 45 mm and penetration depth (fully embedded depth), $L_{embedded}$ = 0.2 m. This results in a prototype pile with diameter of 4.5m and penetration length 20m ($L_{embedded} = 4.44 d_{pile}$). The dimension is a typical size of a large rigid monopile for wind turbine foundation. The width of the model container is 1.2 m, and the depth is 1.5 m. This width is bigger than the model in Duan and Cheng (2016a)in order to further eliminate the boundary effect ($d_{bp} = 12.33\ d_{pile}$,

and ($D - L$) = 8.89 d_{pile}). A view of the particle assembly is also shown in the subset of Figure 4.3.1, and d_{50} = 5.85 mm (d_{pile} = 7.69 d_{50}). The different definitions are shown in Figure 4.3.2. H and u_y show the applied force and the corresponding displacement.

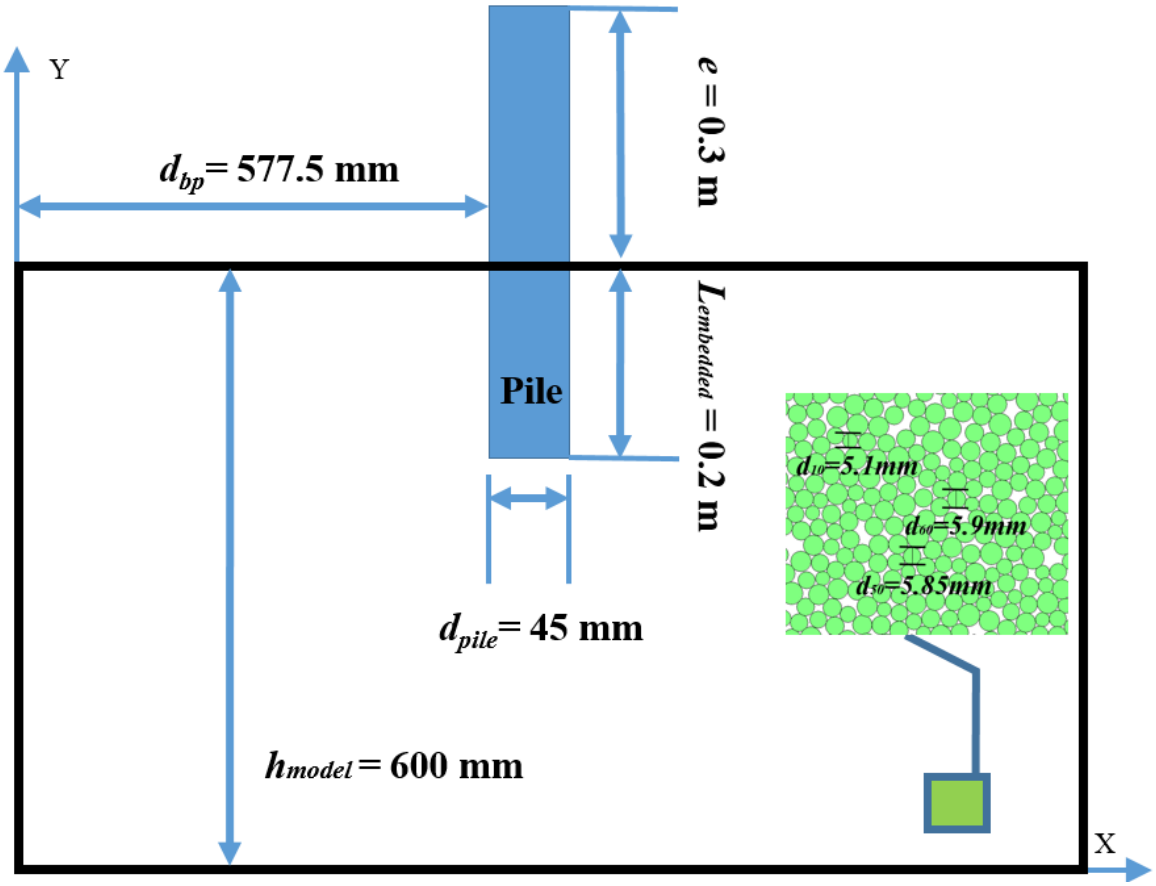

Figure 4.3.1. Schematic view of the PFC model. (Subset shows a typical particle assembly at equilibrium before pile installation.)

Centrifuge testing allows small models to be used to accurately represent the behaviours of prototype (full-scale) geotechnical problems. In this study, all simulations were conducted under 100 time's gravity field.

For larger scale soil-structure interaction problems, current DEM techniques used for generating specimens hardly result in homogeneous and realistic specimens. Hence, a modified particle generation method, referred to as the Grid-Method (GM), was proposed

to generate a homogeneous and realistic specimen for this DEM study (Duan and Cheng, 2016a). During the process of GM specimen generation, particles in the first grid were generated at the initial porosity of 0.25 without gravity, then the grid was cycled until equilibrium. Afterwards, a100 time's gravity was applied to all the particles in this grid, and the system was cycled to equilibrium again. The same process runs for all other grids until the whole system reaches the final static equilibrium state, which has an average porosity of 0.185. Table 4.3.1 shows the DEM model input parameters. The material modelled is composed of disks with a maximum diameter of 7.05 mm, a minimum diameter of 5.5 mm, an average grain diameter d_{50}=5.85 mm and uniformity coefficient $C_u = d_{60}/d_{10}$ = 1.26.

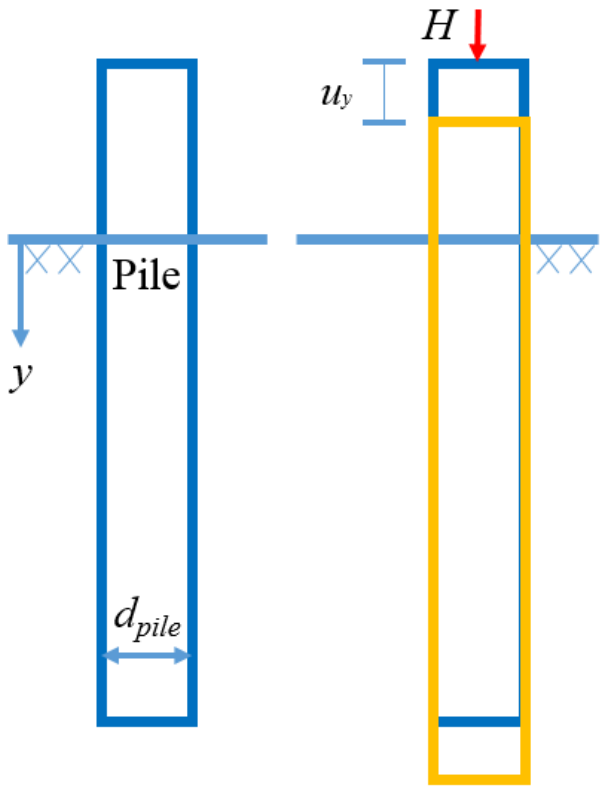

Figure 4.3.2. Schematic view of the model under vertical load.

Based on a comparison of parameters used in other experiments and DEM simulations, it was found that the parameter d_{pile}/d_{50} was related to the accuracy of experiment and

numerical modelling. In this model, for the aim of efficiency, the value of d_{pile}/d_{50} was chosen around 8 which was close to Vallejo and Lobo-Guerrero (2005). A comparison of a range of model parameters with other published data is shown in Table 4.3.1.

Table 4.3.1 General test configurations for various laboratories.

Diameter of pile, d_{pile} (mm)	Average grain diameter, d_{50} (mm)	$\frac{d_{pile}}{d_{50}}$	$\frac{w_{model}}{d_{pile}}$	$\frac{h_{model}}{d_{pile}}$	Gravity (9.8 m/s^2)	Case
1	0.172	5.81	12	25	2000	Zhang and Wang (2015) [3D]
8	0.1735	46.1	30	30	50/100/ 150	Wang and Zhao (2014) [2D]
159.98	7.6	21.1	31.25	10.16	20	Jiang et al. (2014) [2D]
71.2	26.5	2.7	16.86	9.83	1	Arroyo et al. (2011) [3D]
71.2	26.5	2.7	16.86	9.83	1	Butlanska et al. (2009) [3D]
36	2.925	12.3	8.75	8	1000	Jiang et al. (2006) [2D]
30	3	10.0	13.33	26.66	1	Vallejo and Lobo-Guerrero (2005) [2D]
10	0.22	45.5	21/ 85		40/70/ 125	Bolton et al. (1999) [centrifuge tests]
45	5.85	7.69	26.67	13.33	100	Present study [2D]

4.3.1 DEM modelling programs

Table 4.3.2 summarises all the DEM simulation tests, "BE" means bored pile with the flat-end, and "DE" means driven pile with flat-end. There were 6 tests in total to compare the effects of different soil characteristics. Numbers "1, 2, 3" mean the different friction 0.2, 0.5, 0.8" of the surrounding soils respectively. For all simulations, the friction coefficient of the pile is always 0.5.

Table 4.3.2 General test configurations for DEM models.

Simulation name	BE1	BE2	BE3	DE1	DE2	DE3
Particles friction coefficient	0.2	0.5	0.8	0.2	0.5	0.8

The embedment depth of the two pile types (driven pile and bored pile) are both 0.2m, but their installation methods are entirely different. For driven pile, it was pushed into the soil by a stepwise increase of vertical load until the desired depth was reached. Under each specific load, the system was cycled to equilibrium until the pile displacement reached its maximum, and then the following load was applied. It should be noted here that the pile was finally driven to the depth that is a little more than 0.2 m depth (0.2007 m, 0.2015 m and 0.2024 m for DE1, DE2 and DE3 respectively). This is to allow for the pile moving upwards slightly to a final 0.2 m depth after the applied force was released. This phenomenon is considered to be the cause of residual force in driven pile (Zhang and Wang, 2007, Zhang and Wang, 2009, Liu *et al*., 2013).

The PFC inherent "measurement circle" function is introduced here to measure the information of soil elements at different locations surrounding the pile. The size and locations of these measurement circles were described in Figure 4.3.3; m_r is the radius of measurement circle and the value is 0.05 m. Note only one side of the model was analysed due to the symmetrical nature of the problem. Four levels of depths (with the deepest Level 1 0.1 m below pile tip, and the shallowest Level 4 at mid-depth of the pile, i.e. 0.1 m above

pile tip) were monitored, together with nine horizontal locations (VL1,VL2…VL9).

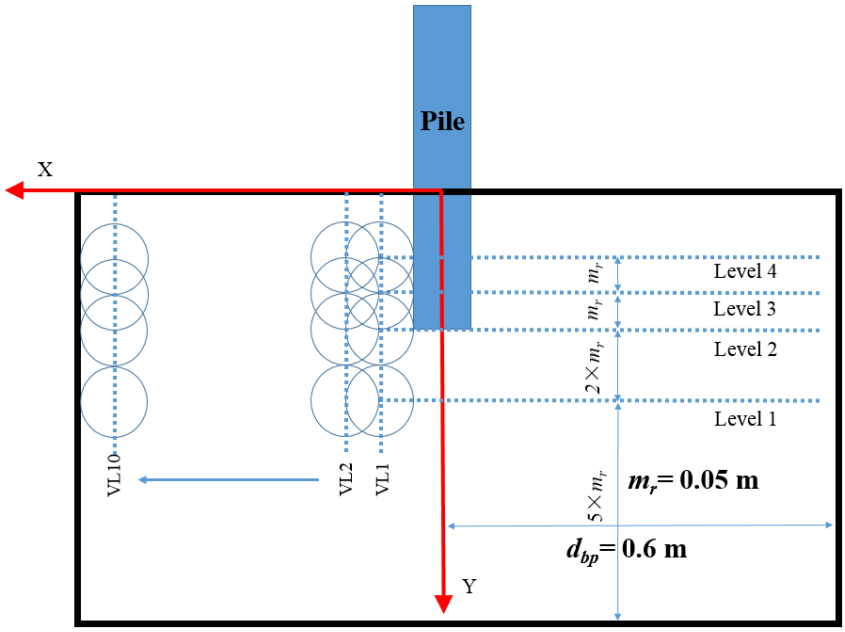

Figure 4.3.3. The new coordination of PFC model for the measurement circle analyses.

4.4 Pile installation

4.4.1 Driven pile

All dimensions and measurements in the following sections are shown in model scale. The driven pile was pushed by the increasing vertical load level, such as 0kN, 20kN, 40kN, 80kN and so on, until around 150kN. The procedure was described in Figure 4.4.1. Figure 4.4.2 (a) plots the vertical load against the normalised pile penetration when installing at different soil conditions, in which the vertical load is calculated by the summation of applied vertical load and the self-weight of pile. Although the slopes of the various load-displacement curves are very similar regardless of soil friction after the pile penetrated the soil, the soil with the highest friction coefficient (DE3, μ=0.8) provides the highest initial penetration resistance, hence requiring the highest vertical force to reach a certain penetration depth. Figure 4.4.2 (b) shows the total, shaft and base resistance developed during installation in the case when the soil friction is 0.5 (DE2). It is clear that total

resistance increases approximately linearly with penetration depth, in which the base resistance contributes to the majority of the total resistance. It is therefore evident that the penetration resistance of piles depends mostly on the base resistance, as reported by Yu (2004) and Liu *et al*. (2012). This should be attributed to the punching shear failure mechanism when the pile tip penetrates the soil.

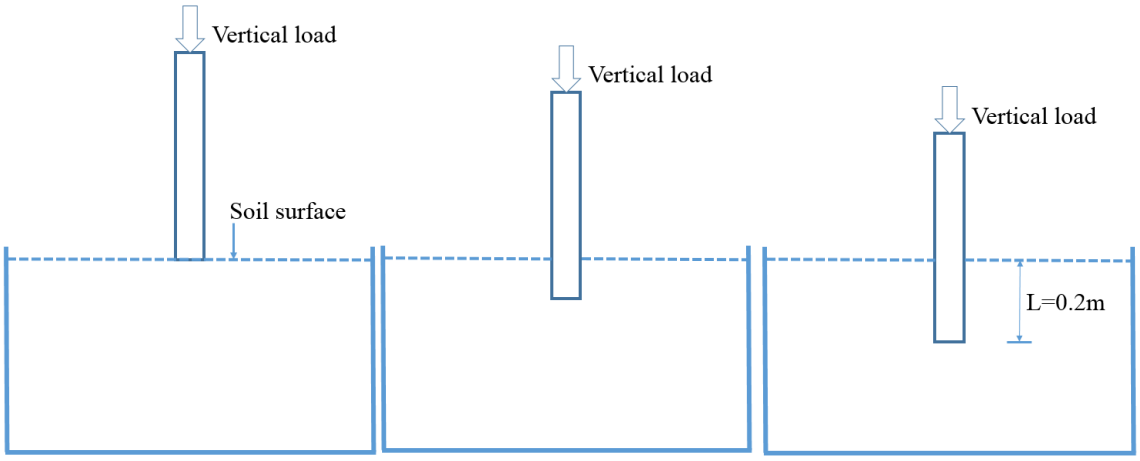

Figure 4.4.1. Procedure of driven pile in DEM model.

The shaft resistance of Figure 4.4.2 (b), on the other hand, increases much more gently than the base resistance, and even experiences some drops during driving. This implies that the unit shaft resistance may possibly decrease as the area of pile-soil contact increases during penetration. This is testified by the profile of unit shaft resistance at different vertical forces, as shown in Figure 4.4.3. Sometimes the unit shaft resistance becomes negative, which means the applied shaft resistance on pile surface is acting downwards. The reasons for this phenomenon are the arching effect and particles size effect. When arching is generated, the affected sand particles within in the range of arching are not affecting the vertical load but only the self-weight. Part of them are in touch with the pile shaft, the friction is bigger than their self-weight. So the shaft resistance will cause the particles to move down with the movement of pile. This phenomenon is referred to as 'friction fatigue' (Heerema, 1980) or the '*h*/*R* effect' (Bond and Jardine, 1991). It is widely accepted that changes in radial

stress are the key factors governing the magnitude of shaft friction. The changes of porosity recorded in the surrounding soil during the pile penetration are shown in Figure 4.4.4. This mainly attributes to the volume reduction of the soil as the sand grains rearrange and repack surrounding the pile, which is captured in this simulation.

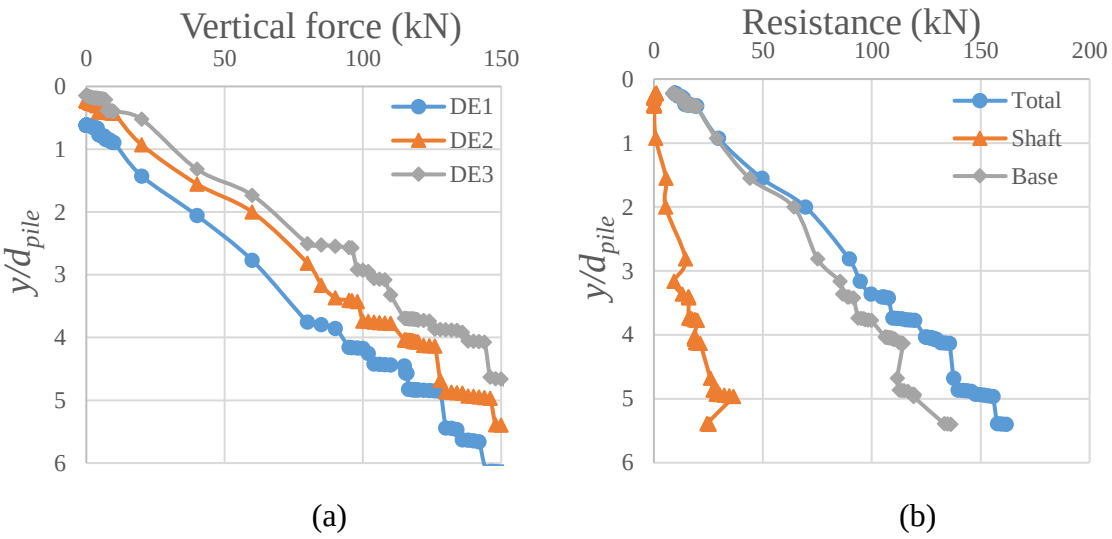

Figure 4.4.2. (a) Load-settlement curves installing at different soil conditions (μ=0.2, 0.5 & 0.8). (b) Vertical force-displacement curves indicating the variation of total, shaft and base capacity for the DE2 (μ = 0.5).

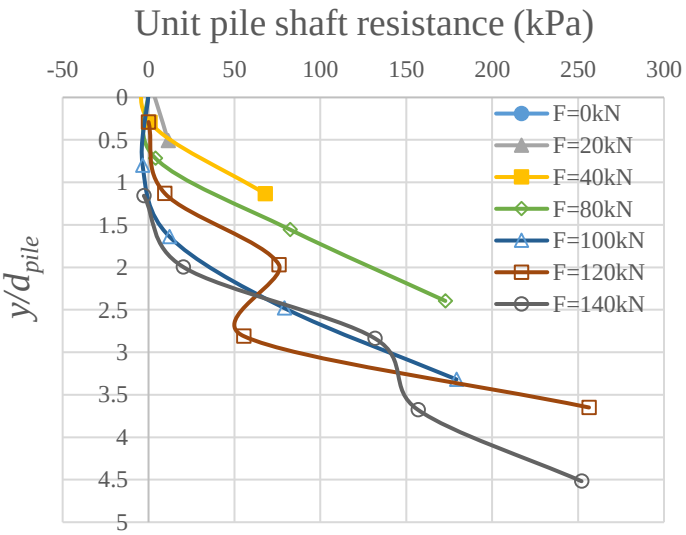

Figure 4.4.3. Unit shaft resistance along the pile at different installation depths (DE2).

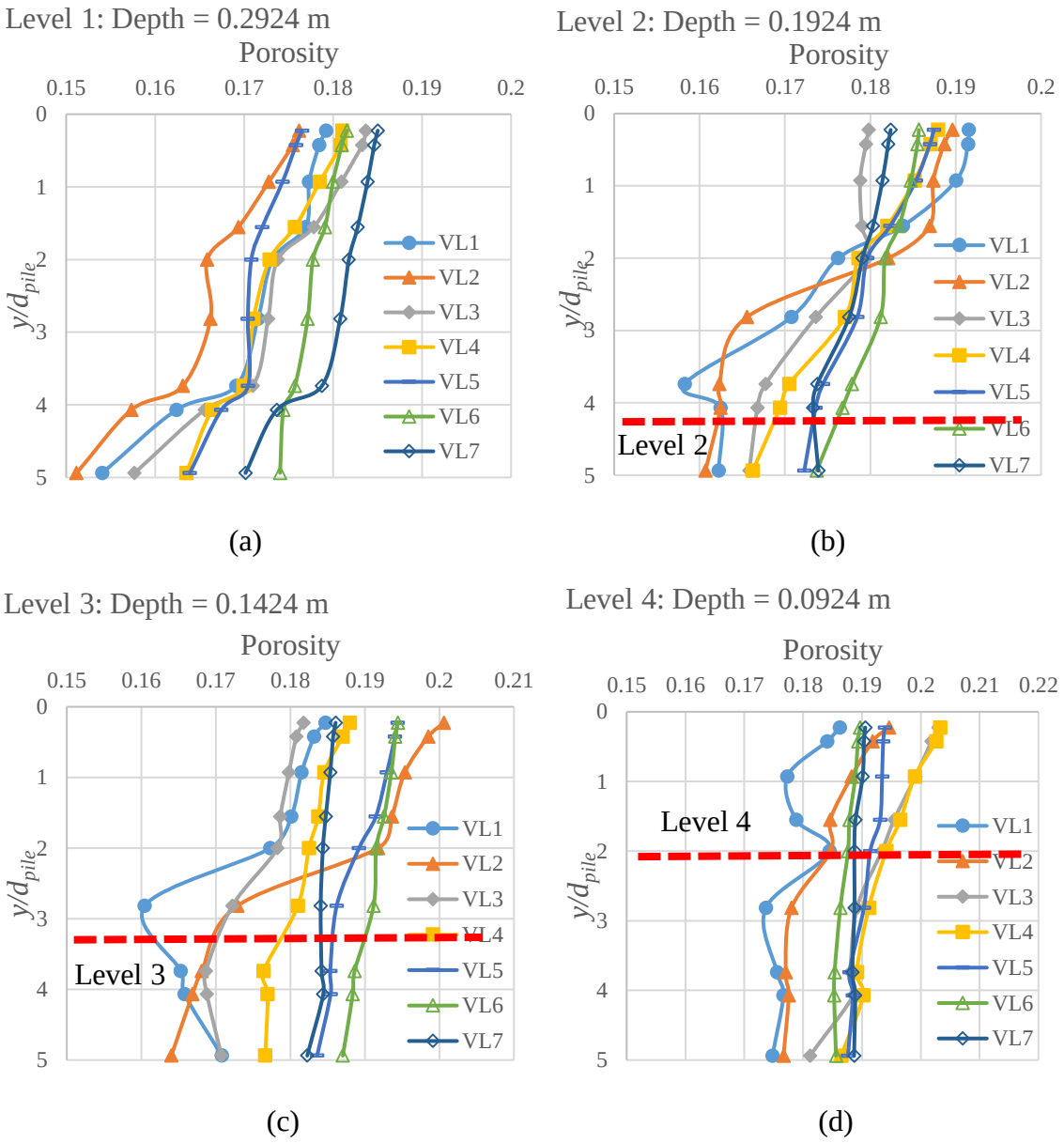

Figure 4.4.4. Porosity distributions during the penetration of driven pile in DEM model.

Figure 4.4.5 shows the lateral soil stresses at 4 specific depths (e.g. Figure 4.4.5 (a): Level 1 at the deepest depth, and Figure 4.4.5 (d): Level 4 at the shallowest depth) and different distances away from the pile (VL1-VL10) while the pile tip has penetrated to different normalised depth (y/d_{pile}). It is clear in Figure 4.4.5 (d) that the lateral stress on the pile-

soil interface reduces drastically lower than the initial K_0 stresses after the pile tip passes by.

At levels 2-4 above the pile tip, the general variation of lateral stress displayed a similar tendency and matched the penetration process fairly well. As the pile tip penetrated the soil and advanced down, the lateral stresses increase sharply as a result of large soil deformation. This phenomenon follows the illustration of Yu (2004) and Liu *et al*. (2012) where a penetrating pile base resembles the expansion of a spherical cavity. In the close regions from the pile shaft, the lateral stresses increase sharply and reach peak values as the pile tip almost penetrates to the level of these locations, and then decreased as the pile tip penetrated deeper. Similar trends of the variation in lateral stress have also been observed in centrifugal model tests (Leung *et al*., 2001, Yang *et al*., 2013) and field tests (Liu *et al*., 2012). As the radial distance from the pile axis increases, this "bend" of curves becomes less remarkable. Beyond around 6 times the pile diameters, the lateral stresses build up uniformly and generally during the whole process penetration. This indicates the zone of the highest stress disturbance, showing significant granular behaviour, has an approximate extent of 6 times of pile diameters.

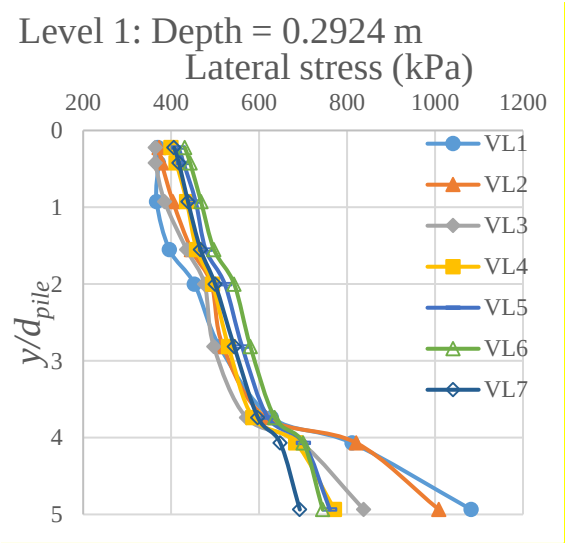

(a)

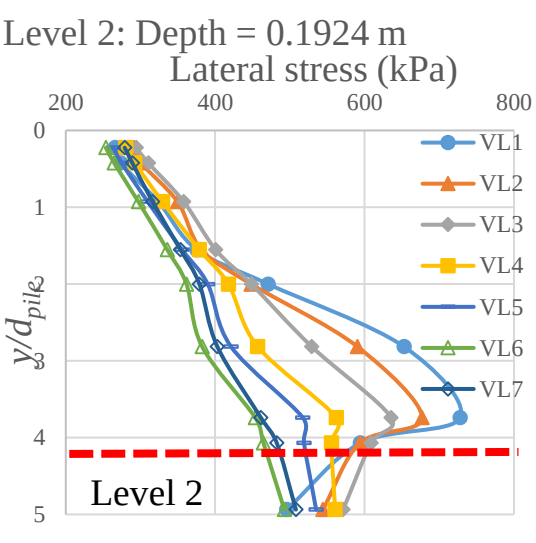

(b)

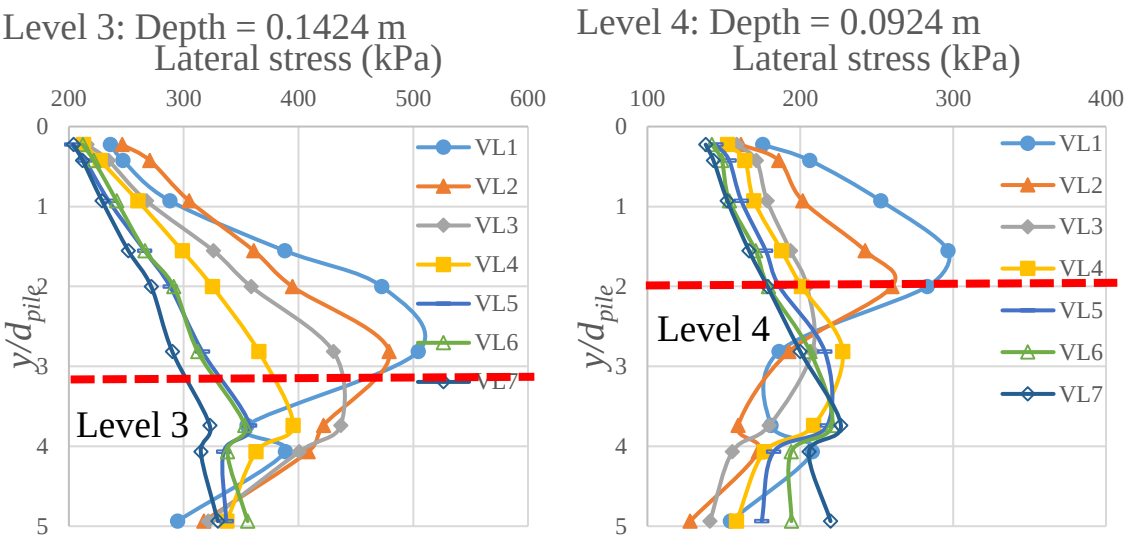

(c) (d)

Figure 4.4.5. Lateral stress distributions during the penetration of driven pile in DEM model.

The greatest % increase of induced lateral stress was registered by level 2 at the full embedment depth (~ 0.2 m), which is 48% and 173% greater than those by level 3 and level 4, respectively. This observation indicates that the magnitude of the induced lateral stress depends not only on the radial distance but also on the embedment depth or the overburden pressure. Hence, the ratio of the increases of lateral stress ($\Delta\sigma_h$) to the initial horizontal K_0 stresses (σ_0) against the normalised horizontal distances are plotted for all the three levels in Figure 4.4.6. It is clear that the curves corresponding to the three levels seemed to exhibit similar distribution, and restricted in an approximately logarithmic distribution zonal region. Then an affecting region of 12~18 pile diameters from the pile shaft can be confirmed according to the enveloping lines. This region is consistent with the experimental observations by Yang *et al*. (2013) and field tests Liu *et al*. (2012).

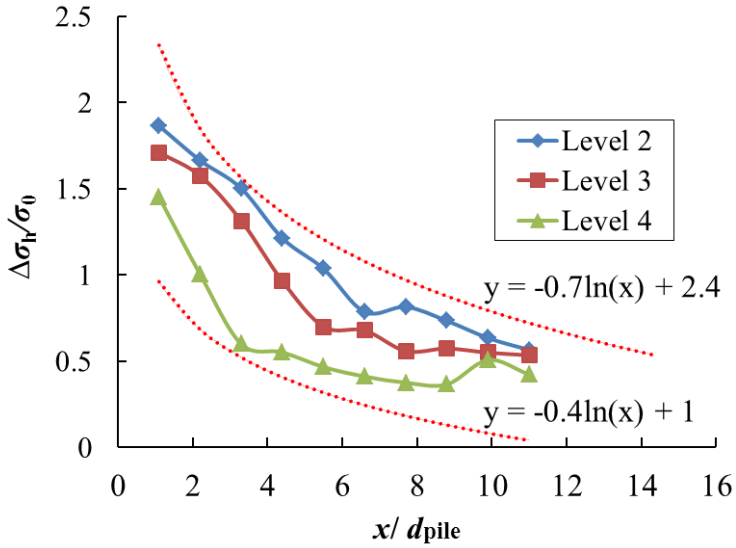

Figure 4.4.6. Variation in normalised maximum increase of lateral stress with normalised horizontal distance.

For level 1, which is 2.2d_{pile} lower than the final depth of pile tip, the lateral stresses build up gently for each record point. For the farthest VL7 (see Figure 4.4.5 (d)) that is 11d_{pile} from the pile shaft, no evident change is recorded at the beginning penetration. This means the affecting distance of pile driving is far more than 11d_{pile} (50 increased), which is obtained from Figure 4.4.6.

In Figure 4.4.7, the x-axis was normalised by x/d_{pile} which means the according lateral distance from the left side of the pile. 0 means the left surface of the pile. When the pile was just penetrated and passed to level 4 (see Figure 4.4.7 (d)), the peak value of lateral stress was reached when the vertical force only achieved about 40-60 kN. Then the lateral stress when near the pile was decreased. The level 3 (see Figure 4.4.7 (c)) is a little deeper than level 4 and the peak value appeared when the applied force was 80 kN. For the level 2 (see Figure 4.4.7 (b)), it is around the pile bottom and much deeper. Therefore the lateral stress maximum value attained when the applied force is 100 kN. Level 4 (see Figure 4.4.7 (a)) is very deep, so the lateral stress keeps increasing.

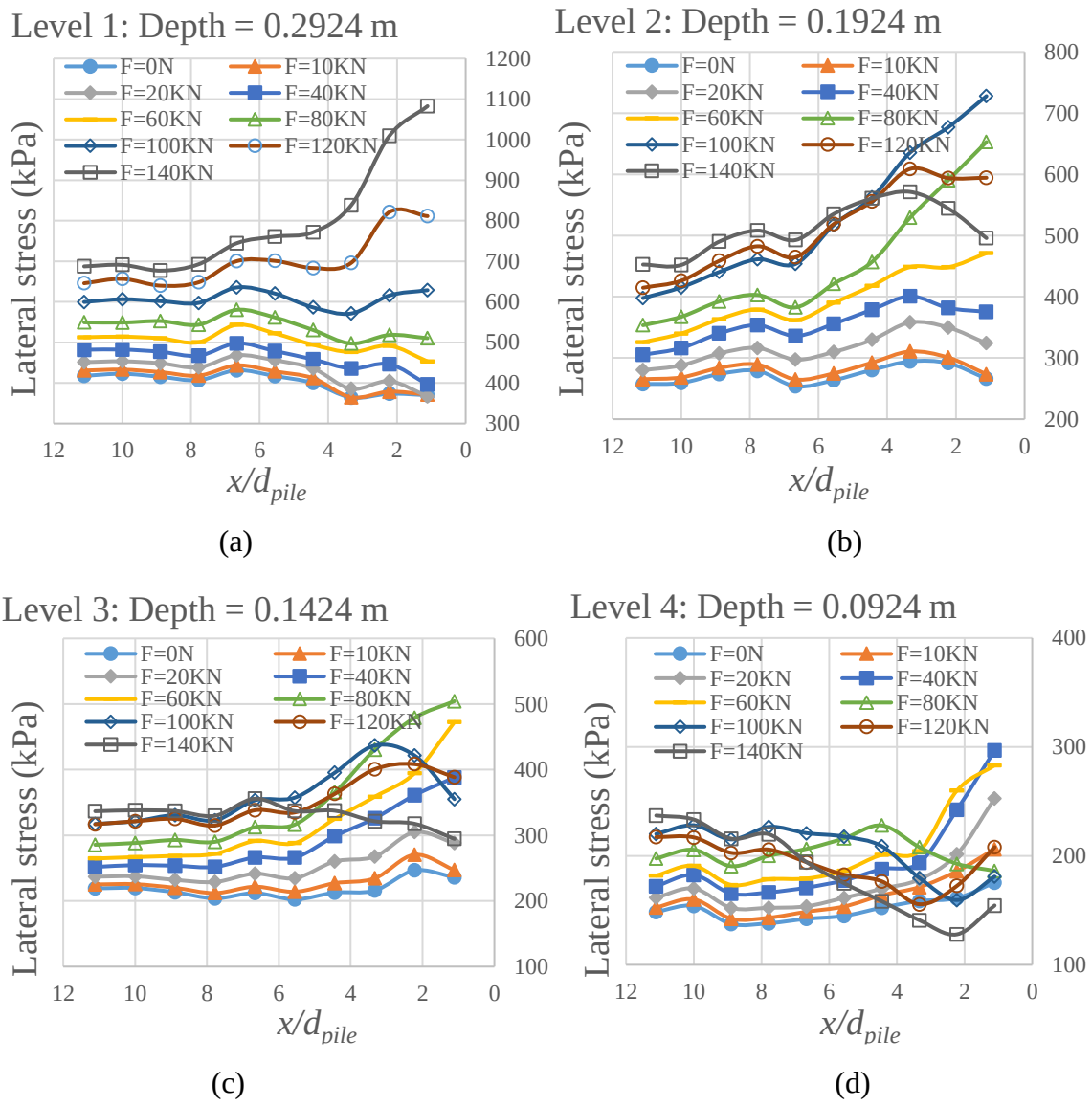

Figure 4.4.7. Lateral stress distribution of different level during the procedure of driven pile in DEM model.

4.4.2 Bored pile

The bored pile is simple compared to the driven pile. Before the bored pile was put in the soil, the soil which is in the same location as the pile was deleted (see Figure 4.4.8). Then the pile was generated instantly and the model kept cycling until equilibrium.

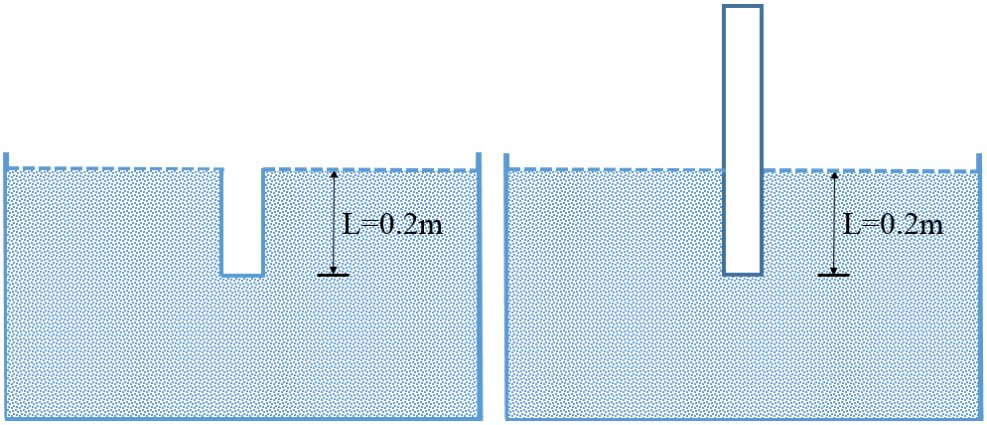

Figure 4.4.8. Procedure of bored pile in DEM model.

The model generation procedure of a bored pile is simpler compared to that of a driven pile. Figure 4.4.9 (a) shows the load-settlement curves of the bored pile after the pile is installed, and the corresponding mobilised shaft resistance against settlement curves in Figure 4.4.9 (b), during the pile load test for piles (Cases 01-04) having different weights. Although the load-settlement curves are different, with the heaviest pile settling significantly more, the development of shaft resistance looks generally similar reaching a similar maximum value of around 20kN. It should be noted, however, that the initial shaft resistance of different piles is not exactly the same (see Figure 4.4.9 (b)) but light pile experiences negative initial shaft resistance while heavy pile experiences positive and high initial shaft resistance. Due to this phenomenon, Case 03 pile (03_BE_2) was chosen for the following tests. Figure 4.4.10 shows the effect of soil friction coefficient to the load-settlement curves for total vertical load (Figure 4.4.10 (a)) and for shaft resistance (Figure 4.4.10 (b)) for case 03. From Figure 4.4.10 (a), the soil friction had more obvious settlement when the vertical load became larger. Moreover, when the friction of particle is bigger, the line remains more linear. This linear range indicates that friction has not been fully mobilised fully throughout the pile hence a smaller percentage of sliding between the pile surface and adjacent soil particles occurs. As more and more particle sliding happens, shaft resistance becomes constant even if vertical load increases.

Table 4.4.1 Comparison of 4 different weight piles.

Simulation name	1	2	3	4	Displaced soil
Density of pile particles (kg/m^3)	66.65	200	500	1000	-
Weight (N)	1282.918	3849.832	9624.482	19249.16	19037.7

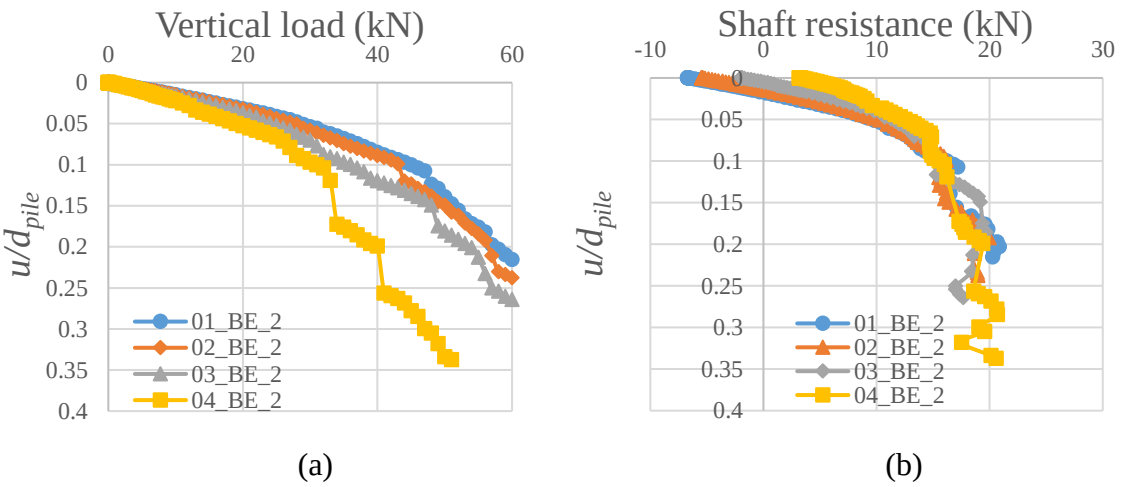

(a) (b)

Figure 4.4.9. Comparison of load-settlement curves with pile having different weights.

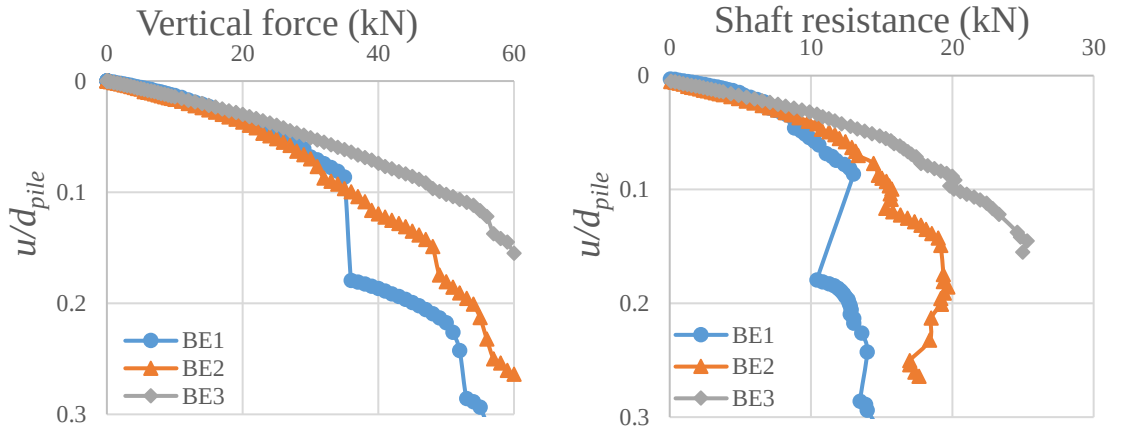

(a) (b)

Figure 4.4.10. Comparison of load-settlement and shaft resistance-settlement curves of bored pile in different soil conditions (μ=0.2, 0.5 & 0.8).

4.5 Comparison and Discussion

4.5.1 The bearing properties

Figure 4.5.1 presents the comparison of total load-settlement curves with different installation methods after the piles have been installed. Due to the different installation methods, the driven pile has higher vertical capacity than the bored pile. When the vertical load is less than 25 kN, the curves below exhibit nearly the same trend for both piles. However, the bored pile goes deeper into the soil at a faster rate with the same load after this point, showing that the driven piles has higher vertical capacity.

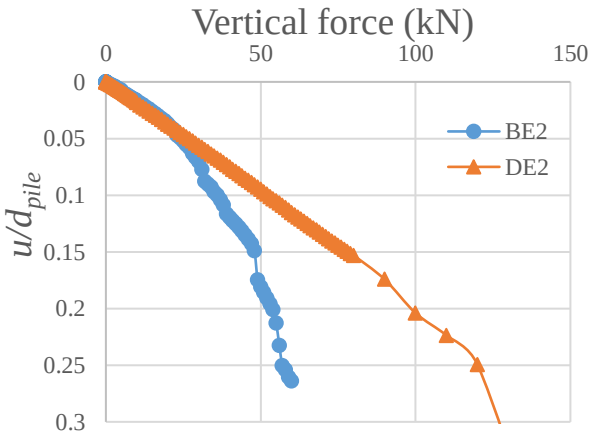

Figure 4.5.1. Comparison of load-settlement curve with different installation.

In Figure 4.5.2, the x-axis was normalised by x/d_{pile} which was similar to Figure 4.4.7. When the pile length was just pushed to level 4 (see Figure 4.5.2 (g) and (h)) it was the first domain which will be affected. This level is relative shallow. Regrading to the level 3 (see Figure 4.5.2 (e) and (f)), for the bored pile (see Figure 4.5.2 (e)), the peak value of lateral stress was reached when the vertical force achieved about 140 kN. However, in terms of driven pile the peak value of lateral stress was reached when the vertical force only achieve about 120 kN. Then the lateral stress when near the pile was decreased. The

level 2 (see Figure 4.5.2 (c) and (d)) is a little deeper than level 3 and around the pile bottom, and the phenomena also were the same. Level 1 (see Figure 4.5.2 (a) and (b)) is very deep, so the lateral stress keeps increasing.

Concerning the lateral stress of bored and driven pile, obviously the driven pile is larger than the corresponding deep level bored pile. This relationship also can be indicated from the Figure 4.5.1.

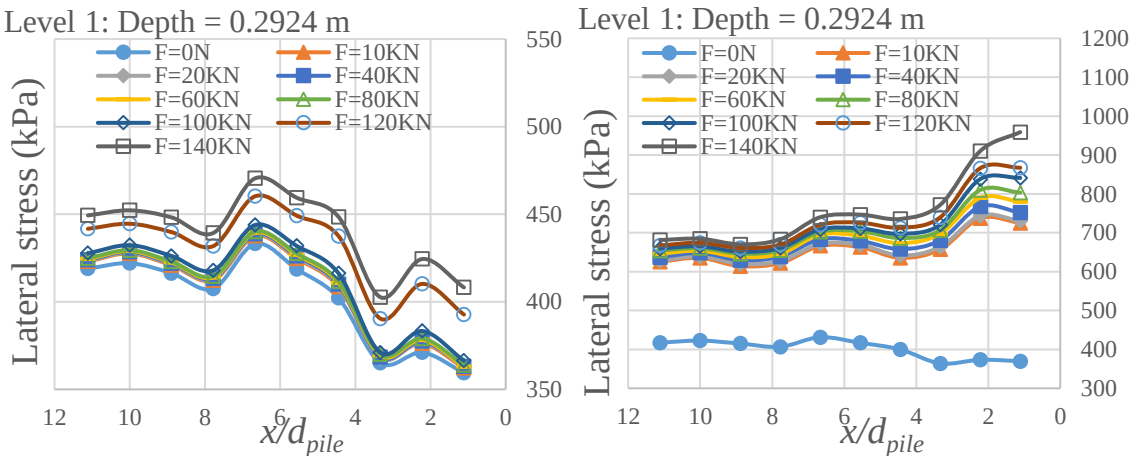

(a) (b)

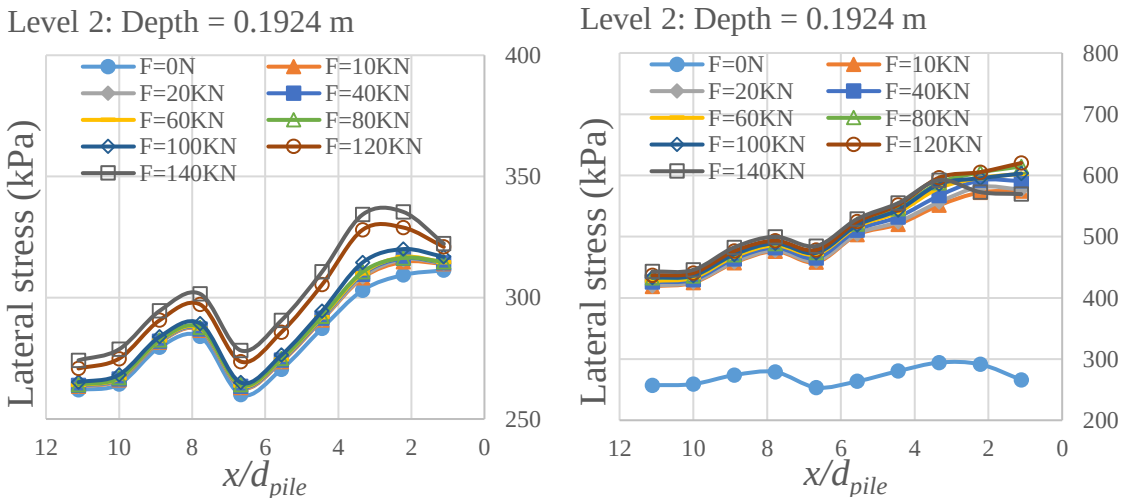

(c) (d)

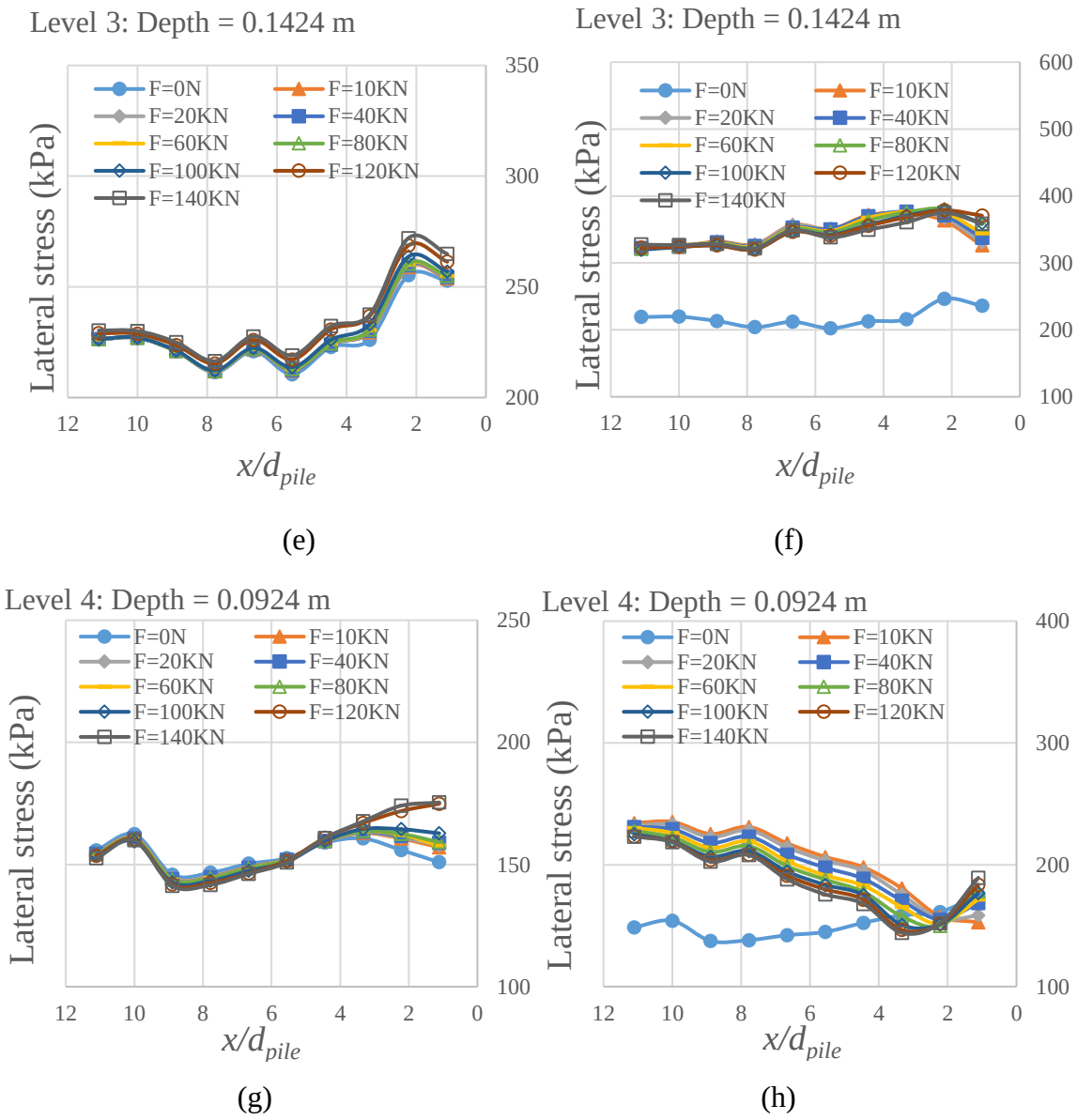

Figure 4.5.2. Comparison of lateral stress at horizontal direction with different installation, (a)(c)(e)(g): bored pile; (b)(d)(f)(h): driven pile.

4.5.2 Mobilisation of shaft resistance

The mobilisations of shaft resistances of pile DE2 and BE2 during loading are shown in Figure 4.5.3. In Figure 4.5.3 (a), the negative shaft friction occurs over the full pile length

before loading. This residual shaft resistance is due to the pile upward moving just after generation as the weight of the pile is lighter than the deleted original soil. When the bored pile applied the vertical force again, the movement of pile began to turn downwards, then the shaft resistance is mobilised and starts to become positive. During the procedure of increasing loads, the shaft resistance is generally small at both ends but large in the middle. At the final load, the maximum unit shaft at the pile bottom is 113 kPa, which is only one third of that for the driven pile as shown in the Figure 4.5.3 (b).

Table 4.5.1 Driven pile rebound record.

Test	Initial vertical load (kN)	Initial depth (m)	Depth after load release (0 kN)	Rebound distance (m)
DE1	116.48	0.210596	0.200756	0.00984
DE2	128.9	0.213526	0.201576	0.01195
DE3	151.4	0.218116	0.202456	0.01566

Figure 4.5.3 (b) shows the changes in shaft resistance of DE2 during load procedure, which looks very different from the bored pile BE2. Although there also exist negative shaft resistances before loading, their magnitudes are much larger than that of the bored pile. The residual shaft resistance exhibits an approximately linear distribution with the depth, and thus the maximum residual load is certainly located at the pile toe. This distribution is similar to those calculated by Poulos (1987) and Altaee *et al*. (1992). After finishing the driving installation and releasing the load, the rebound of soil blows the pile bottom and pushed the pile shaft upwards. The rebounds of these three piles are in Table 4.5.1, which are enough to reverse the direction of the unit shaft resistance from an upward direction during driving to a downward direction.

With the static loads applied and with the pile DE2 settlements, the direction of shaft resistance is reversed again, and the positive shaft resistances are generally mobilised. When the load is added to 40 kN, the shaft resistance along the whole depth becomes

positive. At this moment, the shaft resistance on the bottom and top of the pile are nearly zero, but on the middle is as high as 58 kPa. With the increasing load, the deeper shaft resistance is further mobilised, and reaches the peak value of 350 kPa at the final load. This value is close to the recommended value for dense sand in the Chinese pile design code.

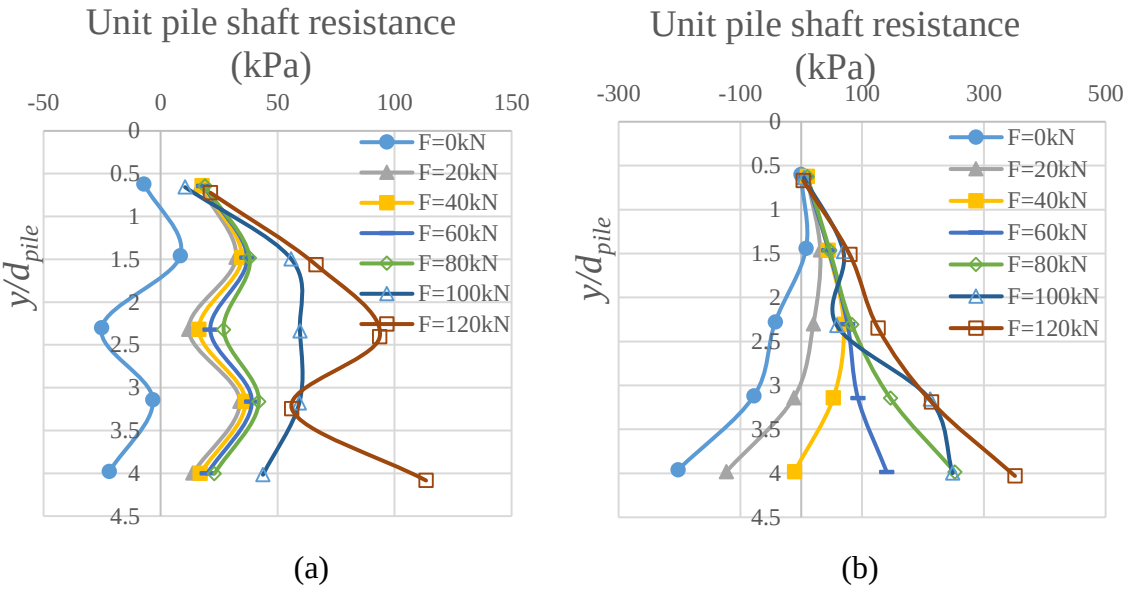

(a) (b)

Figure 4.5.3. Mobilisation of unit shaft resistance of pile, (a) BE2, (b) DE2, during pile load tests.

4.6 Summary

In this chapter, a discrete numerical modelling of pile installation tests was proposed. For larger scale soil-structure interaction problems, a modified particle generation method, referred to as the Grid-Method (GM), was proposed to generate a homogeneous and realistic specimen for this DEM study. Regarding the driven pile, the lateral stress change of specific location was recorded. It indicated that the peak value of lateral stress always reached before the pile passed this area.

The tests were conducted with two different processes: bored pile and driven pile. Both conditions were performed with similar magnitude of pile embedded depth. Shaft

resistance, base capacity and lateral stress were tested. Bored piles were observed to develop large settlements immediately during the test, while driven piles initially withstood settlements owing to an increase in available base capacity at the start of the penetration. For bored and driven pile, the soil with the highest friction coefficient proved the highest capacity.

The main content of this chapter was submitted to Granular Matter for review as a potential journal paper with title “DEM analysis of pile installation effect: comparing a bored and a driven pile”.

Chapter 5

A micromechanical study of monopile under monotonic loading using DEM

5.1 Introduction

This chapter presents the data of a numerical model that is used to study the soil-structure interaction of a rigid monopile under monotonic loading using the 2D-DEM. At present, monopile foundations are widely used to support wind turbines. The response of a monopile supporting an offshore wind turbine is still not well described and more research is therefore needed. Existing studies of monopiles recorded in the literature mainly adopt experimental techniques, including small-scale models in the laboratory or centrifuge models under high gravity level, and numerical techniques of FEM. Compared to the conventional techniques, DEM has the capability of simulating the discrete movements of the granular soil particles around a pile. In this chapter, the DEM numerical method is adopted to show the mechanisms governing the soil-structure interaction of the model monopole. It is found that the load-displacement curves of the DEM simulations compared well with a set of published centrifuge tests data. The vertical and horizontal stress distributions at various levels of horizontal load are presented. The information in this research has offered insights into further research to improve the design of monopile foundations to resist live loads in service.

5.2 Literature review

The monotonic response has been investigated by different authors. Zhang *et al*. (2005) collected data from 17 different tests both centrifuge and full-scale. They presented a method to determine the ultimate capacity of a pile. The model consists of a contribution

from the side friction and the resultant soil pressure. The best result was obtained by using Rankine's passive soil pressure coefficient squared for the ultimate soil pressure.

In order to investigate the pile soil interaction, there are different approaches which can be taken. In principle the approaches can be divided into three groups: scaled model, full scale model and numerical model. The 1g experiments are relative easy to access and instrument, and series with many load cycles can therefore be carried out. The stress distribution in a 1g experiment is not identical with full-scale condition, therefore scaling to prototype is difficult. Centrifuge experiment at *N*g is carried out at a stress level corresponding to prototype. This makes the scaling to prototype easier but still scaling laws should be used with care. When using models in reduced scale the soil sample can be created artificially and the soil which is used in the test can therefore by quantified in a high degree. The big advantage of the numerical model is that it can investigate stress paths, soil-pile interaction.

5.2.1 *p-y* curve methodology

The *p-y* curves originally introduced by Reese and Matlock (1956) and McClelland and Focht (1958) are modelled using the Winkler approach with decoupled springs along the pile, each supporting a pile division. For each spring a non-linear *p-y* curve is created. This method evolved primarily from research in the oil and gas industry, as the demand for large pile-supported offshore structures increased during the 1970s and 1980s.

The *p-y* curve for pile in sand led to recommendations in the standards (API, 2000; DNV, 2009) for oil and gas installations. In 2004 these recommendations were adopted in the standard DNV (2009), which represents the current state-of-the-art for design of monopiles in the offshore wind industry.

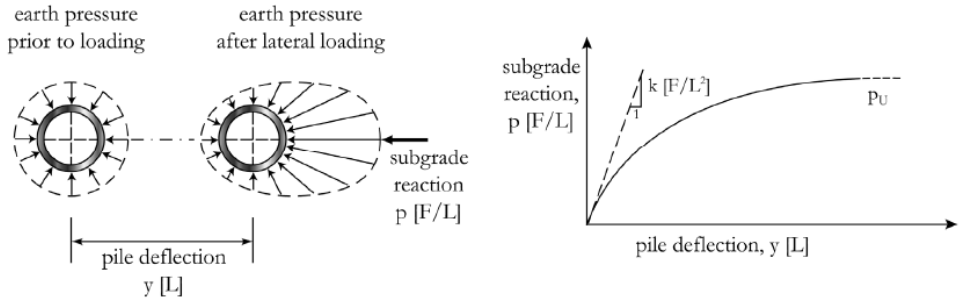

Figure 5.2.1 Graphical definition of p and y, after (Reese et al., 1974)

Reese *et al*. (1974) and O'Neill and Murchison (1983) had formulated the theory on *p-y* curves for sand to describe the relationship between soil resistance created in the non-uniform stress field surrounding the pile and the lateral displacement of the pile under lateral load (see Figure 5.2.1). The bending of the pile is described by the fourth-order differential equation for beam bending.

Recommendations for constructing static *p-y* curves that reproduce local horizontal soil-pile interactions under monotonic loading can also be found in offshore codes and standards, considering soils from silica or carbonate sands to soft or stiff clays. They are based on either laboratory data, or in situ data (Jardine *et al*., 2012). The interactions between soil and laterally loaded piles are typically accounted for by the use of *p-y* curves.

5.2.2 FEM

In the early stage of FEM, Randolph (1981) presented a 2D FEM solution modelling soil as an elastic continuum and the pile as an elastic beam. Muqtadir and Desai (1986) studied the behaviour of a pile-group using a 3D programme with nonlinear elastic soil model. An axisymmetric model with elastic-perfectly plastic soil was used by Pressley and Poulos (1986) to study group effects. Brown and Shie (1991), Brown and Shie (1990b), Brown

and Shie (1990a) and Trochanis *et al*. (1991) conducted a series of 3D FEM studies on the behaviour of single pile and pile group with elastic-plastic soil model. In particular, interface element was used to account for pile-soil separation and slippage. Moreover, Brown and Shie derived *p-y* curves from FEM data, which provide some comparison of the FEM results with the empirical design procedures in use. A number of model tests of free- or fixed-headed pile groups under lateral loading has been simulated by Kimura *et al*. (1995) and Wakai *et al*. (1999) using 3D elasto-plastic FEM. A good correlation between the experiments and the analysis has been observed in these studies. All these results demonstrated that FEM can capture the essential aspects of the non-linear problem. It is noted that there is not much literature reporting on FEM studies of pile behaviour under lateral loading in layered soil system. In addition to that, there is a very small number of studies on the effects of layering system on the commonly used *p-y* curve approach.

With the advance of FEM computing techniques, it is now possible to use 3D FEM modelling techniques. For example, Yang and Jeremić (2002), and Fan and Long (2005) presented a 3D FEM analysis of laterally loaded piles in soils by modelling soil as an elasto-plastic material and the pile as a linear-elastic material. Sanjaya *et al*. (2007) used ABAQUS and the *p-y* method to study the behaviour of laterally loaded pile foundations in high marine clay with high potential to swell upon wetting and shrink upon drying. Recently, Chik *et al*. (2009) and Taha *et al*. (2009) presented a 3D FEM analysis to simulate a lateral load test using PLAXIS where soil is modelled with a Mohr-Coulomb elasto plastic model. The numerical modelling techniques based on the FEM provide versatile tools that are capable of modelling soil continuity, soil nonlinearity, soil-pile interface behaviour, and 3D boundary conditions.

5.2.3 Summary

The pile design for the lateral loads is today normally based on a Winkler model. Recently, several empirical and numerical methods have been proposed for analysing the load-

deformation behaviour of piles subjected to a lateral load. Although these methods make lightly different assumptions, they can generally be classified into three main groups: (1) empirical methods (Hansen and Christensen, 1961, Broms, 1964), (2) load transfer curve methods (Matlock, 1970, O'Neill and Murchison, 1983, Jeong and Seo, 2004), and (3) elastic and FEM (Mardfekri et al., 2013, Yang and Jeremić, 2002). Jeong and Seo (2004) reported comprehensive studies of laterally loaded structures. They conclude that the load transfer curve method for the design of laterally loaded piles is of intermediate complexity between the first and third methods. The lateral load transfer curve method, often referred to as the *p-y* curve method, has been studied for many applications in engineering practice. However, the response of a monopile supporting an offshore wind turbine is still not well described and more research is therefore needed. In order to investigate the response of a monopile, it is important to investigate the micro mechanics effects. Only in this way, is it possible to determine the mechanism of failure. The monotonic loading is used to determine the monotonic pile-soil interaction curves as well as being reference to the cyclic tests. And DEM is keen to use for the further micro mechanics research.

5.3 DEM centrifuge modelling

To investigate the pile-soil interaction under monotonic loading, monotonic tests have been modelled by GM-DEM centrifuge model. The sample preparation method was mentioned at Duan and Cheng (2016a). Table 3.3.2 shows the model parameters used in the numerical model.

In the PFC-2D model, the boundary was first set in such a way that the size of the model was similar to that of Klinkvort (2013). The width of the model is 0.6 m and depth is 0.6 m. Rigid walls were used to model the boundary. All DEM analyses in this investigation were performed using the DEM-centrifuge program. Figure 5.3.1 shows a sketch for analysis of pile-soil interaction. $L_{embedded}$ means the penetration depth, e is the load eccentricity. The PFC model of centrifuge test simulated a solid steel pile with diameter

d_{pile} = 45 mm and penetration depth 0.2m. There are four horizontal level (level 1, level 2, level 3 and level 4) and four vertical levels (VL1, VL2, VL3 and VL4) to measure the soil parameters.

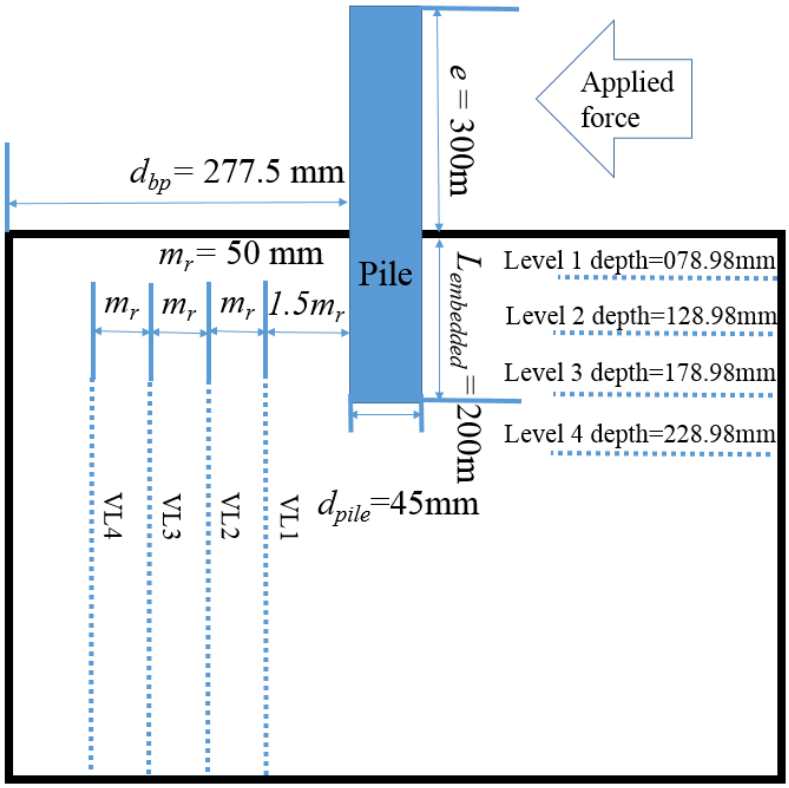

Figure 5.3.1 Schematic view of the PFC model.

5.4 Dimensional analysis

Centrifuge testing allows small models to be used to accurately represent the behaviour of prototype (full-scale) geotechnical problems. In this paper all centrifuge tests were conducted at 100 g.

Normally dimensional analysis is used to transform results from model to prototype scale (Fuglsang and Ovesen, 1988), however, this requires some knowledge of the relevant phenomena to be able to determine the governing parameters for lateral loading of piles, e.g. Randolph (1981). Quasi-static lateral loading of the monopile is assumed in this

analysis, with no pore pressure build up during loading. The normalised force and deflection are defined as

$$P = \frac{H_{lateral}}{\gamma \cdot {d_{pile}}^3}$$

5.4.1

$$U = \frac{u_x}{d_{pile}}$$

5.4.2

The basic idea in dimensional analysis is that the governing parameter is a function of a set of known independent variables. The goal of the analysis is to reduce the number of parameters and to form dimensionless groups, which can be used in the extrapolation to prototype (Fuglsang and Ovesen, 1988). The basis for the dimensional analysis is the Buckingham Theorem, which states that if an equation is dimensionally homogeneous, it can be transformed to a set of dimensionless products. The governing parameters should be identified in a dimensional analysis. The response is assumed to depend on a set of parameters for a laterally loaded stiff monopile, as shown in Klinkvort (2013). Only quasi-static monotonic and cyclic loading will be investigated in this thesis. This implies that no inertia forces are affecting the response and also that only the fully drained case is considered.

First, the governing parameters controlling the total response of a laterally loaded pile are identified. The total response is governed by the applied lateral load, $H_{horizontal}$, the corresponding displacement, $u_{horizontal}$, the geometry and material of the pile and the sand behaviour. The pile geometry is described by: penetration depth, L, load eccentricity, e, diameter, d_{pile}. The pile material is described by the stiffness which is the same as the particle, k_n, k_s, and the surface roughness of the pile, μ. Finally the sand is described by: submerged unit weight γ', sand stiffness, k_n, k_s, and the mean sand particle size d_{50}. The

parameters with the corresponding dimensions are shown in **Error! Reference source not found.**.

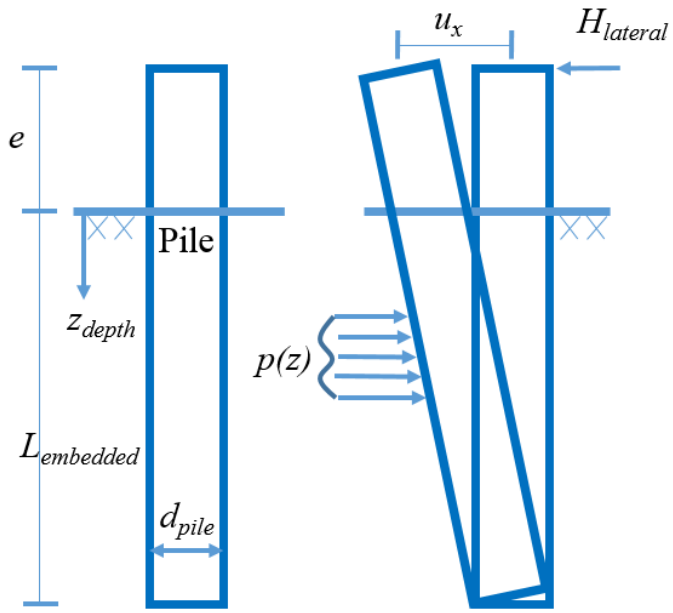

Figure 5.4.1 Schematic view of the model.

5.5 Relationship between load and lateral displacement

Figure 5.5.1 shows that there is a clear difference in the load-deflection curve for eccentricity of $6.5d_{pile}$ and $4.5d_{pile}$ or $2.5d_{pile}$. The results matched well with the experiment data of Klinkvort and Hededal (2010). Failure is defined as the load corresponding to a settlement equal to 10% of the pile diameter. The figures show that, before the failure, the results of the DEM model are nearly the same as the centrifuge experiment. Due to the good match of the relationship between lateral load and horizontal displacement, it is concluded that the numerical scheme adopted in the present investigation should be capable of modelling the pile-soil interaction under higher gravity conditions (100 g). In the following sections, the case of "$2.5d_{pile}$" will be studied for the mechanical analysis.

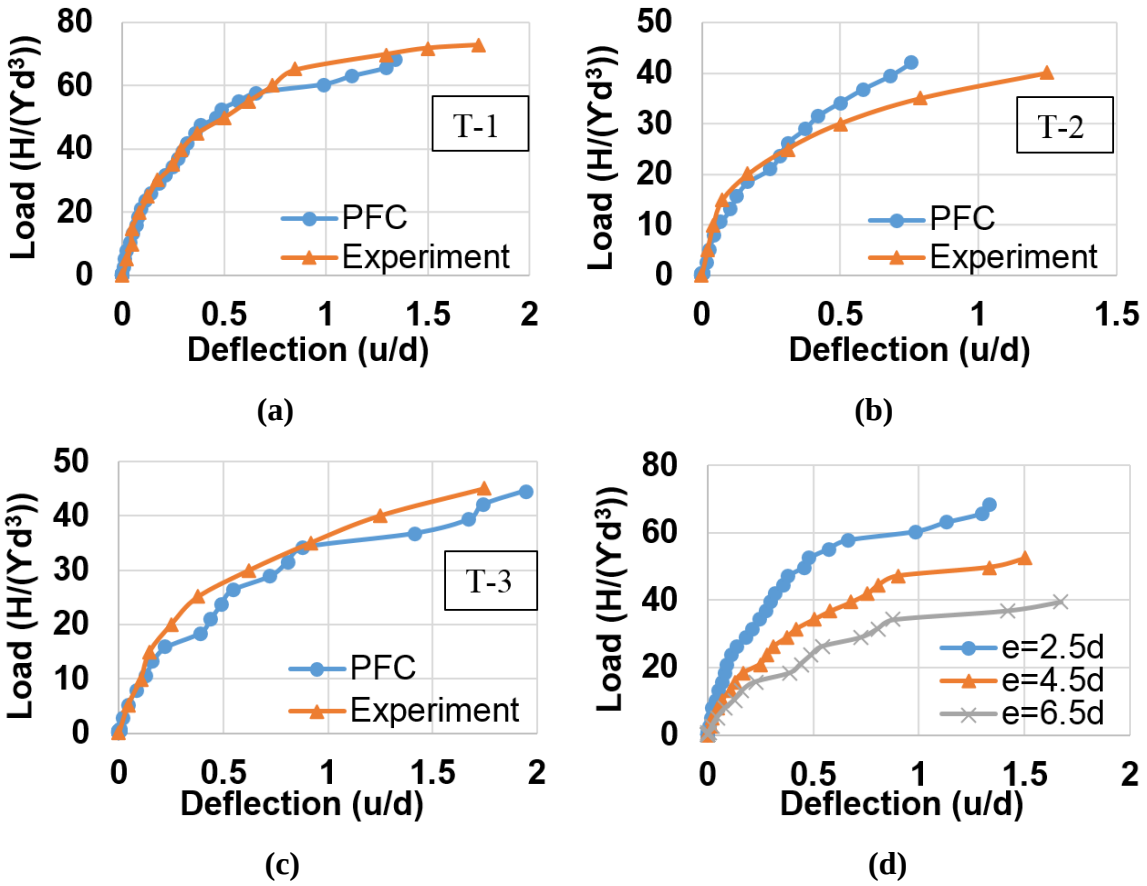

Figure 5.5.1 Comparison of DEM lateral response of pile with experimental test data of Klinkvort et al. (2010): (a) $e=2.5d_{pile}$; (b) $e=4.5d_{pile}$; (c) $e=6.5d_{pile}$; (d) comparison of three conditions (Duan and Cheng, 2016a)

5.6 Mechanical analysis

For the mechanical analysis, there were two symbols which were used to explain. P_R (3496 N) is the maximum horizontal loads, and this magnitude is equal to the applied load when the pile top displacement reaches 10% pile diameter d_{pile}. P_{max} is the maximum applied loading, P_{min} is the minimum applied load, positive means the left direction and negative means the right direction. From equations 5.6.1 and 5.6.2, the ζ_b can show the magnitude of applied loading, ζ_c will describe the direction of applied loads.

$$\zeta_b = \frac{P_{max}}{P_R}$$

5.6.1

$$\zeta_c = \frac{P_{min}}{P_{max}}$$

5.6.2

From Figure 5.6.1, it shows the lateral and vertical stress distribution at different loads level. Figure 5.6.1 (a) and (b) describe the vertical stress comparison at passive and active sides. These two side trends are opposite. On the passive side, the vertical stress increases with the bigger horizontal load. There was the opposite phenomenon which happened on the active side.

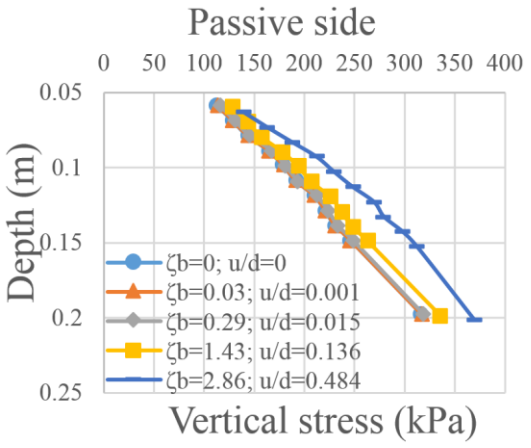

(a)

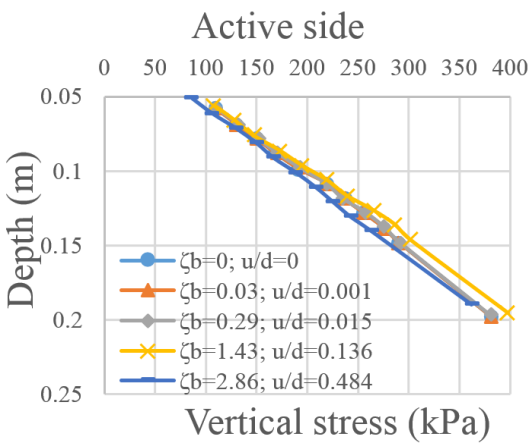

(b)

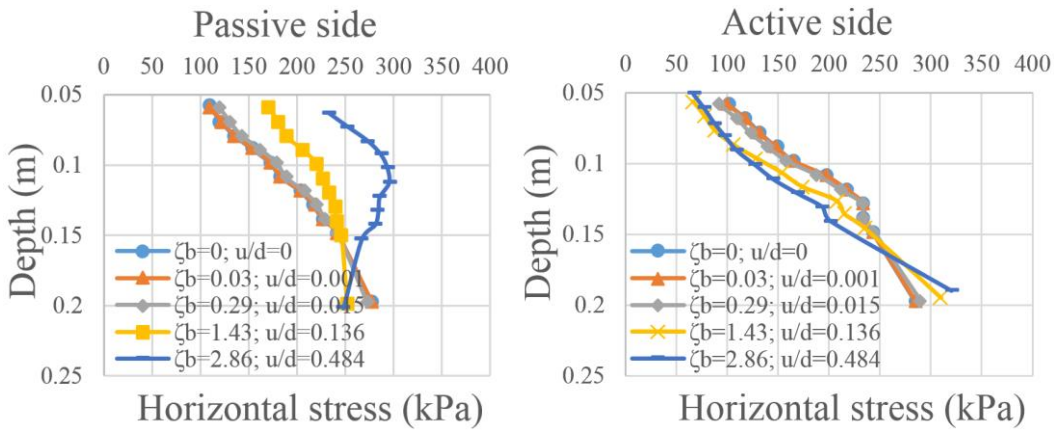

(c) (d)

Figure 5.6.1 Vertical and horizontal stress distribution comparison of different loads level.

Figure 5.6.1 (c) and (d) describe the horizontal stress comparison on the passive and active sides. These two side trends are opposite. On the passive side, the horizontal stress above a certain point increases with the raising horizontal load. However, the horizontal stress above the certain point decreases with the raising horizontal load on the active side. The contrary phenomenon occurs again below a certain point.

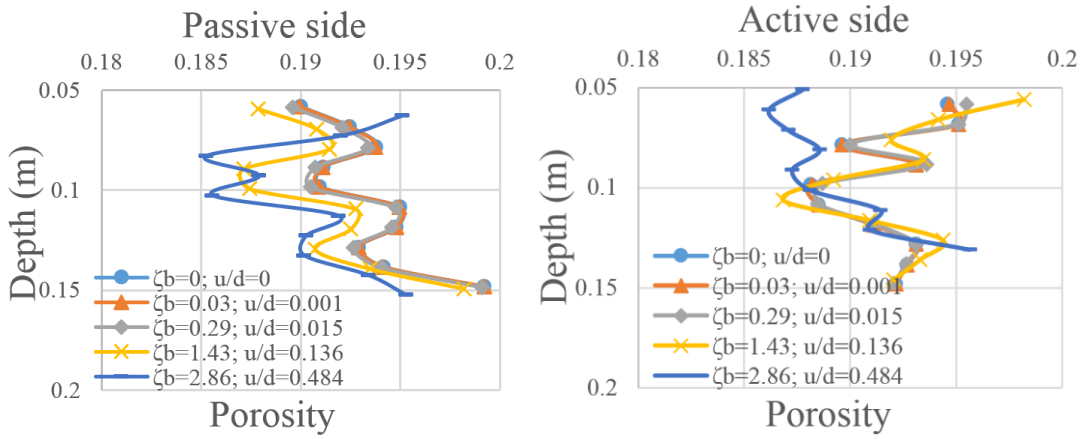

(a) (b)

Figure 5.6.2 Porosity number comparison under different loads level.

From Figure 5.6.2, it show the porosity distribution at different load levels. The porosity decreases slowly with the increasing lateral load on the passive side. However, the phenomenon is complex on the active side. Before the load reached 5000 N, the porosity increased a little. During the load 5000 N to 10000 N, the porosity suddenly diminished. The reason should be due to the consolidation.

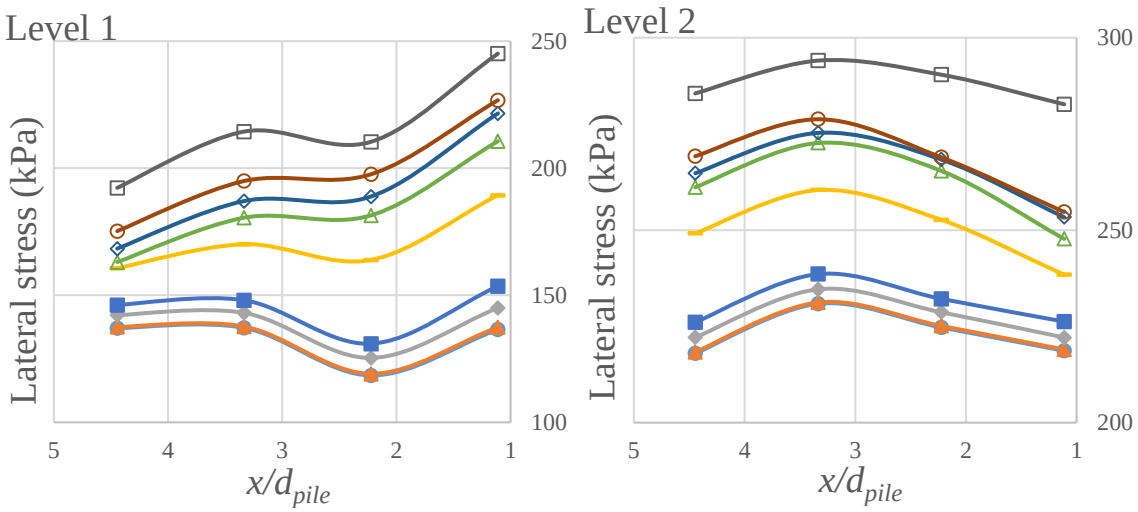

(a)

(b)

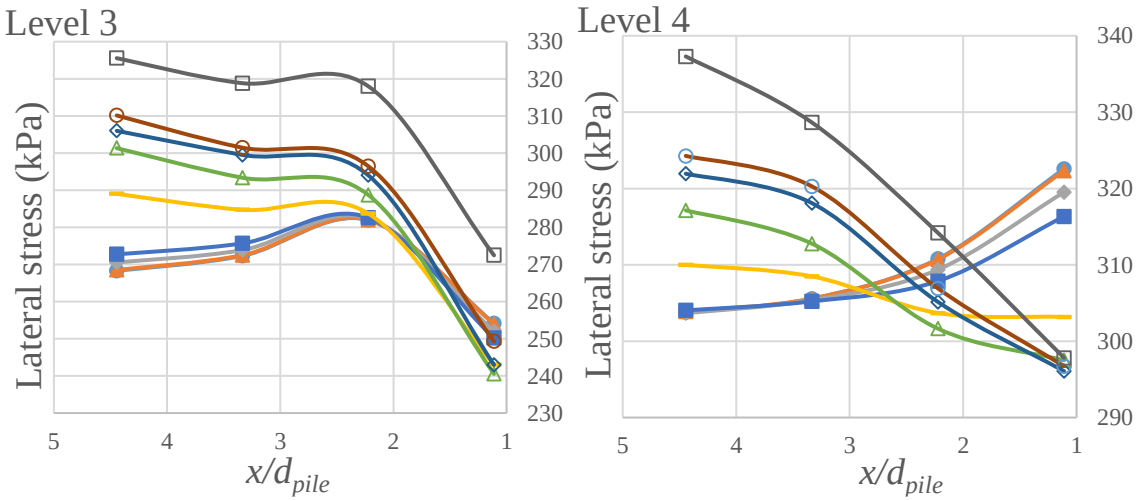

(c)

(d)

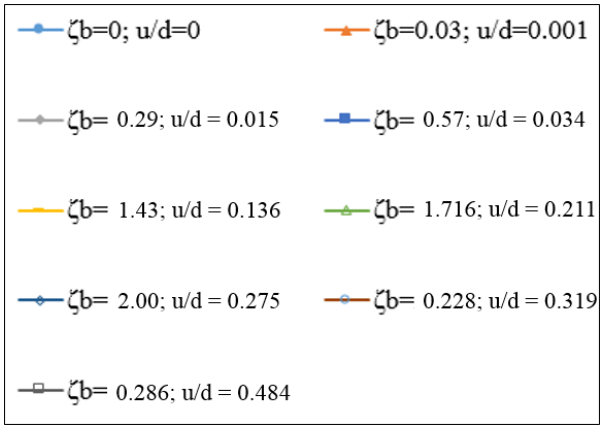

(e)

Figure 5.6.3 Passive side lateral stress distribution comparison of different loads level.

In Figure 5.6.3, the x-axis was normalised by x/d_{pile} which means the according lateral distance from the left side of the pile. 0 means the left surface of the pile. When the pile length was just pushed to left side (see Figure 5.6.3 (a)), the lateral stress where it is near pile increases larger than the far area. Peak value of lateral stress was reached when the lateral force achieved the maximum. Then the lateral stress when near the pile was decreased. The level 2 (see Figure 5.6.3 (b)) is a little deeper than level 1 and the lateral stress increases entirely. For the level 3 (see Figure 5.6.3 (c)), it is around the pile bottom and little lower. Due to the rotation of pile, the lateral stress of far area increases larger than the parts near the pile. However, the lateral stress of pile closed was decreased first, after that, it increased again. The pile tip moved to right, then the left side of pile tip caused the gap which reduced the lateral stress. With the movement of pile, the little upper part of pile tip kept compacting the left side soil. Hence, the lateral stress increased again. Level 4 (see Figure 5.6.3 (d)) is very deep and around the pile tip and little deeper, so the lateral stress keeps decreasing until ζ_b=1.5, then the lateral stress near the pile keep same, the lateral stress of far area increased quickly.

In Figure 5.6.4, the trends indicate that the lateral stress distribution of different vertical area. It is found that the lateral stress of vertical upper area near the pile (Figure 5.6.4 (a))

increases more than the far area (Figure 5.6.4 (d)). However, the upper layer of pile closed area change obviously more than deeper area. Further area change more linear. At the deeper area near the pile, there show up the decrease of lateral stress when the lateral force increase (Figure 5.6.4 (a), (b)). For the area where is around pile tip, when the applied lateral force is same, the lateral stress of far vertical area is larger than the pile closed area. When the depth is deeper than the pile tip, the lateral stress nearly keeps same.

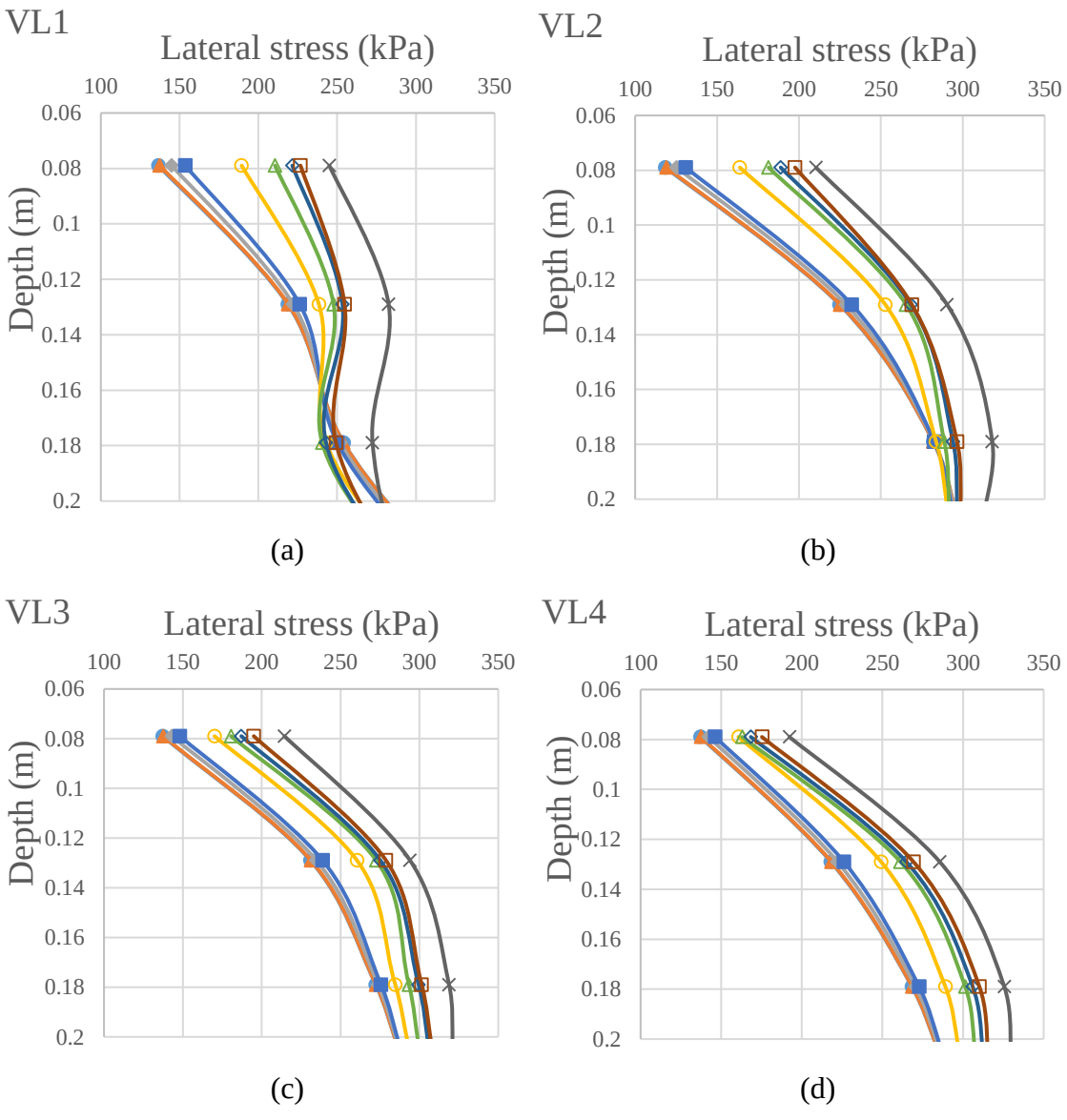

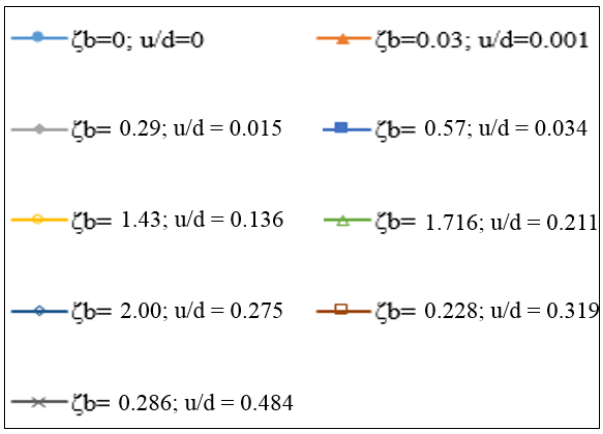

(e)

Figure 5.6.4 Passive side lateral stress distribution comparison of different loads level at different vertical locations.

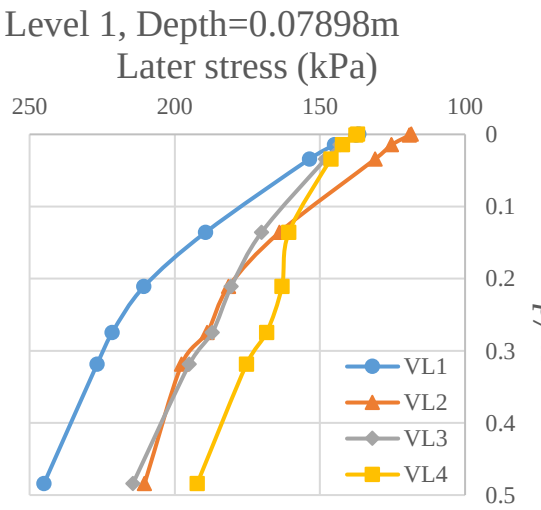

(a)

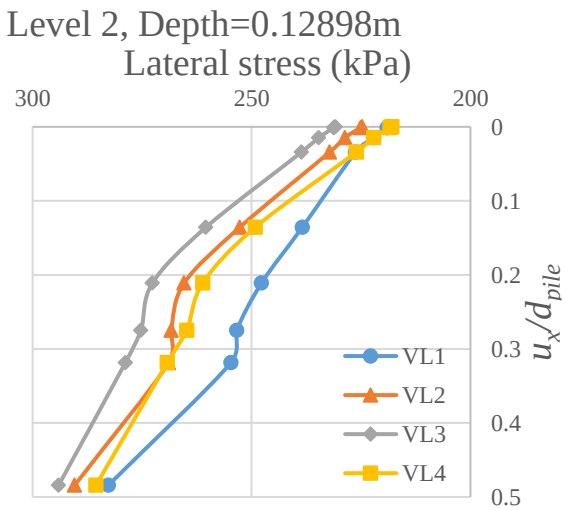

(b)

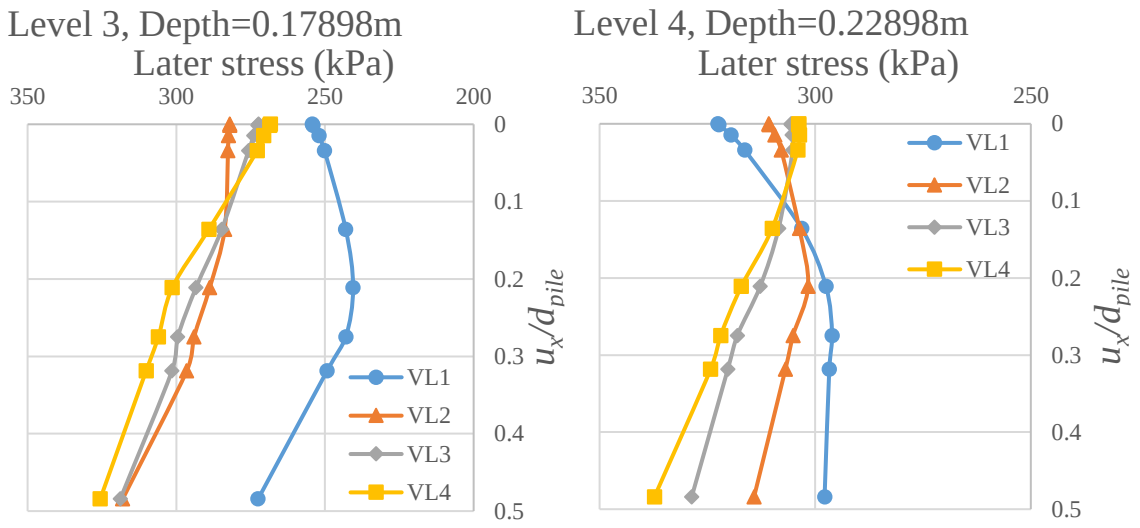

(c) (d)

Figure 5.6.5 Passive side lateral stress distribution during the lateral loads increasing.

Figure 5.6.5 shows the lateral soil stresses at 4 specific depths (e.g. Figure 5.6.5 (d): Level 4 at the deepest depth, and Figure 5.6.5 (a): Level 1 at the shallowest depth) and different distances away from the pile (VL1-VL4) while the pile head has been pushed to different normalised distance (u_x/d_{pile}). It is clear in Figure 5.6.5 (c), (d) that the lateral stress on the pile-soil interface reduces drastically first and increases again after the pile was pushed. These figures indicates that the change of lateral stress is depended on the locations of model. Below the pile tip, the lateral stress is decreasing, and the lateral stress where is above the pile rotation centre is increasing.

5.7 Summary

The key issue was investigated for the design of a monopile support for an offshore wind turbine, such as the accumulation of displacements. It was clearly seen that the accumulation of displacement compared well with the experimental data. This can prove that DEM also is an effective method to research the big scale problems. Before the failure

state, the lateral stress of passive side did not change obviously. During the lateral loads, the soil state of different depth is different. Also monotonic loading tests can help with the analysis of cyclic loading test.

The content of this chapter was submitted to 7th Civil Engineering Conference in the Asian Region and published as a conference paper with title “A Micromechanics Study of Monopile under Monotonic Loading using DEM”.

Chapter 6

A discrete element method centrifuge model of monopile under cyclic lateral loads

6.1 Introduction

Pile foundations are widely used to support various types of structures for situations when shallow foundations undergo excessive settlements or have insufficient bearing capacity. Monopile foundations are the main type used for wind turbines at present. They are always subjected to significant cyclic lateral loads due to wind and wave actions (Duan and Cheng, 2016b). These cyclic loads will rock the pile and restructure the soil grains surrounding the pile. This may change the stiffness of the combined pile-soil system and induce accumulated rotation of the tower due to this change. Change in the stiffness of the pile-soil system changes the frequency of this system which then can interfere with the excitation frequencies. The excitation frequencies are the frequencies of the rotor and the blades, approximately 0.3 Hz and 1.0 Hz, respectively (Rasmussen *et al*., 2013). The natural frequency of the tower is normally designed to be in-between to avoid resonance (Leblanc *et al*., 2010a). The design criteria are often very strict due to operating behaviour and often the accumulated permanent rotation of the tower must not exceed 0.5^{o}. As the rotation is an important factor in the design criteria, it is important to investigate the effect of long-term cyclic loading on the pile-soil system. However, in the present standards, i.e. DNV (2010) and API (2007) cyclic loading is not given much attention. These standards use *p-y* curves based on few full-scale experiments for laterally loaded slender piles and use a simple reduction factor to reduce the ultimate soil resistance for cyclic loading. The effect of long-term cyclic loading of monopiles placed in sands is possible to be a critical design factor and the effect of change in load characteristic, number of load cycles have not been properly examined.

In field tests, it is difficult to exert cyclic loading on monopiles with large diameters due to the limitations of test facilities and high costs. However, centrifuge modelling offers an effective way to understand the influence of cyclic loads on piled foundations. Compared with field tests, centrifuge tests are more convenient, efficient and cheaper. Centrifuge modelling provides an effective tool for researchers in geotechnical engineering as it allows the study of geometrically complex problems involving soil non-linearity. Centrifuge testing is, however, expensive and time consuming. Consequently, the number of tests performed in the study of a given problem is usually low. In addition, there are limitations on the amount of data that can be obtained during a centrifuge test. For these reasons, it is often beneficial to supplement a centrifuge study with numerical analyses. The numerical analyses can provide additional insights into the observed behaviour from the centrifuge experiments and allow investigation of certain experimental conditions.

In this research, a series of cyclic lateral load tests were conducted in the GM DEM-centrifuge model. The frequency of cyclic loading used in model was discussed. Also, the influence of cyclic lateral loads on the pile lateral displacement is investigated.

6.2 Literature review

6.2.1 The influence of long-term lateral cyclic loading

The characteristics of the cyclic lateral load include the cycle numbers, the cyclic load ratio (minimum load/maximum load in a cycle), and the maximum magnitude of load. The cyclic lateral loads can influence aspects of the pile behaviour, including pile head displacements, pile secant stiffness, *p-y* curves, and so forth (Verdure *et al*., 2003). For a safe design of a monopile foundation, fatigue design consisting of cyclic failure manifested by dimension of pile, long-term accumulated rotation, deformation and degradation of the pile stiffness, should also be addressed besides the maximum static load (Jardine *et al*.,

2012). These aspects are the main concerns of monopile behaviour under long-term cyclic loading and have to be controlled within the serviceability limit.

Different research activities have been presented and there is no clear agreement on how to deal with possible diameter effects, failure mechanisms etc. The increase in subgrade modules was seen to increase proportionally with the depth by Juirnarongrit and Ashford (2005) and Fan and Long (2005). However, the investigations were based on slender piles. Lesny and Wiemann (2006) and Sørensen *et al*. (2010) report a diameter effect, but in their research the geometrical similarity was not kept constant, which could influence the failure mechanisms. The different observations reported show that there is still a need to improve the knowledge of rigid laterally loaded monopiles, not only for cyclic loading but also for monotonic loading. A more general model describing the soil pile interaction is needed.

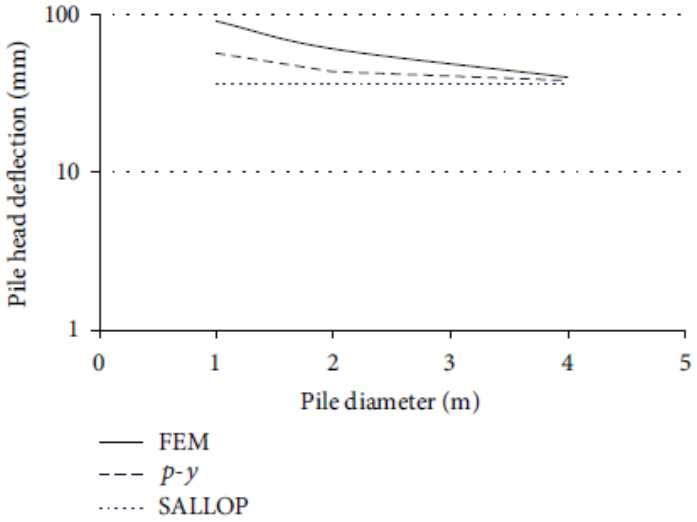

Figure 6.2.1 Variation of pile head displacement versus pile diameter in nonlinear analyses for sand (Mardfekri et al., 2013)

The effect of the pile diameter with a constant value of the E_pI_p of the pile was again investigated by Mardfekri *et al*. (2013) for the nonlinear case. Figure 6.2.1 presents the results of the three methods for diameters of 1, 2, and 4 m. Again since the SALLOP

method is based purely on a Winkler foundation with horizontal springs the results are independent of the diameter for a fixed E_pI_p. The *p-y* curves give results that vary with the diameter but less significantly than the 3D solution. It is interesting to notice that for the sand the best agreement is obtained for a diameter of 4 m. For the 1 m diameter the prediction of the SALLOP method would be about 40% of the FEM result; with the *p-y* curve it would be about 62%. It seems also that given the lack of a spring acting on the bottom face of the pile in the *p-y* model, for the larger diameter pile the assumption of a hinged tip might be more realistic whereas for the smaller diameters it is better to consider a free tip. Alderlieste *et al*. (2011) indicated that pile diameter increases had a more than linearly proportional effect on spring stiffness and also improved the static and cyclic lateral capacity more than expected by the API formulation.

The primary design drivers for offshore wind turbine foundations are deformation and stiffness rather than ultimate capacity (Leblanc *et al*., 2010). It is generally assumed that the cyclic lateral loading of piles in sand normally involves a rather benign behaviour of the pile: an attenuation of the cyclic displacements and only potential serviceability problems rather than an eventual loss of mechanical equilibrium. However, such assumption is based mainly on experimental tests with a low number of load cycles (Cuéllar *et al*., 2012).

6.2.2 Related theories

6.2.2.1 p-y method

Reese and Matlock (1956) developed a method to consider the effect of cyclic loads. It is based upon a closed-form solution for a beam on an elastic foundation with a linearly increasing soil reaction modulus (LISM) that changes proportionally with depth. The LISM method provides a simple procedure for predicting the effect of cyclic lateral loads; however, it cannot explicitly account for effects of nonlinear soil response. According to field test results of instrumented piles subjected to cyclic loads, Reese *et al*. (1974)

developed a semi-empirical, nonlinear *p-y* (soil resistance-pile deflection) approach, in which degradation factors obtained empirically are used to predict cyclic *p-y* relationships based upon degraded static *p-y* curves. Additionally, O'Neill and Murchison (1983) suggested to generate cyclic *p-y* curves by reducing the static soil resistance for a given deflection. In both approaches mentioned above, the cyclic *p-y* curves are independent of the number of cycles. However, parameters required in this sophisticated approach are difficult to obtain from site characterisation studies. Based on previous test data, Long and Vanneste (1994) improved the *p-y* approach to consider the effect of the number of cycles. Nevertheless, only 50 or less cycles of lateral loads are executed in most of the tests considered. Moreover, the use of *p-y* curves often fails to account for the permanent deformation that accumulates with increasing cycles (Moss *et al*., 1998). Therefore, additional cyclic load tests need to be conducted with many more cycles than previously to better understand the influence of cycle numbers.

Cyclic *p-y* curves were derived in the 1970s on the basis of tests performed on relatively small-diameter piles for soft clays (Matlock, 1970), stiff clays (Reese *et al*., 1975), and sands (Cox *et al*., 1974). A cyclic loading is considered by reducing *p* by a constant factor 0.9 (see equation 6.2.4). The experiments encompass both static and cyclic test with up to 100 load cycles. The number of load cycles is obviously low. The *p-y* curves for piles in sand were developed based on full-scale load tests on long, slender (slenderness ratio about 30) and flexible piles with a diameter of 0.61m (Reese *et al*., 1974). Other tests have been conducted validating the *p-y* curves but all tests are also conducted using slender piles. The basis for the *p-y* curves differs significantly from the piles used as monopiles today as the difference in slenderness ratio is pronounced and the amount of load cycles in the tests are limited (Rasmussen *et al*., 2013).

The shape and magnitude of the *p-y* curves have often been defined on the basis of full-scale field tests, simply by measuring the curvature of the pile with strain gauges. The double integration (eq.6.2.1) and double derivation (eq.6.2.2) of the pile's moment M_{pile}

profile provide the lateral displacement $y(z)$ and soil's reaction $p(z)$ respectively. *z* means the depth $E_{pile}I_{pile}$ and is the pile's bending stiffness.

$$y(z) = \iint \frac{M_p(z)}{E_p I_p} {dz_{depth}}^4$$

6.2.1

$$p(z) = \frac{d^2 M_p(z)}{{dz_{depth}}^2}$$

6.2.2

For the case of piles embedded in sand, the piece-wise definition of the curves proposed by Reese *et al*. (1974) was later examined and simplified by Murchison and O'Neill (1984) in what is the version ultimately adopted by the API committee. Given its relevance in the practice it may be worth briefly summarising the procedure here:

1. Define at each depth the ultimate soil resistance P_U, as the smallest of the values given by the two types of failure (the passive wedge and the lateral flow types of failure described before) taking into account that $p = Pd_{pile}$. *P* is the pressure exerted by the soil at any given point of the pile. The coefficients C_1 through C_3 can be obtained from Figure 6.2.2(a).
2. Compute the adjustment coefficient *A*(*z*) as

$$A(z) = (3.0 - 0.8\frac{z_{depth}}{d_{pile}}) \geq 0.9$$

6.2.3

$$A(z) = 0.9 \qquad for\ cyclic\ loading$$

6.2.4

3. Estimate the initial modulus of subgrade reaction K on the basis of the angle of internal friction φ', using the chart in Figure 6.2.2 (b).
4. Approximate the *p-y* curve at each depth by the following expression

$$p(y) = A\,P_U(z)\,tanh\left(\frac{K z_{depth}}{A\,P_U}y\right) \qquad 6.2.5$$

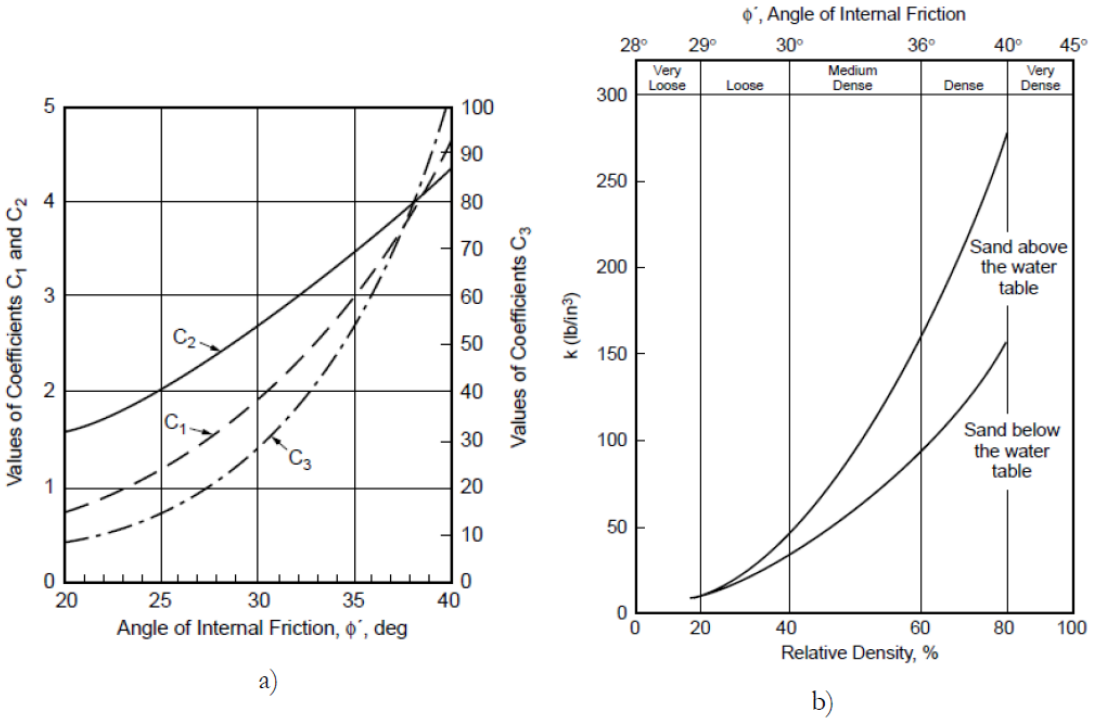

Figure 6.2.2 Determination of constants for the p-y curves of a pile embedded in sand (API, 2007). a) Coefficients for the ultimate soil resistance. b) Initial modulus of subgrade reaction.

It can be noted that the modulus of subgrade reaction K is here assumed to be independent of the pile's diameter d_{pile}, however, Terzaghi (1955) showed that the coefficient of subgrade reaction is inversely proportional to d_{pile}. This was confirmed in Juirnarongrit and Ashford (2005) on the basis of FE calculations and full-scale tests, but its adequacy for

the large pile diameters that could be required for the monopile foundations of offshore wind turbines was questioned in Wiemann (2007), where the following correction for the initial modulus of subgrade reaction proposed a new equation. However, this modification has been found to have little influence on the overall behaviour of the large-diameter piles and to still underestimate the pile head displacement when compared to FEM solutions (Lesny, 2008).

Little and Briaud (1988b) proposed an estimation of the lateral deformations of piles in sand due to cyclic lateral loading by means of a *p-y* curve developed on the basis of pressure meter tests with monotonous and cyclic loading. From a cyclic test the "secant shear stiffness" *G* is obtained as a function of the number of cycles. The degradation of *G* with N_{cycle} is described by $G(N) = G(N_{cycle} = 1){N_{cycle}}^{-a}$. The constant a in the exponent would solely depend on the soil's relative density. The lateral deformations of the pile after N_{cycle} cycles can be estimated by using a modification of the *p-y* curve from the monotonous test: $y(N) = y(N_{cycle} = 1){N_{cycle}}^{a}$. The method could be approved by re-calculations of model tests. However, its application to large pile diameters is not confirmed yet and the extrapolation of the pressure meter data to large N_{cycle} -values seems doubtful.

Some extensions of *p-y* curve by the number of cycles N_{cycle} were proposed in the literature (Swinianski and Sawicki, 1991, Welch and Reese, 1972). The latter ones e.g. recommended the relationship $y(N) = y_s + y_{50}C_1\log(N_{cycle})$ for dry, stiff clay. Therein y_s and y_{50} are the deformation at 100% and 50% of the bearing capacity, respectively, and the factor C_1 considers the amplitude.

The current methodology accounts for cyclic loading in an incomplete manner. Repetitive lateral load tests on two offshore piers in Tampa Bay, reported by Long and Vanneste (1994), showed much greater displacements than predicted using the *p-y* curve proposed by Reese *et al*. (1974). According to Long and Vanneste (1994), the reason for this discrepancy is that the cyclic *p-y* curve does not account for such factors as installation method, load characteristics or number of load cycles. The adequacy of the *p-y* curves used

in the current practice for the design of rigid pile foundations with a large diameter, as in the case of monopile foundations of offshore wind turbines, has been widely questioned.

Generally, the recommended *p-y* curve for cyclic loading is designed primarily for evaluation of the ultimate lateral capacity. Important design issues, such as accumulated rotation and stiffness changes due to long-term cyclic loading, are poorly accounted for. Long-term cyclic loading is likely to densify, or in some circumstances possibly loosen, the surrounding soil, resulting in changes to the stiffness of the foundation. Additionally, an accumulated rotation during the lifetime of an offshore wind turbine is expected, since the cyclic loading often occurs from one direction. The OWT is in dire need of the mechanics research of soil around pile. The cyclic loading should be considered by "suitable" *p-y* reduction factors, which are not further specified. Concerning the serviceability limit state a calculation of the cumulative deformations in the soil in a "suitable manner" is demanded. However, no such method is specified, and the limitations are as follows:

- Cyclic *p-y* curves are applicable for modelling the head displacements and maximum bending moments of long flexible piles of moderate diameter after a storm loading history. However, they are inappropriate to model the response of large-diameter piles.
- Cyclic *p-y* curves are also inappropriate for modelling cases where horizontal displacements remain small, as they assume mechanisms that require relatively large displacements (Tjok *et al*., 2005).
- It does not consider the transitional period between the static and ultimate cyclic curve and thus does not provide a method of considering the pile rotations or accumulated displacements during cycling.

6.2.2.2 Degradation law

In order to incorporate the effect of long-term cyclic loading of a pile, the concept of degradation is adopted by means of different methods. Little and Briaud (1988a), followed by Long and Vanneste (1994), proposed modifying the static *p-y* curves by applying a "degradation" factor to the static soil modulus. Levy *et al*. (2009) point out that two types of degradation of the soil-pile system are postulated to occur during cyclic loading, named 'material' and 'mechanical' degradation. Material degradation occurs due to a change in soil properties, such as increased changes in the soil density. Several experimental studies are available that investigate reductions in soil strength and stiffness under cyclic loading conditions. Numerical studies were undertaken into material degradation using both elastic continuum and subgrade reaction methods, with degradation factors applied to soil strength and stiffness.

The mechanical degradation is caused by soil yield occurring along the pile (which induces plastic displacements) or by gaps developing between the pile and the soil. An experimental study completed by Rao and Rao (1993) on rigid piles in soft clay observed that cyclic lateral loading can weaken piles and cause an increase in deflection, particularly at load levels beyond 50% of the static capacity.

The degradation factor has become a generally adopted concept in determining cyclic load effects, leading to explicit methods for determining the stress-strain relations for cyclic loading. A degradation index was presented by Idriss *et al*. (1978) which described the change in stiffness and shape of the hysteresis loop as a function of the number of cycles. The concept was continued by Little and Briaud (1988b) who proposed a power function for degrading the soil resistance as a function of the number of load cycles. With origin in this formulation and the static *p-y* curves analysed results from 34 full-scale laterally loaded pile tests to investigate which model parameters influenced the behaviour of the pile when repetitively loaded (Long and Vanneste, 1994). The 34 tests varied in many aspects from each other: pile type and installation method, length and diameter of the pile, soil density, number of cycles, and load characteristic. The slenderness ratio spanned from 3 to 84

covering both very rigid and flexible piles placed in different cohesionless soils varying from loose to dense compaction. The piles were loaded differently: one and two-way loaded, subjected from 5 to 500 load cycles (Rasmussen *et al.*, 2013).

Long and Vanneste (1994) adopted a method, originally introduced by Little and Briaud (1988a), to account for cyclic loading. The method is based on the deterioration of the static *p-y* curve, which is taken into account by reducing the static soil reaction modulus according to

$$\frac{E_N}{E_0} = N_{cycle}{}^{-a}$$

6.2.6

in which E_0 and E_N denote the soil reaction modulus on the first and *N*th load cycle respectively, and a is an empirically determined degradation parameter that depends on the installation method, soil density and load characteristics.

By investigating a subset of the full-scale tests, Lin and Liao (1999) proposed that the accumulated displacement of piles can be predicted by

$$\frac{u_N - u_0}{u_0} = \beta \ln\left(N_{cycle}\right)$$

6.2.7

in which u_0 and u_N denote the pile-head deflection in the first and *N*th load cycle respectively, and β is an empirical degradation parameter, similar to a, depending on the installation method, soil density and load characteristics.

Lin and Liao (1999) and Long and Vanneste (1994) found that the degradation factor can be determined based on installation method, soil density and load ratio. They suggested a power and a logarithmic expression, respectively. Both expressions give a simple estimate of the accumulated rotation for the number of cycles applied. Lin and Liao (1999) also

included a depth degradation parameter t (eq. 6.2.8), to account for different model properties with the purpose of calculating the accumulation of pile displacements. However, the methods are not clear on whether the rotation should be found as the maximum or the minimum rotation for a load cycles. It is the author's opinion that the minimum rotation in a load cycle represents the permanent rotation best as the elastic deformation is at its minimum as well.

$$R_s = \frac{\varepsilon_N}{\varepsilon_1} = 1 + t\, ln\left(N_{cycle}\right) \qquad 6.2.8$$

R_s is cyclic strain ratio, ε_N is strain accumulation after N_{cycle} cycles. A development in the concept of degradation was made by Achmus *et al*. (2009) who researched the degradation of stiffness in cohesionless soils as a consequence of cyclic loading (see Figure 6.2.3 and Figure 6.2.4). Based on triaxial tests and FEM, design charts for determining deflection along a pile as a function of the number of cycles were developed. The degradation was expressed by means of the ratio of the secant elastic modulus. Figure 6.2.3 and Figure 6.2.4 can help to explain the method 1 in Table 6.2.1.

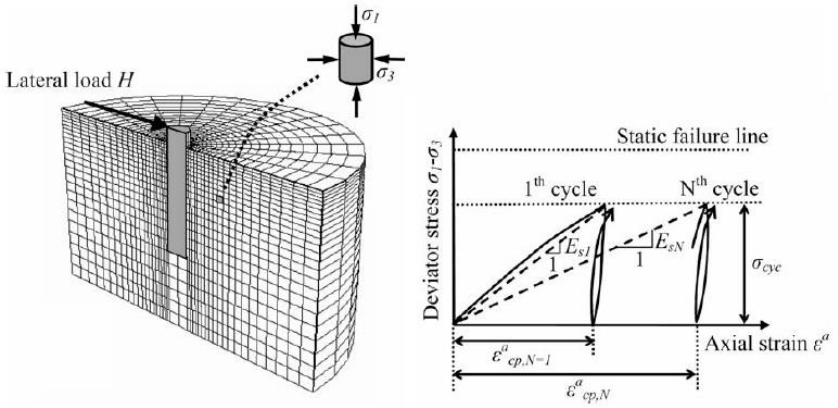

Figure 6.2.3. Degradation of secant modulus under cyclic loading in the pile-soil model (Achmus et al., 2009).

Achmus *et al*. (2010) presented a FEM model based on strain degradation to verify the results obtained by Leblanc *et al*. (2010b) and found good agreement between the simulations and the test results. Based on the method by Leblanc (2009) and a super positioning concept similar to Miner's rule, Leblanc *et al*. (2010a) created design charts for determining the accumulated pile rotation due to random two-way loading. The procedure is based on a limited amount of empirical data from small-scale tests and further research should be carried out to investigate the complicated behaviour of change in parameters.

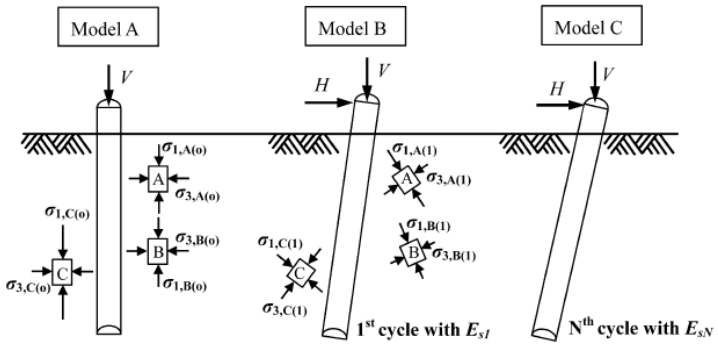

Figure 6.2.4 Schematic sketch of the determination of degradation stiffness in the pile–soil system (Achmus et al., 2009)

Table 6.2.1 Degradation summary

No	Author	Definition
1	Achmus *et al*. (2009), Achmus *et al*. (2007)	$N_{cycle}{}^{-a} = \frac{E_{sN}}{E_{s1}} \cong \frac{\varepsilon_{cp,1}}{\varepsilon_{cp,N}}$ $a = -b_1(X)^{-b_2}$ $X = \frac{\sigma_{1,cyclic}}{\sigma_{1,f}}$ $X_c = \frac{X^{(1)} - X^{(0)}}{1 - X^{(0)}}$ $X^{(1)} = \frac{\sigma_1{}^{(1)}}{\sigma_{1,f}{}^{(1)}}$, $X^{(0)} = \frac{\sigma_1{}^{(0)}}{\sigma_{1,f}{}^{(0)}}$

2	Leblanc *et al*. (2010b)	$\frac{\Delta\theta(N)}{\theta_s} = \frac{\theta_N - \theta_1}{\theta_s} = T_b(\zeta_b, R_d)T_c(\zeta_c)N_{cycle}{}^{0.31}$
3	Lin and Liao (1999)	$R_s = \frac{\varepsilon_N}{\varepsilon_1} = 1 + t\ ln(N_{cycle})$ $t = \eta \frac{L}{T}\phi\xi\beta$ $T = \sqrt[5]{\frac{EI_p}{n_h}}$
4	Long and Vanneste (1994)	$k_s(z) = N_{cycle}{}^{-m} n_{h,1} z$ $y_N = y_1 N_{cycle}{}^{\alpha m}$ $p_N = p_1 N_{cycle}{}^{(\alpha-1)m}$ $m = 0.17 F_L F_I F_D$

Different load scenarios with varying load characteristics and amplitude is tested with the outcome that Peng *et al*. (2006), Peralta (2010) and Leblanc *et al*. (2010b) agree that the pile will keep deforming and the exponential expression by Long and Vanneste (1994) fits rigid piles behaviour.

Peralta and Achmus (2010) indicated that the results from flexible piles fitted the logarithmic function best while the power function (Method 2, 3) fitted the results from the rigid piles best. However, method 1 lacks the support of full or small scale tests, what is more, there is a problem in the application of the stiffness degradation model because the pile-soil system is the reasonable definition of the initial stress state and the cyclic load level for each element of the discretized system. On the one hand, the initial stress state is not isotropic, and on the other hand the principal stress orientation changes during loading and the minor principal stress does not in general remain constant. Method 3 and 4 use an empirical foundation: their methods are based on experiments conducted on slender piles cyclically loaded to a maximum of 500 cycles. When using these explicit methods for larger numbers of cycles, variation in characteristic and model dimensions should be investigated.

Rasmussen *et al*. (2013) showed that the study on the change in stiffness of the soil-pile system did not provide such clear results as the rotation accumulation. It cannot be concluded how the stiffness is affected by the relative density. However, similar for all tests is an increase in stiffness with an increase in the number of load cycles. This increase is contradictory to current methodology which uses degradation of static *p-y* curves to account for cyclic loading.

6.2.3 Phenomena during the lateral cyclic loading

The phenomena and mechanics of lateral cyclic loading might shed some light on the complex circumstances related to the pile-soil interaction in the upper layers of the bedding, which are normally the main contributor for the lateral load-bearing capacity of piles. The references to subsidence or soil densification near the pile head are scarce in such literature, in part due to the inability of the most commonly used constitutive models to take into account the changes in density of the soil under cyclic condition (Cuéllar *et al*., 2009).

Doherty and Gavin (2012) summarised the main results of cyclic loading:

- Both deflection and moment increase with the increasing number of cycles and load magnitude,
- The ultimate lateral load capacity decreases with the increasing number of cycles and load magnitude,
- The main features of pile response to cyclic loading are practically unaffected by soil inhomogeneity,
- The loading rate has a significant effect on the pile response, with the deflections at a given load decreasing as the loading rate increases,
- The location of the plastic hinge moves deeper when the pile is subjected to fully cyclic loading than to monotonic loading, due to soil stiffness degradation (Tuladhar, Maki, & Mutsuyoshi, 2008),

- One-way cyclic lateral loads induce more permanent strains and greater cumulative deformations of the piles than the two-way cyclic lateral loads (Long & Vanneste, 1994).

Doherty and Gavin (2012) indicated that soil stiffness decay and strength degradation had appeared during the cyclic lateral loading. Change in the stiffness of the pile-soil system changes the frequency of this system which then can interfere with the excitation frequencies (Rasmussen et al., 2013, Cui and Bhattacharya, 2015). Leblanc *et al*. (2010b) also indicated that the long-term cyclic loading of the foundation is likely to change the stiffness of the surrounding soil and therefore the interaction of the foundation and the soil, owing to the accumulation of irreversible deformations. Thus it is important to assess the concepts of stiffness and/or strength changes during long-term cyclic loading.

Achmus *et al*. (2009) reported for the shorter monopile, the soil along the whole length of the pile is subject to stiffness decrease as well. As for the longer pile, only the soil stiffness in the upper half of the pile degrades significantly. However, this stiffness variation in the opposite direction of loading is negligible for a monopile subjected to one-way cyclic loading and will not affect the accumulated displacement of the pile. Achmus *et al*. (2009) also pointed out that the numerical model is capable of accounting for that, whereas the results of existing empirical models are independent of the magnitude of loading and the system boundary conditions. Thus, the pile performance under cyclic horizontal loading is dependent on the embedded pile length. Then, to improve monopile performance the increase of the pile length is much more effective than the increase of pile diameter. However, the model still needs to be verified by further experimental evidence (large-scale tests, field measurements and observations), and there is no micro mechanical interpretation of the results. There is a need for experimental work that can validate and improve the theoretical basis so it fits today's problem of cyclic long-term loading of monopiles (Rasmussen *et al*., 2013).

6.2.3.1 Pile head displacement and rotation

A long-term lateral loading may create rotation (tilt) of the pile by change in the soil-pile system which is critical in the serviceability limit state. The accumulated rotation due to long-term lateral loading is therefore a current issue as today's design guidances have little knowledge in this area.

The maximum permanent rotation of a monopile at mudline is 0.5 º in German (Achmus *et al*., 2009), 0.25 º in the UK and 0.17 º in China. $\Delta\theta(N)$ stands for the accumulated turning angle as shown in Figure 6.2.5, and k_0 and k_N indicating the dynamic stiffness of the pile. The published Det Norske Veritas regulations (DNV, 2009) proposed analysing the dependence of pile head displacement on the embedded pile length and choosing the pile length. However, all these criteria are based only on intuition, so their suitability needs to be proved (Kuo *et al*., 2012).

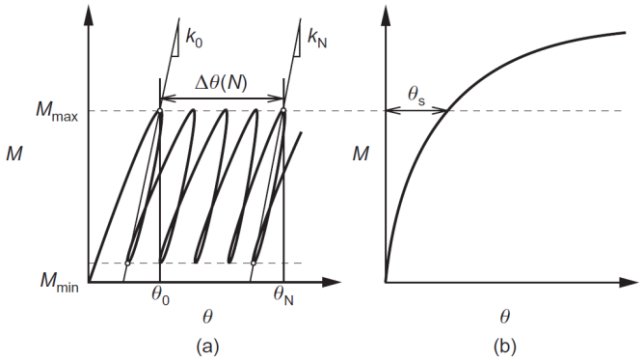

Figure 6.2.5 Method for determination of stiffness and accumulated rotation: (a) cyclic test; (b) static test (Leblanc et al., 2010b)

As the rotation is an important factor in the design criteria it is important to investigate the effect of long-term cyclic loading on the pile-soil system. In the present standards, i.e. DNV (2010) and API (2007) cyclic loading is not given much attention (Rasmussen *et al*., 2013). Although many useful methods have been proposed to predict the response of piles to

lateral cyclic loading, methods predicting the accumulated rotation and resulting stiffness due to long-term cyclic loading are limited.

6.2.3.2 Grain migration

Cuéllar *et al*. (2009) observed that the grain migration towards the pile never ceased nor seemed to slow down significantly during the procedure of cyclic loading. Then, once the soil depression reaches a rather constant depth, a second phase starts, namely the convection-dominated phase. During such a phase, rather than producing further densification of the soil, the cyclic lateral movements of the pile would mainly cause a convective ratcheting displacement of the sand particles. When lateral loading is applied one must also consider whether gapping may develop along the upper part of the pile.

Along their way through the soil mass, the migrated grains would be pushed forward by the following grains, and also move towards areas of lower confining stresses, i.e. upwards, setting in motion a whole ratcheting convective cell within the pile-head vicinities. Although this phenomenon has already been described by the painted sands method in experiment (Cuéllar *et al*., 2009), the procedure and mechanism was not recorded, so further research still needs to be validated.

6.2.3.3 Soil subsidence

It has been observed that there is local subsidence on the surface of the surrounding soil and a continuous grain migration towards the pile. A series of experiments were carried out by using coloured bands (Cuéllar *et al*., 2009, Cuéllar *et al*., 2012). Part of the local subsidence might be also caused by a mere plastic deformation of the soil without reduction in volume, meaning that the subsided volume emerges somewhere else. This might have happened to some extent in the presented test, where the sand was already quite dense and

some slight local heave was observed right outside the subsided area. In any case, it did not appear that the heaved volume of soil could account for the whole subsidence, so it seems that some densification happened indeed (Cuéllar *et al*., 2009). However, these studies did not show the clear evidence for the relationship between the local heave and subsidence, because there still has not a clear routine for the mechanism of soil subsidence.

6.2.3.4 Densification

Cyclic lateral loads can cause densification of the soil around the pile and a reduction of the radial stress, axial pile capacity can potentially be affected by lateral cycling. This effect has not yet been assessed thoroughly through field or scale model tests. Cyclic lateral loading of piles can reduce the axial and lateral stiffness of the surrounding soil over a certain depth below the ground surface (Cuéllar *et al*., 2012).

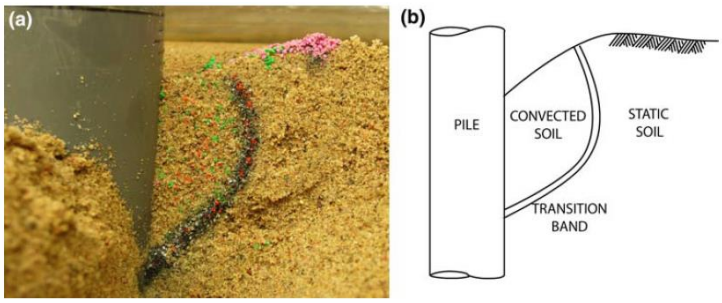

Figure 6.2.6 (a) Vertical cut of the soil, along the loading direction. (b) Sketch of soil domains (Cuéllar et al., 2009)

Cuéllar *et al*. (2012) presented that the soil behaviour around the pile under cyclic loading can be defined as two distinct phases: First phase: Densification-dominated phase and Second phase: Convection-dominated phase according to the plot in Figure 6.2.7. The progressive sand densification leads to subsidence of the soil surface and a significant stiffening of the pile behaviour. Conversely, the ratcheting convective motion of two closed cells of soil beneath the pile-head is responsible for an endless grain migration at the soil

surface, the inverse grading of the convected material and a direct shear of the sand at the distinct boundary of the revolving soil domain (see Figure 6.2.6). In this respect, and from a macro-mechanical perspective considering the soil as a continuum, it appears that the convecting material tends to follow gradient lines of shear stress during its ratcheting motion (Cuéllar *et al*., 2012). The densification phase starts immediately characterised by progressive reduction of the amplitude of cyclic pile displacement and progressive subsidence. Cyclic pile displacement leads to grain rearrangement and reduction of inter-granular voids until it reaches the maximum density influenced by the magnitude of the pile displacement and the relative density of the soil. The convection-dominated phase starts when the soil depression reaches a constant depth. A fairly constant amplitude of cyclic pile displacements is maintained in this phase and also no more significant plastic volumetric strains would take place around the pile. The convective ratcheting displacement is caused by cyclic lateral movements which are endless. In addition, these two phenomena are not completely decoupled. Giannakos *et al*. (2012) pointed out soil densification due to voids reduction, and "system" densification due to the gradual enlargement of the resisting soil mass to greater depths with cyclic loading. In experiment, it is hard to measure the void ratio, but PFC can help to record that.

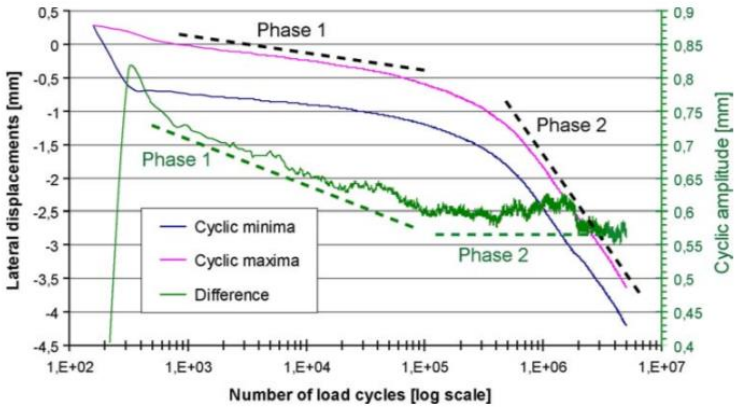

Figure 6.2.7 Measured lateral displacements and cyclic amplitude in logarithmic scale (Cuéllar et al., 2009)

6.2.4 DEM research on lateral cyclic loading

Cui and Bhattacharya (2015) reported that the DEM simulations and small scale tests provide good understanding on soil-structure interaction of offshore wind turbines (see Figure 6.2.8). Various features observed in model tests could also be replicated in DEM studies and thus provides confidence in the small scale physical model tests. They also point out the stiffness of granular soils increases under cyclic load. Therefore, the stiffness of monopiles founded on granular material is expected to increase with cycles of loading and this increase may cause a change in natural frequency of the wind turbine system. Following their research, it may be concluded that a "soft-stiff" will move towards the 3Ω frequency (see Figure 1.1.5). It is necessary for designers to predict the change in frequency which is essential to predict the fatigue life. It is observed from DEM simulations that the stiffness of the soil increased irrespective of the strain levels i.e. 0.1% and 0.01%. The rate of increase diminishes with cycles of loading. These observations match quite well with the small scale model tests. The circulation of soils observed in soils next to the pile could also be observed in the DEM simulations.

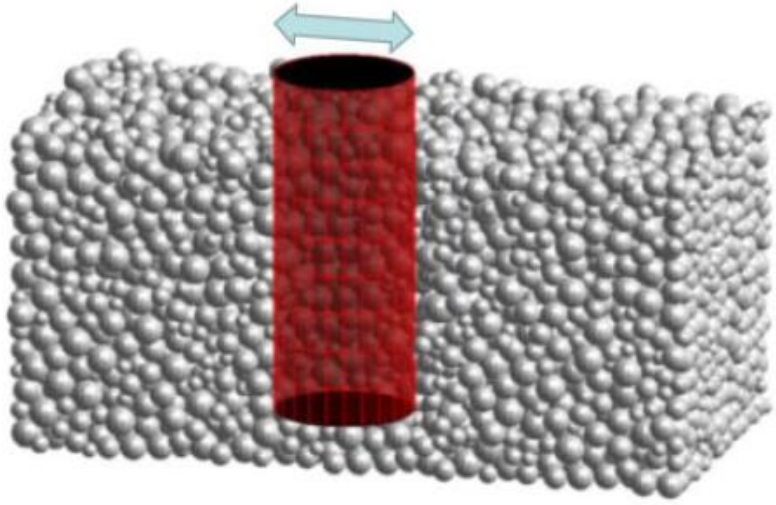

Figure 6.2.8. Configuration of soil tank and pile (Cui and Bhattacharya, 2015).

6.2.5 Summary

Offshore wind turbines are relatively new structures and are designed to provide an increasing proportion of wind energy generation capacity. This is because of the fact that offshore sites are characterised by stronger and more stable wind conditions than the corresponding land sites and thus have a higher capacity factor when compared to equivalent onshore turbines. There is also a deficiency of knowledge concerning the influence of the monopile-soil foundation system and its structural stability under long-term cyclic lateral loading. Existing literature includes Kuo *et al*. (2012), Cuéllar (2011), Achmus *et al*. (2010), Wichtmann (2005), Matlock (1970), Reese *et al*. (1974), Little and Briaud (1988b), Ismael (1990) and Long and Vanneste (1994). In the empirical field, experiments of model pile in sand exposed to large numbers of cycles typically ranging from 10^4 to 10^5, have been undertaken under 1g purely drained conditions at both Oxford (Leblanc *et al*., 2010) and Leipnitz University (Peralta, 2009). Though many authors have studied the area it is clear that no general approach has been accomplished yet and further studies are needed (Rasmussen *et al*., 2013).

There is only a limited amount of load cycles address the effects of cyclic loading on pile response. Different methods with varying degrees of accuracy have been used, incorporating simplified (Dawson, 1980, Lin and Liao, 1999, Long and Vanneste, 1994) or advanced numerical models (Achmus *et al*., 2009, Bourgeois *et al*., 2010, Grashuis et al., 1990, Hutchinson et al., 2005). Centrifuge experiments (Verdure et al., 2003, Kirkwood and Haigh, 2013a, Klinkvort, 2013) and full-scale tests have also been performed on the cyclic behaviour of piles embedded in sand (Brown et al., 1987, Tuladhar *et al*., 2008, Rollins *et al*., 2006, Klinkvort *et al*., 2012, Lau *et al*., 2014, Li *et al*., 2010). Niemunis *et al*. (2004) suggested a model to predict accumulated deformations based on laboratory tests on sand. Small-scale experiments were conducted by Peng *et al*. (2006), Leblanc *et al*. (2010b) and Peralta (2010) using theories on degradation and the concept of superposition to evaluate the cyclic loading effect on displacement and change in soil

stiffness. The accumulated rotation was found to be dependent on relative density, and was strongly affected by the characteristics of the applied cyclic load.

An overview of the numerous models available in the literature is briefly presented, which provides the basis for the choice of a model suitable for the simulation of a pile under cyclic lateral loading. The DEM study can be used to analyse the cyclic behaviour of a laterally loaded pile, provided that a suitable constitutive model is used. The main interest of the approach is to solve the effect of ζ_b and ζ_c and the soil micro mechanics of the soil-pile interaction.

6.3 DEM modelling of centrifuge model under cyclic loading

6.3.1 Sample characteristics and model setup

This research is based on the scaling laws similar to centrifuge modelling. Centrifuge testing experiments allow small models to be used to accurately represent the behaviour of the prototype (full-scale) geotechnical problems. In this paper all DEM-centrifuge simulations were conducted at 100 g.

In the PFC-2D model, the dimension of boundary walls was first set to be the same as Kirkwood and Haigh (2013b). This dimension was also similar to Klinkvort (2013). The width of model was 0.6 m and depth was both 0.6 m. Rigid walls were used to model the boundary. All DEM analyses in this investigation were performed using the GM DEM-centrifuge method under 100 g. Table 3.3.2 shows input parameters used in the DEM simulations.

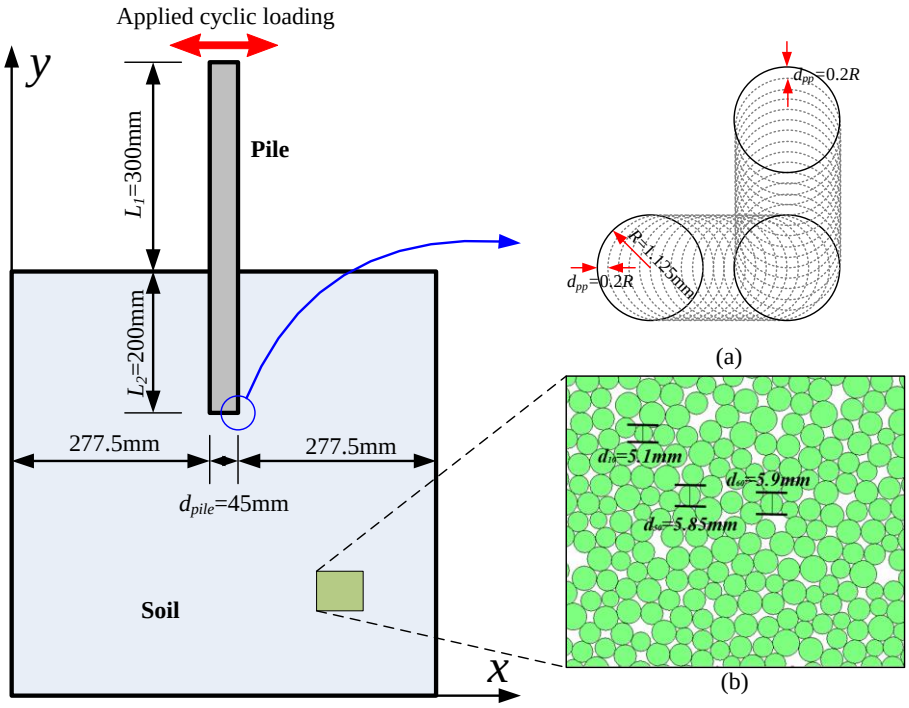

Figure 6.3.1. Schematic view of the PFC model and a typical particle assembly at equilibrium before pile installation.

Generally, at the first stage of generation, when the initial average porosity was reached, the model was cycled to equilibrium. At the second stage, the special gravity (100 g) was added, and the PFC model was cycled to equilibrium again. This moment, the porosity was the final average porosity. At the third stage, before the pile was formed, the particles inside the same area were deleted. In this research, "clump" was used to model the rigid pile. The system was then cycled to equilibrium again with the pile in place. For each grid, when particles inside each grid were created, the particles were given properties as shown in **Error! Reference source not found.** and the number of particles in every grid is 280. In every grid, the sample followed the size distribution and initial porosity of 0.25. All particles within each grid were added the designated gravity when the initial average porosity was reached, then the model was cycled to equilibrium. The detailed sample preparation process was described as the "GM" method (Duan and Cheng, 2016a).

6.3.2 Loading characteristics

A set of load characteristic constants were used to describe the cyclic loading. The load characteristics are denoted by ζ_b and ζ_c (Leblanc *et al*., 2010b, Long and Vanneste, 1994, Rosquoet *et al*., 2007, Klinkvort, 2013). They are determined as shown in Equation 5.6.1 and 5.6.2.

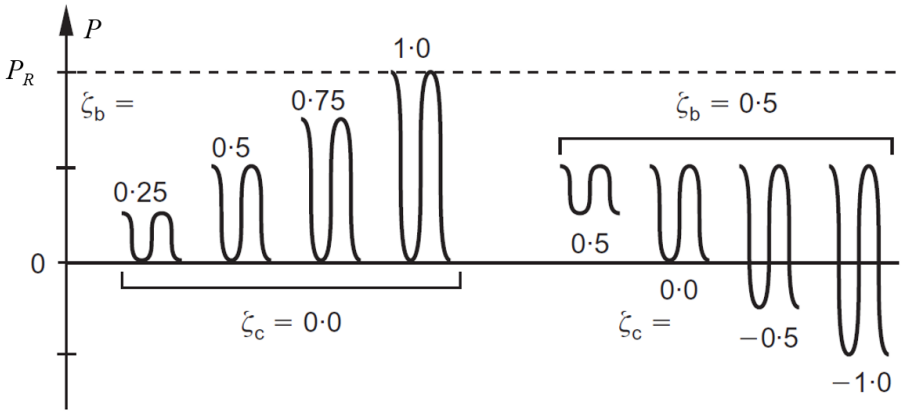

Figure 6.3.2. Characteristics of cyclic loading forces defined in terms of ζ_b and ζ_c.

Here, P_R is 1850 N in this research. ζ_b is a normalised force parameter that describes how close the cyclic magnitudes are carried out to the static bearing capacity. For instance, when $\zeta_b = 1$, the cycles are carried out at a magnitude reaching the static bearing capacity. On the other hand, ζ_c describes the direction of the cyclic loading with $\zeta_c \geq 0$ for a one-way loading and $\zeta_c < 0$ for a two-way loading. When using dimensional analysis to transform results from a model to a prototype scale, some knowledge of the relevant phenomena is normally required to determine the governing parameters (Randolph, 1981). Quasi-static lateral loading of the monopile is assumed here with no pore pressure build up during loading. For example, Equations 6.3.1 to 6.3.4 show the relationship between cyclic loading magnitude and direction, as proposed by (Klinkvort, 2013), using normalised forces and deflections:

$$\tilde{Y}_{max,N}/\tilde{Y}_{max,1} = N^{\alpha}$$

6.3.1

$$\alpha(\zeta_c, \zeta_b) = T_c(\zeta_c) \cdot T_b(\zeta_b)$$

6.3.2

$$T_b(\zeta_b) = 0.61\zeta_b - 0.013$$

6.3.3

$$T_c(\zeta_c) = (\zeta_c + 0.63)(\zeta_c - 1)(\zeta_c - 0.64)$$

6.3.4

Where $T_c(\zeta_c)$, $T_b(\zeta_b)$ are the non-dimensional functions. The function T_b cannot be negative, hence cyclic loading with a small magnitude $\zeta_b \leqslant 0.02$, will lead to a value $T_b = 0$, implying that the pile-soil interaction is reversible and no accumulation of displacements will occur. The function 6.3.4 ensures that α = 0 for monotonic loading, $\zeta_c = 1$. The maximum value of the function is found at $\zeta_c = -0.01$, which means that the most damaging load situation is when the monopile is subjected to a more or less pure one-way loading. When $\zeta_c \leqslant -0.63$, the function Tc becomes negative, which means that the accumulation of displacement is reversed and the pile moves towards its initial position.

In order to incorporate the effect of long-term cyclic loading of a pile, the concept of degradation is adopted by means of different methods. Lin and Liao (1999) and Long and Vanneste (1994) found that the degradation factor can be determined based on installation method, soil density and load ratio. They suggested a power and a logarithmic expression, respectively. Achmus *et al*. (2010) indicated that the results from flexible piles fitted the logarithmic function best while the power function (such as Klinkvort (2013)) fitted the results from the rigid piles best.

6.4 Comparison with centrifuge experiment

6.4.1 Selection of loading frequency

Long-term cyclic loading of wind turbine foundations may change the soil's stiffness, and hence resonant frequencies, which can lead to the accumulation of irreversible deformations. Site-specific spectral densities for wind and waves can be derived from available measured data, met-ocean databases or numerical models. The excitation ranges of 1Ω and 3Ω, the realistic normalised power spectra representing aerodynamic and hydrodynamic excitation are illustrated in Figure 1.1.5. So far, offshore wind turbines are designed with the 1st natural frequency, f_1, which is between 1Ω to 3Ω. In the wind industry sector, this is referred to as a "soft-stiff" structure. However, it is possible to design a "soft-soft" structure with f_1 below 1Ω, or a "stiff-stiff" structure with f_1 above 3Ω. The choice of frequency range for f_1 depends on the stiffness of the foundation. In general, less steel is required for a soft structure (Leblanc, 2009, Cui and Bhattacharya, 2015, Cuéllar, 2011, Arshad and O'Kelly, 2013).

Table 6.4.1 Model frequency used in published centrifuge experiment tests.

No	Loading frequency (Hz)	g (N/m^2)	Authors
1	0.106	1	Leblanc *et al*. (2010b)
2	0.1	1	Roesen *et al*. (2013)
3	0.02-0.7	100	Li *et al*. (2010)
4	Not clear	25~125	Klinkvort (2013)
5	Not clear	100	Kirkwood and Haigh (2013b)

In previous centrifuge experiment tests, as shown in Table 6.4.1, the loading frequency was simply chosen to lie between 0.02 and 0.7 Hz. If the realistic frequency is 0.1 Hz, the frequency in 100g centrifuge test should then be 10 Hz according to the scale law. For the

DEM model, when the frequency was set too low, such as 0.1 Hz, computation would take a very long time. For example, a test of 10 cycles of 0.1 Hz requires one week to run and it is inefficient. Therefore, it is essential to find an appropriate loading frequency for the DEM model which is efficient and reasonable.

Table 6.4.2 Loading cases of centrifuge experimental tests (Klinkvort, 2013).

Experiment	ζ_b	ζ_c	Diameter of pile (mm)
E1-2	0.18	-0.46~-0.32	28
E1-3	0.36	-0.46~-0.32	28
E1-4	0.08	-0.46~-0.32	28
E2-3	0.25~0.29	0.54	40
E3-1	0.33~0.34	-0.5	40
E4-3	0.15~0.36	0.05	40

Figure 6.4.1 shows the comparison between DEM model and centrifuge experiment results at different loading frequencies with the same loading magnitude ζ_b = 0.36. With ζ_b fixed but the loading direction ζ_c changing, the DEM results with 40 Hz loading frequency compare the best with the centrifuge experiment data in all three experiments (Klinkvort, 2013). For high loading frequency of 50 Hz, the maximum displacements of the pile are larger than that of lower frequencies. Since the simulation result of 40 Hz frequency compares better with experimental data, this loading frequency was chosen in all the following DEM simulations in this research. Table 6.4.3 summarised all the simulations of 40Hz frequency under various loading cases. There was a total of 15 cyclic simulation tests performed in this investigation, the simulation cases comparable with that published by Klinkvort (2013) are listed in Table 6.4.2. Additional simulation cases with a range of other cyclic loading magnitudes and loading directions were also simulated.

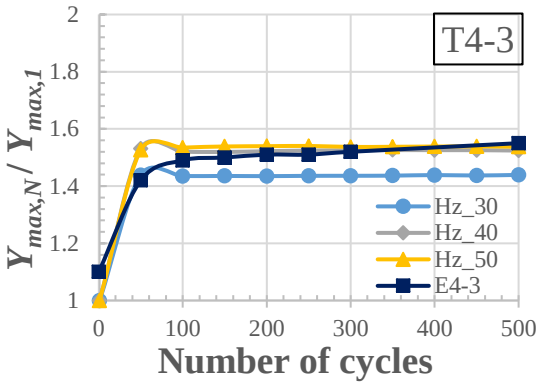

(a) $\zeta_c = 0$, $\zeta_b = 0.36$

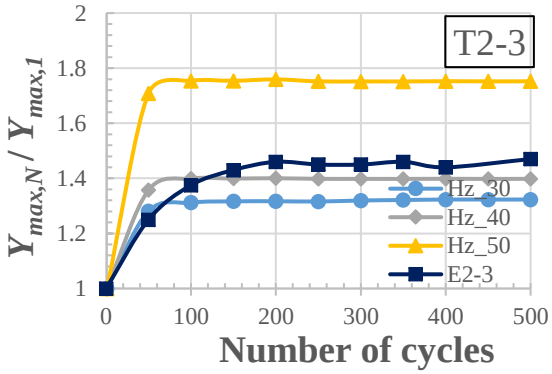

(b) $\zeta_c = 0.5$, $\zeta_b = 0.36$

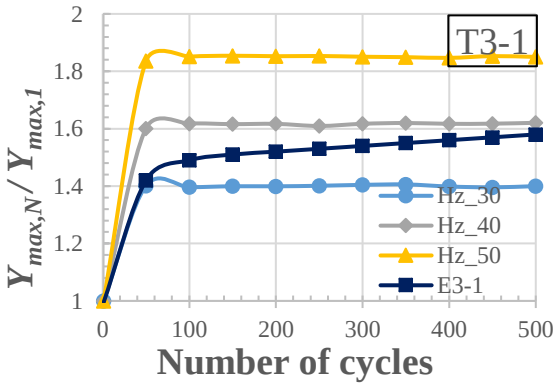

(c) $\zeta_c = -0.5$, $\zeta_b = 0.36$

Figure 6.4.1. Comparison of GM-DEM model and centrifuge experiment results at different loading frequencies with same ζ_b.

Table 6.4.3 Loading cases of the GM DEM-Centrifuge simulations.

DEM	ζ_b	ζ_c	Y_1(mm)	Y_{500}(mm)
T1-2	0.18	-0.5	0.4393	0.6970
T1-3	0.36	-0.37	0.9326	1.4648
T1-4	0.08	-0.5	0.2095	0.2887
T2-1	0.3	-0.8	0.7213	1.1719
T2-2	0.3	-0.9	0.7166	1.1358
T2-3	0.36	0.5	1.0215	1.4194

T3-1	0.36	-0.5	0.9061	1.4448
T4-3	0.36	0	0.9711	1.4802
T5-1	0.3	0	0.8300	1.1800
T5-2	0.4	0	1.0500	1.6700
T5-3	0.5	0	1.3300	2.2600
T5-4	0.6	0	1.5900	2.7400
T6-2	0.5	-0.5	1.2400	2.1900
T6-3	0.5	-0.37	1.2500	2.1700
T6-4	0.5	0.5	1.4000	2.2000

6.4.2 The effect of pile diameter

For the experiment tests shown in Table 6.4.2, following Klinkvort (2013), some of the cyclic tests were performed with a different pile diameter d_{pile} = 28 mm instead of d_{pile} = 40 mm. Figure 6.4.2 compares the evolution of lateral displacement GM-DEM model to centrifuge experimental data with different pile diameters, including both the centrifuge experiments E3-1 and E1-3 (by Klinkvort (2013)) and the DEM simulation tests T3-1 and T1-3. For the data of E3-1 and E1-3, although their ζ_c were slightly different, their maximum lateral displacements were nearly same. This confirms that some variations in the loading direction ζ_c do not affect the ultimate lateral displacement of cyclic tests too much for a constant ζ_b, which is particularly obvious when ζ_b is relatively big. Figure 6.4.2 also shows that even the diameters of the pile were different, the maximum lateral displacement results were nearly the same when the cycle number was bigger than 200.

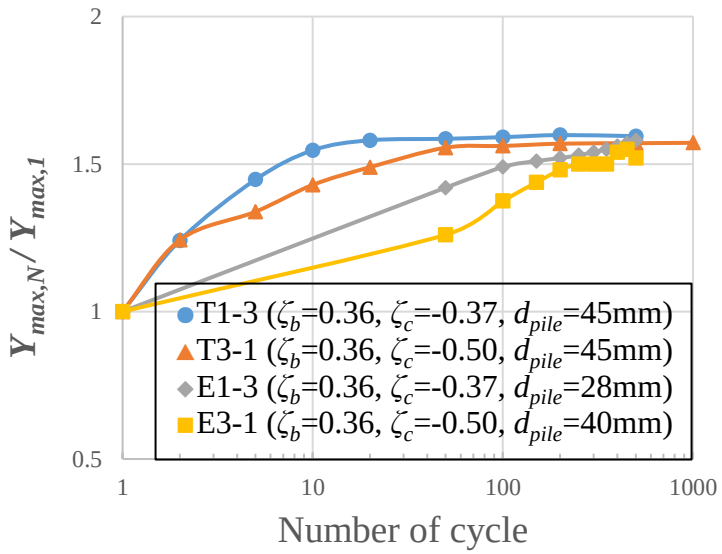

Figure 6.4.2. Comparing GM-DEM model and centrifuge experiment data with different pile diameters and the same frequency of 40 Hz.

6.4.3 Evolution of lateral displacement

In Figure 6.4.3 (a), (b) and (c), all tests used the same ζ_c = -0.5 which meant their loading direction were the same. The DEM result (T1-4) shown in Figure 6.4.3 (a) is more different from the centrifuge experiment (E1-4). Under this very small ζ_b value of 0.08, this low magnitude in the DEM numerical test still results in obvious displacement, whereas the centrifuge experiments do not generate significant displacement. However, when ζ_b ranges from 0.18 to 0.36, the increase in displacement was relatively small. The accumulated displacement obtained from both the DEM tests and the centrifuge experiments compares well, as shown in Figure 6.4.3 (b) & (c). Hence, a larger ζ_b value results in a better comparison between the 2D simulation and the 3D centrifuge cyclic tests.

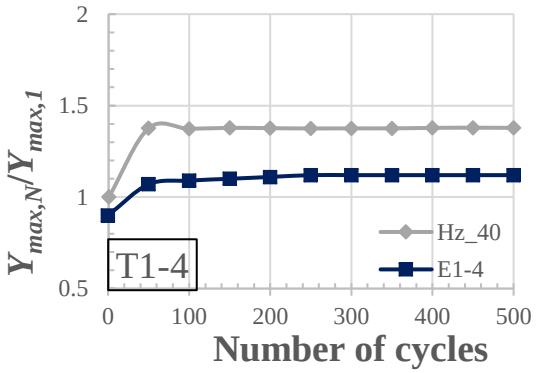

(a) ζ_c = -0.5, ζ_b = 0.08

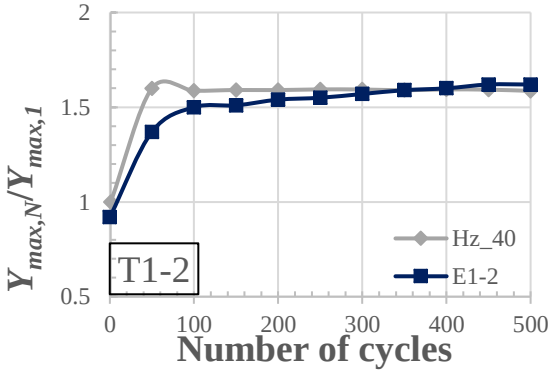

(b) ζ_c = -0.5, ζ_b = 0.18

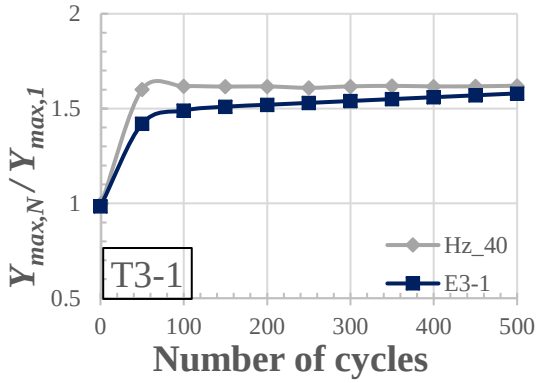

(c) ζ_c = -0.5, ζ_b = 0.36

Figure 6.4.3. Comparison of GM-DEM model and centrifuge experiment results at different ζ_b and the same ζ_c.

6.5 Results and discussions

6.5.1 Effect of loading characteristics

To highlight the influence of loading characteristics, Figure 6.5.1 and Figure 6.5.2 present a comparison of normalised lateral displacement for different value of ζ_b and ζ_c, respectively. It can be seen from Figure 6.5.1, for both cases with ζ_c = -0.5 and ζ_c = 0, as ζ_b increases from 0.08 to 0.5, the normalised accumulated displacement increases. There is very limited increase of normalised lateral displacement when the value of ζ_b increases from 0.3 to 0.6. This is most likely due to the limitations in soil densification or the

boundary effect, as when ζ_b reaches 0.6, which is a very large loading amplitude within the normal service time.

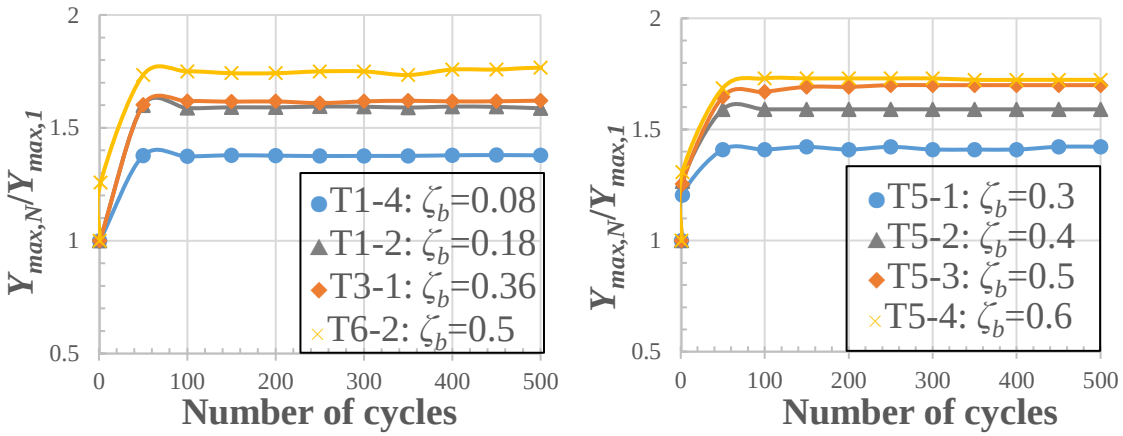

(a) ζ_c = -0.5 (b) ζ_c = 0

Figure 6.5.1. Comparison of model and experiment results at different ζ_b and same ζ_c.

Figure 6.5.2 (a) and (b) show all simulation tests under the same ζ_b = 0.36 and ζ_b = 0.5, respectively. Both figures show very similar phenomenon. The results showed that when ζ_c is negative with -0.5, the two-way loading test resulted in the greatest pile head displacement. Whereas when ζ_c is positive of 0.5, the one-way loading test resulted in the smallest pile head displacement. This means that, for any two-way test with the same ζ_b, displacement increases with the absolute value of ζ_c. And for any one-way test with the same ζ_b, displacement decreases with the increasing ζ_c. Hence, the loading direction ζ_c controls the magnitude of pile head displacement substantially. Both Figure 6.5.1 and Figure 6.5.2 present a phenomenon that the main lateral displacement occurs in the first ten cycles, then tends not to vary afterwards. This characteristic is similar in Chen *et al*. (2015).

Figure 6.5.3 summarises the influence of two loading characteristics, ζ_c and ζ_b, on the normalised lateral displacement. It can be observed from the Figure 6.5.3 (a) that $Y_{max,N}/Y_{max,1}$ generally increases as the increasing of ζ_b. This trend is in line with the

published data from centrifuge modelling. For the effect of ζ_c, on the other hand, it is more complex. Interestingly, both the DEM modelling results and centrifuge modelling data show very similar influencing trend, though with different transition points. In general, the obtained DEM modelling data is comparable with that from centrifuge modelling results.

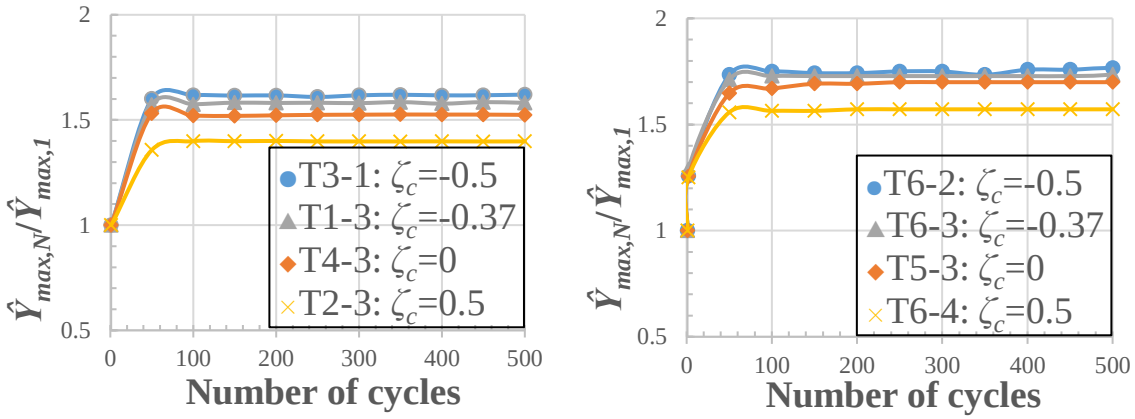

(a) ζ_b = 0.36 (b) ζ_b = 0.5

Figure 6.5.2. Comparison of model and experiment results at different ζ_c and same ζ_b.

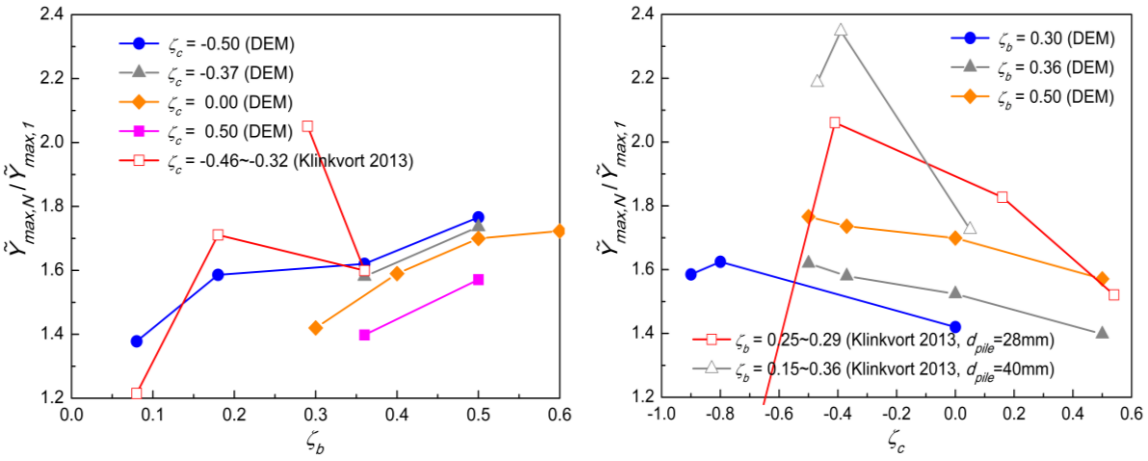

(a) (b)

Figure 6.5.3. Relationship between ζ_c and ζ_b (cycle number at 500) (Klinkvort, 2013).

6.5.2 Accumulated lateral displacements related to cyclic loads ratio

Figure 6.5.4 presents 3 lateral force-displacement curves of the monopile under different directions of cyclic lateral loads of the same amplitudes. The lateral displacements of the pile were measured at the head of pile. In Figure 6.5.4 (a) when ζ_c is negative implying a two-way test, the form of two-way test will lead to larger displacements compared to one-way tests (see Figure 6.5.4 (b) & (c)). It is clear from Figure 6.5.4 that k_N is smaller than k_1 in any of the three figures. The stiffness reduces with cyclic loading. Clearly, the soil-pile reactions of all the three cases are showing the less voids in the soil when soil densifies with increasing number of cyclic loading, hence the incremental accumulation of permanent displacement reduces.

In general, the loading and unloading in the first cycle exhibits evident soil nonlinearity, so the loading secant stiffness reduces with increasing lateral displacement in the first cycle, when ζ_c decreases. In addition, the unloading stiffness gradient k_1 also decreases with a more negative ζ_c when the loading direction becomes more two-way. As the number of loading cycle increases, there is a gradual accumulation of both the maximum loading displacement (cyclic maxima) and the minimum unloading displacement (cyclic minima). And, the unloading stiffness k_N continues to reduce slightly from its respective first cycle, these accumulations of displacement and changes in stiffness, however, are not as dominant as that induced by the direction of loading, i.e. what happened in the first cycle. For example in test T3-1, the first unloading from 666 to -333 N created a recoil of 0.79 mm and the final unloading created a recoil of 1.12 mm at the 10^{th} cycle. It may be seen in Figure 6.5.4 (b) that the first reloading induced 0.4 mm lateral displacement at 666 to 0 N and the final unloading created a recoil of 0.606 mm at the 10^{th} cycle. In Figure 6.5.4 (c), the first reloading induced only 0.146 mm lateral displacement at 666 to 0 N and the final unloading created a recoil of 0.2716 mm at the 10^{th} cycle. From the Table 6.5.1, when ζ_c, increases, both k_1 and k_N increase. Nonetheless, the value of k_N/k_1 decrease dramatically. Which means the change of stiffness is more obviously as long as ζ_c increases.

Table 6.5.1 k_1, k_2 and k_{10} of selected model tests.

DEM	ζ_b	ζ_c	k_1	k_2	k_{10}	k_2/k_1	k_{10}/k_2	k_{10}/k_1
T3-1	0.36	-0.5	1.814	1.693	1.516	93.32%	89.55%	83.57%
T4-3	0.36	0	3.201	2.561	1.750	80.00%	68.33%	54.67%
T2-3	0.36	0.5	10.476	4.888	2.667	46.66%	54.56%	25.46%

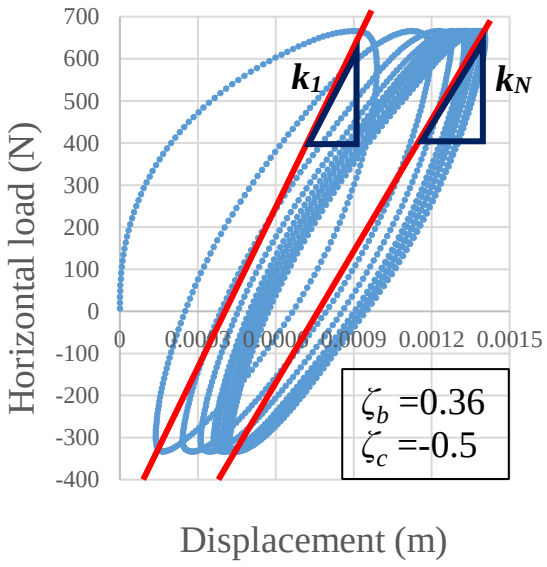

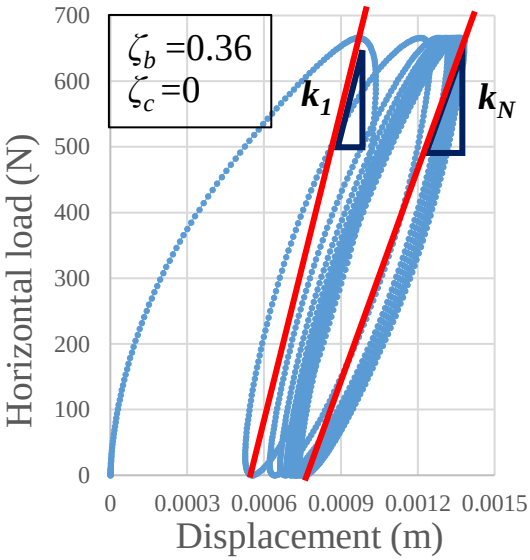

(a) T3-1, cycle number 0-10. Max 0.001404 (b) T4-3, cycle number 0-10. Max 0.001384

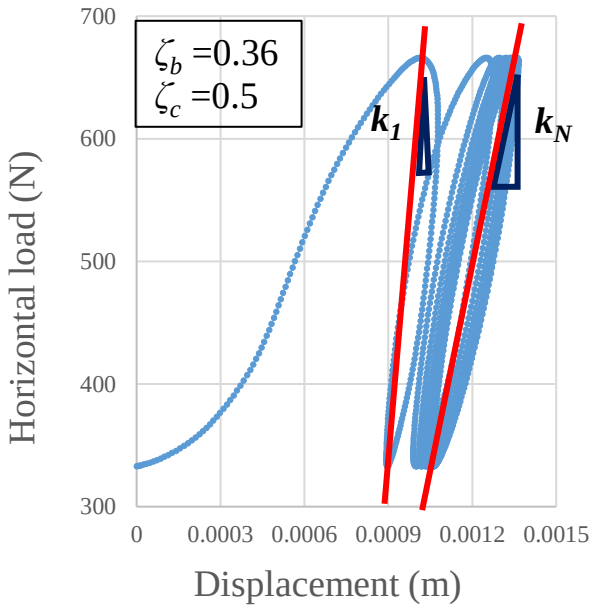

(c) T2-3, cycle number 0-10. Max 0.001366

Figure 6.5.4. Pile shaft lateral load-displacement response during cyclic lateral load tests (Cycle number 0-10.)

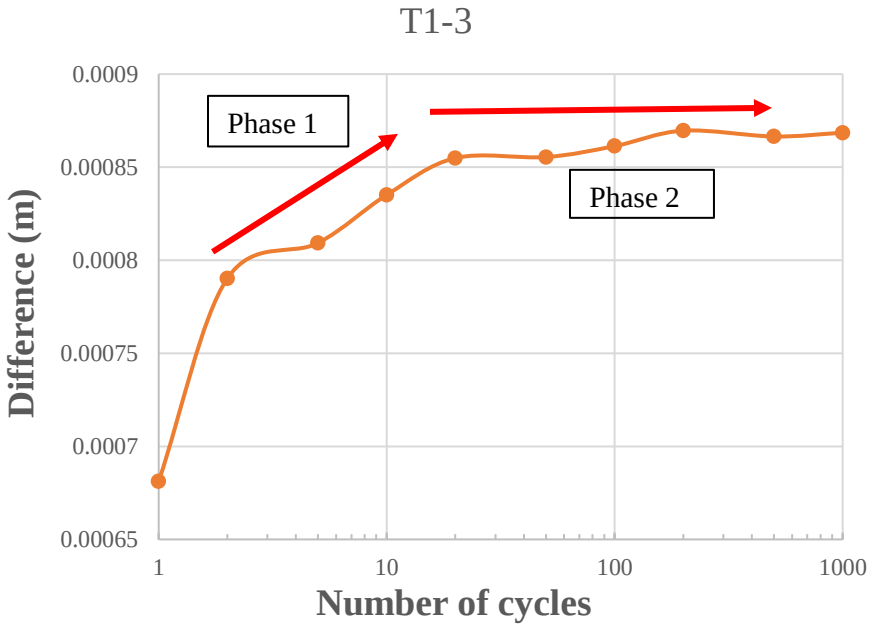

Figure 6.5.5. Difference of maximum and minimum displacement of PFC.

Figure 6.5.5 describes a plot of the difference in pile-head displacements in a logarithmic scale, and suggests the existence of two distinct phases during the cyclic loading. It shows two rather linear consecutive domains. The first phase is from the first cycle until the first hundred thousand cycles experimentally, and until the first 10 cycles in 2D DEM simulation tests. Incidentally, this is the moment when the soil densification appears to stabilise. Furthermore, the second phase extends from the end of the first phase to the end of the cyclic tests when the difference in cyclic amplitudes becomes a constant.

6.5.3 Evolution of secant stiffness

From Figure 6.5.6 (a), the trends of different ζ_c show that the change of stiffness ratio (K_N/K_1) will be affected by the magnitude of applied loading (ζ_b). When ζ_c is positive, the increase of ζ_b will cause the enhancement of stiffness ratio. However, there is clear that the stiffness reduces with cyclic loading (after 500 cycles). In Figure 6.5.6 (a), when $\zeta_c = 0$, the loading characteristic is one way, and the stiffness ratio decreases a little with the increase of ζ_b. When $\zeta_c > 0$, the loading characteristic is one way as well, the change of stiffness ratio becomes fluctuation during the decrease. However, in Figure 6.5.6 (b), when $\zeta_c < 0$, the stiffness ratio drop with the increase of ζ_c. When $\zeta_c > 0$, the change is relative flat.

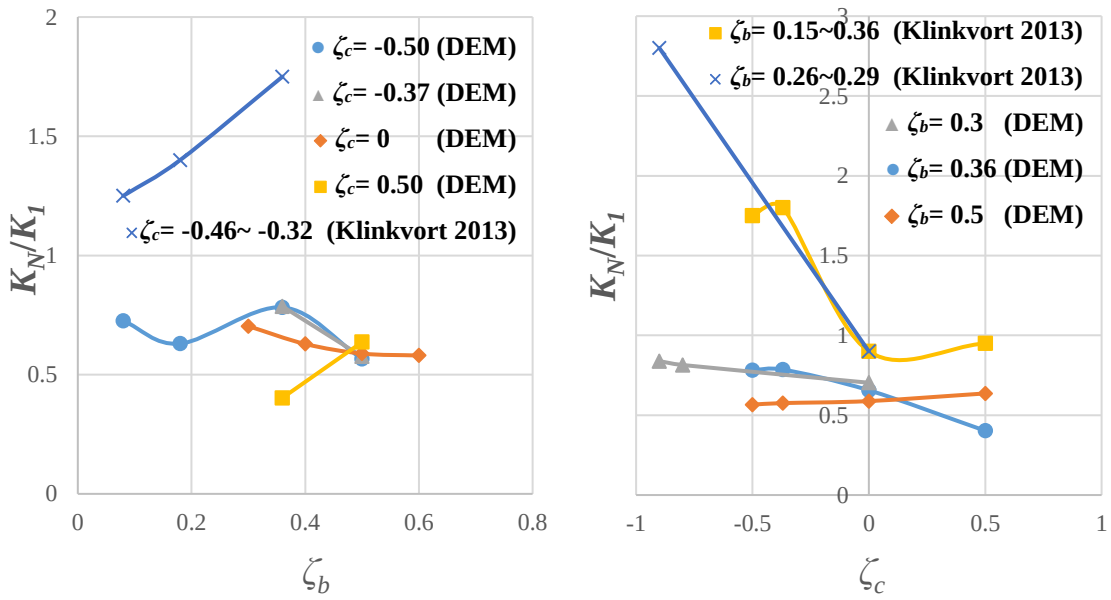

(a) (b)

Figure 6.5.6. Relationship between ζ_c and ζ_b (cycle number at 500) (Klinkvort, 2013).

6.5.4 Particle-scale observations

Particle-scale information is extracted from the whole DEM sample, to explore the fundamental mechanism of the different behaviour of mono-pile under various loading characteristics.

6.5.4.1 Effect of ζ_b

Figure 6.5.7 performs a comparison of the accumulated particle displacement fields, with ζ_b ranging from 0.08 to 0.50 (ζ_c =-0.50). In these figures, positive displacement means particles move to right, and negative displacement means particles move to left. For each case, the particle displacement fields at the 1st cycle (see Figure 6.5.7 (a), (b), (c) and (d)), the 500th cycle (see Figure 6.5.7 (e), (f), (g) and (h)) and the normalised particle displacement (see Figure 6.5.7 (i), (j), (k) and (l)) are plotted (the 500th particle displacement divided by the 1st). Note that the legend scale of the first two cases (case *A*:

ζ_b =0.08 and case *B*: ζ_b =0.18) is 10 times smaller than that of the last two cases (case *C*: ζ_b =0.36 and case *D*: ζ_b =0.50).

For all the 4 cases presented here, the influencing zones are almost of the same conical shape, with relatively larger area on the passive side than that of the active side. The influence of ζ_b on the particle displacement field is evident from these figures. At the 1st cycle, the minimum left particle displacements at the pile head of case *A* (see Figure 6.5.7 (a)) and *B* (see Figure 6.5.7 (b)) are 0.07895 mm and 0.123 mm, respectively. Taking the cut-off particle displacement as 0.002mm in these two cases, their influencing zones are about $1.35d_{pile}$ and $3.35d_{pile}$. Meanwhile, the maximum right particle displacements at the toe of pile are 0.0216 mm and 0.0535 mm, respectively. Very similar phenomena can also be observed in the other two cases, case *C* and case *D*, where the minimum left particle displacements at the pile head are 0.246 mm and 0.337mm, respectively.

As the number of cycle increases, the cyclic loading effect is gradually accumulated. At the 500th cycle, the area of the influencing zones is almost doubled, comparing to that of the 1st cycle, as highlighted in Figure 6.5.7 (e)~(h). The minimum left particle displacements at the pile head are 0.089 mm, 0.215 mm, 0.399 mm, and 0.584 mm, for case *A*, *B*, *C* and *D*, respectively.

This is further elaborated in Figure 6.5.7 (i)~(l), where the normalised particle displacements are plotted. The location of "zero" value boundary at the first cycle is horizontal, and change to slope away to the passive side after 500 cycles. However the "zero" boundary of particles displacement contour which was contact to the pile nearly keep same location. This change can help to find the affected soil area expansion during the cyclic loading. This expansion is also due to the transfer of contact force from the pile movement. This procedure is similar as the spread of fan (SOF).

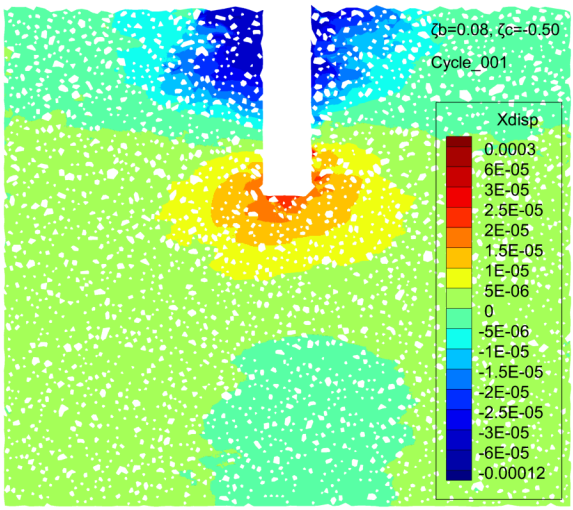

(a) ζ_b = 0.08 (N = 1)

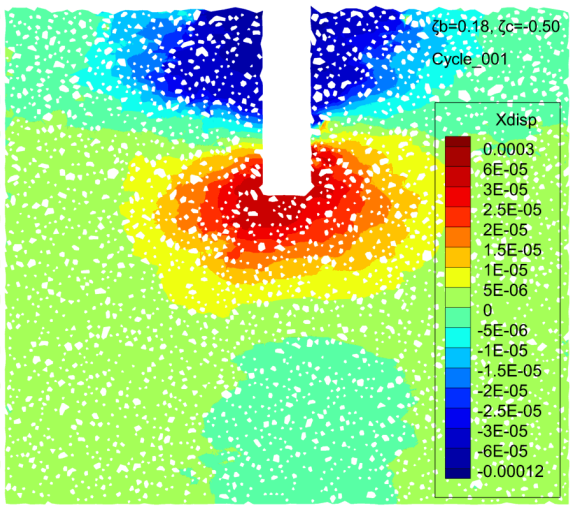

(b) ζ_b = 0.18 (N = 1)

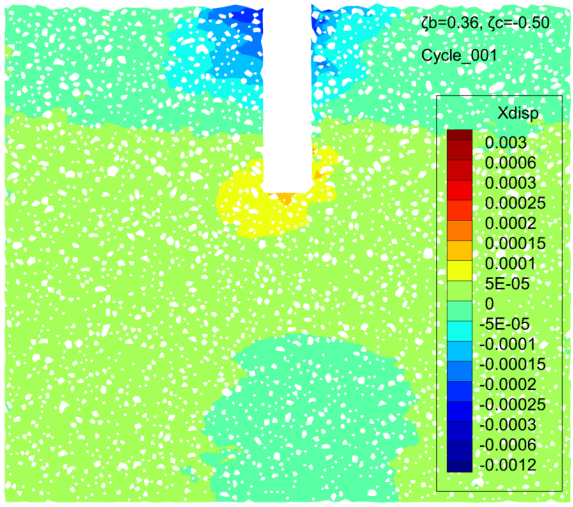

(c) ζ_b = 0.36 (N = 1)

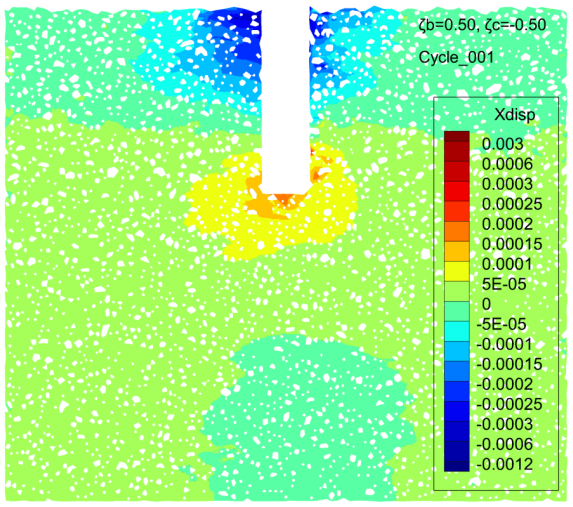

(d) ζ_b = 0.50 (N = 1)

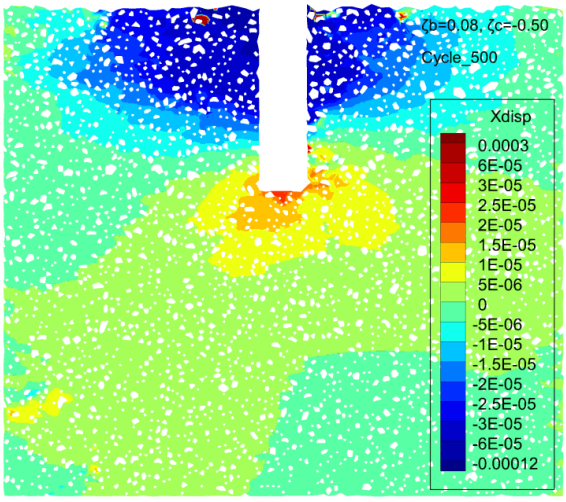

(e) ζ_b = 0.08 (N = 500)

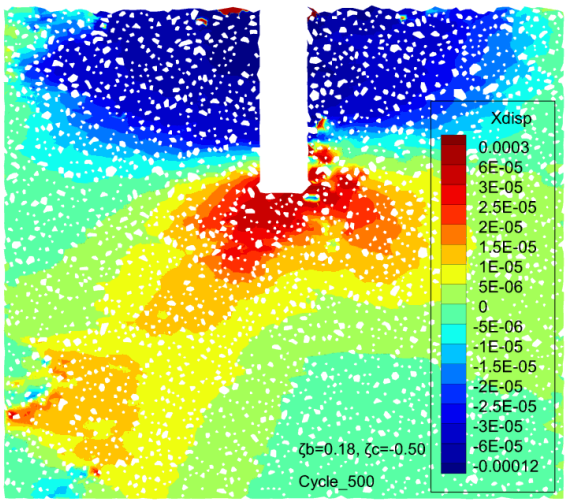

(f) ζ_b = 0.18 (N = 500)

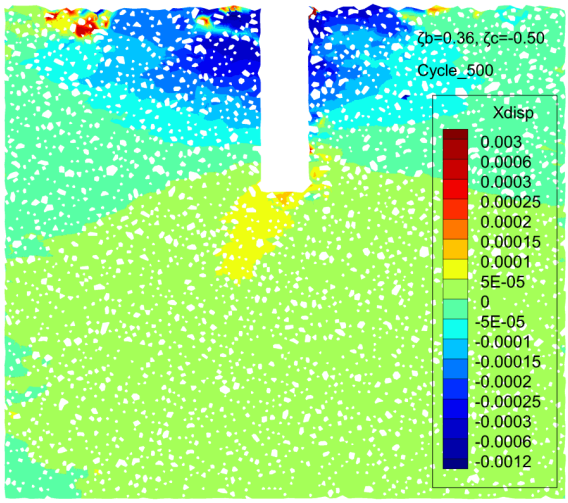

(g) ζ_b = 0.36 (N = 500)

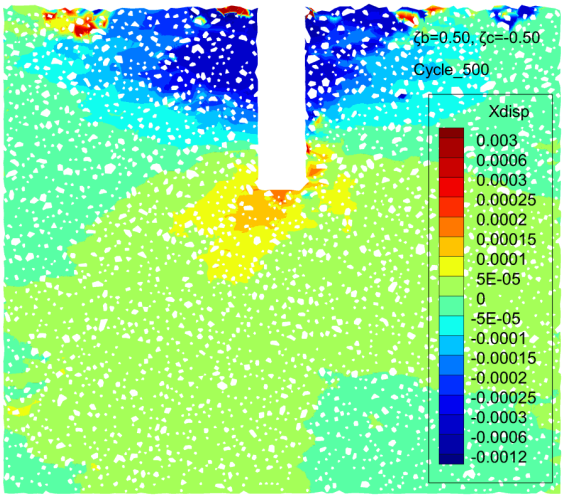

(h) ζ_b = 0.50 (N = 500)

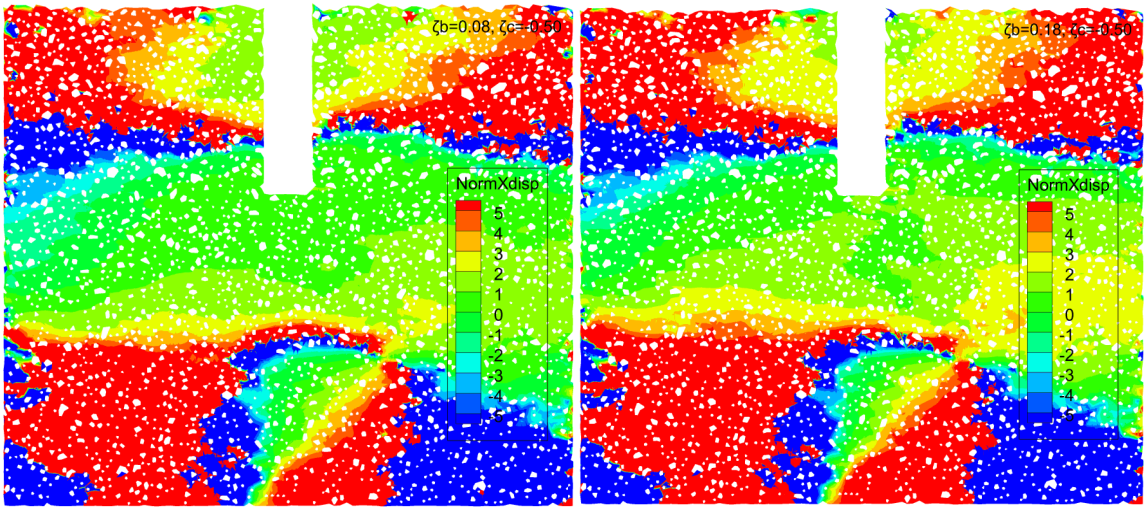

(i) ζ_b = 0.08 (Norm) (j) ζ_b = 0.18 (Norm)

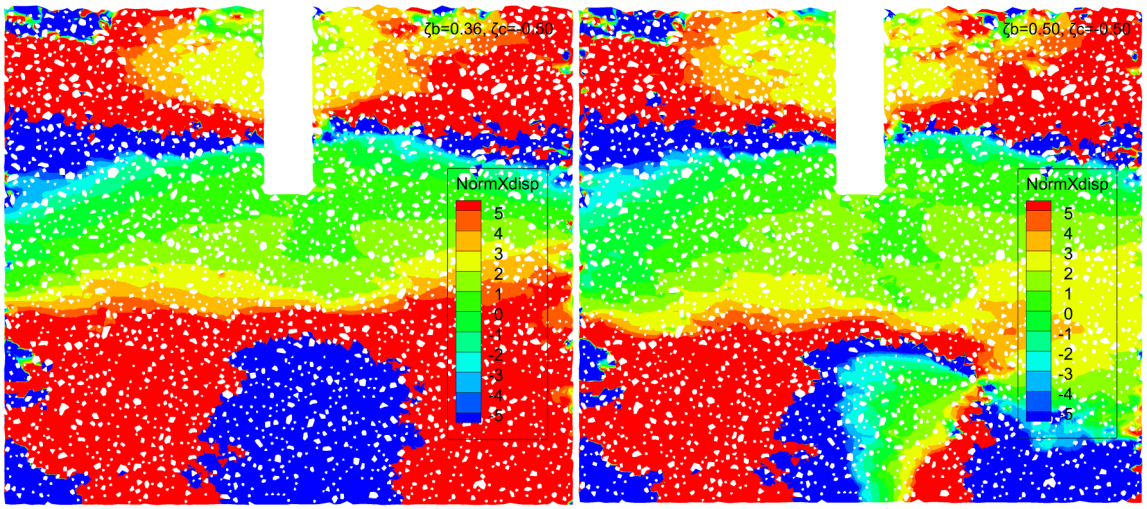

(k) ζ_b = 0.36 (Norm) (l) ζ_b = 0.50 (Norm)

Figure 6.5.7. Effect of ζ_b on the accumulated particle displacement field (ζ_c=-0.50).

For all the 4 cases presented here, the influencing zones are almost of the same conical shape, with relatively larger area on the passive side than that of the active side. The influence of ζ_b on the particle displacement field is evident from these figures. At the 1st cycle, the minimum particle displacements at the pile head of case *A* (see Figure 6.5.7 (a)) and *B* (see Figure 6.5.7 (b)) are -0.07895mm and -0.123mm, respectively. Taking the cut-off particle displacement as -0.002mm in these two cases, their influencing zones are about

1.35d_{pile} and 3.35d_{pile}. Meanwhile, the maximum particle displacements at the toe of pile are 0.0216mm and 0.0535mm, respectively. Very similar phenomena can also be observed in the other two cases, case C and case D, where the minimum particle displacements at the pile head are -0.246mm and -0.337mm, respectively. As the number of cycle increases, the cyclic loading effect is gradually accumulated. At the 500th cycle, the area of the influencing zones is almost doubled, comparing to that of the 1st cycle, as highlighted in Figure 6.5.7 (e)~(h). The minimum particle displacements at the pile head are -0.089mm, -0.215mm, -0.399mm, and -0.584mm, for case *A*, *B*, *C* and *D*, respectively. This is further elaborated in Figure 6.5.7 (i)~(l), where the normalised particle displacements are plotted. It should be noted that the larger. And then link with Figure 6.5.6 (a).

Rotational point: The location of "0" value boundary at the first cycle is horizontal, and change to slope away to the passive side after 500 cycles. However the "0" boundary of particles displacement contour which was contact to the pile nearly keep same location. This change can help to find the affected soil area expansion during the cyclic loading. This expansion is also due to the transfer of contact force from the pile movement. This procedure is similar as the spread of fan (SOF).

Further explain the mechanism using the void ratio and coordination data, as shown below.

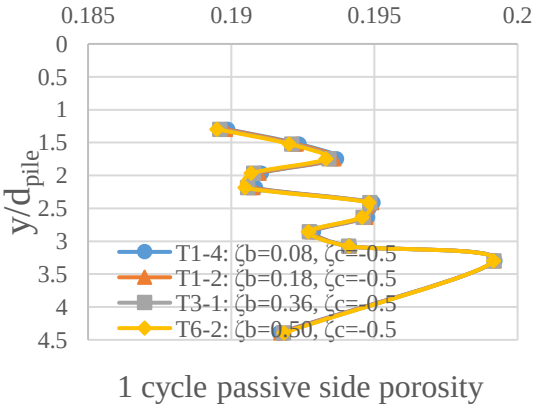

1 cycle passive side porosity

(a)

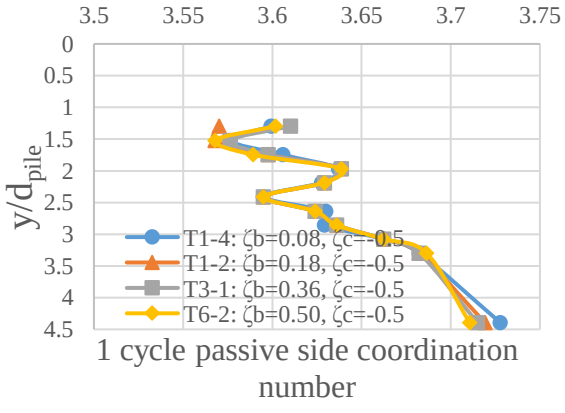

1 cycle passive side coordination number

(b)

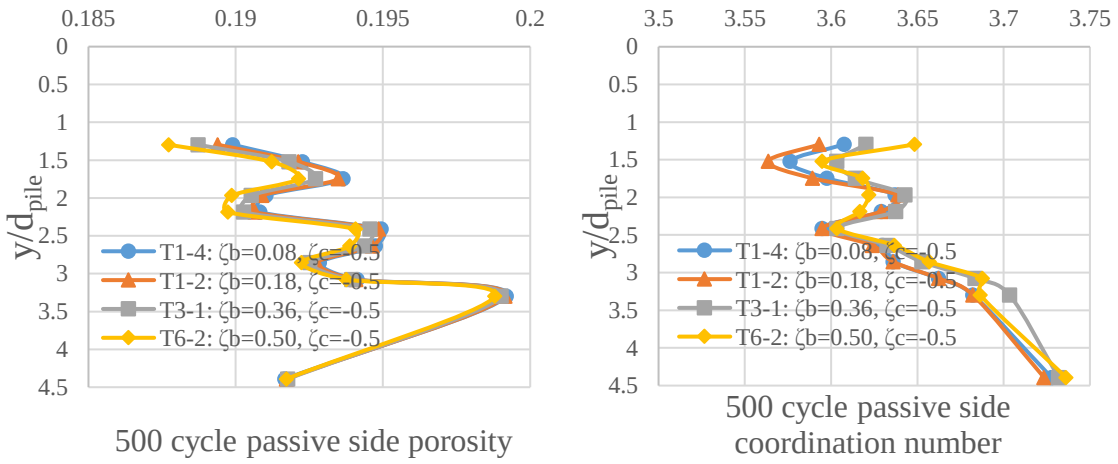

Figure 6.5.8. How the effect of ζ_b for the various parameter of passive side from 1st cycle to 500th cycle.

From Figure 6.5.8, these figures show the two parameter changes when comparing the 1st cycle and 500th cycle, such as porosity and coordination number.

Figure 6.5.8 (a) and (c) compare the change of passive side porosity. When ζ_b is increased, at the 1st cycle, porosity nearly did not change. However, at the 500th cycle, porosity in most areas decreases. But when $y/d_{pile} > 3$, porosity is nearly unchanged even at the 500th cycle.

Figure 6.5.8 (b) and (d) compare the change of passive side coordination number. The trend of these two figures is opposite to that of (a) and (c). Noticeably, in Figure 6.5.8 (d), when ζ_b is increased, the change in coordination is rather obvious.

6.5.4.2 Effect of ζ_c

From Figure 6.5.9, there shows 4 cases with the same ζ_b, but ζ_c increased from case T1-4 to T6-2. Because of the same ζ_b, the distribution of Figure 6.5.9 (a), (b), (c) and (d) are same. The smaller ζ_c cause the larger displacement. The trend is similar as the Figure 6.5.7.

As mentioned before, the ζ_c is negative, which means the cyclic loading is two way, and positive means the one way cyclic loading. Regarding the displacement of these figures, the two way is obvious larger than one way.

After 500 cycle (see Figure 6.5.9 (e), (f), (g) and (h)), the distensible area of displacement range -0.00005~ -0.0001 m is smaller than the displacement range -0.0006~ -0.0012 m, which means the particles near the pile move increase. From the area near pile tip of Figure 6.5.9 (e), (f), (g) and (h), it can be found that the phenomenon of SOF is shrinking during the cyclic test, however this trend is opposite for the upper area near the pile. At the same time, when the value of ζ_c is small (negative), the "zero" value line incline a lot. From the Figure 6.5.9 (i), (j), (k) and (l), the change is obvious than Figure 6.5.7 (i), (j), (k) and (l).

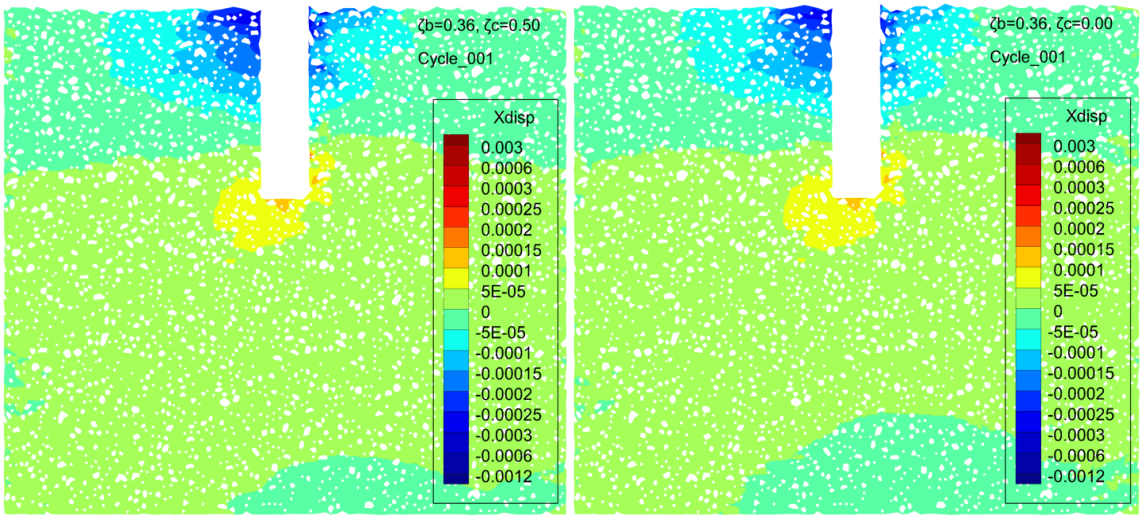

(a) ζ_c = 0.50 (N = 1)

(b) ζ_c = 0.00 (N = 1)

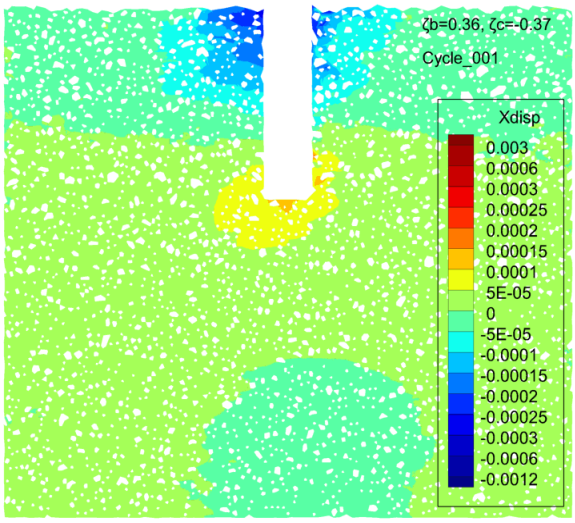

(c) ζ_c = -0.37 (N = 1)

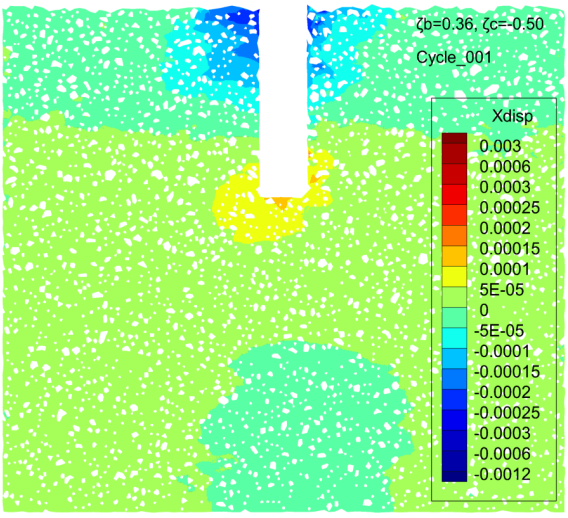

(d) ζ_c = -0.50 (N = 1)

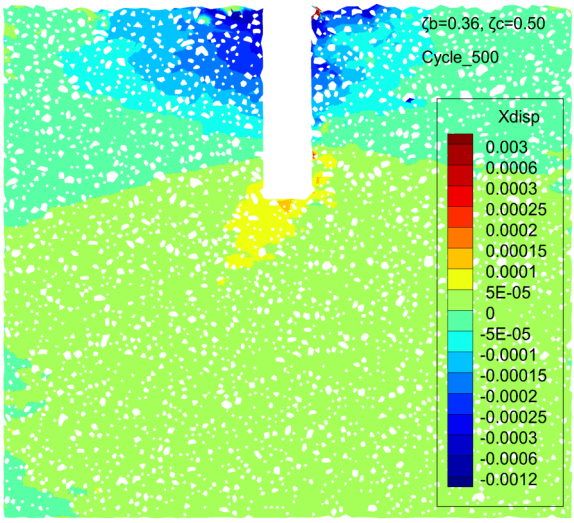

(e) ζ_c = 0.50 (N = 500)

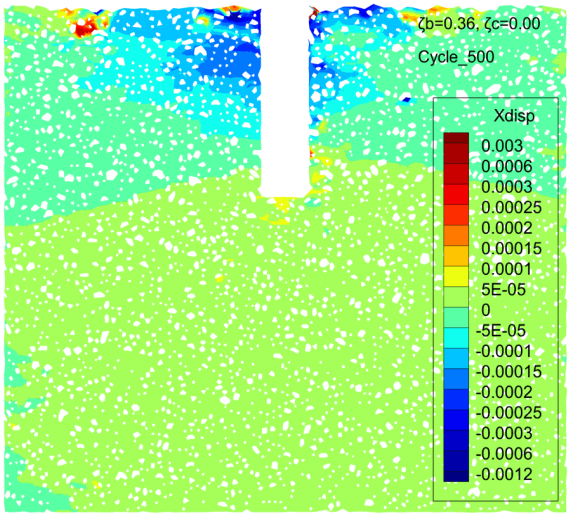

(f) ζ_c = 0.00 (N = 500)

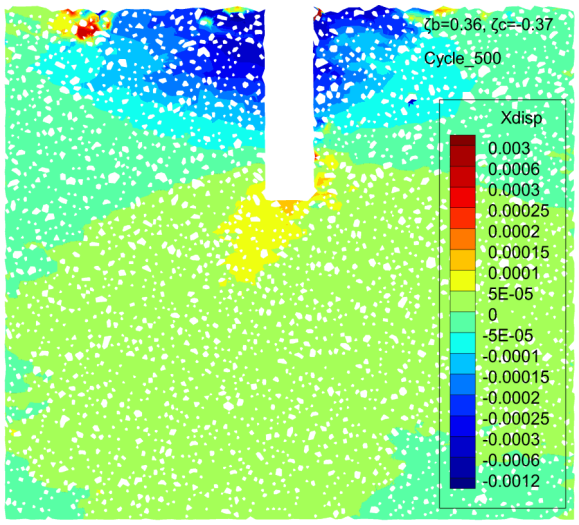

(g) ζ_c = -0.37 (N = 500)

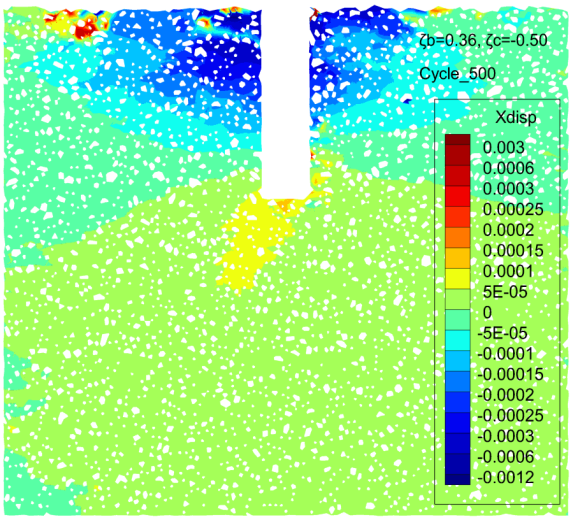

(h) ζ_c = -0.50 (N = 500)

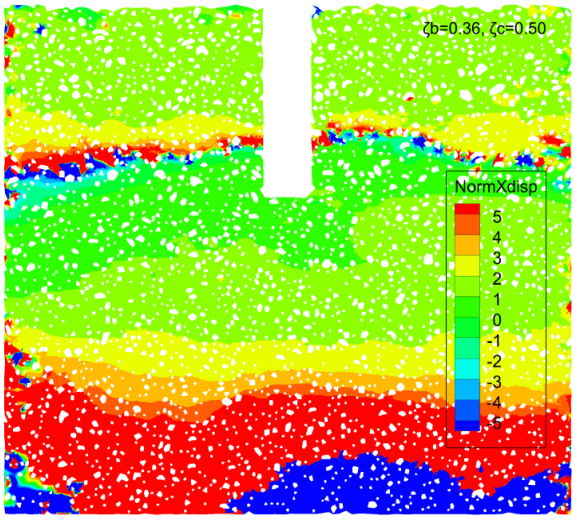

(i) ζ_c = 0.50 (Norm)

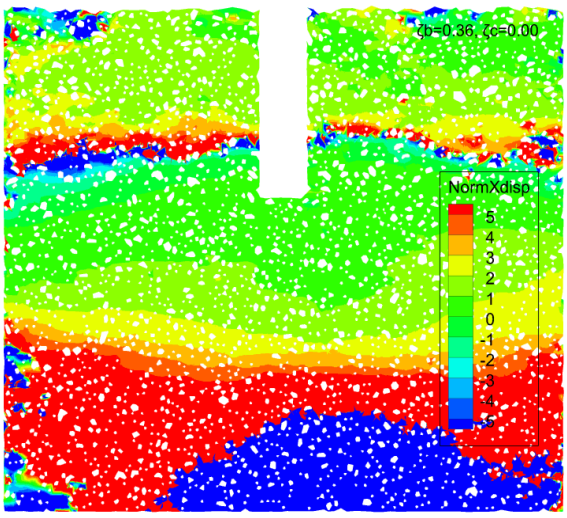

(j) ζ_c = 0.00 (Norm)

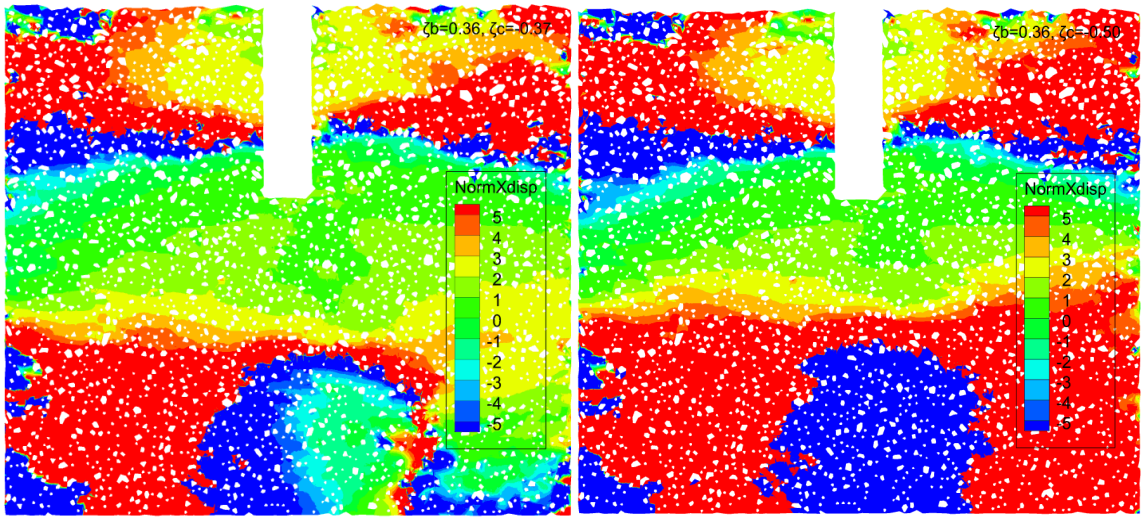

(k) ζ_c = -0.37 (Norm) (l) ζ_c = -0.50 (Norm)

Figure 6.5.9. How the effect of ζ_b for the various parameter of passive side from 1st cycle to 500th cycle.

Again, provide the further discussion with the void ratio and coordination number data, as shown below.

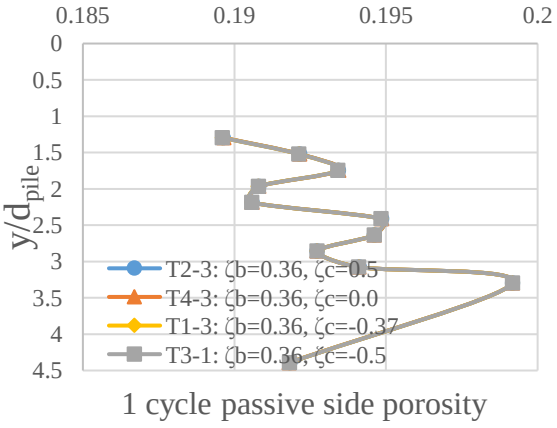

(a)

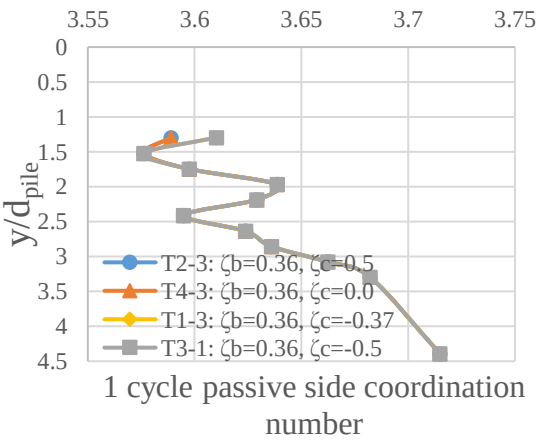

(b)

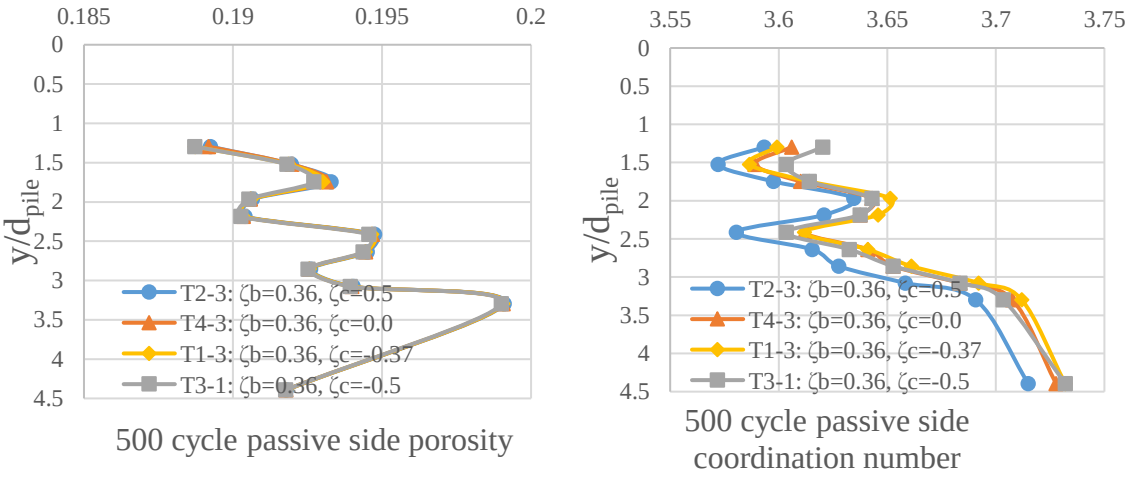

(c) (d)

Figure 6.5.10. How the effect of ζ_c for the various parameter of passive side from 1st cycle to 500th cycle.

From Figure 6.5.10, these Figures show the various parameter changes when comparing the 1st cycle and 500th cycle.

Figure 6.5.10 (a) and (c) has a similar trend as (a) and (c) of Figure 6.5.8, same applied to (b) and (d). Comapre to Figure 6.5.10 (b), Figure 6.5.10 (d) has a more obvious change in coordination number when ζ_c changes from large to small.

6.6 Summary

A series of model tests was carried out on a GM-DEM centrifuge test which was modelled by a rigid monopile subjected to various lateral cyclic loading and the cyclic displacement accumulation was measured up to 500 load cycles. These cyclic load tests included a range of load amplitudes that increased gradually throughout the test. The low-level cyclic loads were chosen to represent the normal working condition on a monopile, while the larger amplitudes considered extreme working conditions, such as storms and strong ocean currents. For the numerical simulation, the frequency also was the very important factor,

and the 40 Hz was choose due to the good comparison.

The main contributions of this paper included:

- The evidence of the first ten cycles has a strong influence on the cyclic responses of a rigid monopile under cyclic loading;
- There are a close relationship between the accumulated displacement and the cyclic load ratio and amplitude. The effect of load amplitude and cyclic load ratio was summarised and analysed. It was indicated that the load amplitude is obvious and cyclic load ratio also can control the change of displacement.
- The normalised lateral displacement decreases when the cyclic load ratio increase. However, the trend of load amplitude is opposite.
- Regarding the first 10 cycles of different cases with same load amplitude, both first cyclic secant stiffness k_1 and 10^{th} cyclic secant stiffness k_{10} will increase when cyclic load ratio increases. Nonetheless, the value of k_{10} / k_1 decrease dramatically. The change of stiffness is more obviously as long as cyclic load ratio increases.
- The rotational centre of the rigid model pile was at approximately 0.853 times the pile buried length during cyclic loading.

The parts of main content of this chapter was published by International Journal of Environmental, Chemical, Ecological, Geological and Geophysical Engineering as a journal paper with title "A Discrete Element Method Centrifuge Model of Monopile under Cyclic Lateral Loads" (Duan and Cheng, 2016b).

The main content of this chapter was accepted by ICE Geotechnical Engineering as a journal paper with title "DEM Investigation on Behaviour of Monopile under Cyclic Lateral Loading".

Chapter 7

Conclusion

7.1 Summary

In this PhD research, a numerical method Discrete Element Method (DEM) was employed to provide the unique particle-scale insight into the granular geomechanical behaviours of monopile foundation for offshore wind turbines. Accordingly, this DEM research mainly contributes five major advances which are summarised below.

7.1.1 Reliable sample preparation method and numerical DEM model

A sample preparation method was researched and created for the big scale DEM modelling. It should be noted that the sample initial state before the testing plays an essential role, and the initial state totally depends on the sample preparation. In order to make a comprehensive study of big scale geotechnical problems and generate homogeneous DEM specimens, a reasonable sample preparation method was modified.

This sample preparation method was tried to follow the experimental process. Particles are divided evenly to form grids. Then the parameters static earth soil pressure coefficient K_0, soil porosity, lateral and vertical stress were calculated to check the accuracy. And the method is quick to generate the sample, also the number of corresponding particle can be control very accuracy.

At the same time, a reliable numerical DEM soil model was build which can be used for the cyclic loading test, and this model and sample can be compared to existing experiment results. The pile was used “clump” which can be applied force directly. This mechanism is more closed to the realistic situation.

7.1.2 Understanding of the results when the monopole was applied the combined loads (see Appendix I)

The phenomenon of a rigid pile under the combined loadings conditions was studied from the microscopic and the macroscopic points of view. The vertical load has a profitable influence on the lateral response of piles embedded in sand. However, this influence depends on the sequence of loading, hence this result is only valid for the condition discussed in this research. The test results imply that it is conservative to design piles assuming that there is no interaction between axial and lateral loads. The test results also show that the larger the axial load, the bigger the ultimate lateral load capacity of the model pile subjected to combined loads. Therefore, the consideration of the effect of axial loads in the design of laterally loaded piles driven in sand is not necessary. The traces of particles movements have showed that there were obvious settlements of the soil particles near the bottom of the pile when there is vertical load. This should lead to soil densification and hence an increase in the lateral pile capacity under the combined loading condition.

7.1.3 Understanding of the physical phenomena during the pile installation.

A DEM modelling of pile installation tests was proposed. The tests were conducted with two different processes: bored pile and driven pile. Both conditions were performed with similar magnitude of pile embedded depth. Shaft resistance, base capacity and lateral stress were tested. Bored piles were observed to develop large settlements immediately during the test, while driven piles initially withstood settlements owing to an increase in available base capacity at the start of the penetration.

7.1.4 Understanding of the physical phenomena surrounding a pile when it is subjected to the lateral loads.

The model was generated for lateral loads and lateral cyclic loads and the analysis of lateral load on pile can be used to better understand the cyclic loads. *p-y* curve of lateral load test can prove that DEM also is an effective method to research the big scale problems. Before the failure state, the lateral stress of passive side did not change obviously. During the lateral loads, the soil state of different depth is different, and the boundaries can be considered as the pile rotation centre and pile tip.

7.1.5 Understanding of the physical phenomena surrounding a pile when it is subjected to the lateral cyclic loads.

A series of model tests was carried out on a GM DEM-centrifuge test which was modelled by a rigid monopile subjected to lateral cyclic loading and the cyclic displacement accumulation was measured up to 500 load cycles. These cyclic load tests included a range of load amplitudes that increased gradually throughout the test. The low-level cyclic loads were chosen to represent the normal working condition on a monopile, while the larger amplitudes considered extreme working conditions, such as storms and strong ocean currents. The DEM model also was proved that a strong influence of the first ten cycles on the cyclic responses of a rigid monopile was the main phenomena during the cyclic loading.

7.1.5.1 The general trend of pile displacement due to cyclic lateral loading in the long term

The accumulation of displacements was investigated for the design of a monopile support for an offshore wind turbine. It was clearly seen that the accumulation of displacement compared well with the experimental data. This can prove that DEM also is an effective

method to research large scale problems. Also monotonic loading tests can help with the analysis of cyclic loading tests. It was clearly seen that the accumulation of displacement is affected by the characteristic of the cyclic loading, and by the load amplitude.

7.1.5.2 The main factors that influence the generation of accumulated displacement

The close relationship was between the accumulated displacement and the cyclic load ratio and amplitude. Generally, the pile head load-displacement became stiffer as the number of load cycles (and the accumulated displacement) increased. In contrast, the unloading stiffness was independent of the cyclic ratio.

The effect of ζ_b and ζ_c also was summarised and analysed. It was indicated that the ζ_b is obvious and ζ_c also can control the change of displacement. The rotational centre of the rigid model pile was at approximately 0.853 times the pile buried length during cyclic loading (y/d_{pile} =3). For the numerical simulation, the frequency also was a very important factor, and the 40 Hz could be chosen due to the good comparison.

7.1.5.3 The mechanical explanations of the main physical phenomena occurring in the surrounding sand in the long term

The accumulation of displacement is the main reason for change of system stiffness. And the particles movement also effects the results.

7.2 Recommendations for further research

In the future, DEM will certainly not replace the continuum modelling as a means to predict sand foundation deformations, nor will it replace the in-situ and laboratory studies as a

means to advance the fundamental understanding of the sediment responses. However, it is definitely a useful tool to provide a unique insight into the geomechanical investigations of large scale problems. Although the DEM simulation results in this study are compared well to the published experimental data, there still presents the limitations of this DEM work. Regarding the sample preparation, there is no fluid or gas included in this DEM model, so that the comparison cannot be made properly. The DEM sand shape is sphere particle rather than the hybrid forms. For the particle size, the simulations carried out in this study used samples comprising big size sand. This was done to reduce the computational time of the simulations. It is possible to investigate the effect of the sand size.

Due to the limitations of the DEM modelling of spherical particles, this study is qualitative rather than quantitative. Examples of some specific recommendations are given below:

1. To perform 3D simulation for all the tests.
2. To generate other particle systems with more realistic size distributions. With the potential offered by parallel computing, and therefore the total number of particles used in a simulation, it will be possible in the near future to examine the mechanical behaviour of well-graded systems and, in particular, gap-graded systems.
3. To examine the use of contact mechanics for real particles such as Hertzian contact mechanics, which provides a more accurate response for a real soil contact model.
4. To examine the influence of using more realistic particle shape models for better results since particle shape has been shown to be an important factor for tip resistance and granular material response. Particle shape was found to significantly affect granular material response. The simulations carried out in this research focused on the use of simple shaped particles to reduce computational time.
5. To present energy interpretations based on the energy tracking of the system requires more refining before a more confident comparison with the theoretical micromechanical based models can be made.

6. To develop an alternative method to model the real flexible boundary conditions. The flexible membrane for the DEM tests was simulated in this research using a rigid wall. In the future study, it is possible to simulate a flexible membrane using a large number of bonded balls, albeit increasing computational time. A periodic boundary which could be used to simulate a large system by modelling a small part could be developed in the future to reduce boundary effects in the simulations.
7. To consider the breakage which will happen during the tests. This may give many insights into the deformation of granular media.
8. To investigate the drained and undrained behaviour of granular material
9. To use a coupled numerical method to solve computational time inefficiency. Two codes, Fast Lagrangian Analysis of Continua (FLAC), a finite difference code and Particle Flow Code (PFC), the discrete element code. Applying the FLAC/PFC coupled approach takes advantage of each modelling scheme and would at the same time reduce the demand for longer computational time. A large number of small particle sizes could be modelled near to the research area using PFC and the particles further away could be modelled with FLAC.

Bibliography

Aas, P. M., Karlsrud, K. & Clausen, C. J. F. 2005. Bearing capacity of driven piles in sand, the NGI approach. *Frontiers in Offshore Geotechnics.* Taylor & Francis.

Achmus, M. & Abdel-Rahman, K. 2005. Finite element modelling of horizontally loaded monopile foundations for offshore wind energy converters in Germany. *Frontiers in Offshore Geotechnics.* Taylor & Francis.

Achmus, M., Abdel-Rahman, K. & Kuo, Y. 2007. Behavior of large diameter monopiles under cyclic horizontal loading. *Twelfth International Colloquium on Structural and Geotechnical Engineering.* Cairo - Egypt: Ain Shams University,Faculty of Engineering,Department of Structural Engineering.

Achmus, M., Albiker, J. & Abdel-Rahman, K. 2010. Investigations on the behavior of large diameter piles under cyclic lateral loading. *Frontiers in Offshore Geotechnics II (Gourvenec S and White D (eds)). CRC Press, Boca Raton, FL, USA***,** 471-476.

Achmus, M., Kuo, Y. & Abdel-Rahman, K. 2009. Behavior of monopile foundations under cyclic lateral load. *Computers and Geotechnics,* 36**,** 725-735.

Achums, M., Abdel-Rahman, K. And Kuo, Yu-Shu 2008. Design of monopile foundations for offshore wind energy plants. *Baltic Geotechnical Conference-Geotechnics in Maritime Engineering, Gdansk***,** 463-470.

Adejumo, T. W. & Boiko, I. L. 2013. Effect of Installation Techniques on the Allowable Bearing Capacity of Modeled Circular Piles in Layered Soil. *International Journal of Science, Engineering and Technology Research (IJSETR),* 2.

Ahmadi, M. M. & Robertson, P. K. 2004. Calibration chamber size and boundary effects for CPT q(c) measurements. *Geotechnical and Geophysical Site Characterization,* 1&2**,** 829–833.

Albuquerque, P. J. R., Massad, F., Fonseca, A. V., Carvalho, D., Santos, J. & Esteves, E. C. 2011. Effects of the Construction Method on Pile Performance: Evaluation by Instrumentation. Part 1: Experimental Site at the State University of Campinas.

Alderlieste, E. A. 2011. *Experimental modelling of lateral loads on large diameter mono-pile foundations in sand.*

Alderlieste, E. A., Dijkstra, J. & Van Tol, A. F. Experimental Investigation Into Pile Diameter Effects of Laterally Loaded Mono-Piles. ASME 2011 30th International Conference on Ocean, Offshore and Arctic Engineering, 2011. American Society of Mechanical Engineers, 985-990.

Alfaro, M. C. & Wong, R. C. K. Some applications of computerized tomography (CT) in experimental geotechnics. Proceedings of the fifteenth international conference on soil mechanics and geotechnical engineering, 2001. International Society of Soil Mechanics and Geotechnical Engineering, 337–342.

Allersma, H. G. B. 1988. Optical analysis of stress and strain around the tip of a penetrating proble. *Penetration Testing.* Balkema, Rotterdam.

Altaee, A., Evgin, E. & Fellenius, B. H. 1992. Axial load transfer for piles in sand. II. Numerical analysis. *Canadian Geotechnical Journal,* 29**,** 21-30.

Api 1969. Recommended Practice for Planning, Designing, and Constructing Fixed Offshore Platforms. American Petroleum Institute, Washington, DC, USA.

Api 2000. Recommended Practice for Planning, Designing, and Constructing Fixed Offshore Platforms. American Petroleum Institute, Washington, DC, USA.

Api 2007. Recommended Practice for Planning, Designing, and Constructing Fixed Offshore Platforms. *Working Stress Design.* American Petroleum Institute, Washington, DC, USA.

Arroyo, M., Butlanska, J., Gens, A., Calvetti, F. & Jamiolkowski, M. 2011. Cone penetration tests in a virtual calibration chamber. *Géotechnique,* 61**,** 525-531.

Arshad, M. & O'kelly, B. C. Offshore wind-turbine structures: a review. Proceedings of the ICE - Energy, 2013. 139-152.

Augustesen, A. H., Sørensen, S. P. H., Ibsen, L. B., Andersen, L., Møller, M. & Brødbæk, K. T. Comparison of calculation approaches for monopiles for offshore wind turbines. The European Conference on Numerical Methods in Geotechnical Engineering, 2010. 901-906.

Baligh, M. 1985. Strain Path Method. *Journal of Geotechnical Engineering,* 111**,** 1108-1136.

Bathurst, R. J. & Rothenburg, L. 1988. Micromechanical Aspects of Isotropic Granular Assemblies With Linear Contact Interactions. *Journal of Applied Mechanics,* 55**,** 17-23.

Been, K., Jefferies, M. G., Crooks, J. H. A. & Rothenburg, L. 1987. The cone penetration test in sands: part II, general inference of state. *Géotechnique,* 37**,** 285-299.

Bolton, M. D. & Cheng, Y. P. 2001. Micro-geomechanics. *Constitutive and centrifuge modelling: Two extremes (ed. SM Springman),* 59-74.

Bolton, M. D., Gui, M. W., Garnier, J., Corté, J. F., Bagge, G., Laue, J. & Renzi, R. 1999. Centrifuge cone penetration tests in sand. *Géotechnique,* XLIX**,** 543-552.

Bond, A. & Jardine, R., J. 1991. Effects of installing displacement piles in a high OCR clay. *Geotechnique,* 41**,** 341-363.

Bourgeois, E., Rakotonindriana, M. H. J., Le Kouby, A., Mestat, P. & Serratrice, J. F. 2010. Three-dimensional numerical modelling of the behaviour of a pile subjected to cyclic lateral loading. *Computers and Geotechnics,* 37**,** 999-1007.

Bowman, E. T., Soga, K. & Drummond, W. 2001. Particle shape characterisation using Fourier descriptor analysis. *Geotechnique,* 51**,** 545-554.

Broere, W. & Tol, A. F. V. 2006. Modelling the bearing capacity of displacement piles in sand. *Proceedings of the ICE - Geotechnical Engineering,* 159**,** 195-206.

Broms, B. B. 1964. Lateral Resistance of Piles in Cohesionless Soils. *Journal of the Soil Mechanics and Foundations Division,* 90**,** 123-158.

Brown, D. A., Reese, L. C. & O'neill, M. W. 1987. Cyclic lateral loading of a large-scale pile group. *Journal of Geotechnical Engineering,* 113**,** 1326-1343.

Brown, D. A. & Shie, C.-F. 1990a. Numerical experiments into group effects on the response of piles to lateral loading. *Computers and Geotechnics,* 10**,** 211-230.

Brown, D. A. & Shie, C.-F. 1990b. Three dimensional finite element model of laterally loaded piles. *Computers and Geotechnics,* 10**,** 59-79.
Brown, D. A. & Shie, C.-F. 1991. Some numerical experiments with a three dimensional finite element model of a laterally loaded pile. *Computers and Geotechnics,* 12**,** 149-162.
Brucy, F., Meunier, J. & Nauroy, J. Behavior of pile plug in sandy soils during and after driving. Offshore Technology Conference, 1991. Offshore Technology Conference.
Burland, J., B. & Cooke, R. W. 1974. The design of bored piles. *Ground Engineering,* 7**,** 33-35.
Butlanska, J., Arroyo, M. & Gens, A. Homogeneity and symmetry in DEM models of cone penetration. Proc. AIP Conf. on Powders and Grains, 2009. 425-429.
Calvetti, F. 2008. Discrete modelling of granular materials and geotechnical problems. *European Journal of Environmental and Civil Engineering,* 12**,** 951-965.
Campos, J., Vargas Jr, E., Bernardes, G., Ibañez, J. & Velloso, R. Numerical experiments with discrete elements to simulate pile penetration in granular soils. Proceedings of the XXVI Iberian Latin-American Congress on Computational Methods in Engineering, 2005.
Chen, R.-P., Sun, Y.-X., Zhu, B. & Guo, W. D. 2015. Lateral cyclic pile-soil interaction studies on a rigid model monopile. *Geotechnical Engineering,* 168**,** 120-130.
Cheng, Y. P. 2004. *Micromechanical investigation of soil plasticity.* PhD, Cambridge University.
Cheng, Y. P., Bolton, M. D. & Nakata, Y. 2004. Crushing and plastic deformation of soils simulated using DEM. *Geotechnique,* 54**,** 131-141.
Cheng, Y. P., Nakata, Y. & Bolton, M. D. 2003. Discrete element simulation of crushable soil. *Geotechnique,* 53**,** 633-641.
Chik, Z. H., Abbas, J. M., Taha, M. R. & Shafiqu, Q. S. M. 2009. Lateral behavior of single pile in cohesionless soil subjected to both vertical and horizontal loads. *European Journal of Scientific Research,* 29**,** 194-205.
Chow, F., Jardine, R., Nauroy, J. & Brucy, F. 1997. Time-related increases in the shaft capacities of driven piles in sand. *Geotechnique,* 47.
Clausen, C. J. F., Aas, P. M. & Karlsrud, K. Bearing capacity of driven piles in sand, the NGI approach. In Frontiers in offshore geotechnics, 2005 London. Taylor & Francis, 677–681.
Cleary, P. W. 2000. DEM simulation of industrial particle flows: case studies of dragline excavators, mixing in tumblers and centrifugal mills. *Powder Technology,* 109**,** 83-104.
Climate, E. O. & Renewables 2011. Offshore Wind Energy Fact Book.
Coop, M. R., Klotz, E. U. & Clinton, L. 2005. The influence of the in situ state of sands on the load–deflection behaviour of driven piles. *Géotechnique,* 55**,** 721-730.
Cox, W. R., Reese, L. C. & Grubbs, B. R. Field testing of laterally loaded piles in sand. Offshore Technology Conference, 1974. Offshore Technology Conference.
Cuéllar, P. 2011. *Pile foundations for offshore wind turbines: Numerical and experimental investigations on the behaviour under short-term and long-term cyclic loading.* University of Technology Berlin.

Cuéllar, P., Baeßler, M. & Rücker, W. 2009. Ratcheting convective cells of sand grains around offshore piles under cyclic lateral loads. *Granular Matter,* 11**,** 379-390.
Cuéllar, P., Georgi, S., Baeßler, M. & Rücker, W. 2012. On the quasi-static granular convective flow and sand densification around pile foundations under cyclic lateral loading. *Granular Matter,* 14**,** 11-25.
Cui, L. & Bhattacharya, S. Dynamic soil-structure interaction around a monopile supporting a wind turbine. Geomechanics from Micro to Macro, 2015 Cambridge. Taylor & Francis Group.
Cui, L. & O'sullivan, C. 2006. Exploring the macro-and micro-scale response of an idealised granular material in the direct shear apparatus. *Geotechnique,* 56**,** 455-468.
Cundall, P. A. A computer model for simulating progressive, large-scale movements in blocky rock systems. Proc. Symp. Int. Rock Mech., 1971.
Cundall, P. A. 1989. Numerical experiments on localization in frictional materials. *Ingenieur-Archiv,* 59**,** 148-159.
Cundall, P. A. & Hart, R. D. 1992. Numerical modelling of discontinua. *Engineering computations,* 9**,** 101-113.
Cundall, P. A. & Strack, O. D. 1979a. A discrete numerical model for granular assemblies. *Geotechnique,* 29**,** 47-65.
Cundall, P. A. & Strack, O. D. 1979b. Formulation of a three-dimensional distinct element model—Part II. Department of Civil Engineering,University of Minnesota.
Dawson, T. 1980. Simplified analysis of offshore piles under cyclic lateral loads. *Ocean Engineering,* 7**,** 553-562.
De, B. C. & Vermeer, P. A. 1984. Finite element analysis of static penetration tests. *Geotechnique,* 34**,** 199–210
De Beer, E. Different behavior of bored and driven piles. Proceedings of the 1st international geotechnical seminar on deep foundations on bored and auger piles (BAP I), 1988 Rotterdam, Balkema. 47–82.
De Gennaro, V., Frank, R. & Said, I. 2008. Finite element analysis of model piles axially loaded in sands. *Rivista Italiana di Geotechnica***,** 44-62.
Desai, C. S. & Christian, J. T. 1977. *Numerical methods in geotechnical engineering. McGraw-Hill, New York.,* New York., McGraw-Hill.
Desrues, J., Chambon, R., Mokni, M. & Mazerolle, F. 1996. Void ratio evolution inside shear bands in triaxial sand specimens studied by computed tomography. *Géotechnique,* 46**,** 529-546.
Dnv 2009. Design of Offshore Wind Turbine Structures. Det Norske Veritas.
Dnv 2010. Design of Offshore Wind Turbine Structures. Det Norske Veritas.
Doherty, P. & Gavin, K. 2012. Laterally loaded monopile design for offshore wind farms. *Proceedings of the ICE - Energy,* 165**,** 7-17.
Doherty, P., Gavin, K. & Casey, B. 2011. The Geotechnical Challenges Facing the Offshore Wind Sector. *Geo-Frontiers 2011.*
Drescher, A. & De Josselin De Jong, G. 1972. Photoelastic verification of a mechanical model for the flow of a granular material. *Journal of the Mechanics and Physics of Solids,* 20**,** 337-340.

Duan, N. & Cheng, Y. A Modified Method of Generating Specimens for a 2D DEM Centrifuge Model. Geo-Chicago 2016, 2016a. American Society of Civil Engineers, 610-620.

Duan, N. & Cheng, Y. P. A 2D DEM mono-pile model under combined loading condition. *In:* AL, S. E., ed. Geomechanics from Micro to Macro, 2015 Cambridge. Taylor & Francis Group, 577-582.

Duan, N. & Cheng, Y. P. 2016b. A Discrete Element Method Centrifuge Model of Monopile under Cyclic Lateral Loads. *International Journal of Environmental, Chemical, Ecological, Geological and Geophysical Engineering,* 10**,** 188-194.

Durgunoglu, H. T. & Mitchell, J. K. Static penetration resistance of soils. Proceedings of the ASCE Specialty Conference on In-Situ Measurements of Soil Properties, 1975 Raleigh. 151–189.

Ei-Keiesh, A. M. & Matsui, T. 2008. Calibration chamber modeling of compaction grouting. *ASTM geotechnical testing journal,* 31**,** 295-307.

Esquivel, E. & Silva, C. 2000. Miniature Piezocone for Use in Centrifuge Testing. *Innovations and Applications in Geotechnical Site Characterization.* American Society of Civil Engineers.

Esteban, M., Lopes Gutierrez, J., Diez, J. & Negro, V. Foundations for offshore wind farms. Proceedings of the 12th International Conference on Environmental Science and Technology, 2011 Rhodes, Greece. 516–523.

Fan, C.-C. & Long, J. H. 2005. Assessment of existing methods for predicting soil response of laterally loaded piles in sand. *Computers and Geotechnics,* 32**,** 274-289.

Farrell, D. & Greacen, E. 1966. Resistance to penetration of fine probes in compressible soil. *Soil Research,* 4**,** 1-17.

Fischer, T. 2011. Executive Summary-UpWind Project. WP4: Offshore Foundations and Support Structures.

Fuglsang, L. D. & Ovesen, N. K. 1988. The application of the theory of modelling to centrifuge studies. *Centrifuges in Soil Mechanics.* Abington, UK: Taylor & Francis.

Gavin, K., Igoe, D. & Doherty, P. 2011. Piles for offshore wind turbines: a state-of-the-art review. *Proceedings of the ICE - Geotechnical Engineering,* 164**,** 245-256.

Gavin, K. & Lehane, B. 2003a. End bearing of small pipe piles in dense sand. *BGA International Conference on Foundations: Innovations, observations, design and practice.* London: Thomas Telford.

Gavin, K. G. & Lehane, B. M. 2003b. The shaft capacity of pipe piles in sand. *Canadian Geotechnical Journal,* 40**,** 36-45.

Gavin, K. G. & O'kelly, B. C. 2007. Effect of friction fatigue on pile capacity in dense sand. *Journal of Geotechnical and Geoenvironmental Engineering,* 133**,** 63-71.

Ghionna, V. N., Jamiolkowski, M., Pedroni, S. & Salgado, R. The tip displacement of drilled shafts in sands. Vertical and Horizontal Deformations of Foundations and Embankments, 1994. ASCE, 1039-1057.

Giannakos, S., Gerolymos, N. & Gazetas, G. 2012. Cyclic lateral response of piles in dry sand: Finite element modeling and validation. *Computers and Geotechnics,* 44**,** 116-131.

Gong, G. 2008. *DEM simulations of drained and undrained behaviour*. PhD thesis, University of Birmingham, UK.
Grashuis, A., Dietermann, H. & Zorn, N. 1990. Calculation of cyclic response of laterally loaded piles. *Computers and Geotechnics,* 10**,** 287-305.
Gupta, R. 1991. Finite Strain Analysis for Deep Cone Penetration. *Journal of Geotechnical Engineering,* 117**,** 1610-1630.
Hansen, J. B. & Christensen, N. H. 1961. *The ultimate resistance of rigid piles against transversal forces,* Copenhagen, Geoteknisk Institut.
Hansen, N. M. 2012. *Interaction between Seabed Soil and Offshore Wind Turbine Foundations.* DTU Mechanical Engineering.
Heerema, E. P. Predicting pile driveability: Heather as an illustration of the" friction fatigue" theory. SPE European Petroleum Conference, 1980. Society of Petroleum Engineers.
Henke, S. & Grabe, J. Numerical modeling of pile installation. International Conference on Soil Mechanics and Geotechnical Engineering, 2009. 1321-1324.
Herrmann, L. R. & Mello, J. 1994. Investigation of an alternative finite element procedure: A one-step, steady-state analysis. DTIC Document.
Hoomans, B. P. B., Kuipers, J. a. M. & Van Swaaij, W. P. M. 2000. Granular dynamics simulation of segregation phenomena in bubbling gas-fluidised beds. *Powder Technology,* 109**,** 41-48.
Hu, G. C. 1965. *Bearing capacity of foundations with overburden shear*.
Huang, A.-B. & Ma, M. Y. 1994. An analytical study of cone penetration tests in granular material. *Canadian Geotechnical Journal,* 31**,** 91-103.
Hutchinson, T., Chai, Y. & Boulanger, R. 2005. Simulation of Full-Scale Cyclic Lateral Load Tests on Piles. *Journal of Geotechnical and Geoenvironmental Engineering,* 131**,** 1172-1175.
Idriss, I. M., Dobry, R. & Sing, R. 1978. Nonlinear behavior of soft clays during cyclic loading. *Journal of Geotechnical and Geoenvironmental Engineering,* 104.
Igoe, D., Gavin, K. & O'kelly, B. 2013. An investigation into the use of push-in pile foundations by the offshore wind sector. *International Journal of Environmental Studies,* 70**,** 777-791.
Ismael, N. 1990. Behavior of Laterally Loaded Bored Piles in Cemented Sands. *Journal of Geotechnical Engineering,* 116**,** 1678-1699.
Itasca 2004. PFC User Manual, version 3.1. USA: Itasca Consulting Group Inc.
Iwashita, K. & Oda, M. 1998. Rolling Resistance at Contacts in Simulation of Shear Band Development by DEM. *Journal of Engineering Mechanics,* 124**,** 285-292.
Jamiolkowski, M., Lo Presti, D. & Manassero, M. 2003. Evaluation of Relative Density and Shear Strength of Sands from CPT and DMT. *Soil Behavior and Soft Ground Construction.* American Society of Civil Engineers.
Jardine, R., J., Chow, F., Overy, R. & Standing, J. 2005. *ICP design methods for driven piles in sands and clays*, Thomas Telford London.
Jardine, R., J., Puech, A. & Andersen, K. H. 2012. Cyclic loading of offshore piles: potential effects and practical design. *Margin,* 40**,** 2.

Jardine, R., J., Zhu, B., Foray, P. & Dalton, C. P. 2009. Experimental arrangements for investigation of soil stresses developed around a displacemnt pile. *Soils and foundations,* 49**,** 661-673.

Jardine, R., Overy, R. & Chow, F. 1998. Axial Capacity of Offshore Piles in Dense North Sea Sands. *Journal of Geotechnical and Geoenvironmental Engineering,* 124**,** 171-178.

Jardine, R. J. & Chow, F. C. 1996. New Design Methods for Offshore Piles. Energy Institute.

Jardine, R. J. & Chow, F. C. Some recent developments in offshore pile design. OFFSHORE SITE INVESTIGATION AND GEOTECHNICS, Confronting New Challenges and Sharing Knowledge, 2007. Society of Underwater Technology.

Jeong, S. & Seo, D. 2004. Analysis of tieback walls using proposed p-y curves for coupled soil springs. *Computers and Geotechnics,* 31**,** 443-456.

Jiang, M., Dai, Y., Cui, L., Shen, Z. & Wang, X. 2014. Investigating mechanism of inclined CPT in granular ground using DEM. *Granular Matter,* 16**,** 785-796.

Jiang, M., Konrad, J. & Leroueil, S. 2003. An efficient technique for generating homogeneous specimens for DEM studies. *Computers and geotechnics,* 30**,** 579-597.

Jiang, M., Yu, H. S. & Harris, D. 2006. Discrete element modelling of deep penetration in granular soils. *International Journal for Numerical and Analytical Methods in Geomechanics,* 30**,** 335-361.

Jin, W. & Zhou, J. A coupled micro-macro method for pile penetration analysis. GeoShanghai International Conference, Shanghai, China, 2010. 234-239.

Juirnarongrit, T. & Ashford, S. 2005. Effect of pile diameter on the modulus of sub-grade reaction. San Diego: Department of Structural Engineering, University of California.

Kallehave, D., Byrne, B. W., Thilsted, C. L. & Mikkelsen, K. K. 2015. Optimization of monopiles for offshore wind turbines. *Philosophical Transactions of the Royal Society of London A: Mathematical, Physical and Engineering Sciences,* 373**,** 20140100.

Kallehave, D., Thilsted, C. L. & Liingaard, M. 2012. Modification of the API Py Formulation of Initial Stiffness of Sand. *Offshore Site Investigation and Geotechnics: Integrated Technologies-Present and Future*.

Katsuki, S., Ishikawa, N., Ohira, Y. & Suzuki, H. 1989. Shear strength of rod material. *Journal of Civil Engineering***,** 1-12.

Kimura, M., Adachi, T., Kamei, H. & Zhang, F. 3-D finite element analyses of the ultimate behavior of laterally loaded cast-in-place concrete piles. Proceedings of the Fifth International Symposium on Numerical Models in Geomechanics, NUMOG V, 1995. AA Balkema, 589-594.

Kiousis, P. D., Voyiadjis, G. Z. & Tumay, M. T. 1988. A large strain theory and its application in the analysis of the cone penetration mechanism. *International Journal for Numerical and Analytical Methods in Geomechanics,* 12**,** 45-60.

Kirkwood, P. & Haigh, S. 2013a. Centrifuge testing of monopiles for offshore wind turbines. *Proc. ISOPE. Anchorage, 30 June–5 July 2013*.

Kirkwood, P. B. & Haigh, S. K. 2013b. Centrifuge testing of monopiles subject to cyclic lateral loading. *ICPMG2014 ? Physical Modelling in Geotechnics.* CRC Press.
Klinkvort, R., Hededal, O. & Svensson, M. 2012. Laterally cyclic loading of monopile in dense sand. *Centrifuge modelling of drained lateral pile-soil response***,** 171.
Klinkvort, R. T. 2013. *Centrifuge modelling of drained lateral pile - soil response: Application for offshore wind turbine support structures.* Technical University of Denmark.
Klinkvort, R. T. & Hededal, O. 2010. Centrifuge modelling of offshore monopile foundation. *Frontiers in Offshore Geotechnics II.* Taylor & Francis.
Klinkvort, R. T. & Hededal, O. 2013. Lateral response of monopile supporting an offshore wind turbine. *Proceedings of the ICE - Geotechnical Engineering,* 166**,** 147-158.
Klinkvort, R. T., Leth, C. T. & Hededal, O. Centrifuge modelling of a laterally cyclic loaded pile. Physical Modelling in Geotechnics, 2010. 959-964.
Kolk, H. J., Baaijens, A. E. & Senders, M. Design Criteria for Pipe Piles in Silica Sands. Kolk, H.J., Baaijens, A.E. and Senders, M., 2005 University of Western Australia, Perth. Taylor & Francis, 711 – 716.
Kuo, Y., Achmus, M. & Abdel-Rahman, K. 2012. Minimum Embedded Length of Cyclic Horizontally Loaded Monopiles. *Journal of Geotechnical and Geoenvironmental Engineering,* 138**,** 357-363.
Lau, B. H., Lam, S. Y., Haigh, S. K. & Madabhushi, S. P. G. Centrifuge testing of monopile in clay under monotonic loads. *In:* WHITE, G., ed. Physical Modelling in Geotechnics, 2014 London. Taylor & Francis Group, 689-695.
Leblanc, C. 2009. *Design of offshore wind turbine support structures: selected topics in the field of geotechnical engineering.* PhD, Department of Civil Engineering, Aalborg University.
Leblanc, C., Byrne, B. W. & Houlsby, G. T. 2010a. Response of stiff piles to random two-way lateral loading. *Geotechnique,* 60**,** 715-721.
Leblanc, C., Houlsby, G. T. & Byrne, B. W. 2010b. Response of stiff piles in sand to long-term cyclic lateral loading. *Geotechnique,* 60**,** 79-90.
Lee, C., Allman, M. & Poulos, H. Static behavior of piles in cemented calcareous sands. Foundation Engineering'sCurrent Principles and Practices, 1989. ASCE, 485-499.
Lee, J. 1999. *Design of foundations bearing in sand based on CPT results.* 9952124 Ph.D., Purdue University.
Lee, J. & Salgado, R. 1999. Determination of pile base resistance in sands. *Journal of Geotechnical and Geoenvironmental Engineering,* 125**,** 673-683.
Lehane, B. & Jardine, R. 1994. Displacement pile behaviour in glacial clay. *Canadian geotechnical journal,* 31**,** 79-90.
Lehane, B., Jardine, R., J., Bond, A. & Frank, R. 1993. Mechanisms of Shaft Friction in Sand from Instrumented Pile Tests. *Journal of Geotechnical Engineering,* 119**,** 19-35.
Lehane, B. M. 1992. *Experimental investigations of pile behaviour using instrumented field piles.* PhD, University of London (Imperial College).
Lehane, B. M., Schneider, J. A. & Xu, X. 2005. A Review of Design Methods for Offshore Driven Piles in Siliceous Sand. University of Western Australia (UWA).

Lesny, K. 2008. Gründung von Offshore‐Windenergieanlagen‐Entscheidungshilfen für Entwurf und Bemessung. *Bautechnik,* 85**,** 503-511.
Lesny, K. 2010. *Foundations for Offshore Wind Turbines - Tools for Planning and Design*, Vge-Verlag.
Lesny, K. & Wiemann, J. 2006. Finite-Element-Modelling of Large Diameter Monopiles for Offshore Wind Energy Converters. *GeoCongress 2006.*
Leung, C. F., Lee, F. H. & Yet, N. S. 2001. Centrifuge model study on pile subject to lapses during installation in sand. *International Journal of Physical Modelling in Geotechnics,* 1**,** 47-57.
Levy, N. H., Einav, I. & Hull, T. 2009. Cyclic shakedown of piles subjected to two‐dimensional lateral loading. *International journal for numerical and analytical methods in geomechanics,* 33**,** 1339-1361.
Li, Y.-N. & Li, J.-P. 2014. Discrete Element Modeling of Jacked Piles in Granular Soil.
Li, Z., Haigh, S. K. & Bolton, M. D. Centrifuge modelling of mono-pile under cyclic lateral loads. 7th International Conference on Physical modelling in Geotechnics, 2010 Switzerland. 965-970.
Lin, S. & Liao, J. 1999. Permanent Strains of Piles in Sand due to Cyclic Lateral Loads. *Journal of Geotechnical and Geoenvironmental Engineering,* 125**,** 798-802.
Little, R. L. & Briaud, J.-L. 1988a. Full scale cyclic lateral load tests on six single piles in sand. DTIC Document.
Little, R. L. & Briaud, J.-L. 1988b. A pressuremeter method for single piles subjected to cyclic lateral loads in sand. DTIC Document.
Liu, J.-W., Yu, F., Zhang, Z.-M. & Wang, N. 2013. Simulation of post-installation residual stress in preformed piles based on energy conservation. *Rock and Soil Mechanics,* 4**,** 041.
Liu, J.-W., Zhang, Z.-M., Yu, F. & Xie, Z.-Z. 2012. Case history of installing instrumented jacked open-ended piles. *Journal of Geotechnical and Geoenvironmental Engineering,* 138**,** 810-820.
Lombardi, D., Bhattacharya, S. & Muir Wood, D. 2013. Dynamic soil–structure interaction of monopile supported wind turbines in cohesive soil. *Soil Dynamics and Earthquake Engineering,* 49**,** 165-180.
Lombardi, D., Cox, J. A. & Bhattacharya, S. Long-term performance of offshore wind turbines supported on monopiles and suction caissons. 8th International Conference on Structural Dynamics, 2011 Leuven, Belgium.
Long, J. & Vanneste, G. 1994. Effects of cyclic lateral loads on piles in sand. *Journal of Geotechnical Engineering,* 120**,** 225-244.
Mabsout, M. E. & Tassoulas, J. L. 1994. A finite element model for the simulation of pile driving. *International Journal for numerical methods in Engineering,* 37**,** 257-278.
Malhotra, S. 2010. Design and Construction Considerations for Offshore Wind Turbine Foundations in North America. *GeoFlorida 2010.* American Society of Civil Engineers.
Mao, X. & Fahey, M. 1999. A method of reconstituting an aragonite soil using a synthetic flocculant. *Geotechnique,* 49**,** 15-32.

Mardfekri, M., Gardoni, P. & Roesset, J. M. 2013. Modeling laterally loaded single piles accounting for nonlinear soil-pile interactions. *Journal of Engineering*.

Masson, S. & Martinez, J. 2001. Micromechanical analysis of the shear behavior of a granular material. *Journal of Engineering Mechanics,* 127**,** 1007-1016.

Matlock, H. 1970. Correlations for design of laterally loaded piles in soft clay. *Offshore Technology in Civil Engineering's Hall of Fame Papers from the Early Years***,** 77-94.

Mcclelland, B. & Focht, J. A. 1958. Soil modulus for laterally loaded piles. *Transactions of the American Society of Civil Engineers,* 123**,** 1049-1063.

Mcdowell, G., Falagush, O. & Yu, H.-S. 2012. A particle refinement method for simulating DEM of cone penetration testing in granular materials. *Géotechnique Letters,* 2**,** 141-147.

Meyer, B. J. & Reese, L. C. 1979. Analysis of single piles under lateral loading. University of Texas at Austin.

Meyerhof, G. G. 1951. The ultimate bearing capacity of foudations. *Geotechnique,* 2**,** 301-332.

Moss, R. E. S., Caliendo, J. A. & Anderson, L. R. 1998. Investigation of a cyclic laterally loaded model pile group. *Soil Dynamics and Earthquake Engineering,* 17**,** 519-523.

Muqtadir, A. & Desai, C. S. 1986. Three‐dimensional analysis of a pile‐group foundation. *International journal for numerical and analytical methods in geomechanics,* 10**,** 41-58.

Murchison, J. M. & O'neill, M. W. Evaluation of p-y relationships in cohesionless soils. Analysis and design of pile foundations, 1984. ASCE, 174-191.

Musial, W., Butterfield, S. & Ram, B. 2006. Energy from Offshore Wind. *Offshore Technology Conference.*

Niemunis, A., Wichtmann, T. & Triantafyllidis, T. 2004. Explicit accumulation model for cyclic loading. *Cyclic Behaviour of Soils and Liquefaction Phenomena***,** 65-76.

O'neill, M. W. & Murchison, J. M. 1983. *An evaluation of py relationships in sands*, University of Houston.

O'sullivan, C. 2011a. Particle-Based Discrete Element Modeling: Geomechanics Perspective. *International Journal of Geomechanics,* 11**,** 449-464.

O'sullivan, C. 2011b. *Particulate Discrete Element Modelling: A Geomechanics Perspective* Lonodn, Taylor & Francis.

O'sullivan, C. & Cui, L. 2009. Micromechanics of granular material response during load reversals: combined DEM and experimental study. *Powder Technology,* 193**,** 289-302.

Oda, M. 1972. Deformation mechanism of sand in triaxial compression tests. *SOILS AND FOUNDATIONS,* 12**,** 45-63.

Oda, M. & Iwashita, K. 1999. *Mechanics of granular materials: an introduction*, CRC Press.

Oda, M. & Kazama, H. 1998. Microstructure of shear bands and its relation to the mechanisms of dilatancy and failure of dense granular soils. *Geotechnique,* 48**,** 465-481.

Oner, M. Analysis of fabric changes during cyclic loading of granular soils. Proc., 8th World Conf. Earthquake Engineering, 1984 San Francisco, Calif. 55-62.
Peiffer, H. & Van Impe, W. Evaluation of pile performance based on soil stress measurements: field-test program. *In:* VAN IMPE, W. F., ed. Deep Foundations on Bored & Auger Piles : Bap II, 1993. A.A. Balkema, 385-389.
Peng, J., Clarke, B. G. & Rouainia, M. 2006. A device to cyclic lateral loaded model piles. *Geotechnical Testing Journal,* 29**,** 341.
Peralta, P. 2009. Investigations on the behaviour of large diameter piles under long-term lateral cyclic loading in cohesionless soil. Hannover.
Peralta, P. 2010. *Investigations on the Behavior of Large Diameter Piles Under Long-term Lateral Cyclic Loading in Cohesionless Soil*, IGtH.
Peralta, P. & Achmus, M. 2010. An experimental investigation of piles in sand subjected to lateral cyclic loads. *Physical Modelling in Geotechnics, Two Volume Set.* CRC Press.
Poulos, H. Developments in the analysis of static and cyclic lateral response of piles. Numerical methods in geomechanics. International conference on numerical methods in geomechanics. 4, 1982. 1117-1135.
Poulos, H. G. 1987. Analysis of residual stress effects in piles. *Journal of geotechnical engineering,* 113**,** 216-229.
Poulos, H. G. & Hull, T. S. 1989. The role of analytical geomechanics in foundation engineering. *In Foundation Engineering: Current Principles and Practice,* 2**,** 1578–1606.
Pressley, J. & Poulos, H. G. 1986. Finite element analysis of mechanisms of pile group behaviour. *International journal for numerical and analytical methods in geomechanics,* 10**,** 213-221.
Randolph, M. F. 1981. The response of flexible piles to lateral loading. *Geotechnique,* 31**,** 247-259.
Rao, S. N. & Rao, K. M. 1993. Behaviour of rigid piles in marine clays under lateral cyclic loading. *Ocean Engineering,* 20**,** 281-293.
Rasmussen, K. L., Hansen, M., Wolf, T. K., Ibsen, L. B. & Roesen, H. R. 2013. A literature study on the effects of cyclic lateral loading of monopiles in cohesionless soils. *DCE Technical Memorandum.* Aalborg: Aalborg University. Department of Civil Engineering.
Reese, L. C., Cox, W. R. & Koop, F. D. Analysis of laterally loaded piles in sand. 5th Ann. Offshore Technology in Civil Engineering, 1974 Houston,Tex. ASCE, 95-105.
Reese, L. C., Cox, W. R. & Koop, F. D. Field Testing and Analysis of Laterally Loaded Piles in Stiff Clay. Offshore Technology Conference, 1975 Houston, Texas.
Reese, L. C. & Matlock, H. Non-dimensional solutions for laterally-loaded piles with soil modulus assumed proportional to depth. 1956 Dallas, Tex.: Association of Drilled Shaft Contractors.
Robertson, P. K. 1986. In situ testing and its application to foundation engineering. *Canadian Geotechnical Journal,* 23**,** 573-594.
Roesen, H. R., Ibsen, L. B., Hansen, M., Wolf, T. K. & Rasmussen, K. L. Laboratory Testing of Cyclic Laterally Loaded Pile in Cohesionless Soil. The Twenty-third

International Offshore and Polar Engineering Conference, 2013. International Society of Offshore and Polar Engineers.
Rohani, B. & Baladixxa, G. Y. 1981. Correlation of mobility cone index with fundamental engineering properties of soil. DTIC Document.
Rollins, K. M., Olsen, R. J., Egbert, J. J., Jensen, D. H., Olsen, K. G. & Garrett, B. H. 2006. Pile spacing effects on lateral pile group behavior: load tests. *Journal of geotechnical and geoenvironmental engineering,* 132**,** 1262-1271.
Rosquoet, F., Thorel, L., Garnier, J. & Canepa, Y. 2007. Lateral cyclic loading of sand-installed piles. *Soils and foundations,* 47**,** 821-832.
Rothenburg, L. & Bathurst, R. 1992. Micromechanical features of granular assemblies with planar elliptical particles. *Geotechnique,* 42**,** 79-95.
Sørensen, S. P. H., Ibsen, L. B. & Augustesen, A. H. Effects of diameter on initial stiffness of p-y curves for large-diameter piles in sand. The European Conference on Numerical Methods in Geotechnical Engineering, 2010. 907-912.
Saleem, Z. 2011. Alternatives and modifications of Monopile foundation or its installation technique for noise mitigation. *Report by Delft University of Technology for Stichting De Noordzee (the North Sea Foundation)*.
Salgado, R., Mitchell, J. & Jamiolkowski, M. 1998. Calibration Chamber Size Effects on Penetration Resistance in Sand. *Journal of Geotechnical and Geoenvironmental Engineering,* 124**,** 878-888.
Sanjaya, K. V., Sharma, K. G. & Varadarajan, A. Behaviour of a laterally loaded pile. Proceedings of the 10th international symposium on numerical models in geomechanics, 2007. 447–452.
Schertmann, J. 1977. *Guidelines for cone penetration test: performance and design,* Washington, Dept. of Transportation, Federal Highway Administration, Offices of Research and Development, Implementation Division.
Schnaid, F. & Houlsby, G. T. 1992. Measurement of the properties of sand in a calibration chamber by the cone pressuremeter test. *Géotechnique,* 42**,** 587-601.
Schneider, J., Xu, X. & Lehane, B. 2008. Database Assessment of CPT-Based Design Methods for Axial Capacity of Driven Piles in Siliceous Sands. *Journal of Geotechnical and Geoenvironmental Engineering,* 134**,** 1227-1244.
Schneider, J. A., White, D. J. & Lehane, B. M. 2005. The influence of effective area ratio on shaft friction of displacement piles in sand. *Frontiers in Offshore Geotechnics.* Taylor & Francis.
Schofield, A. N. 1980. Cambridge Geotechnical Centrifuge Operations. *Géotechnique,* 30**,** 227-268.
Sharp, M. K., Dobry, R. & Phillips, R. 2010. CPT-based evaluation of liquefaction and lateral spreading in centrifuge. *Journal of geotechnical and geoenvironmental engineering,* 136**,** 1334-1346.
Sheng, D., Axelsson, K. & Magnusson, O. Stress and strain fields around a penetrating cone. *In:* BALKEMA, R., ed. In: Proceedings of the 6th International Symposium on Numerical Models in Geomechanics – NUMOG-VI, , 1997 Montreal, Canadan. 456–65.

Skempton, A. W. 1959. Cast In-Situ Bored Piles in London Clay. *Géotechnique,* 9**,** 153-173.
Sladen, J. A. 1989. Problems with interpretation of sand state from cone penetration test. *Géotechnique,* 39**,** 323-332.
Swinianski, J. & Sawicki, A. 1991. A model of soil–pile interaction owing to cyclic loading. *Canadian Geotechnical Journal,* 28**,** 11-19.
Taha, M. R., Abbas, J. M., Shafiqu, Q. S. M. & Chik, Z. H. 2009. The performance of laterally loaded single pile embedded in cohesionless soil with different water level elevation. *Journal of Applied Sciences,* 9**,** 909-916.
Tempel, J., V & Molenaar, D., P 2002. Wind turbine structural dynamics – a review of the principles for modern power generation, onshore and offshore. *Wind Engineering,* 26**,** 211–220.
Terzaghi, K. 1943. *Theoretical Soil Mechanics,* New York, Wiley.
Terzaghi, K. 1955. Evalution of Conefficients of Subgrade Reaction. *Geotechnique,* 5**,** 297-326.
Thorel, L. 2013. Centrifuge Modelling of foundations subjected to cyclic loading. *Centrifuge Modelling of foundations subjected to cyclic loading,* pp. 45-76.
Thornton, C. 2000. Numerical simulations of deviatoric shear deformation of granular media. *Géotechnique,* 50**,** 43-53.
Thornton, C. & Antony, S. 2000. Quasi-static shear deformation of a soft particle system. *Powder technology,* 109**,** 179-191.
Ting, J., Corkum, B., Kauffman, C. & Greco, C. 1989. Discrete Numerical Model for Soil Mechanics. *Journal of Geotechnical Engineering,* 115**,** 379-398.
Tjok, K. M., Li, Y., Audibert, J. M. E. & Cao, J. 2005. Validation of the use of beam-column method for suction caisson design. *Frontiers in Offshore Geotechnics.* Taylor & Francis.
Tricklebank, A. H. 2008. Briefing: Offshore wind energy-a challenge for UK civil engineering. *Proceedings of the ICE - Energy,* 161**,** 3-6.
Trochanis, A. M., Bielak, J. & Christiano, P. 1991. Three-dimensional nonlinear study of piles. *Journal of Geotechnical Engineering,* 117**,** 429-447.
Tuladhar, R., Maki, T. & Mutsuyoshi, H. 2008. Cyclic behavior of laterally loaded concrete piles embedded into cohesive soil. *Earthquake Engineering & Structural Dynamics,* 37**,** 43-59.
Vallejo, L. & Lobo-Guerrero, S. 2005. DEM analysis of crushing around driven piles in granular materials. *Géotechnique,* 617-623.
Verdure, L., Garnier, J. & Levacher, D. 2003. Lateral Cyclic Loading of Single Piles in Sand. *International Journal of Physical Modelling in Geotechnics,* 3**,** 17-28.
Vesić, A. S. 1972. *Expansion of cavities in infinite soil mass,* Durham, N.C., Duke University.
Wakai, A., Gose, S. & Ugai, K. 1999. 3-D elasto-plastic finite element analyses of pile foundations subjected to lateral loading. *Soil and Foundations,* 39**,** 97-111.
Wang, J. & Zhao, B. 2014. Discrete-continuum analysis of monotonic pile penetration in crushable sands. *Canadian Geotechnical Journal,* 51**,** 1095-1110.

Wehnert, M. & Vermeer, P. 2004. Numerical analyses of load tests on bored piles. *Numerical methods in geomechanics–NUMOG IX***,** 505-511.
Wei, L. 2004. *Numerical simulation and field verification of inclined piezocone penetration test in cohesive soils.* Tongji University, China, 2000.
Wei, L., Abu-Farsakh, M. Y. & Tumay, M. T. 2005. Finite-element analysis of inclined piezocone penetration test in clays. *International Journal of Geomechanics,* 5**,** 167-178.
Welch, R. C. & Reese, L. C. 1972. Lateral load behavior of drilled shafts. University of Texas at Austin.
Whitaker, T. & Cooke, R. W. An investigation of the shaft snd base resistance of large bored piles in London clay. Proceeding Symposium on Large Bored Piles, ICE, 1966 London. 7-49.
White, D. J. & Bolton, M. D. 2004. Displacement and strain paths during plane-strain model pile installation in sand. *Géotechnique,* 54**,** 375-397.
White, D. J. & Lehane, B. M. 2004. Friction fatigue on displacement piles in sand. *Géotechnique,* 54**,** 645-658.
Wichtmann, T. 2005. *Explicit accumulation model for non-cohesive soils under cyclic loading.*
Wiemann, J. 2007. *Bemessungsverfahren für horizontal belastete Pfähle: Untersuchungen zur Anwendbarkeit der py Methode*, Verlag Glückauf.
Yang, Z., Jardine, R., Zhu, B. & Rimoy, S. 2013. Stresses Developed around Displacement Piles Penetration in Sand. *Journal of Geotechnical and Geoenvironmental Engineering,* 140**,** 04013027.
Yang, Z. & Jeremić, B. 2002. Numerical analysis of pile behaviour under lateral loads in layered elastic–plastic soils. *International Journal for Numerical and Analytical Methods in Geomechanics,* 26**,** 1385-1406.
Yu, F. 2004. *Behavior of large capacity jacked piles.* Ph.D, University of Hong Kong.
Yu, H.-S. 2013. *Cavity expansion methods in geomechanics*, Springer Science & Business Media.
Yu, H., Herrmann, L. & Boulanger, R. 2000. Analysis of Steady Cone Penetration in Clay. *Journal of Geotechnical and Geoenvironmental Engineering,* 126**,** 594-605.
Yu, H. & Houlsby, G. 1991. Finite cavity expansion in dilatant soils: loading analysis.
Yu, H. S. 2006. The First James K. Mitchell Lecture In situ soil testing: from mechanics to interpretation. *Geomechanics and Geoengineering,* 1**,** 165-195.
Zhang, L., Silva, F. & Grismala, R. 2005. Ultimate Lateral Resistance to Piles in Cohesionless Soils. *Journal of Geotechnical and Geoenvironmental Engineering,* 131**,** 78-83.
Zhang, L. M. & Wang, H. 2007. Development of Residual Forces in Long Driven Piles in Weathered Soils. *Journal of Geotechnical and Geoenvironmental Engineering,* 133**,** 1216-1228.
Zhang, L. M. & Wang, H. 2009. Field study of construction effects in jacked and driven steel H-piles. *Géotechnique,* 59**,** 63-69.

Zhang, Y. & Cundall, P. A. Numerical simulation of slow deformation. Proc.,Symp. On the Mechanics of Particulate Media, 10th National Congress on Applied Mechanics, 1986 Austin,Tex.

Zhang, Z. & Wang, Y.-H. 2015. Three-dimensional DEM simulations of monotonic jacking in sand. *Granular Matter,* 17**,** 359-376.

Zhao, X. & Evans, T. 2009. Discrete Simulations of Laboratory Loading Conditions. *International Journal of Geomechanics,* 9**,** 169-178.

Zhou, J., Jian, Q.-W., Zhang, J. & Guo, J.-J. 2012. Coupled 3D discrete-continuum numerical modeling of pile penetration in sand. *Journal of Zhejiang University SCIENCE A,* 13**,** 44-55.

Zhu, B. T., Jardine, R., J. & Foray, P. 2009. The use of miniature soil stress measuring cells in laboratory applications involving stress reversals. *Soils and Foundations,* 49**,** 675-688.

Appendix I: (Conference paper: A 2D DEM monopile model under combined loading condition)

A 2D DEM mono-pile model under combined loading condition

N. Duan
Department of Civil, Environment & Geomatic Engineering, University College London, Gower Street, London WC1E6BT, UK

Y.P. Cheng
Department of Civil, Environment & Geomatic Engineering, University College London, Gower Street, London WC1E6BT, UK

ABSTRACT: This paper presents a 2D-Discrete Element Method (DEM) model that is used to study situations when vertical, lateral and combined loads are applied to a rigid mono-pile. At present, mono-pile foundations are widely used to support tall and heavy wind turbines, which are subjected to significant wind and wave actions. A safe design must address issues such as rotations and changes in soil stiffness subject to these loading conditions. Design guidance on the issue is limited, as well as the availability of laboratory and field test data. The interpretation of these results in sand, such as the relation between loading and displacement, relies mainly on empirical correlations to pile properties. Regarding numerical models, only data from Finite Element Method (FEM) can be found. They are not comprehensive enough, and most of the FEM results are sensitive to input parameters. Micro scale behaviour, such as movement and densification of discrete particles near a pile could change the mechanism of the soil-structure interaction. A DEM model was used in this paper to study the combined loading behaviour. By explicitly considering the particulate nature of the granular sand around a model pile, the micro-mechanism governing the complex soil structure was investigated. Verification of the DEM model was carried out by comparing simulation data against a model pile. Analyses of the model pile under pure vertical, pure lateral and combined loads are presented. A discussion about the permanent accumulated pile displacements caused by the combined loads is presented, together with analyses on the sand micromechanics. They should offer insights on further research to optimise the design of mono-pile foundations to resist live loads in service.

1 INTRODUCTION

Pile foundations are widely used to support various types of structures for situations when shallow foundations undergo excessive settlements or have insufficient bearing capacity. These piles are not only used to support vertical loads, but also lateral loads and a combination of both vertical and lateral loads. According to the current practice, piles are independently analysed first for the vertical load to determine their bearing capacity and settlement and then for the lateral load to determine the flexural behaviour (Anagnostopoulos & Georgiadis 1993). This approach, assuming the unrelated vertical and lateral pile response, is not comprehensive. Studying the interaction effects due to combined vertical and lateral loads for a systematic analysis, therefore it is essential.

The amount of literature on the effects of combined loads is scare. There is hardly any concerted effort to study the influence of vertical loads on the lateral response of piles, which is more appropriate to the situation of mono-pile. And it is very difficult to make clear the soil behaviour from the site experiments. The limited research based on analytical approaches (Goryunov 1973) revealed that for a given lateral load, the presence of vertical load increases the lateral deflection of the pile head. But laboratory testing Anagnostopoulos and Georgiadis (1993) suggested a decrease in the lateral deflection under the presence of vertical loads. Lee et al (2011) summarised all the results and proposed lateral deflection of the model pile head increased with increasing axial load.

The methods of analysis commonly used in predicting the behaviour of piles under pure axial loads could be categorized into: (a) subgrade reaction method (b) elastic continuum approaches, and (d) FEM (Karthigeyan et al. 2006, Karthigeyan et al. 2007). However, experimental and field investigations suggest a decrease in lateral deflection with the combination of vertical loads. Anagnostopoulos & Georgiadis (1993) attempted to explain this phenomenon through an experimental model supported

by 2D FEM analysis. They reported that the modified state of the soil stresses and the local plastic volume changes in the soil mass under the combined vertical and lateral loads cannot be taken into account by the conventional subgrade reaction analysis, nor the elastic half space methods.

However there are limitations on FEM, as soil is not always a continuum. The particles of soil may slide, rotate, deform or crush; some of them may also move across the space through the voids, or they lock in certain locations forming soil arch. There are example features that cannot be modelled easily by FEM. In view of the above issues, the 2D DEM was used in this research to analyse the combined loading effect, and the present paper focuses on the influence of axial load on the lateral response of a pile. The details of model setup, the parameters used and the verification of the model against laboratory testing cases are presented. Combined loading tests were performed for axial loads equal to 0%, 33%, 66%, and 83% of the ultimate axial capacity (defined as the load corresponding to a settlement equal to 10% of the pile diameter) of the model pile.

2 NUMERICAL MODEL

The DEM is referred to, by Cundall & Strack (1979), as the particular discrete element scheme that uses deformable (soft) contacts and an explicit time-domain solution of the original equations of motion. The Particle Flow Code in 2-Dimensions (PFC2D) is a programming code which is developed by Itasca. This software uses the DEM to simulate the movement and interaction of circular particles and observe their strain and fracturing behaviour, and all DEM programs allow finite displacements and rotations of discrete bodies, including complete detachment (Cheng 2004). PFC2D can model either bonded (cemented) or unbounded (granular) group of particles (Itasca 2008), and also particles of any shape using the clump logic. Therefore it is a powerful tool to simulate complex problems in solid mechanics, rock mechanics, and granular flow. At the same time, it allows for a detailed study of the micro-mechanics, such as the force networks formed by a granular media.

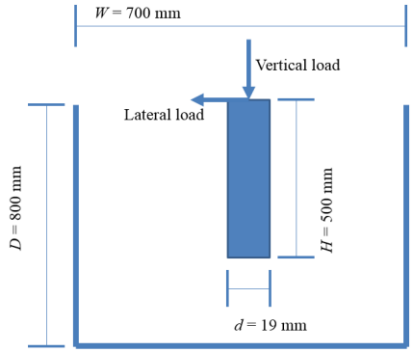

Figure 2 Schematic view of the PFC model

All DEM analyses in this investigation were performed using the 2D PFC program. Figure 1 shows a sketch for analysis of pile-soil interaction and Figure 2 gives the particles size distribution. The pile was treated as a rigid material in view of high rigidity of a typical monopile, hence the consideration of bending moment was ignored. The vertical load and lateral load was applied to the ground surface on the top of pile.

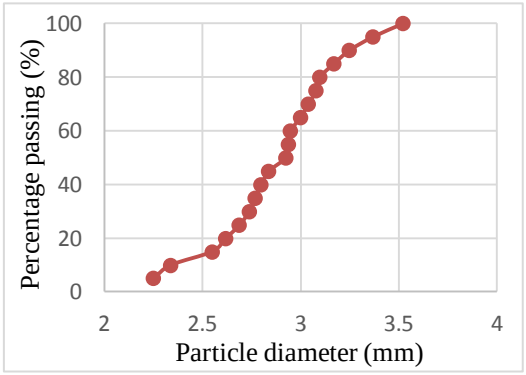

Figure 1 Particles size distribution in DEM simulation

2.1 *Validation of the numerical model employed in the program*

2.1.1 *Procedure of model generation*

The validity of the numerical model was verified by checking the pile load test data against a comprehensive published case. The laboratory tests performed by Anagnostopoulos & Georgiadis (1993) were a single pile under both vertical and lateral loads applied to the pile head at ground elevation.

In the 2D PFC model, the boundary was first set in such a way that the size of the model was the same as that of Anagnostopoulos & Georgiadis (1993). Rigid walls were used to model the boundary. The second step was the generation of particles. The particles were given properties as showed in Table 1. At the first stage, when the initial average porosity was nearly reached, the model was cycled to equilibrium. At the second stage, the gravity was added, and the PFC model was cycled to equilibrium again. This moment, the porosity was the final average porosity. At the third stage, before the pile was formed, the particles inside the same area were deleted. In this research, “clump” was used to model the rigid pile with a finite surface roughness. The system was then cycled to equilibrium again with the pile in place. Vertical and lateral forces were then applied to the top of pile directly.

2.1.2 *Input parameters*

Table 1 shows the model parameters. From the 2D PFC manual, the particle normal stiffness is equal to twice the particle Young’ modulus.

Table 1 Input parameters for DEM simulations

Density of sand particles (kg/m^3)	2650
Particle diameters, d (mm)	Fig. 2
Sand grain size, d_{50} (mm)	2.925
Friction coefficient of the particles μ(-)	0.5
Sand Young's Modulus, E_p(Pa)	1e7
Contact normal stiffness of particles, k_n (N/m)	2e7
Particle stiffness ratio (k_s/k_n)	1
Contact normal stiffness of walls, k_n (N/m)	2e7
Initial average porosity	0.28
Final average porosity	0.19
Bulk unit weight γ_{bulk} (kN/m^3)	18

2.1.3 *Lateral stress distribution*

Figure 3 shows that the lateral stress distributions acting on the pile and on the far wall are similar. It means this model is reasonable. Using the trendline shown in Figure 3 and the bulk unit weight calculated from the average porosity of the particles, the coefficient of earth pressure is approximated to be 0.8. The fluctuation around the pile tip at 0.5m depth was an error induced by deleting particles in an area that was slightly smaller than the pile size.

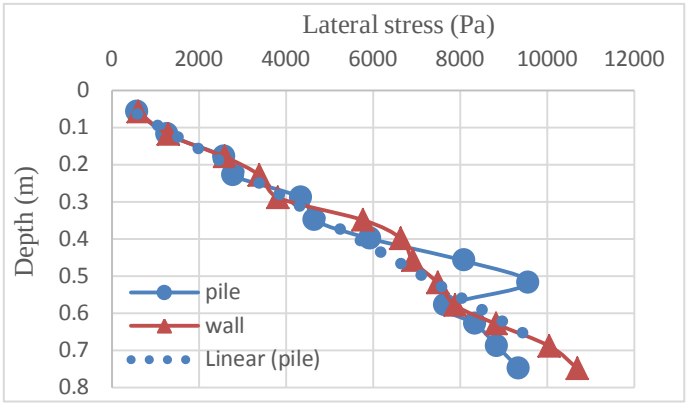

Figure 3 Lateral soil stress distribution in front of the pile at static state

2.1.4 *Displacement VS Force*

The sequence of the load application used in the current DEM analysis is the same as that used in the laboratory tests (Anagnostopoulos & Georgiadis 1993). The comparison between the test data and the predicted results of piles under pure vertical load and combined vertical and lateral loads are shown in Figure 4. Figure 4(a) shows that the comparison is very good both at small and larger load levels for vertical response of pile. For the lateral responses of the pile, shown in Figure 4(b), the comparison is good at a smaller horizontal load, but the percentage difference increases at the larger load levels. Up to a lateral displacement equal to 0.33% of the pile diameter, the difference between the measured and predicted pile loads is less than 6.25%. At a larger displacement equal to 0.84% of the pile diameter, the difference increases to approximately 54.28%. This deviation is acceptable in view of the many uncertainties in choosing the sand properties in the analysis, and also due to the rigid assumption of the monopile model. And the other main reason is that the actual experiment was performed in three-dimensions. Due to the good match at the relationship between vertical load and axial displacement, it is concluded that the numerical scheme adopted in the present investigation should be capable of modelling the pile-soil interaction under pure vertical load, lateral load, and a combination of vertical and lateral loads.

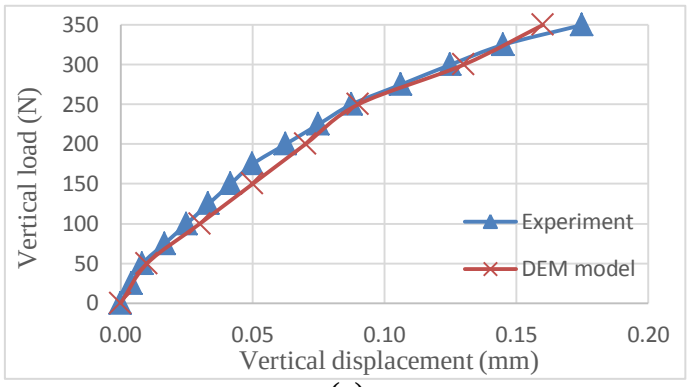

(a)

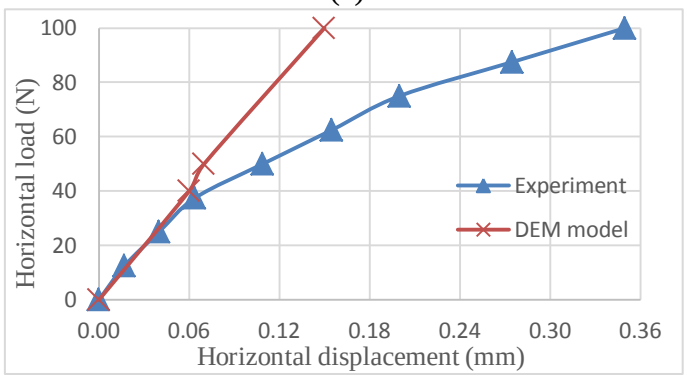

(b)

Figure 4 Comparison of DEM predicted vertical and lateral response of pile with experimental test data of Anagnostopoulos & Georgiadis (1993)*: (a) vertical response of pile; (b) lateral response of pile*

3 COMBINED LOADS RESULT AND DISCUSSION

The analyses were performed to study the influence of the vertical load on the lateral response of pile. A series of analyses have been carried out to study the behaviour of piles under pure lateral loads and the influence of different levels of vertical load on the lateral responses of piles. The details of the PFC2D model and the results are discussed in this section.

3.1 *Macroscopic load displacement data*

In this study, a particular vertical load was applied first, and then, lateral loads were applied incrementally to the pile head and then the model was carefully cycled to equilibrium at each step while the vertical load was kept constant.

The ultimate vertical load (V_{ult}) capacity of a single pile was evaluated a priori by separate numerical analyses. Then the response of piles under combined loading was analysed separately with the vertical load equal to zero (pure lateral load case), $0.33V_{ult}$ and $0.66V_{ult}$. The ultimate vertical load capacity was estimated as 1200 N, and the ultimate horizontal load (H_{ult}) capacity of a single pile was 400 N.

Figure 5 plotted the different curves of model pile head lateral deflection versus lateral load for the combined loading simulations under axial load V equal to 0%, 33% and 66% of the ultimate axial load V_{ult}, where the value of V_{ult} was obtained from the pure axial loading test. $0V_{ult}$ means that there was no axial loading applied to the pile head. It is seen from this figure that the vertical load has only a marginal influence on the lateral response of pile.

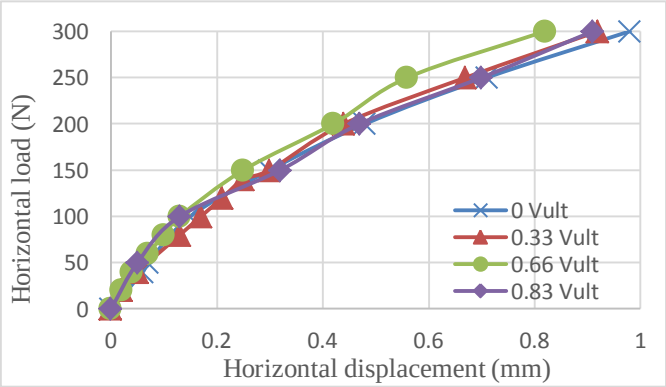

Figure 5 Lateral load-deflection behaviour of a pile in sands

The results shown in Figure 5 is very similar to the FEM reults of Karthigeyan et al. (2006). Compare with the FEM's outcome, the trend of DEM model is similar and resonable. In gernal, the larger is the vertical load (up to $0.66V_{ult}$), the smaller is the horizontal displacement induced by the horizontal load. The interesting phenomenon in Figure 5 is the line of $0.83V_{ult}$. This line is not behind $0.66V_{ult}$, but is between 0Vult and 0.6Vult. This is the same as Karthigeyan et al. (2006); the line of $0.83V_{ult}$ is in front of 0.66Vult.

Since the lateral deflection of the model pile head decreases with increasing axial load, this means that the presence of an axial load is good to the lateral capacity of driven pile in sand. Therefore, it is usually not necessary to consider the effect of axial loads in the design of laterally loaded pile in sand.

Following Karthigeyan et al. (2006), the Percentage Improvement in lateral Capacity (PIC) is defined here in terms of displacement to measure the influence of vertical loads on the lateral response of piles in sands:

$$PIC = \frac{LDNV - LDWV}{LDNV} \times 100$$

where 'LDNV' is the Lateral load Displacement under pure lateral load (with No Vertical load), 'LDWV' is the Lateral load Displacement With Vertical load. The PIC analyses have been summarized in Table 2.

It shows clearly that the lateral capacity of pile in sand improves in general under the presence of vertical loads. The PIC increases (e.g. from 6.1% to 14.3% at a lateral load of $0.75H_{ult}$) when the axial load increases from $0.33V_{ult}$ to $0.66V_{ult}$. When comparing the same level of lateral load, the improvement in lateral capacity becomes bigger under a larger vertical load. It proves that the improvement of pile lateral capacity is generally in proportion to the vertical load. And the increase of horizontal capacity of pile has been obvious even when the vertical and horizontal load are both small.

Table 2 Percentage Improvement in the lateral Capacity (PIC) with respect to different vertical load levels

Vertical load in terms of V_{ult}	Lateral deflection (mm) at lateral load of 0.5 H_{ult}	PIC at lateral load of 0.5 H_{ult}	Lateral deflection (mm) at lateral load of 0.75 H_{ult}	PIC at lateral load of 0.75 H_{ult}
0	0.48	-	0.98	-
0.33	0.44	8.3%	0.92	6.1%
0.66	0.42	12.5%	0.82	14.3%

This impact of vertical load may be attributed to the higher vertical soil stress develop in the soil along the pile surface, which in turn leads to higher lateral stresses acting on the pile. This phenomenon will be explored further in the following sections.

3.2 *Lateral soil stress*

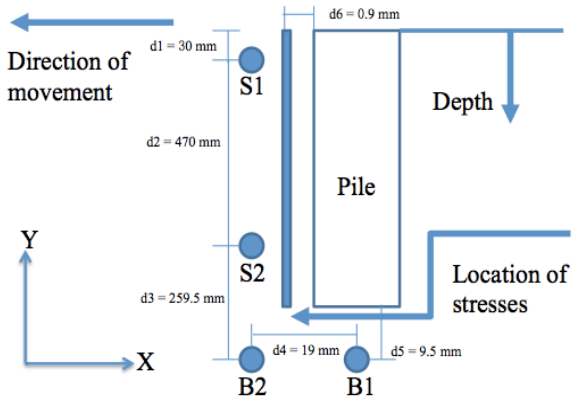

Figure 6 A sketch showing the locations of lateral stress records and trace particles

Figure 6 shows the locations of the four traced particles (S1, S2, B1, B2), and also the locations in front of the pile, at which the lateral soil stress was measured. The distributions of the lateral soil stresses in front of the pile at a specific lateral deflection of $0.75H_{ult}$ are shown in Figure 7. The X-direction and Y-direction movements of the traced particles were recorded and are shown in Figure 8 & 9.

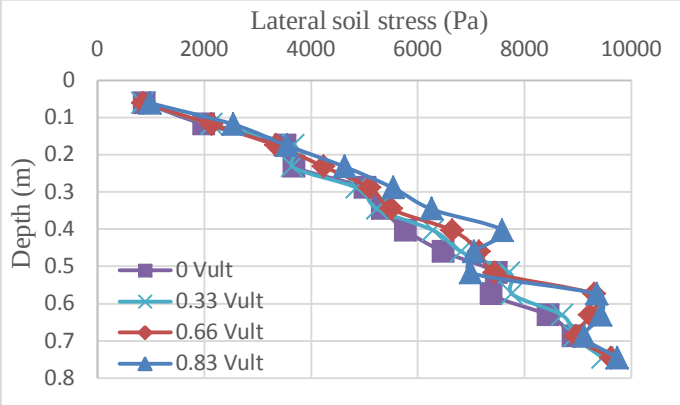

Figure 7 Distributions of lateral soil stress in front of the pile at a lateral deflection of $0.75H_{ult}$ in sand

It is clearly found in Figure 7 that the lateral soil stresses are affected by the existence of vertical loads. The static state was a reference, showing the stress distribution when the pile was not under any load. Above 0.2m depth, the lateral stress did not increase with existence of vertical load, in fact the lateral stress decreases a little. Below 0.2m depth, the horizontal stress increases. This increase happens only between 0.2m and 0.45m depth along the pile. Below 0.7m depth under the pile, the lateral stress remains more or less the same with the existence of larger vertical load. Above 0.4m depth, where also was the centre of pile rotation, the lateral stress increased with the vertical loads. The interesting phenomenon took place around the pile tip at 0.5m depth. When the pile was under smaller vertical loads ($\leq 0.33V_{ult}$), the lateral stress at this depth remained approximately the same. However, when it was under larger vertical loads, a smaller lateral stress was recorded at this depth. In general a larger lateral stress was induced along the pile with the existence of axial load. This implies that a larger force was needed in order to move the pile head to the same level of deflection of e.g. $0.75H_{ult}$, which means a higher lateral capacity. Figure 7 is related to Figure 5, it can be used to explain the macro phenomenon from the micro mechanics. This is also similar as Karthigeyan et al. (2006).

3.3 *Microscopic movement of traced particles*

Further analysis is performed by tracing the X-plane and Y-plane displacements of four representative particles in this pile model, the results are shown in Figure 8 & Figure 9. According to the pile model in Figure 6, Particle B1 is located immediately under the pile in the pile's vertical central axis, and the particle B2 is chosen at the same Y-level of B1. Particle S2 is located slightly above B2 but along the pile shaft. Particle S1 is also along the pile shaft but closer to the soil surface.

Figure 8 shows the variations on the displacements of the four particles in both directions under pure lateral load. In Figure 8, X-plane means the horizontal direction and Y-plane means the vertical direction. Figure 8(a) is the X-direction summary of all of the four particles traces. It can be seen that only particle S1 moved to left, although the pile was moved to left, all other particles moved to the right. This is because S2, B1 and B2 are all near or below the centre of rotation of the pile. Form the record data, the centre of rotation of the pile was not a constant but varied within a small range at around 4:1, the length above the centre is four times bigger than the length under. It can be seen that the particle S2 along the pile moved more than B1 and B2 under the pile. And particle B2 moved more than B1 due the distance away from the centre of the pile.

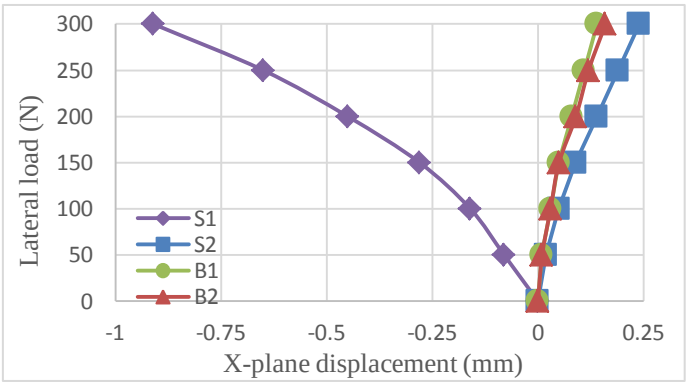

(a)

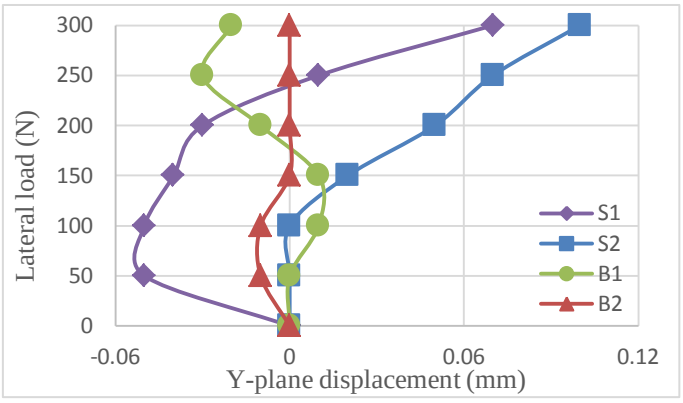

(b)

Figure 8 Displacement of traced particle under pure lateral load (a) X-displacement of four particles, (b) Y-displacement of four particles

In Figure 8(b) showing the vertical displacements, particles B1 and B2 remain nearly unmoved. S2 moved upwards. S1 moved downwards first and then moved upwards as well. The depth of B1 and B2 were same and under the pile, perhaps these two particles were too deep, so the two particles B1 and B2 were not affected too much. In contrast, S1 was situated near the soil surface, it shows that the soils settled and then followed by dilation. And the movement of particle S2, above B1 and B2, was mainly dominated by dilation.

However, a different the lateral pile response was observed with a vertical load of $0.33V_{ult.}$ The results

are shown in Figure 9. The X-direction displacements of three particles (S1, B1, B2) are now similar. In the vertical direction from Figure 9(b), all particles S2, B1 and B2 moved downwards. S2 settled with vertical load instead of dilated. B1 was immediately under the pile so settled more than B2. S1 near the surface moved slightly downwards and then slightly upwards. In general, the movement of particle S1 followed a similar trend regardless of vertical load. However, all other particles were affected much by vertical load. These settlements of the particles near the pile end should increase the density of the soil around the pile, leading to a higher capacity.

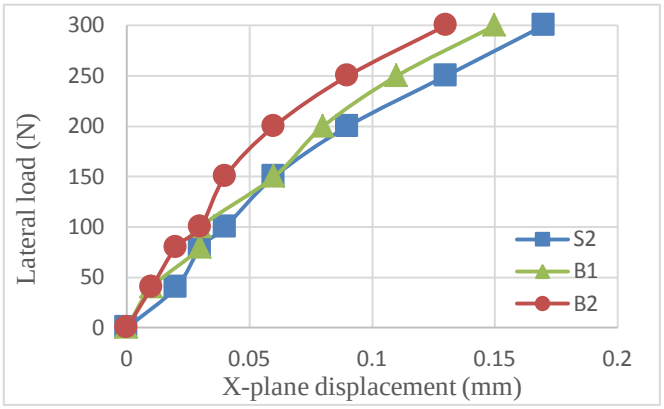

(a)

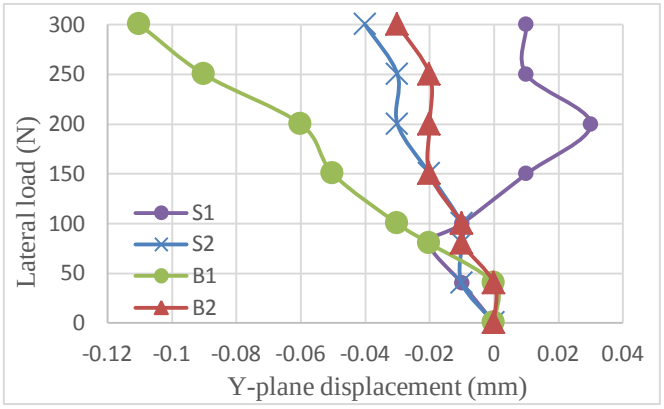

(b)

Figure 9 Displacements of traced particle under 0.33Vult (a) X-displacement of three particles (b) Y-displacement of four particles

Tracing representative particle displacements demonstrates well that pile penetration is a dynamic process and shows how the sand has been influenced during pile penetration.

4 CONCLUSION

In this research, DEM simulations have been adopted in analysing the phenomenon of a rigid pile under the combined loadings conditions from the microscopic and the macroscopic points of view. The main conclusions can be drawn as follows:

1. The vertical load has a profitable influence on the lateral response of piles embedded in sand. However, this influence depends on the sequence of loading, hence this result is only valid for the condition discussed in this paper.

2. The maximum percentage improvement in lateral capacity is up to 14.3% in this model. Even at the bigger vertical load condition, the lateral capacity improvement remains at 14.3%. This is attributed to the decline of additional lateral soil stresses around the pile tip in front of the pile.

3. The test results imply that it is conservative to design piles assuming that there is no interaction between axial and lateral loads. The test results also show that the larger the axial load, the bigger the ultimate lateral load capacity of the model pile subjected to combined loads. Therefore, the consideration of the effect of axial loads in the design of laterally loaded piles driven in sand is not necessary.

4. This DEM method may provide a foundation for the further study of the micro mechanisms of soil variation around a pile in the course of combined loads. The traces of particles movements have showed that there were obvious settlements of the soil particles near the bottom of the pile when there is vertical load. This should lead to soil densification and hence an increase in the lateral pile capacity under the combined loading condition.

Further data regarding the impact of boundary condition, pile stiffness, aspect ratio of pile and the density of soils, etc., will be shown in the long version of this paper.

References

Anagnostopoulos, C. & Georgiadis, M. 1993. Interaction of axial and lateral pile responses. J Geotech Eng, 119(4), 793–798.

Cheng, Y.P. 2004. Micromechanical investigation of soil plasticity. PhD thesis, Cambridge University.

Cundall, P. & Strack, O. 1979. A discrete numerical model for granular assemblies. Geotechnique, 1, 47–65.

Goryunov, B. 1973. Discussion on analysis of piles subjected to the combined action of vertical and horizontal Loads. J Soil Mech Foundation Eng, 3, 6–8.

Itasca, 2008. PFC User Manual, Version 4.0.

Karthigeyan, S., Ramakrishna, V.V.G.S.T. & Rajagopal, K. 2006. Influence of vertical load on the lateral response of piles in sand. Computers and Geotechnics, 33(2), 121–131.

Karthigeyan, S., Ramakrishna, V.V.G.S.T. & Rajagopal, K. 2007. Numerical Investigation of the Effect of Vertical Load on the Lateral Response of Piles. J Geotech Geoenviron Eng, 133(5), 512–521.

Lee, J., Prezzi, M. & Salgado, R. 2011. Experimental Investigation of the Combined Load Response of Model Piles Driven in Sand. Geotechnical Testing Journal, 34(6), 1–15.